CNR Istituto di Cristallografia

UNIVERSITY OF CATANIA

DEPARTMENT OF CHEMICAL SCIENCES

INTERNATIONAL PhD IN CHEMICAL SCIENCES – XXXIII CYCLE

MARIE CURIE fellowship – EU COFUND project "INCIPIT"

SARA GARCÍA VIÑUALES

Silybins as multi-target proteostasis rescuers in Alzheimer's Disease and Type II Diabetes Mellitus

PhD Thesis

Academic cycle 2017-2020

CNR tutor: Dr. Danilo Milardi

University tutor: Prof. Roberto Purrello

PhD Coordinator:
Prof. Salvatore Sortino

TABLE OF CONTENTS

Abstract

A defective protein folding and its abnormal aggregation and accumulation is the central pathogenic event in Protein Conformational diseases (PCDs), such as Alzheimer`s Disease (AD) and Type II Diabetes Mellitus (T2DM), which are characterized by the accumulation of the amyloid-β (Aβ) peptide in neuronal tissues and islet amyloid polypeptide (IAPP) in pancreatic β-cells, respectively.[1] So far, all the designed anti-aggregating drugs (amyloid hypothesis) have failed in clinical trials and the latest studies suggest that pathological conditions occur when the equilibrium between production and clearance of the involved protein results unbalanced.[2] For this reason, currently, new drugs are designed to restore the proteostasis network (PN) targeting any of its components and not just simple anti-aggregating compounds. However, due to the multifactorial nature of protein diseases, it may be difficult to find effective drugs by screening molecules on a single target, and very few molecules, if any, selected by using this strategy, have shown to have the potential to be pipelined to clinical trials.

Due to the significant interconnection between AD and T2DM which share common pathogenic mechanisms,[3] we have proposed here a new multi-target strategy against both diseases, to profile small molecules for their potential to be used as Aβ/hIAPP proteostasis rescuers. In particular, we have investigated the cytoprotective effect of two natural compounds (Silybin A and Silybin B) extracted from the plant *Silybum marianum.*

Both compounds have shown to halt and rescue the cytotoxicity of Aβ oligomers in differentiated SH-SY5Y neuroblastoma cells, a neuron-like cell system. The use of several spectroscopic, biophysical, biochemical, and computational techniques has allowed us to establish with high-level of accuracy the molecular reasons that entail their cytoprotective effect and the important role of the stereochemistry in this processes; in particular, silybins may i) inhibit Aβ/hIAPP aggregation; ii) counteract amyloid-mediated membrane disruption, iii) enhance 20S proteasome activity, iv) foster ubiquitin signaling and v) protect from oxidative stress.

However, despite the high potential of silybins as anti-AD and -T2DM drugs, their use is limited due to their scarce solubility and bioavailability. We have overcome these limitations by conjugating silybins with a trehalose moiety through a phosphate linker, following a pro-drug approach. This approach allows the administration of higher amounts of the pro-drug and the progressively release of the parental compound on a time scale of days. In addition, the synthesized pro-drugs are not devoiced of activity but, rather, partially maintain or, in some cases, even increase the ability of silybins against the studied targets. The activity of the pro-drugs represents an additional advantage, addressing not only the solubility related problem and permitting the delivery of the drug, but furthermore, being a part of the whole drug system where both drug and pro-drug present desirable activities in restoring proteostasis.

Abbreviations

Aβ	Amyloid beta peptide
ABTS	2,2'-azinobis(3-ethylbenzothiazoline -6-sulfonic acid)
ACE	Angiotensin converting enzyme
AC	Amyloid core
AD	Alzheimer`s Disease
ADDL	Aβ-Derived Diffusible Ligand
AFM	Atomic force microscopy
ALP	Autophagy-lysosome pathway
ALS	Amyotrophic lateral sclerosis
APP	Amyloid precursor protein
APF	Annular protofibril
ATP	Adenosine triphosphate
αs	α-synuclein
BBB	Blood-brain barrier
CE	Cyanoethyl
CHC	Central hydrophobic cluster
CD	Circular Dichroism
ChT-L	Chymotryptic-like
CP	Core Particle
CPE	Carboxypeptidase E
CLM	Crystallization-like model
CMA	Chaperone-mediated autophagy
CNS	Central Nervous System
CNT	Classical nucleation theory
CSF	Cerebrospinal fluid
DCI	4,5-dicyanoimidazole
DIEA	Diisopropylethylamine
DLS	Dynamic light scattering
DM	Diabetes mellitus
DNA	Deoxyribonucleic acid
DSSP	Dictionary of Secondary Structure of Proteins
DTM	tert-Butyldithiomethyl
DTT	Dithiothreitol
DUBs	Deubiquitinating enzymes
δ	Asphericity
E1	Ubiquitin-activating enzyme
E2	Ubiquitin-conjugation enzyme
E3	Ubiquitin-ligase enzyme
EELS	Electron energy loss spectroscopy
ER	Endoplasmic reticulum
ECE	Endothelin-converting enzyme
FDA	United States Food and Drug Administration
GDP	Gross domestic product
GUV	Giant Unilamellar Vesicle
HD	Huntington`s Disease
HPLC	High performance liquid chromatography
HSP	Heat Shock Protein
HSQC	Heteronuclear Single-Quantum Correlation spectroscopy
IAPP	Islet amyloid polypeptide or amylin
IDE	Insulin degrading enzyme
IDF	International diabetes federation
IDP	Intrinsically disordered protein
IDR	Intrinsically disordered region
LRP1	Lipoprotein receptor related protein 1
LTP	Long term potentiation
LUV	Large Unilamellar Vesicle
LYS	Lysozyme
MAP	Microtubule-associated protein
MD	Molecular dynamics
MM	Molecular mechanics

MP Metalloprotease

MTT 3-(4,5-Dimethylthiazol-2-yl)-2,5-diphenyltetrazolium bromide

MW Molecular weight

NCC Nucleated conformational conversion

NEP Neprilysin

NFT Neurofibrillary Tangles

NMR Nuclear magnetic resonance

NOE Nuclear Overhauser Effect

NOESY Nuclear Overhauser Enhancement Spectroscopy

oAβ Aβ oligomer

PAGE Polyacrylamide gel electrophoresis

PC2 Pro-hormone convertase 2

PC3 Pro-hormone convertase 1/3

PCD Protein conformational disease

PD Parkinson's disease

PDB Protein data bank

PGPH Peptidylglutamyl-peptide hydrolyzing

PHF Paired helical filament

PN Proteostasis network

POPC phopsphatidylcholine

POPS phosphatidylserine

PQC Protein quality control

PF Protofibril

PR Proline-rich

PPi Pyrophosphate

PPII Poly-L-proline II

PrP Prion protein

RAGE Receptor for advanced glycation end products

Rg Radius of gyration

RMSD Root-mean-square deviation of atomic positions

RNS Reactive nitrogen species

ROS Reactive oxygen species

RP Regulator particle

SA Systemic amyloidosis

SAA Serum amyloid A

SAPPHIRE States and pathways projected with high resolution

SD Standard deviation

SDS Sodium dodecyl sulfate

SEM Scanning electron microscopy

Sil A Silybin A

Sil B Silybin B

SP Senile plaque

STD Saturation transfer difference

SUV Small unilamellar vesicles

tau Tubule-associated unit

TBHP tert-Butyl hydroperoxide

TEAC Trolox equivalent antioxidant capacity

TEM Transmission electron microscopy

TH Trehalose

ThT Thioflavin T

T-L Tryptic-like

T1DM Type I diabetes mellitus

T2DM Type II diabetes mellitus

Ub Ubiquitin

UBP Ubiquitin-binding protein

UCH-L1 Ubiquitin carboxyl-terminal hydrolase L1

UPS Ubiquitin-proteasome system

WHO World health organization

Chapter 1. Introduction

1.1. Protein misfolding and amyloid diseases

In the last two decades, an increasingly large body of evidence has pointed to the misfolding, aggregation, and accumulation of structurally abnormal proteins, termed amyloids, as the common pathogenic mechanism of more than 50 degenerative diseases, known as protein conformational diseases (PCDs) or proteopathies.[4] These disorders include Alzheimer's disease (AD), Parkinson's disease (PD), type II diabetes mellitus (T2DM), and systemic amyloidosis (SA), among others (see table 1).

Each one of these diseases is associated with the aggregation of a specific protein that might occur in a specific or multiple organs. The first group includes maladies as AD or PD, in which amyloid-β/tau or α-synuclein deposits, respectively, are found in the brain, or T2DM, characterized by the accumulation of amylin in the pancreas. By contrast, in systemic amyloidosis, protein aggregates affect multiple organs as the liver or the heart, among others.[1] Depending on the disease, these amyloid deposits are found extracellularly, in the cytosol, or in both intra- and extracellular species. Usually, they are found in the same cellular space where the protein is secreted or resides.[1]

These diseases can be sporadic or familial. Most of the PCD cases belong to the first group and are caused by the stochastic misfolding and aggregation of the protein, which is promoted by an age-dependent decline of the proteostasis network (PN), the cellular machinery responsible for maintaining the proteome integrity. Differently, in some cases, a genetic disorder, i.e. a heritable mutation, causes the misfolding and aggregation of the protein.[5] Despite the advances achieved in our understanding of the complex network of biological mechanisms involved in PCDs, currently, there is no cure for any of these diseases.

Amyloid protein	Clinical syndromes
Amyloid-β peptide (Aβ)	Alzheimer's disease, hereditary cerebral hemorrhage with amyloidosis
Amylin or Islet amyloid polypeptide (IAPP)	Type 2 diabetes mellitus, insulinoma
α-Synuclein (αs)	Parkinson's disease, Multiple system atrophy, Dementia with Lewy bodies
Prion protein (PrP)	Transmissible spongiform encephalopathies (Creutzfeldt-Jakob disease, Fatal insomnia, Gerstmann-Sträussler-Scheinker disease, variant Creutzfeldt-Jakob disease, Kuru, among others)[6]
Tau protein	Tauopathies (Alzheimer's Disease, progressive supranuclear palsy, corticobasal degeneration, frontotemporal dementia with parkinsonism-17, among others)[7]
Huntingtin (polyQ expansion)[8]	Huntington's disease
Lysozyme (LYS)	Lysozyme systemic amyloidosis
β_2-Microglobulin (β_2-m)	Dialysis-related amyloidosis, hereditary visceral amyloidosis
Transthyretin (TTR)	Senile systemic amyloidosis, familial amyloid polyneuropathy, familial amyloid cardiomyopathy, leptomeningeal amyloidosis
Serum amyloid A (SAA)	AA amyloidosis
Immunoglobulin light chains	Light-chain amyloidosis
Immunoglobulin heavy chains	Heavy-chain amyloidosis
Insulin	Injection-localized amyloidosis
Cystatin C	Hereditary cystatin C amyloid angiopathy (HCCAA)[9]
ABri peptide	Familial British dementia
ADan peptide	Familial Danish dementia
Apolipoprotein A-I (ApoAI)	ApoAI amyloidosis
Apolipoprotein A-II (ApoAII)	ApoAII amyloidosis
Apolipoprotein A-I V(ApoAIV)	ApoAVI amyloidosis
Apolipoprotein C-II (ApoCII)	ApoCII amyloidosis
Apolipoprotein C-III (ApoCIII)	ApoCIII amyloidosis
Gelsolin	Familial amyloidosis, Finnish type
Fibrinogen α-chain	Fibrinogen amyloidosis
Calcitonin	Medullary carcinoma of the thyroid
Atrial natriuretic factor	Atrial amyloidosis
Prolactin (PRL)	Pituitary prolactinoma
Medin	Aortic medial amyloidosis
Lactotransferrin	Gelatinous drop-like corneal dystrophy
Odontogenic ameloblast-associated protein (ODAM)	Calcifying epithelial odontogenic tumors
Pulmonary surfactant associated protein C (SP-C)	Pulmonary alveolar proteinosis
Leukocyte cell-derived chemotaxin-2 (LECT-2)	Renal amyloidosis
Galactin 7 (Gal-7)	Lichen amyloidosis, macular amyloidosis
Corneodesmosin (CDSN)	Hypotrichosis simplex of the scalp
Kerato-epithelin (βig-h3)	Lattice corneal dystrophies (type I, type 3A and Avellino type)
Semenogelin-1 (SGI)	Seminal vesicle amyloidosis
Proteins S100A8/A9	Prostate cancer
Enfuvirtide	Injection-located amyloidosis

Table 1. Peptides involved in the formation of amyloid deposits and related proteins. This table has been adapted from Chiti et al. 2017.[1]

1.1.1. Alzheimer's disease

AD is a neurodegenerative disorder of the central nervous system (CNS) characterized by a gradual loss of cognitive function which, finally, leads to a loss of autonomy and total dependence of medical care. From all the dementia cases, 60-70% are associated with AD.[10] It is the most common cause of dementia in elderly people and is strongly associated with aging (32% of people age 85 and older have AD).[11] This pathology is the main cause of disability and dependency of aged people,[12] and it has been listed as the seventh cause of death worldwide and one of the principal causes of morbidity.[11] Nowadays, AD affects a large number of people, and estimations lead to expect a progressively increasing number of cases in the next decades. In fact, according to World Health Organization (WHO), around 50 million people are living with dementia, with an increase of nearly 10 million new cases every year; WHO estimations for the next decades are overwhelming and suggest that worldwide dementia cases will reach 82 million people in 2030 and 152 million in 2050.[10] In addition to the so daunting human costs occasioned by the disease in terms of lost lives, reduction of quality of life, and disability, AD results in dramatic social and economic costs. In point of fact, total global economic costs of dementia were estimated in 2015 at around $ 818 billion, which constitutes 1.1% of global gross domestic product (GDP).[10]

The accumulation of the amyloid-β (Aβ) peptide and the protein tau in neuronal tissues, forming neuritic/senile amyloid plaques (SPs) and neurofibrillary tangles (NFTs) outside and inside neurons, respectively, are considered the hallmarks of AD (see figure 1). In physiological conditions, Aβ peptide is soluble and contributes to the normal function of the brain regulating the activity of hippocampal synapses by stimulating glutamatergic and cholinergic receptors.[13] However, when AD pathology occurs, Aβ peptides self-assemble and accumulate forming SPs. Tubule-associated unit (tau) protein belong to the microtubule-associated protein (MAP) group and its physiological role is to induce and stabilize the assembly of tubulin proteins into microtubules in the brain, allowing the extension of neurites.[14] Once tau protein is expressed, it undergoes different post-translational modifications; however, its abnormal hyperphosphorylation has been identified in AD, with cytosolic hyperphosphorylation levels 3-4 fold higher

than in healthy brains.[15] The ability of tau to bind with microtubules is decreased when tau is phosphorylated. Thus, its abnormal hyperphosphorylation leads to an increase of unbonded tau, being more available for aggregation.[16] Eventually, hyperphosphorylated tau evolves in the formation of insoluble fibers, known as paired helical filaments (PHFs), which accumulate in NFTs, leading to an impaired microtubule assembly, hampering axonal transport and contributing to neurodegeneration.[7] In AD synapses information transfer begins to fall, the number of synapses declines, and neurons death is observed. It is believed that Aβ aggregates interfere in the neurons communication and tau tangles block the transport of nutrients contributing to cell death.[1]

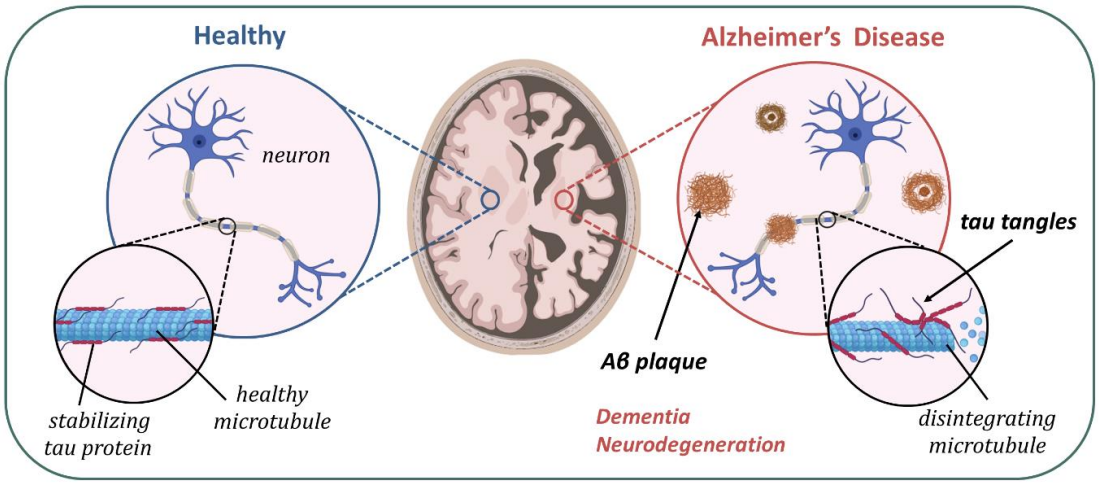

Figure 1. Comparison of a neuron in the healthy brain and Alzheimer's disease with amyloid plaques and tau tangles.

This syndrome is marked by a great complexity at cellular and molecular level, with different brain cells (neurons, microglia, astroglia, and oligodendrocytes) involved and interacting with each other.[17] Aβ deposition is an early event in the development of the disease, preceding brain structural changes and cognitive decline, while tau tangles are formed after Aβ accumulation but also previously to clinical symptoms.[18] Cognitive decline occurs progressively, and it can take much time, even decades, to show the patient recognizable symptoms because of the compensation mechanisms of the brains, making it difficult to identify the disease in its preclinical phase. Thus, when dementia is identified, the pathological development of the disease has already been progressing for many years.[19]

1.1.2. Type II Diabetes Mellitus

Diabetes mellitus (DM) is a chronic metabolic disorder that presents physiological dysfunctions as hyperglycemia, insulin resistance, and insulin deficiency.[20] Depending on the cause of the pathology, it is classified in Type I (T1DM) or Type II Diabetes Mellitus (T2DM), being the second one the most common (90% of all the DM cases).[21] T1DM (also denominated juvenile diabetes or insulin-dependent diabetes) is an autoimmune condition whereby the immune system destroys the pancreatic β-cells, responsible for the secretion of insulin and therefore leading to the lack of this hormone.[22] Differently, T2DM (also known as non-insulin-dependent diabetes or adult-onset diabetes) belongs to the family of PCDs because it is mainly associated with the accumulation of islet amyloid polypeptide (IAPP; also known as amylin) deposits in pancreatic islet cells (see figure 2). IAPP accumulation is believed to cause β cells failure and, in turn, a reduced response to insulin in peripheral tissues (i.e. insulin resistance).[23]

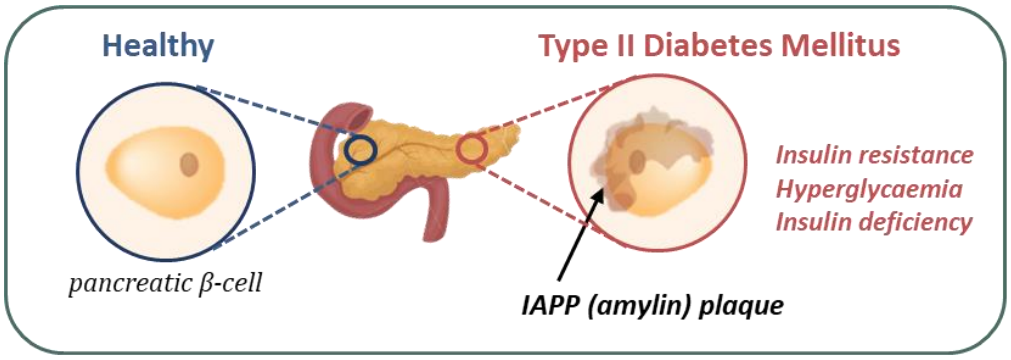

Figure 2. Comparison of pancreatic β-cell in the healthy pancreas and Type II Diabetes Mellitus with amylin plaques.

T2DM is widely associated with obesity and a sedentary lifestyle and its complications lead to premature mortality and lower quality of life. The International Diabetes Federation (IDF) considers diabetes a pandemic, affecting nowadays the alarming number of 463 million people (9.3% of the global population) and estimates that the number of affected people will continue growing to achieve 578 million people in 2030 and 700 million people in 2045.[24] It is in the top ten global causes of mortality, with an estimation of 11.3% global deaths associated with diabetes. Furthermore, the direct economic cost of diabetes health care achieved only in 2019 $ 760 billion, and IDF estimates that will continue growing.[24] As in AD, the great magnitude of the devasting

human, social and economic costs associated with this disease, that still has no known cure, makes imperative the research on this field, allowing to understand the biochemical mechanisms involved in its pathological development, a fundamental issue to face this disorder.

1.1.3. Cross-disease analysis and comorbidities in AD and T2DM

Both AD and T2DM present an overlap of pathogenic mechanisms characterized by the accumulation of abnormal protein aggregates, impairment of the Ubiquitin-Proteasome System (UPS), oxidative stress, mitochondrial dysfunction, lipid dysmetabolism, apoptosis, impaired insulin signaling, and insulin resistance. Intriguingly, recent epidemiological data have shown that patients suffering from T2DM have an increased risk to develop AD and vice versa.[25,26] Both AD and T2DM are multimorbidity diseases, with patients presenting in most cases another (or more) chronic condition, thus making much more difficult any therapeutic treatment. T2DM is the most common disease which presents comorbidity with AD.[27] As in T2DM, the impairment of glucose metabolism is also present in AD, even in the early stage of the disease, decades before the manifestation of symptoms.[28] Moreover, Aβ and IAPP are present in some biological fluids at comparable concentrations, and mixed IAPP and Aβ aggregates have been found in the brain of T2DM and AD patients.[29] Furthermore, tau and Aβ deposits have been localized in pancreatic β cells, as well as IAPP deposits have been found in the hippocampus of both AD or T2DM patients without neuropathologies.[30] Moreover, cognitive impairment has been observed in T2DM, brain insulin resistance and insulin deficiency models, while treatment with insulin or insulin sensitizer compounds produces cognitive improvement in patients with AD.[3] The degree of interrelation between AD and T2DM is so extended that AD has been considered as the diabetes of the brain and has been denominated “type 3 diabetes”.[3]

All this evidence supports the hypothesis that AD and T2DM are multifactorial diseases sharing common pathogenic mechanisms. Currently, no effective treatment exists for both diseases and their incidence is substantially increasing due to their link with factors associated with the modern lifestyle such as the above-mentioned sedentary lifestyle, obesity, and/or aging. Driven by this imperative medical need, a

substantial effort has been made in the last 30 years to develop AD and T2DM therapies. The strong interconnections between these pathologies suggest that it may be convenient to group Aβ and IAPP in a unique research project aimed at designing a therapy suitable for both the two diseases. For this reason, the design of new therapeutic strategies with multitarget/multifunctional to prevent amyloid-related disorders is becoming more important than ever.

1.2. From the "amyloid hypothesis" to the proteostasis imbalance

Both AD and T2DM are characterized by the accumulation of amyloid proteins in cells, implicitly suggesting that targeting protein misfolding and self-assembly would prevent the diseases ("The Amyloid Hypothesis").[1] However, the failure of all clinical trials focusing on anti-aggregating drugs has demonstrated that a deeper understanding of the mechanisms involved in proteome maintenance is needed.

It is widely known that cells express an integrated array of proteolytic machinery that controls protein homeostasis (proteostasis) in a given range of adverse environmental conditions. As a matter of fact, the latest studies suggest that pathological conditions occur when the equilibrium between the production and the clearance of the involved proteins results unbalanced, or, in other words, when proteome surveillance by the proteolytic machinery of the cell is compromised.[2]

The synthesis, folding, disaggregation or aggregation, trafficking, and degradation of proteins are controlled and regulated by a combination of an intricate network of many intertwined of biochemical pathways. The system that coordinates the whole process is the proteostasis network (PN).[2] In a healthy cell, the expression of PN components is regulated by the different proteomic demands, but in presence of physiological alterations or stress, the activity of the PN is permanently altered evolving in a pathology[31] (see figure 3). For this reason, new drugs are designed to restore the whole proteostasis network (PN), and not just as simple anti-aggregating compounds.

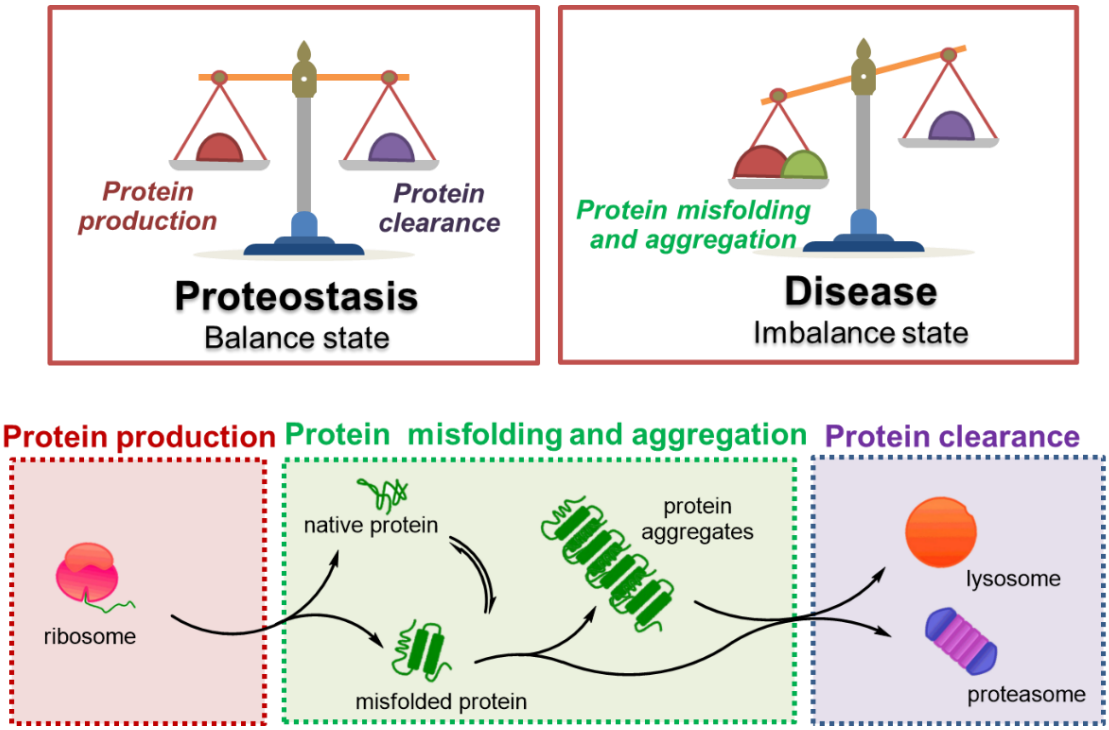

Figure 3. The proteostasis balance.

The PN deterioration is age-related leading to degenerative disorders.[2] Even if the cause of the decline of the PN is complex, it seems to be related to a lack of evolutionary pressure in its preservation once the organism has had progeny and thus the genome has already been passed to the offspring.[32] In fact, studies performed in *C. elegans* suggest the existence of a programmed aging event in the onset of reproduction, associated with a decline in proteostasis because of the competitive requirement of resources between the germline and soma.[33] The high resources expenditure with could imply the full maintenance of the soma in a fail-safe manner, considering the extrinsic mortality of organisms, is inefficient from an evolutionary point of view; thus, the soma proteostasis is error-prone and the resources aimed to its maintenance are limited when are also required for reproduction.[34] This theory is known as "disposable soma theory of aging" and suggest a high expenditure to maintain the proteostasis of the germline is in detriment of somatic cells, causing a decreased somatic protein quality control (PQC).[34]

PQC network comprises the set of mechanisms that maintain the integrity of the proteome, by assisting the correct folding of nascent proteins, controlling proteins folding status, and clearing misfolded and aggregated proteins.[2,35] Albeit the ubiquitin-

proteasome system (UPS) and the autophagy-lysosome pathway (ALP) are the major PQC pathways, other factors such as folding chaperones and metalloproteases are known to play a significant role in proteome maintenance. UPS is the primary proteolytic route for misfolded and damaged proteins, while ALP acts as a bulk recycling system, removing dangerous cellular components, including large protein aggregates; ubiquitination is utilized as a protein degradation signal being involved in both pathways. Both systems form part of the PQC system and are closely interconnected, taking part of an adaptive mechanism allowing the cell to properly regulate protein homeostasis against cellular stress.[36]

Within this frame, in the research of drugs for PCDs, many researchers have screened several molecules targeting different components of the UPS[37] and the ALP.[38,39] However, very few molecules, if any, selected by using this strategy, have shown to have the potential to be pipelined to clinical trials. Actually, due to the multifactorial nature of protein diseases, it may be difficult to find effective drugs by screening molecules on a single target.

Indeed, in the last 25 years, many Big Pharma companies including Monsanto, Novartis, Pfizer, and Eli Lilly, have endeavored a large number of expensive research projects focusing on finding therapies for amyloid diseases. Despite all efforts in this regard, an alarming huge failure of all clinical trials has occurred (99.6%),[40] and to date, only symptomatic medications have been approved.[41] This has resulted in a massive shift of Big Pharma companies to other topic projects.[42] This massive exodus of pharmacological companies from neurodegenerative research makes that studies in the academic area are becoming more and more relevant for the treatment of these diseases and the implementation of alternative approaches becomes indispensable due to the complexity of these diseases along with the high risk of failure.

1.2.1. Amyloids monomers and their structural plasticity

Aβ and IAPP, as well as main amyloid proteins, are largely unstructured, lacking a defined globular folded and exhibiting extraordinary conformational flexibility. A large percentage of proteins (around 50%) present this behavior and are known as intrinsically

disordered proteins (IDPs).[43,44] Others, however, contain an intrinsically disordered region (IDR) that is intersected with structured ones.[45] It is now accepted that the lack of stable tertiary and/or secondary structure does not preclude proteins from being biologically active. The conformational flexibility of these proteins (intrinsic disorder), i.e. the possibility to adopt different conformations depending on their physiological ligand, defines the ability of these proteins to exert different functions. Furthermore, the "disorder" level found in eukaryotic proteins (52–67% proteins have long IDRs) is higher than in prokaryotic (26–51 and 16–45% proteins contain long IDRs in archaea and bacteria, respectively) highlighting the relationship between these proteins and the complexity of organisms and their functions and suggesting that disordered proteins are the result of evolutionary pressure.[43]

The free energy landscape of folded proteins shows a potential energy profile with a unique global energy minimum corresponding to the protein native structure, while IDPs present several energetically similar minimums with small barriers between them. This results in structural instability and conformational flexibility, wherefore the protein could adopt a large number of conformations (see figure 4). The interconversion between all of them is strictly regulated by the PN and an imbalance of proteostasis can lead to the formation of intra- or extra-cellular pathological aggregates, which mainly are amyloids fibrils and, to a lesser extent, amorphous aggregates.[45]

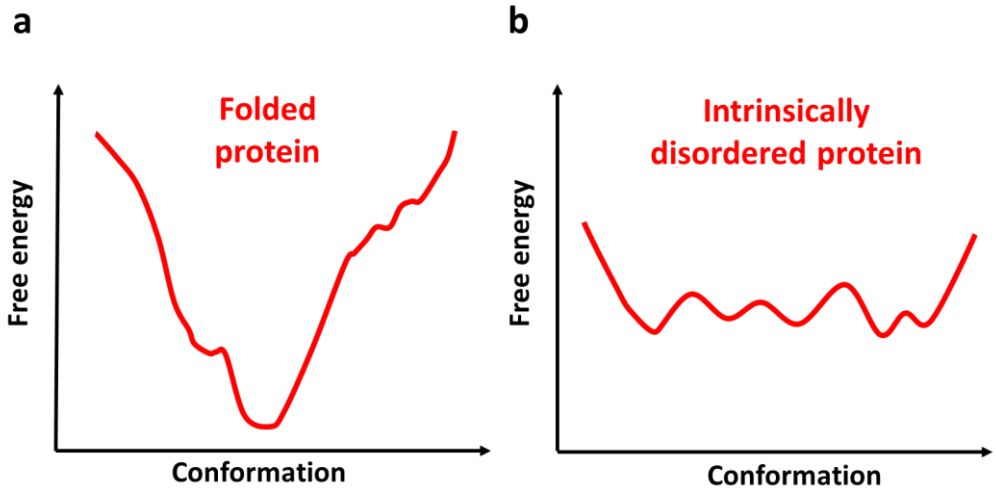

Figure 4 – Free energy landscape representation. (a) Free energy landscape of a folded protein. **(b)** As (a) except for an intrinsically disordered protein.

1.2.1.1. Amyloid β (Aβ)

Amyloid β (Aβ) peptide is a small hydrophobic peptide originated by the cleavage of a transmembrane protein called amyloid precursor protein (APP) by β- and γ-secretases. In vivo, different Aβ peptides can be found, from 36 to 43 amino acids, but $Aβ_{1-40}$ and $Aβ_{1-42}$ are the most common isoforms; the first one is the most abundant (the $Aβ_{1-40}$ /$Aβ_{1-42}$ molar ratio in the cerebrospinal fluid (CSF) is 9:1) while the second one is the most fibrillogenic.[46] APP is located in the cell membrane but also in intracellular membranes (mitochondrial, trans-Golgi, endoplasmic reticulum, endosomal and lysosomal membranes) and therefore, Aβ is released in both extra- and intracellular spaces.[47] Furthermore, the uptake of extracellular Aβ and its internalization in neurons has been observed[48] and the accumulation of Aβ inside the cell seems to be an early event in the pathology, preceding the extracellular accumulation of amyloid plaques.[47]

It is important to remark that, despite its detrimental role widely associated with AD, Aβ has also an important physiological role in the CNS (e.g. in the control of synapsis) and its pathological effects are evidenced only if its levels become excessive.[49–51]

Figure 5 – Schematic representation of amyloid $β_{1-40}$. N-terminus, Central hydrophobic cluster, turn and C-terminus regions are highlighted in different colors.

The Aβ secondary structure is related to its toxicity, in with the β-sheet rich conformations playing a major role. The stretch V12-V24 of Aβ is known as "central hydrophobic cluster" (CHC) and is considered essential for peptide aggregation; this hydrophobic region and the hydrophobic residues from the C-terminal region (residues I30-V40) form a parallel β-sheet structure thanks to the turn region (residues G25-G29) which permits intermolecular hydrogen bonding between both β-strands (see figure 5).[52] The isoform $Aβ_{42}$ contains two more hydrophobic residues in the C-terminus than $Aβ_{40}$, I41 and A42, entailing higher propensity of the peptide to aggregate.[53]

1.2.1.2. Human islet amyloid polypeptide (hIAPP)

hIAPP (human islet amyloid polypeptide or human amylin) is a hydrophobic peptide of 37 amino acids that encompasses a disulfide bridge between residues C2 and C7 which is required to the biological activity of the peptide. It is co-expressed and co-secreted with its synergistic partner insulin, in β-cells pancreatic islets, in response to glucose stimulation due to nutrients intake; the molar ratio IAPP/insulin varies from 1:10 to 1:100.[54] IAPP is expressed as a pre-prohormone and it is posteriorly cleavage by peptidases in the endoplasmic reticulum (ER) generating the prohormone and then, in the Golgi apparatus, it is processed by the prohormone convertase2 (PC2), prohormone convertase 1/3 (PC1/3) and carboxypeptidase E (CPE) generating the final mature form, which finally is C-terminally amidated leading to the active hormone.[55]

IAPP exerts autocrine actions in β-cell signaling.[56,57] Both insulin and IAPP play an important role in metabolism and glucose homeostasis. While insulin controls the transport of glucose from the blood into insulin-dependent tissues, amylin is involved in the control of glucose uptake from the digested carbohydrates by regulating the gastric emptying.[55] Furthermore, IAPP acts as a satiation signal in the CNS suppressing appetite, controlling the intake of food as well as the body weight.[58] However, a malfunction in cellular proteostasis machinery can generate IAPP misfolding and, eventually, the formation of amyloid deposits in pancreatic islets, leading to type-2 diabetes.[59]

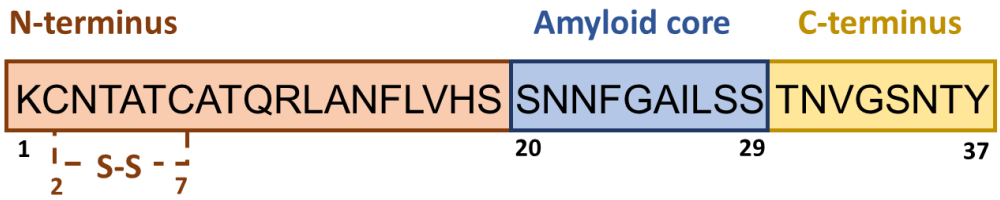

Figure 6 – Schematic representation of the human amylin sequence. The disulfide bridge is indicated as S-S. N-terminus, amyloid core, and C-terminus regions are highlighted in different colors.

As above mentioned, hIAPP is an IDP, presenting a wide conformational variety and may adopt many diverse structures, although the random coil structure is predominant when hIAPP is in its monomeric state. In fact, several experimental CD studies and computational calculations on hIAPP have allowed to characterize a large

variety of elements of secondary structure: unstructured coil, disordered conformation with transient α-helix structure, mixed α-helix, and short antiparallel β-sheet, extended antiparallel β-hairpin, and a compact helix-coil structure.[60] As indicated in figure 6, the stretch S20-S29 is known as the amyloidogenic core region, which is essential for amyloid aggregation; conformational transitions of this region toward β-rich states seed protein aggregation, fibrillogenesis and, eventually, lead to toxicity. As a matter of fact, the non-amyloidogenic rat IAPP (rIAPP) differs from hIAPP in 6 residues, 5 of them sited on of the amyloid core, which are responsible for the lack of aggregation tendency of the peptide.[61,62] Three of these residues (in positions 25, 28, 29) of rIAPP are prolines and have been identified as β-sheet breakers, destabilizing and inhibiting β-sheet secondary structure, which explains the different aggregation behavior of both hIAPP and rIAPP.[63] The amyloidogenic ability of the C-terminal region T30-Y37 has been also described as a key player in IAPP fibril formation.[64] The N-terminal stretch K1-S19 is involved in the initial interaction of the peptide with lipid membranes, poorly contributing to aggregation when lipid bilayers are present;[65,66] however, in their absence, the ability of the stretch A13-H18 to play a role in amyloid formation has been also described.[67] Despite the disulfide bridge does not participate in amyloid core structure, it contributes to fibril aggregation; in fact, its absence reduces the secondary nucleation fibrillation kinetics.[68]

1.2.2. Aggregation of amyloid peptides and amyloid fibrils

Amyloid aggregation is a process by which amyloid peptides self-assemble forming fibrillar aggregates (see figure 7). Amyloid fibrils are highly structured, since as they possess a β-rich secondary structure, organized in parallel or antiparallel strands arranged perpendicularly to the longitudinal axis of the fibril. These highly ordered structures contain a large number of H-bonds between the β-sheets, providing high stability and mechanical strength. Amyloidogenic proteins are smaller in length in comparison with the average length of all the human proteins. Several pieces of evidence indicate that the ability to aggregate of these peptides is not related to their sequence per se, but instead is associated with their physical characteristics, playing the hydrophobicity of these peptides a key role in the aggregation process. In fact, the

peptide regions with belong to the β-rich amyloid core contain a high level of hydrophobic residues.[1,32]

The morphology of amyloid fibrils has been widely characterized by SEM,[69] TEM,[70–72] AFM,[73] Cryo-EM,[72,74] X-ray diffraction,[74,75] and solid-state NMR.[52,70,71,74] Highly heterogeneous structures have been characterized which could differ depending on the growth conditions.[76] However, despite the polymorphism presented in amyloid fibrils, they also share some common structural features. All of them are composed by 2 or more protofibrils of 2-5 nm width,[77] the basic building blocks, which are integrated by amyloid molecules stacked perpendicularly to the longitudinal axis of the fibril, organized in parallel in-register cross-β structures, forming fibrils from around 7-8 nm to some nm width, depending on the number of involved protofibrils, with few hundred nm of length.

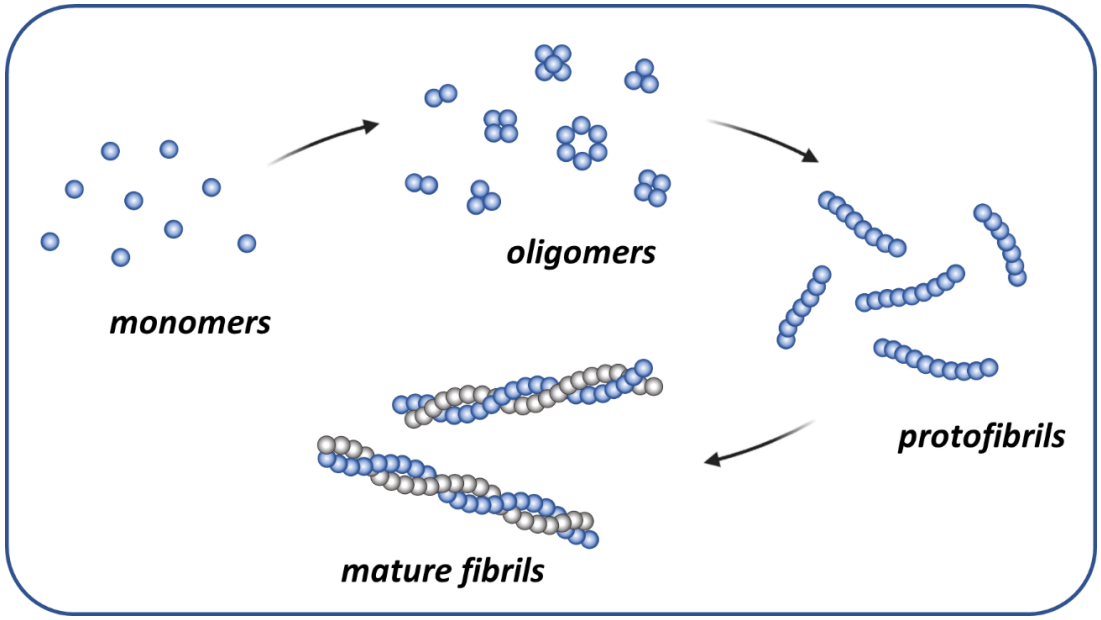

Figure 7. Representation of amyloid fibrils formation.

To study the amyloid aggregation, Thioflavin T (ThT) assays are commonly used. These studies are based on the assumption that the fluorescent dye ThT increases its fluorescence upon binding to β-rich structures, as amyloid fibrils, allowing the study of fiber growth kinetics. ThT contains a benzylamine ring and benzothiazole ring which freely rotate mutually thorough a C-C bond, quenching the fluorescence. Upon binding to amyloid structures, the free rotation of these rings is not allowed, delocalizing π-

electrons, increasing the fluorescence, and producing a redshifting (λ_{exc} from 385 nm to 450 nm and λ_{em} from 455 nm to 482 nm).[78] ThT is a highly specific probe of fibrillar structures, showing no changes in its fluorescence when other kinds of structures are present as, for example, the monomer or amorphous aggregates. The typical ThT profile is sigmoidal; it presents a lag phase where oligomerization processes take place but the amyloid formation is yet minimal; this phase is followed by an elongation phase that starts when oligomeric nuclei achieve a critical concentration from which fibrils begin to grow; the elongation phase continues while fibrils continue growing up to a maximum, termed "plateau" (see figure 8).

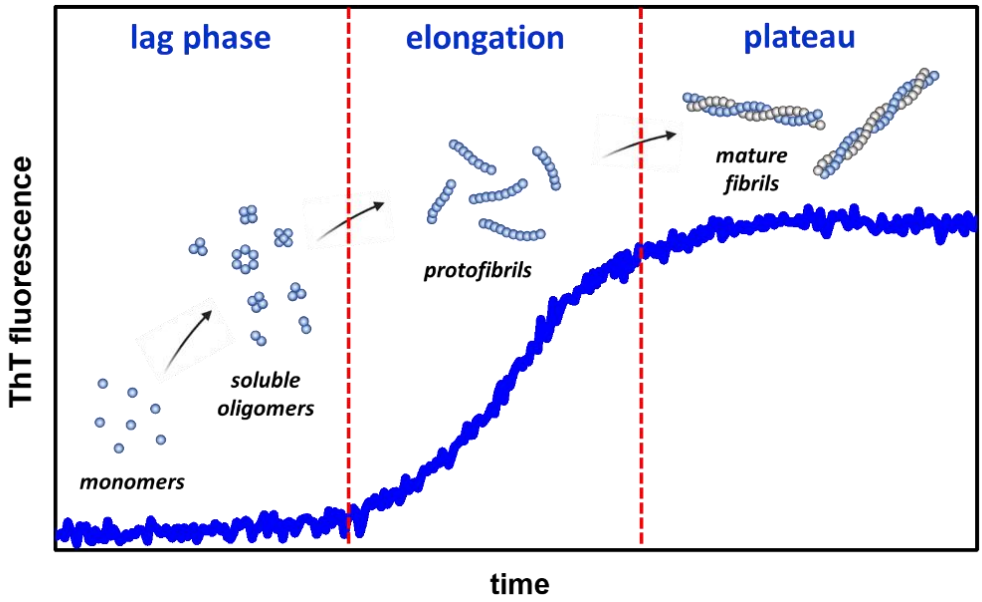

Figure 8. Typical amyloid aggregation kinetics obtained by using the ThT assay.

The rate-limiting step of amyloid growth is the nucleation process. Nuclei are the smallest species able to promote the growth of fibrils. The most extended mechanism by which amyloid fibrils are formed is the nucleation-dependent polymerization pathway where the structurally disordered monomers assemble converting to nuclei in a thermodynamically unfavorable process and adopting a defined conformation that is prone to aggregate forming the fibrils.[79] Nuclei interact with other monomers, working as templates, initiating the fibril elongation, a process that is considered thermodynamically favorable. Fibril growth leads to an increase of the β-sheet structure, resulting in higher compactness and an increase of stability.[1] This mechanism is based

on the classical nucleation theory (CNT) widely used to study the growth of crystals, which also presents the thermodynamically unfavorable nucleation process. In fact, a crystallization-like model (CLM) has been proposed to describe amyloid growth, showing good fitting with experimental data.[80] According to this model, the overall amyloid kinetics are predominantly determined by both nucleation and elongation kinetics; the most common sigmoidal profile occurs when the nucleation rate is significantly smaller than the elongation rate. However, when nucleation represents the most important step, hyperbolic kinetics are observed.[80]

Nevertheless, some evidence, as the presence of poorly structured oligomers, or a fibril elongation rate proportional to the number of oligomers, suggested an alternative multi-step nucleation mechanism to explain the amyloid formation: the nucleated conformational conversion (NCC) pathway. In this case, monomers ensemble forming misfolded prenucleation clusters that are not able to form fibrils, but instead are nucleation precursors.[79] These clusters are unstable and, eventually, an internal reorganization turns them in stable oligomeric species, by acquiring a β-sheet rich structure, i.e. the nuclei structure; this reorganization is the rate-determining step. These nuclei induce the conformational change of other misfolded oligomers to the amyloid conformation, acting as a template, thus giving rise to the fibril growth (see figure 9).[1]

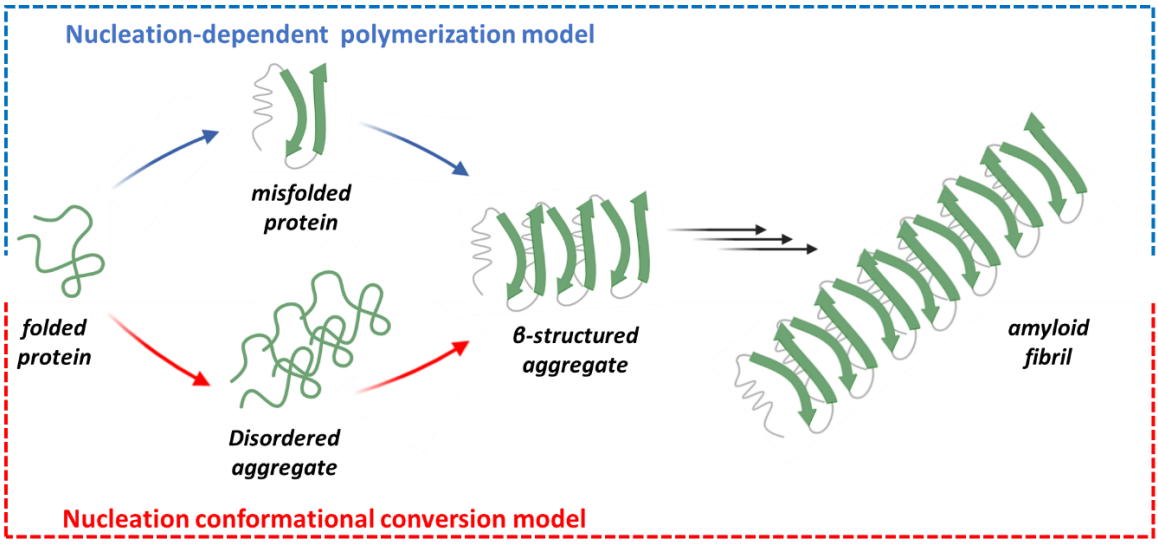

Figure 9. Amyloid fibrillation models.

Other secondary processes as fragmentation of fibrils or secondary nucleation reactions can also take place. When fibrils break, the smaller fragments can act like seeds, catalyzing the aggregation process; this process has been denoted as secondary nucleation to differentiate it from the primary nucleation, which happens in the absence of fibrils.[81]

It has been proposed that depending on the chemico-physical characteristics of the peptide and the biological milieu, peptides can aggregate following one of the two nucleation mechanisms. In particular, the nucleation mechanism is determined by the relationship between intermolecular interactions and structural order. Peptides that contain numerous hydrophobic residues present a high propensity to interact with other peptides forming pre-nucleation oligomers; in this case, the intermolecular interactions responsible for oligomer formation occur before the structural rearrangement responsible for nuclei behavior and nucleation follows a two-step mechanism termed the NNC pathway. By contrast, when intermolecular interactions and gain of structural order occurs simultaneously, the nucleation follows a 1-step mechanism named the nucleation-dependent polymerization pathway (see figure 10).[79]

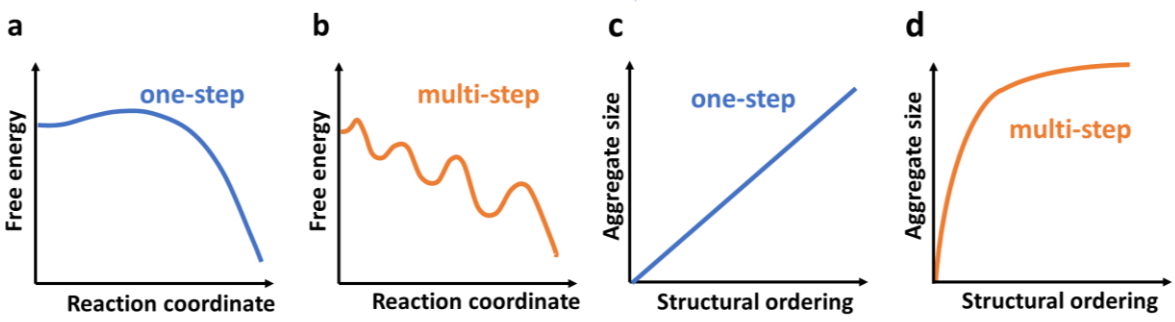

Figure 10 – Representations of one-step and multi-step amyloid nucleation. **(a)** Schematic free energy representation of a one-step nucleation mechanism corresponding to the nucleation-dependent polymerization pathway. **(b)** Schematic free energy representation of a multi-step nucleation mechanism corresponding to the NNC pathway. **(c)** Aggregation size vs structural ordering of the one-step nucleation mechanism represented in (a). **(d)** Aggregation size vs structural ordering of the multi-step nucleation mechanism represented in (b).

1.2.3. Amyloid oligomers

The first evidence of Aβ fibrils was found by Alois Alzheimer in 1907 when he noticed the presence of particularly thick fibrils with distinctly stainable properties in the cerebral cortex of a patient with had presented cognitive decline and other clinical symptoms not-related with any known disease.[82,83] After those early reports, amyloid deposits were fully characterized[84,85] and research focused on "the amyloid cascade hypothesis", which points to amyloid plaque deposition as the main event triggering the pathology.[86] It was not until 1998 that neurotoxicity of amyloid oligomers was also proposed by Lambert et al. They found that soluble Aβ oligomers, which were denoted as "Aβ-Derived Diffusible Ligands" (ADDLs) to emphasize their solubility, could inhibit synapses long-term potentiation (LTP).[87] Since then, different Aβ oligomeric species as dimers,[88–94] trimers,[88,89,93,95] tetramers,[89,92,93] pentamers,[91,93] hexamers,[92,93,95,96] decamers,[92] dodecamers [95,96] (known also as Ab*56 due to their MW of 56 KDa), and 24-mer[97,98] have been identified.

Although the accumulation of insoluble amyloid aggregates was initially considered as the cause of the related disorders, in the last years, the scientific community agrees that the main neurotoxic species are not mature amyloid aggregates but, rather, β-structured small-sized oligomeric species, which are intermediates of the aggregation process. These oligomers can self-aggregate to form structurally well-defined fibrils with cross-β structure giving rise to the mature fibrils.[1] Depending on their different ability to self-assemble into fibrils, they are classified as on-pathway or off-pathway oligomers. The first group includes those oligomers that can be incorporated in the fibril structure, while the second one comprises those with cannot do it directly and require a previous dissociation of the oligomer to the monomer to be hijacked to amyloid growth.[99]

However, the role and nature of oligomers are still controversial, and in many cases, it may be challenging to distinguish between on- or off-pathway oligomeric species. Indeed, in vitro aggregation studies needs higher peptide concentrations (in the order of μM) respect to the extracellular concentrations of the peptide in the brain (in the order of nM) and generates fewer toxic oligomers than those isolated from AD

brains.[100] Although different mechanisms have been proposed to explain these discrepancies (i.e. the increase of the local concentration of the peptide in vivo, thanks to its interaction with the cell membrane[101] or the internalization and concentration of the extracellular peptide in vesicles (endosomes/lysosomes) forming high MW species which act as seeds[102]), it is still uncertain whether in vitro oligomers are structurally, morphologically and behaviorally similar to the pathological ones. On the other hand, the low endogenous concentration of oligomers, their dynamic and transient behavior, and the impossibility to fully reproduce their biological environment, represent a significant problem in the *ex vivo* characterization of these species. The isolation of cellular oligomers involves several steps that deeply modify the oligomers' environment and peptide concentration, producing changes in the oligomeric distribution. SDS-PAGE is a technique commonly used in the identification of oligomeric species. Unfortunately, the known ability of SDS to induce conformational changes on Aβ monomer,[103] and to influence the formation of oligomers may lead to biased data readout.[104–106]

The principal isoforms of Aβ, i.e. $A\beta_{40}$ and $A\beta_{42}$, oligomerize through distinct pathways. Both peptides present different folding states with differences in the hydrophobic surfaces exposed to the solvent, resulting in a different ability to form larger structures.[107] $A\beta_{42}$ dimers present a higher propensity to form β-strands in the main amyloidogenic regions than $A\beta_{40}$.[108] Several studies have been carried out to study the oligomeric distribution of both $A\beta_{40}$ and $A\beta_{42}$ in vitro, indicating a higher propensity of $A\beta_{42}$ to form larger oligomers than $A\beta_{40}$, that acts as paranuclei evolving in the formation of protofibrils. [93,96] Different studies indicate the fundamental importance of the $A\beta_{42}/A\beta_{40}$ ratio in the toxicity of the formed oligomers. Oligomers formed by both peptides in an equimolar ratio are smaller, more stable, more toxic, and formed by different pathways than the oligomers formed by either of the isoforms alone.[109,110] Notably, a reduction of this ratio in the CSF has been also reported in AD patients when compared to healthy people.[111]

Amyloid oligomers are heterogeneous not only in size but also in structure, morphology, and stability.[99] Despite there is no consensus regarding the toxicity of oligomers, it seems to increase with oligomer size until dodecamers and decrease when larger oligomeric species are formed. Small oligomers usually possess a globular

morphology and evolve in the formation of protofibrils (PFs) with an increase in β-sheet structure along the entire aggregation process. In the presence of lipid bilayers, the formation of β-rich annular protofibrils (APFs) has been observed.[112] APFs have attracted increasing attention over the last few years due to several reports focusing on amyloid oligomers-mediated toxicity via the disruption of the cell membrane through APFs insertion in the lipid bilayer and formation of pore-like structures.[113,114]

1.2.4. Amyloid-mediated cellular damage

1.2.4.1. Amyloid-mediated cell membrane damage and toxicity

Amyloid oligomers are considered toxic because they can interact and damage the cell membrane causing disturbances in the homeostasis of small molecules and ions. The toxicity of oligomers depends on their binding affinity with cell membranes, which in turn, depend on the structural and physicochemical properties of both oligomers and membranes (particularly, their lipid composition).[115–117] The initial interaction of the cationic Aβ or IAPP peptides with lipid membranes, that contain anionic head-groups in their surface, is driven by electrostatic interactions.[101,118] Once Aβ or IAPP oligomers interact with neuronal or pancreatic membranes, they are accumulated in lipid rafts,[119–121] microdomains of the cell membrane which are rich in cholesterol and glycosphingolipids:[121] due to their components, lipid rafts have a reduced membrane fluidity and their physical state may be considered a liquid-ordered state.[122,123] Both Aβ and IAPP interact with GM1 ganglioside-containing lipidic membranes which catalyze fibril growth,[124,125] leading to LTP impairment.[126] In fact, a direct correlation between GM1 levels on the cell membrane and the toxicity of $A\beta_{42}$ oligomers,[115] as well as between ganglioside and cholesterol levels and hIAPP amyloid deposits on cell membranes has been established.[119] The reduction of GM1 levels in the cell membrane results in a reduction of membrane poration[127] and neurotoxicity;[127,128] notably, a similar effect has been also observed by blocking Aβ-GM1 interaction.[127] The affinity of Aβ with GM1 has been estimated (~ 10^{-5}M) and increased binding capacities have been observed when GM1 levels increase, indicating the presence of a GM1-cooperative phenomenon in the binding. The Aβ conformation shifts from α-helix to β-sheet rich

structures of these when higher cooperative states are formed.[129] Cholesterol facilitates the formation of GM1 clusters and induces the formation of GM1/Aβ complex.[129,130]

The interaction between amyloid oligomers and lipidic membranes is a phenomenon which produces two disruptive interconnected processes: on one side, amyloid oligomers produce the disruption of cellular membranes and, on the other side, the lipid bilayer catalyzes peptide aggregation acting as nucleation site of Aβ or IAPP, enhancing the local protein concentration in the membrane surface and fostering protein self-assembly.[131]

Under these premises, different mechanisms of oligomer-mediated toxicity have been proposed. The "Channel Hypothesis" or "pore-like mechanism" suggests the formation of Ca^{2+}-permeable pores across the lipid membrane by annular oligomeric species as a pathological event that induces cytotoxicity. According to this mechanism, soluble amyloid oligomers insert into membranes facing the hydrophobic residues to the lipidic bilayer, forming a pore-like structure, and exposing hydrophilic residues to the interior of it (see figure 11).[114,132,133] These pores are "ion channel" structures leading to Ca^{2+} dyshomeostasis. In fact, several reports have been shown an increase in the intracellular Ca^{2+} levels in neuronal cells of AD and β-cells of T2DM, as well as other amyloid-pathologies.[114,134,135]

Another proposed disruptive process is the "carpet-like mechanism", according to which the interaction of prefibrillar species with the lipid bilayer surface can result in an asymmetric pressure between both layers, destabilizing the lipidic membrane and eventually, leading to membrane damage.[136]

Remarkably, despite Aβ oligomers are considered the most cytotoxic species, fibrils are not devoided of toxicity. According to the "detergent-like mechanism", fibrils can also interact with the lipid membrane *via* non-specific bindings, with results in its thinning and finally, in the disruption of the cell membrane integrity (see figure 11).[133] This is due to the amphiphilic character of amyloid peptides which reduces the surface tension of the membrane, promotes the removal of lipids from the membrane surface forming peptide-lipid micelles and, ultimately, disrupts it.[137] Furthermore, as above mentioned, fibrils are also able to catalyze the formation of toxic oligomers acting as

nuclei through a secondary nucleation process.[81] It is thought that all of these mechanisms are possible to occur *in vivo* and are not mutually exclusive.[133]

Moreover, it has been shown that insulin suppresses the fiber-dependent membrane disruption by amylin, but not the pore-formation dependent membrane disruption.[138] Therefore, the insulin deficiency present in T2DM could promote hIAPP fibrils-mediated toxicity through a detergent-like mechanism.

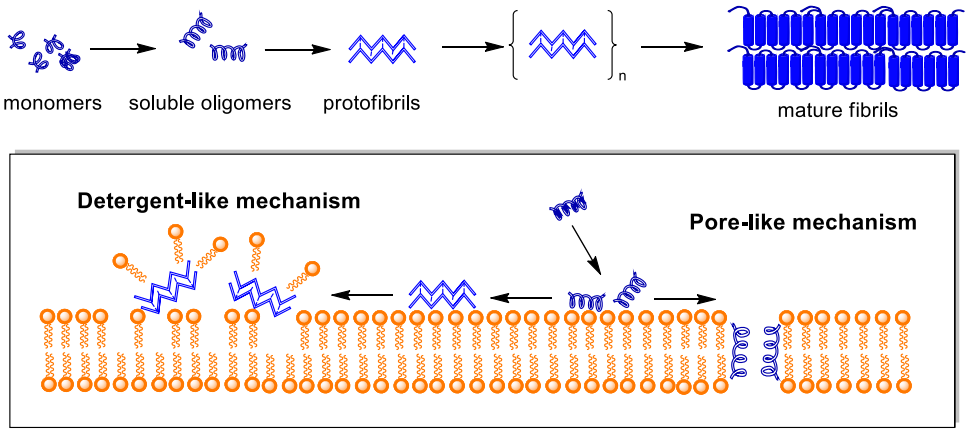

Figure 11 – Membrane disruption mechanisms. Scheme of both pore and detergent-like mechanisms.

Model membranes, vesicles, or liposomes are extensively used in biophysical studies mimicking cell membrane disruption by amyloids. Vesicles may be represented as spherical lipidic bilayers filled with water and are the most biologically relevant model of natural cell membranes. Depending on their diameter they are divided into three groups: small unilamellar vesicles (SUVs, ϕ=20-50nm), large unilamellar vesicles (LUVs, ϕ=100nm), and giant unilamellar vesicles (GUVs, ϕ≥1000nm).

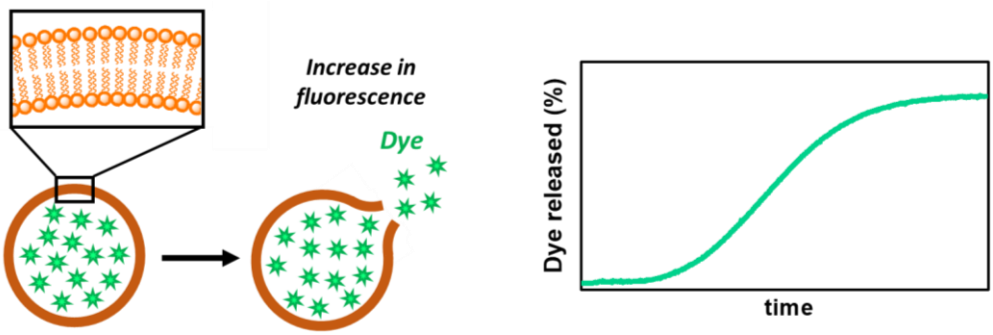

Figure 12. Scheme of the dye-leakage assay.

To study the mechanism of amyloid-mediated disruption of membranes, LUVs can be filled with a fluorescent dye, as 6-carboxifluorescein, which allow monitoring the disruption of membranes over time[117,132] (see figure 12), which, in parallel with ThT assays, allows to identify which species (oligomers or fibrils) are triggering vesicle leakage and, thus, hypothesize the disruption mechanism.

1.2.4.2. Oxidative stress and neuroinflammation by amyloid accumulation

Oxidative stress represents the imbalance between free radicals and antioxidant defenses in our body, producing cell damage. At low levels, free radicals are beneficial but when their levels increase, oxidative stress becomes detrimental. Free radicals or reactive species include reactive oxygen species (ROS) and reactive nitrogen species (RNS). ROS are by-products formed mainly during mitochondrial electron transport because of the partial reduction of O_2 and include superoxide radical ($O_2^{\bullet -}$), hydroxyl radical ($HO^{\bullet}$), and hydrogen peroxide (H_2O_2), among others. RNS include nitric oxide ($NO^{\bullet}$), which is generated during the metabolism of L-arginine, and peroxynitrite ($ONOO^-$), a much more oxidant derivative of $NO^{\bullet}$.[139]

Despite the brain constitutes 2% of the total body mass,[28] it represents 20% of the total body consumption of O_2;[140] this, coupled with its limited antioxidant defense, makes it very sensitive to oxidative damage.[141] The sensibility to oxidative stress increases with age, as happens in AD, and large pieces of evidence situate oxidative stress as an important factor in the pathogenesis of AD,[142] T2DM,[143] and other PCDs.

β- and γ-secretases, which cleave APP to generate the Aβ peptide, are activated by oxidative stress, increasing the generation of Aβ.[144] Redox metal-ions bounded with Aβ can catalyze the production of reactive oxygen species (ROS), resulting in a vicious cycle and contributing to oxidative damage on both Aβ peptide and surrounding molecules (proteins, lipids, DNA, etc.). The oxidation of membrane lipids and cholesterol is also related to membrane damage.[145]

In T2DM patients, physiological defenses from ROS are decreased while oxidative stress biomarkers are increased respect to healthy people.[146] In fact, it has

been observed that the fluctuation of glucose levels that occurred during diabetes leads to increased production of ROS and RNS.[147] Furthermore, prolonged exposure of hyperglycemia is responsible for non-enzymatic protein glycation and ultimately, generation of oxidative stress.[146] Moreover, the treatment of cultured cells with IAPP leads to the downregulation of both thioredoxin dependent peroxide reductase and peroxiredoxin 1, which are involved in the inactivation of cytotoxic ROS.[148] Besides this, it is known that insulin is able to inhibit IAPP amyloid aggregation;[149,150] moreover, in the presence of oxidative stress, the expression of insulin in pancreatic β-cell is decreased.[151] Of note, lipid profiles are altered in T2DM cell, which makes it more vulnerable to be peroxidated.[152]

The generation of H_2O_2 has been observed during the early stages of aggregation of both Aβ and hIAPP;[153,154] notably H_20_2 is not produced in presence of the non-amyloidogenic rIAPP,[153] indicating that ROS generation is a process linked with amyloid aggregation. In the case of hIAPP aggregation, the generation of H_20_2 is catalyzed by Cu^{2+},[153] which in turn is present at higher concentrations in the plasma of T2DM patients.[155]

Oxidative stress increases the permeability of the Blood-Brain Barrier (BBB) and induces neuroinflammation and neuronal apoptosis, events closely related to an increase of Aβ deposition.[156] BBB is formed by capillary endothelial cells and its main function is to regulate, in a highly selective way, the passage of ions, molecules, and cells from the circulating blood to the extracellular fluid of the CNS, permitting the correct neuronal function and protecting neurons from toxins and pathogens. The malfunction of the BBB is a crucial event in the development of neurological pathologies.[157] In AD, oxidative stress produces the oxidation of the lipoprotein receptor-related protein 1 (LRP1) and the upregulation of the receptor for advanced glycation end products (RAGE), increasing the permeability of BBB and causing a decrease in the clearance of Aβ.[144,145]

The CNS can respond to several injuries by activating its immune system, triggering complex and dynamic biochemical and cellular responses in a cascade of processes collectively termed neuroinflammation, intending to counterbalance the threat and mitigate the potential damage.[158,159] However, this term is also widely used

to refer to chronic neuroinflammation which produces detrimental effects in the cell. When the neuroinflammation response is unable to restore the brain homeostasis, as in AD, it is maintained over time, becoming chronic and shifting the normal response to injury, producing neurodegeneration.[158] Neuroinflammation is normally associated with the above-mentioned blood-brain barrier alterations and dystrophic supportive cells termed glia. Microglia are the main components of the intrinsic immune system of the brain and are fundamental in the neuroinflammation response. In the presence of neurotoxic stimuli, glial activation occurs producing the upregulation of inflammatory signals, as inflammatory cytokines.[160] Inflammation is present in both AD and T2DM, as in other amyloidogenic disorders, where the ratio between pro- and anti-inflammatory cytokines is shifted leading to inflammation.[161,162] Oxidative stress produces neuroinflammation which, in turn, promotes oxidative stress evolving in irreversible neuronal dysfunction and abnormal Aβ accumulation.[144]

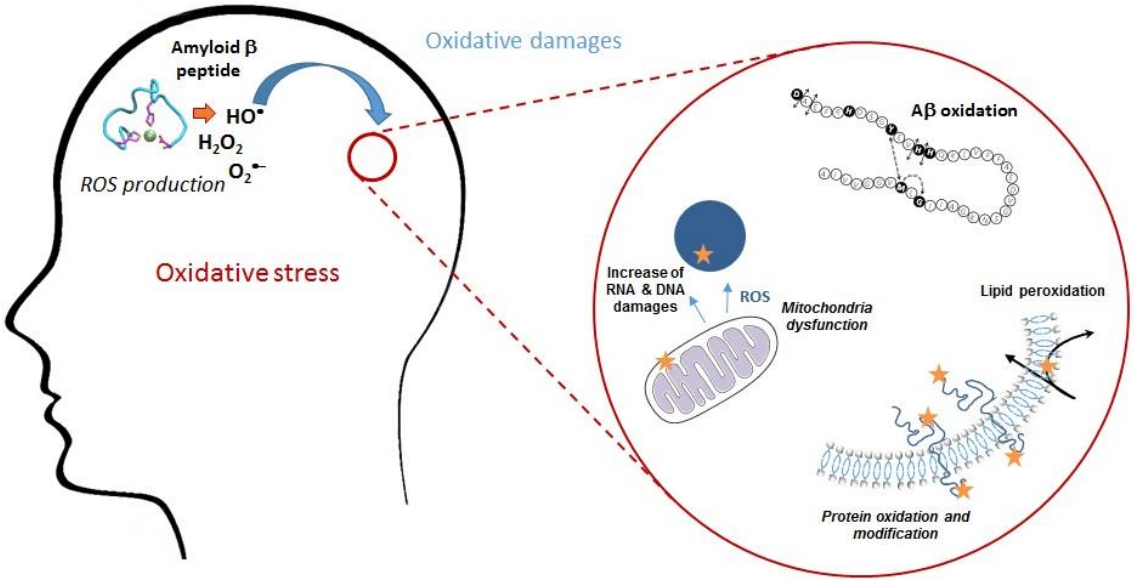

Figure 13. Oxidative stress in Alzheimer's Disease.[145]

Picture reprinted from Cheignon, C. *et al.* Oxidative stress and the amyloid beta peptide in Alzheimer's disease. *Redox Biol* 14, 450–464 (2018), under the Public License CC BY-NC-ND (http://creativecommons.org/licenses/by-nc-nd/4.0/).

Oxidative stress triggers apoptosis in both T2DM[163] and AD[144] via both intrinsic and extrinsic pathways. In the intrinsic pathway, oxidative stress, in particular mitochondrial stress, induces the release of signal factors by the mitochondria that activate the apoptotic signaling. When apoptosis takes place via the extrinsic pathway,

oxidative agents act as signal molecules binding to transmembrane receptors (as Far receptor) activating it and leading to the neuronal death.[144]

Although oxidative stress is not the direct cause of AD and T2DM, it is an important factor in the development of these pathologies. For these reasons, free radical scavengers, or in other words, compounds with antioxidant properties, are desirable in the fight against AD and T2DM.

1.2.5. Maintenance of proteostasis: chaperones and amyloid clearance systems

The PN aims at maintaining the proteostasis balance. As such, a sophisticated and tightly regulated cellular machinery is involved in counteracting the toxicity of amyloid species. On the front line are molecular chaperones, developing a preventive role against aggregation. If molecular chaperons are not able to restore this imbalance, the protein clearance systems, i.e. the ubiquitin-proteasome system (UPS), the autophagic–lysosomal pathway (ALP), and proteases among other, come into play degrading misfolded proteins and removing aggregates from the cell. However, with aging, this precise machinery is not more able to counterbalance amyloid toxicity giving rise to proteostasis dysregulation and leading to the degenerative pathologies as AD or T2DM.[32]

1.2.5.1. Molecular chaperones

Molecular chaperones are proteins that are normally involved in the process of aggregation, folding, assembly, and transport of other proteins. They can act alone or forming cooperative networks with other molecular co-chaperones.[164] Some molecular chaperones (families HSP90, HSP70, HSP60, HSP40, and sHSPs) are also known as heat shock proteins (HSPs)[165] because the presence of different stresses, e.g. thermal stress, leads to the upregulation of HSPs families genes expression.[166] In conditions of stress the production of misfolded proteins increases and therefore, the role of HSPs is fundamental to regulate the correct proteostasis. HSPs interact with the exposed hydrophobic regions of misfolded or unfolded proteins, helping them to achieve its

correct folded state and avoiding aberrant interactions with other misfolded proteins; when the refolding fails, they are also capable to turning the misfolded proteins to the protein clearance systems (UPS and ALP) where they will be degraded.[164] Furthermore, some chaperones interact with amyloid aggregates sequestering them in chaperone-rich inclusions preventing the fragmentation of aggregates and thus, avoiding secondary nucleation processes.[165]

However, with aging, approx. one-third of the HSPs (which mainly correspond to ATP-dependent HSPs) present decreased levels in the brain, and chaperones fail to avoid amyloid peptides aggregation; this effect is more pronounced in neurogenerative diseases as AD.[167] A downregulation of HSPs has been also observed after the administration of IAPP.[168]

1.2.5.2. The Ubiquitin-Proteasome System (UPS)

The ubiquitin-proteasome system (UPS) is the major cellular proteolytic system, being responsible for the degradation of more than 80% of intracellular proteins.[169] It represents a major protein quality control system in the cell, regulating the half-life of every protein, degrading inert and defectives ones.

The endpoint of the UPS is the 26S proteasome, a huge endoprotease (about 2.5 MDa) that functions primarily to degrade proteins that have been modified by the attachment of ubiquitin (see chapter 1.2.5.3). The proteasome, or more exactly proteasomes, are super-assemblies sharing a common unit termed “catalytic core”, “core particle” (CP), or “20S proteasome”.[170] The CP interacts with the regulatory particles (RPs) which allosterically regulate the 20S catalytic action and lead to super-assemblies that can be single or double capped, even forming hybrid proteasomes when two different activators bind the two sides of CP.[171]

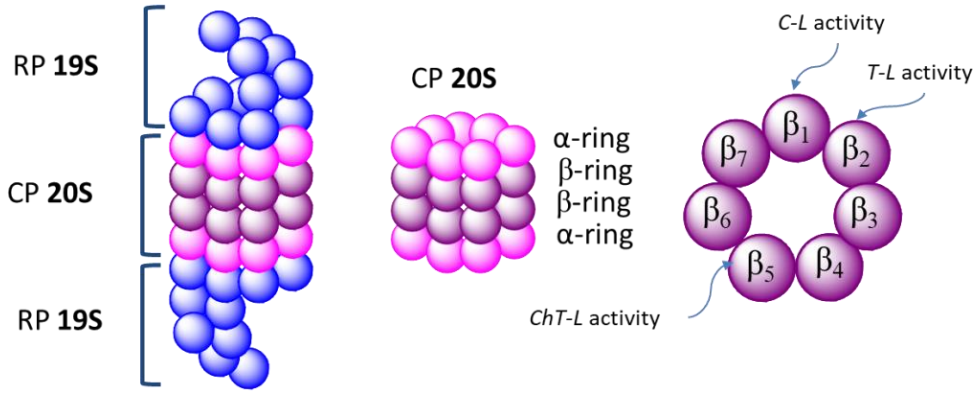

Figure 14 – The core particle (CP) or 20S proteasome. The blue spheres embody the subunits of the RPs 19S while the pink and blue spheres represent the α and β subunits of CP 20S, respectively.

The 20S CP has a barrel-like structure, composed by 28 subunits arranged in four hetero-heptameric rings, stacked in an α-β-β-α pattern (see figure 14).[170] The six catalytic sites are located in the two inner β-rings facing in the internal catalytic chamber of the barrel and are located in the β1, β2, and β5 subunits which possess peptidylglutamyl-peptide hydrolyzing (PGPH), trypsin-like (T-L), and chymotrypsin-like (ChT-L) activities, respectively. PGPH active sites cleave specifically after acid residues while T-L and ChT-L cut with specificity after basic and hydrophobic residues, respectively.[172]

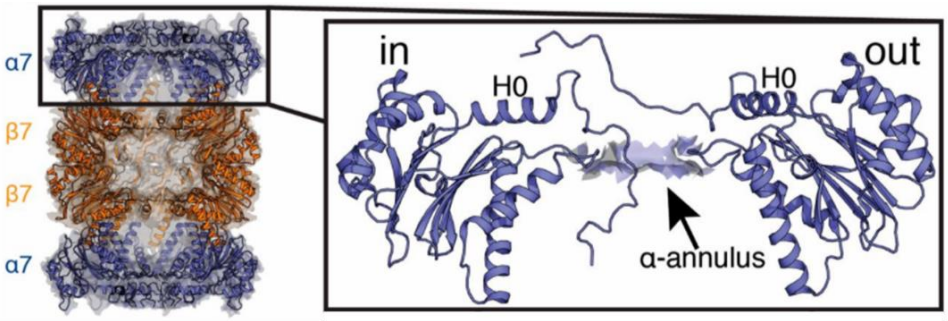

Figure 15. α-ring gating residues in the open (out) and closed (in) conformations.[173]

Picture reprinted from Latham, M. P. et al. Understanding the mechanism of proteasome 20S core particle gating. *Proc Natl Acad Sci USA* 111, 5532 (2014).

The external rings of 20S CP - the alpha rings - are the binding sites of the regulatory particles. In the center of the alpha ring, there is a dynamic gate, formed by the N-termini of alpha subunits, guarding the substrate entrance to the central

channel.[174] Al the α-subunits present an α-helix in their N-terminal region called H0 helix which presents great flexibility and is fundamental in the opening and closure of the gate. The short N-terminal "tails" extend to seal the gate completely or bend at the pivot points to open the entrance to the catalytic chamber. The conformation of the gate (closed or open), determines whether the 20S proteasome is in the "latent" or "activated" state[175] (see figure 15). Only unfolded proteins may enter the open 20S proteasome. Indeed, a narrow opening just in the middle of the alpha rings, termed the alpha-annulus, has a diameter of 13Å and prevents the entry of folded peptides.[176]

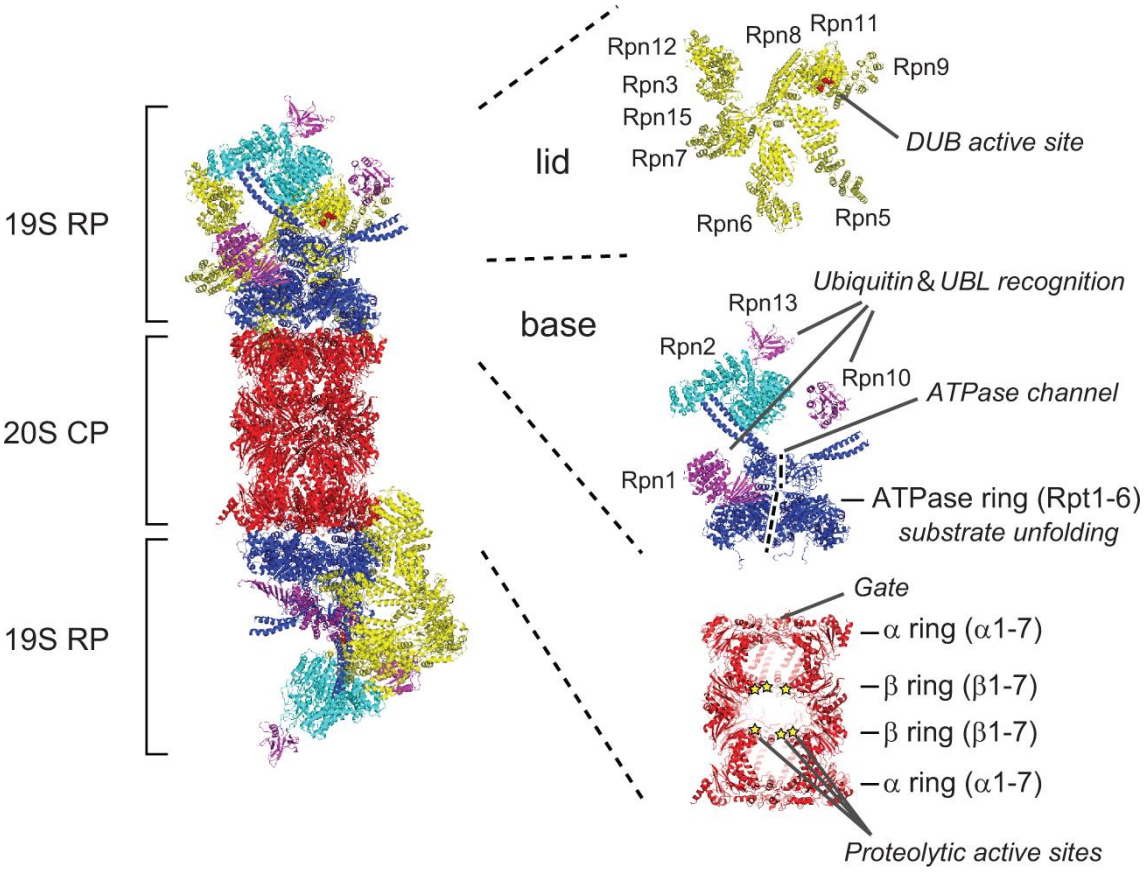

Figure 16. The 30S proteasome assembly.[177]

Picture reprinted from Saeki, Y. Ubiquitin recognition by the proteasome. *J Biochem* 161, 113–124 (2017), reproduced by permission of Oxford University Press.

The regulatory particle 19S (also known as PA700) associates with the catalytic core 20S forming the 26S or the 30S proteasome (single or double capped, respectively) and stimulates the activity of all three proteolytic activities of 20S in a ubiquitin- and

ATP-dependent manner.[178] It is composed of 18 different subunits arranged in two components which 9 subunits each: a base- and a lid-like structure, containing ubiquitin receptors to recognize the polyubiquitinated protein and deubiquitination enzymes (DUBs) which cleave Ub from it (see figure 16). The ATPase ring is also located in the base-like structure; it is composed of six different AAA-ATPases (subunits Rpt1-6) which allow the unfolding of the substrate, the gate opening, and the insertion of the substrate within the 20S.[179] In other words, the 19S particle recognizes, deubiquitinates and unfolds polyubiquitinated peptides/proteins before their entry to the 20S.[36,180]

Differently from 19S, the regulatory particles 11S (also known as PA28; PA26 in yeast) and PA200 (Blm10 in yeast) are ATP-independent activators and promote the hydrolysis of poorly folded peptides, but are not able to permit the entry in the 20S CP of folded proteins.[181]

Three different PA28 isoforms have been identified; the heptapolymerics PA28α and PA28β are expressed in the cytoplasm, while the homopolymer PA28γ is located in the nucleus. [182] The PA28α/β heptameric ring activates all three catalytic sites of the 20S, stabilizing an open conformation of the CP, while the monomeric PA200 stimulates almost 3 times more the PGPH activity than ChT-L and T-L activities.[181]

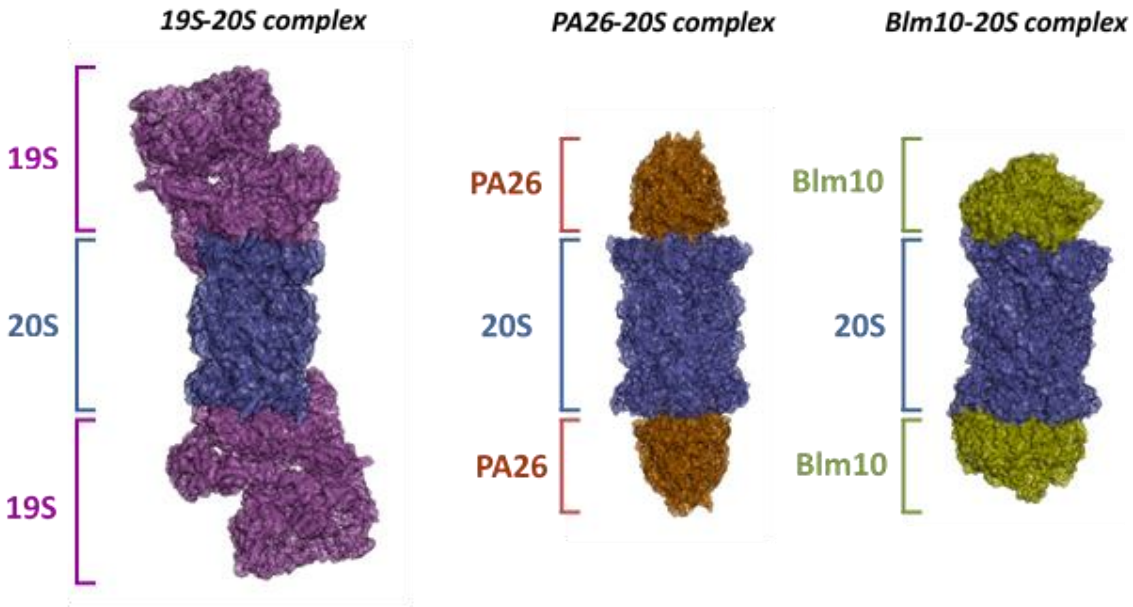

Figure 17. Structure of the assemble of the 20S proteasome with different regulatory particles.

The C-terminal motif HbYX (Hb=hydrophobic group, Y=Tyrosine, and X= any amino acid) is highly conserved in both 19S and PA200 and plays a fundamental role in the activation of the CP. These motifs insert into the grooves created by the α subunits of the 20S, interacting with these and promoting its rotation, leading to the opened conformation.[183,184] However, the interaction of a single HbYX motif, as is the case of the monomeric PA200, is not enough to allow the complete gate opening, and additional interactions are also needed.[185] Although the 11S activator lacks the HbYX motif, it also binds the 20S proteasome thought its C-terminal region and the repositioning of a 9-residues region called "the activation loop" promotes the gate opening of the 20S proteasome.[186] All the so far reported crystal structures of regulatory particles in complex with the 20S proteasome exhibit a close interaction of the RP C-termini tails with the 20S α-grooves (see figure 17). For example, the C-terminal tail of the heptameric PA26 complex anchors the α2/α3, α3/α4, α4/α5, and α5/α6 pockets[187] while the monomeric Blm10 can only bind the α5/α6 pocket, thus promoting a partial opening of the entrance gate.[188] Thus, a common mechanism of activation by the regulatory particles in modulating the proteasome activity has been proposed. According to this mechanism, activators anchor to the alpha 20S surface leading to the reorganization of N-termini by the α subunits, particularly the α-grooves. This reorganization induces the displacement and repositioning of Pro17 reverse turn loop, prompting the open-gate conformer and allowing the entry of substrate into the catalytic chamber.[185]

The 20S CP can also exist and work independently of the RP caps and is capable of degrading substrates in a ubiquitin and ATP-independent manner. In fact, under oxidative stress or mitochondrial dysfunction, the 26S proteasomes are disassembled in 19S and 20S particles, thus facilitating an Ub-independent degradative function.[36] The substrates for the 20S proteasome are proteins that contain unstructured regions, either as a result of mutation or damage or as an intrinsic feature of the proteins themselves, as is the case for IDPs. Recently, it has been demonstrated that the uncapped CP free-form is present in a significant amount in the cell and plays a role in vivo protein lysis, mainly misfolded proteins.[189] Therefore, CP gating phenomena play a critical role in the proteolysis of misfolded proteins.

In addition to the constitutive proteasome, the presence of higher levels of the immunoproteasome in neurons, astrocytes, and endothelial cells of some brain areas of elderly people with regard to young people has been reported, and a higher expression of immunoproteasome has been found in AD brains.[190] The immunoproteasome is a proteasome isoform which differs from the constitutive proteasome in the three catalytic subunits (β1,β2, and β5) which in the case of immunoproteasome are LMP2, MECL-1, and LMP7, also denominated as "inducible subunits".[191] Both isoforms can coexist; differently from constitutive proteasome that is present in almost all cells, immunoproteasome expression depends on the cell type and it is widely expressed in immune cells. Furthermore, some factors as oxidative stress and proinflammatory cytokines, that are involved in AD and T2DM, upregulate its expression.[191,192]

Moreover, ample evidence points to a dysregulation of the UPS in neurodegenerative disorders as AD,[193,194] and in the development of insulin resistance and diabetes as well.[195] For example, the chronic hyperglycemic exposure of human islets in diabetic subjects significantly reduces the activity of all the three proteasome activities and increases the levels of polyubiquitinated proteins. The higher levels of polyubiquitinated proteins have been ascribed to an observed deficiency of the deubiquitinating enzyme ubiquitin carboxyl-terminal hydrolase L1 (UCH-L1) enhancing the impairment of the UPS.[196] Decreased levels of UCH-L1 has been also observed in brains of AD and PD.[197]

Despite Aβ,[198] tau,[199] and IAPP[200] are degraded by the proteasome, they are also known to interfere with the proteasome activity. For example, IAPP inhibits proteasome activity by interacting with the 20S catalytic domain.[200] It has been reported that PHF-tau inhibits proteasome activity leading to neurodegeneration.[201] Furthermore, Aβ oligomers interact allosterically with the proteasome on the gate region, blocking the assembly of the 19S RP and impairing the 20S CP, reducing both ubiquitin-dependent and -independent proteasome activities,[202] and enhancing both Aβ and tau accumulation.[203]

1.2.5.3. Ubiquitin and its role in the clearance of proteins

Ubiquitin is a highly evolutionary conserved small protein (76 a.a., 8.5 KDa) with specific roles in the regulation of many intracellular processes including protein degradation and trafficking; ubiquitin marks the proteins that must be destroyed.

The ubiquitination cascade of proteins or peptides is a three-step ATP-dependent process and involves three different enzymes: E1, E2, and E3. In the first step, the Ub is activated in an ATP-dependent reaction catalyzed by the ubiquitin-activating enzyme E1. This reaction generates a high energy intermediate, where E1 and Ub are linked through a thiol ester. Then Ub is transferred from E1 to E2 or ubiquitin-conjugation enzyme. In the last step, a ubiquitin-ligase enzyme E3 interacts with both Ub and substrate and catalyzes the link of Ub from E2 to the substrate (see figure 18).

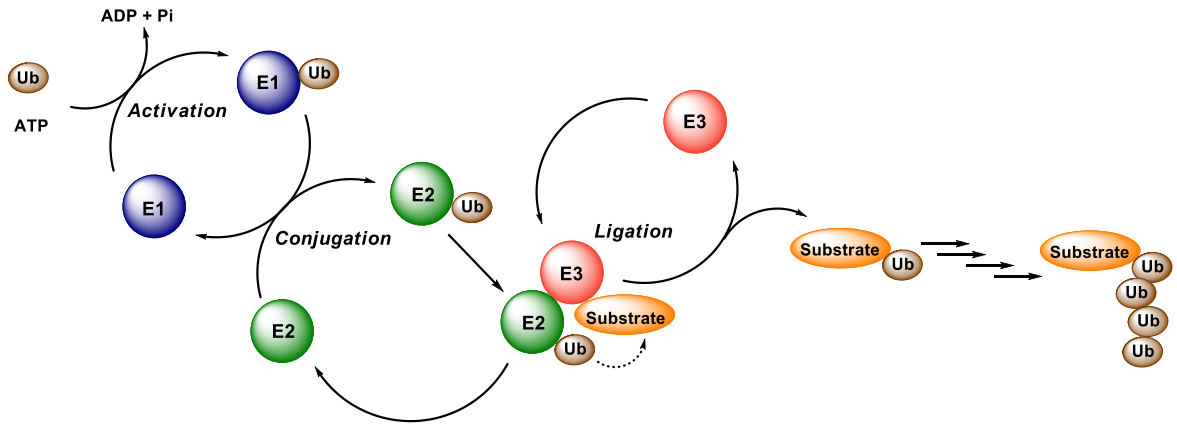

Figure 18. The ubiquitination cascade.

Then, other ubiquitin units are incorporated by an identical mechanism, forming different types of Ub chains that vary in length and linking position, forming linear or branched chains that can be homogeneous (formed only by ubiquitin units) or mixed/heterogeneous (containing other ubiquitin-like proteins).[204] The links are formed through an isopeptide bond between the amine group of one of the lysine residues of the ubiquitin (K6, K11, K27, K29, K33, K48, or K63) to be linked and the C-terminus of the ubiquitin that already belong to the chain.[204] The ubiquitination position determines the pathway of degradation of the misfolded peptide. K48 and K63 ubiquitin links are the most abundant; K48-linked polyubiquitin chains address both proteasomal and

autophagic degradation while K63-linked chains are recognized only by autophagy receptors.[205]

It is widely known that there is a significant correlation between the length of the polyubiquitin chain and its recognition by the proteolytic pathways. In addition to the broadly accepted linkage-position specificity, length-specificity has been also observed when polyubiquitinated substrates interact with ubiquitin-binding proteins (UBPs).[206] Despite it has been reported that tetra-ubiquitin is the minimum signal recognized by the proteasome,[207] several pieces of evidence indicate that ubiquitination signaling is a highly adaptative process and, in some cases, also smaller ubiquitin chains have been observed being recognized by the proteasome.[208]

The hierarchical organization of ubiquitination enzymes allows a strict regulation of the process: only three different E1 enzymes are known, while the number of E2 is approximately 40 and E3 enzymes are more than one thousand, each characterized by a high specificity.[205]

Reduced activity of both E1 and E2 enzymes has been reported in AD brains, suggesting that the failure of ubiquitination cascade could be involved in the pathogenesis of AD.[209] Furthermore, recent work from our lab reported that the interaction of Ub with Aβ delays and reduces the Aβ fibrils formation and inhibits both K48- and K63-linked polyubiquitination reactions.[210]

1.2.5.4. Other clearance systems

In addition to the UPS, which is the main clearance system of misfolded proteins, the PN also involves other secondary clearance pathways which play a role in the degradation of amyloids, the autophagy–lysosomal pathway (ALP) and amyloid digestion by metalloproteases.

Autophagy is a bulk recycling system whereby large cytoplasmatic materials, which include protein aggregates, misfolded proteins, organelles, and microbes, are degraded. Depending on the way that the cargo is delivered into the lysosomes, three principal types of autophagy pathways have been described: macroautophagy,

microautophagy, and chaperone-mediated autophagy (CMA).[36] Macroautophagy is the best characterized and is the only autophagic pathway able to degrade large substrates, as is the case of protein aggregates.[211] Macroautophagy starts with the formation of a double membrane structure, the phagophore, which evolves engulfing the substrates in the autophagosome. Autophagosomes are then transported along microtubules and fused with lysosomes to create the autolysosome, where lysosomal hydrolases degrade their content and the degraded autophagosomal cargo is released into the cytoplasm to be used in the synthesis of proteins or production of energy (see figure 19).[36,211]

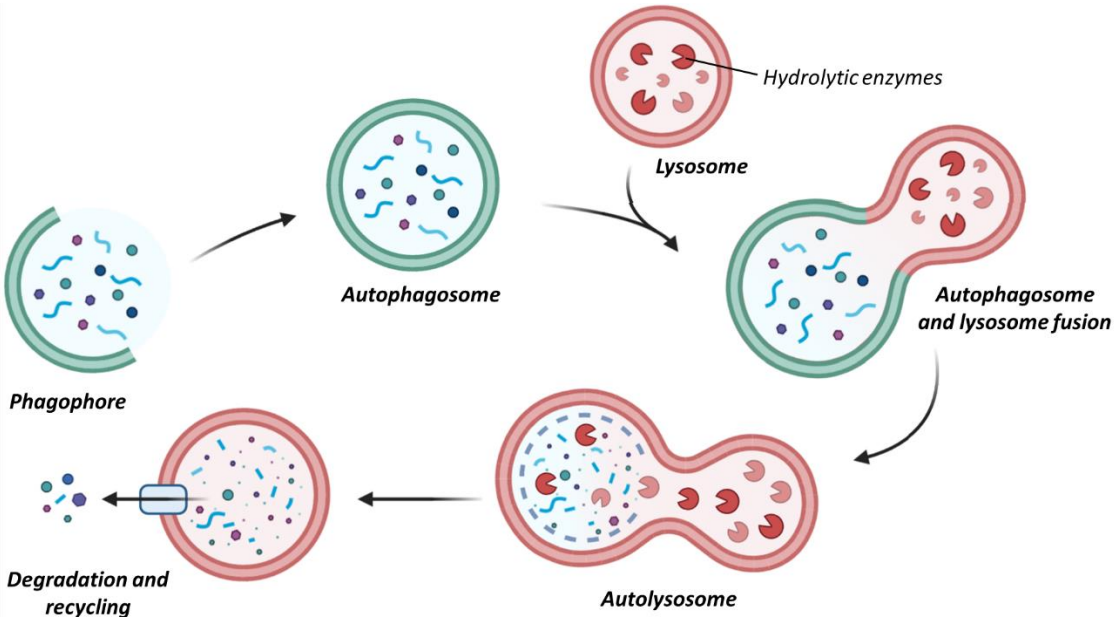

Figure 19. Macroautophagy process.

Several data suggest that the impairment of the ALP precedes the accumulation of extracellular aggregates in AD. It is known that neurons present a basal level of autophagy and an autophagic regulation which are different from the other cells, being neurons more vulnerable to autophagic basal changes. In PCDs, autophagic dysfunction contributes to the formation of aggregates. Impaired autophagosome formation[212] and dysfunction in lysosomal digestion have been observed in AD, as well as in other neurodegenerative disorders.[39] Furthermore, it has been observed an accumulation of autophagosomes in dystrophic neurites in AD because the impairment of the microtube-mediated axonal transport of autophagosome caused by the hyperphosphorylation of the microtubule-associated protein tau.[213]

Besides UPS and ALP, many other mechanisms are involved in the surveillance of the PN. The extracellular proteolytic degradation of amyloids is mainly carried out by metalloproteases. They are important targets for therapeutic purposes in the field of AD and T2DM, but it is also important to remark that they carry out other functions. The most studied are the insulin-degrading enzyme (IDE) and neprilysin (NEP); other enzymes as matrix metalloproteinases (MPs), angiotensin-converting enzyme (ACE), endothelin-converting enzyme (ECE), and plasmin are less characterized.[214]

IDE is a 110-kDa ubiquitous zinc metalloprotease playing a crucial role in insulin degradation. Although IDE has been mainly found in the liver and pancreas, it is also present in other tissues such as the brain.[215] Beside insulin, it is also involved in the degradation of different substrates as glucagon, amylin, calcitonin, and Aβ.[216] NEP is a zinc-metalloprotease found in several organs as such as the kidneys and the brain, playing different roles depending on the tissues where it is expressed. NEP can degrade a wide range of substrates, and its specific activity is cross-correlated to availability of substrates in the tissue.[217]

IDE and NEP can degrade both Aβ and IAPP and their malfunction is associated with the pathogenesis of AD and T2DM;[217–219] in fact, a decrease in IDE and NEP expression with normal aging,[214,220,221] as well as a reduced expression of IDE with diabetes[220] and of NEP with AD and a concomitant accumulation of IAPP and Aβ, respectively, has been reported.[221] Furthermore, age-dependent oxidative stress has been shown to leads to NEP oxidation and increased levels of oxidized NEP have been observed in AD brains.[222]

1.3. Natural products as a source of drugs: silybins

Natural products have been used from antiquity in the treatment of several maladies and currently, they continue been widely used in the treatment of numerous diseases and are also the source of inspiration in the design of pharmacophores and drugs (mimics of natural products, natural derivatives, etc.). The importance of natural compounds in drug development is such that more than half of all the drugs approved by the United States Food and Drug Administration (FDA) in the last 40 years proceed from natural sources, are derivatives or are inspired on it.[223]

Natural compounds are, in general, highly attractive candidates to be screened for AD and T2DM treatment. It is known that in general, nutraceutical compounds possess several antiaging properties, e.g. antioxidant and anti-inflammatory.[224] They are secondary metabolites generated by the plants in response to different stresses, as an evolutive result of their defense system,[225] and despite their simple chemical structure they mostly interact with several targets as "multifunctional drug-like molecules".[226] In fact, although natural medicines are often less potent in comparison to synthetic drugs, they are in general better tolerated by the organisms and are then more useful when prolonged treatments are needed.[227] Furthermore, the role of a healthy diet in reducing the risk of suffering from AD has been determined by several studies.[228] A clear example of the benefits of phytochemical compounds is found in Mediterranean Diet, with including a high intake of fruits, vegetables and olive oil which has been associated with a slower cognitive decline and a reduced risk of developing dementia.[229–232]

Natural compounds present the advantage that can be applied not only in the treatment of the disease but also with the intake of food as a preventive approach against the development of the malady. Next, the low cost of raw materials and the relatively simple reaction protocols designed to obtain the final products make them a reliable target for pharma companies focusing on cost reduction in the production processes.

1.3.1. Chemistry, bioavailability, metabolism, and therapeutic uses of silybins

Silibinin is the major (50-70%) and most active component of silymarin, an extract of milk thistle seed. It is constituted by a (1:1) mixture of silybin A (Sil A) and silybin B (Sil B), two flavonolignan diastereoisomers (see figure 20).

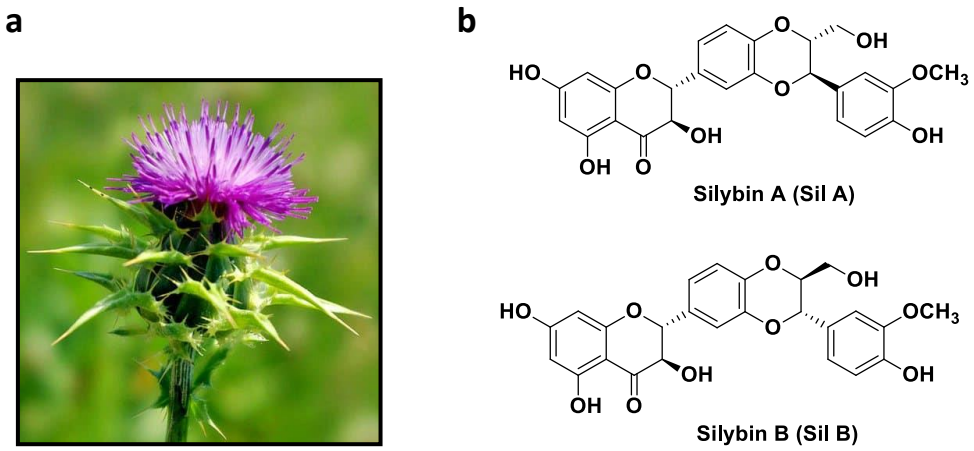

Figure 20. (a) *Silybum marianum* or milk thistle. **(b)** Chemical structure of silybin A and silybin B.

Silybins are small and highly functionalized molecules with alternate benzenic rings and O-heterocycles; in particular, their chemical structure is composed of two main groups, the flavonol group taxifolin and the phenylpropanoid group coniferyl alcohol, which are linked through an oxeran ring[233] (see figure 21). Sil A and Sil B are trans-diastereoisomers presenting a different configuration of their stereocenters C-10 and C-11 (10R,11R in Sil A and 10S,11S in Sil B) and the same configuration in the other two present stereogenic centers (1R,2R in both cases). They present 5 hydroxyl groups, of which 3 of them are phenolic (5-OH, 7-OH, and 20-OH) with pK_a values in aqueous solution of around 6.6, 7.7-7.9, and 11.0, respectively.[234] The oxo group in position 3 is conjugated with the adjacent aromatic ring and interacts with 5-OH through a hydrogen bond, acting as a free electron-pair donor. The 3-OH hydroxyl is easily oxidable forming 2,3-dihydrosilybins, compounds that are also present in the silymarin extract.[233]

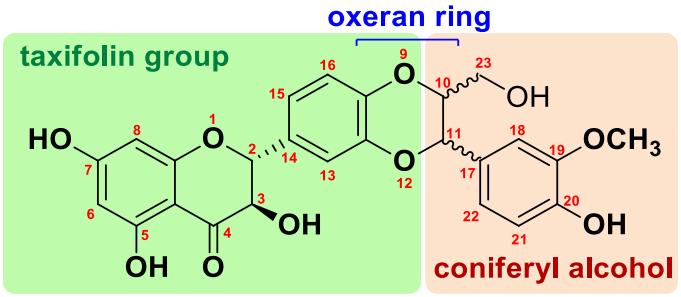

Figure 21. Chemical structure of silybins and nomenclature

Silybins are hydrophobic molecules with a very low water solubility, which limits notably their bioavailability. After oral administration, silybins are quickly but poorly absorbed in the stomach, metabolized, and eliminated with a half-life of approximately 6h.[235] Only a small fraction (2-8%) is eliminated in the urine while the main absorbed compound (around 80%) is biotransformed in the liver forming glucuronide and sulfate conjugates, which are excreted with the bile via feces.[236–238] The stereospecificity of biotransformations lead to more efficient glucuronidation of Sil B than Sil A: it occurs in both C-7 and C-20 positions for Sil A, while Sil B is preferably glucuronidated in C-20.[239]

The hepatoprotective activity of silymarin, and in particular of silybins, has been widely reported[240] and several pharmacokinetic and toxicity studies demonstrate its pharmacological safety.[241,242] The use of milk thistle seed to treat liver disorders traces back to the ancients Greece and Rome and has been also used by Chinese and Indian traditional medicines.[237] In addition to their hepatoprotective use, silymarin, and particularly silybin, also possess several pharmacological activities such as antioxidant,[243] anti-inflammatory,[244–247] anti-arthritic,[247] neuroprotective,[248] nephroprotective,[249] cardioprotective,[250] anti-cancer[251–253] activities.

1.3.2. Promising effects and limitations of silybins in the treatment of AD and T2DM

Drug repositioning may represent an attractive strategy that allows minimizing risks reducing the cost and time required in the drug development process (10-15 years). These drugs have already been tested in humans and the information of their pharmacological, safety, and toxicology information is already available.[254] Several

reports show the high potential of silymarin as an anti-AD drug due to its anti-aggregating properties,[255–257] their ability to suppress APP expression[258] and to inhibit cholinesterase activity.[259] Recent studies of our research group have also probed the critical role of the stereochemistry of these compounds in the inhibition of $A\beta_{1-40}$ aggregation in aqueous media, being Sil B more active than Sil A due to different preferential interactions with the peptide.[260] While Sil A interacts with the stretches L17-F20 and N27-I32 resulting in bend, turn, and β-sheets structures, Sil B interacts preferably with the C-terminal hydrophobic region (residues 35M-V40) maintaining $A\beta_{40}$ unstructured, and therefore inhibiting more effectively $A\beta_{40}$ aggregation. Furthermore, the alteration of the IAPP oligomerization process,[261] the inhibition of IAPP aggregation,[262] as well as the attenuation of glucose release in blood plasma by improving the glycemic control in presence of silibinin have been reported, suggesting the potential use of these natural molecules to treat T2DM.[263] However, despite the promising potential of silybins in the treatment of AD and T2DM, their use is highly limited, as discussed above, due to their low solubility and bioavailability.

1.3.3. Drug delivery: glycoconjugation

To enhance the therapeutic efficacy of silybins, we need to i) increase their water solubility, ii) prolong their half-life, and iii) ameliorate their bioavailability. To accomplish these needs, a suitable strategy may be the conjugation of the drug with a pro-moiety, (the pro-drug approach). The pro-drug approach is based on the conjugation of the active drug with a pro-moiety which confers to the precursor or parental drug better pharmacokinetic properties. After the administration, the parental drug is activated thanks to its bioconversion or enzymatical cleavage, releasing the active drug.[264] Phosphate, ester, and carbamates or amidines groups are commonly used in the design of pro-drugs because are cleaved by alkaline phosphatases, esterases, and amidases, respectively. This approach has attracted increasing attention in the last few years and several successful prodrugs have been approved: currently, around 10% of the traded drugs worldwide are prodrugs.[265]

Usually, polar or ionizable pro-moieties are used to increase the solubility of parental prodrugs. While ionizable pro-moieties (phosphate, succinate…) increase the solubility in several magnitude orders, polar but non-ionizable moieties (glycol, sugars, polyethylene glycol…) produce an increase in solubility rather more modest, around 2-3 folds.[265]

On one side, the conjugation with a phosphate group could represent a good choice in the design of our pro-drug, not only because of the increase in solubility, but also because it is known that phosphate prodrugs are chemically very stable in solution and, *in vivo,* the cleavage by endogenous plasma phosphatases take place quantitatively.[265] On the other hand, although conjugation with a sugar moiety increases the solubility to a lesser extent than ionizable moieties, it presents other advantages. The sugar moieties of glycoconjugates are specifically recognized by lectins, cell membrane receptors, and thus the glycoconjugates are internalized by endocytosis.[266] Among all the possible carbohydrates that can be chosen as pro-moiety in the design of a silybin precursor, the nonreducing disaccharide trehalose (TH) deserves particular focus on the field of PCDs, because of its osmolytes properties. TH has been used as a chemical chaperon,[267] stabilizing the structure of proteins preventing protein misfolding, and diminishing their susceptibility to aggregation. Furthermore, TH has shown neuroprotective properties in animal models of some neurodegenerative disorders (AD[268,269], PD[270–272], HD[273] and ALS[274]), their ability to inhibit Aβ aggregation has been reported,[275] as well as their autophagy promoting and anti-neuroinflammatory effects.[276]

Chapter 2. Objectives

Inspired by the reported promising results and on the basis of all the above-mentioned premises, this project proposes a multi-target strategy to develop new drugs against AD and T2DM. The novelty of this project is based on a synergistic action, focalizing efforts in regulating many actors of the proteostasis network rather than a unique target. Thereby, this project focuses on the evaluation of the ability of two natural small molecules, the diastereoisomers silybin A and silybin B, following a drug repurposing strategy, to rescue the proteostatic balance of the amyloidogenic peptides Aβ and IAPP, which results compromised in pathological conditions. The effects of the compounds will be evaluated against several targets involved in proteostasis regulation (see figure 22), paying special attention to the stereochemistry of the investigated molecules, and with the long-term goal aim of designing drug candidates with better pharmacological properties.

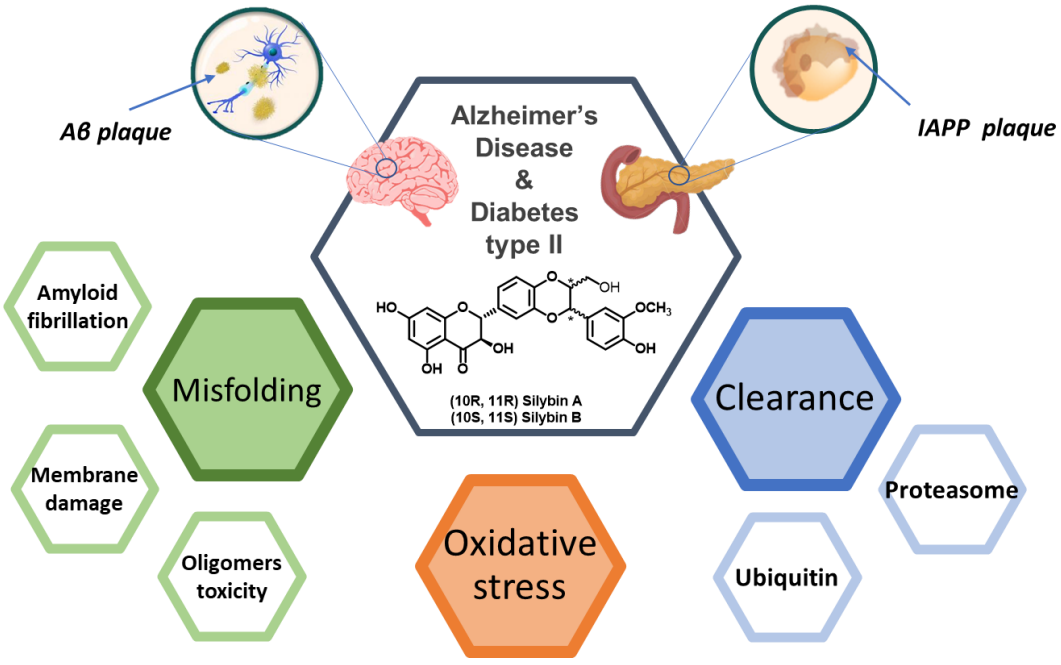

Figure 22. Scheme of the multi-target strategy followed in this thesis.

First, cell viability studies of neuron-like cells have been carried out to assess the non-toxicity of our drugs (silybins), to verify their ability to inhibit the cytotoxicity triggered by Aβ oligomers, as well as their ability to rescue the already produced amyloid oligomers-mediated damage. Then, Sil A and Sil B have been conjugated with a trehalose moiety thought a phosphodiester linker to improve their pharmacological properties, by increasing solubility and bioavailability. The increase in solubility of the trehalose derivatives has been confirmed by DLS. To assess their half-life in human plasma, the bioconversion of glycoconjugates, i.e. its hydrolysis by phosphatases which are present in serum, and the release of silybins over the time have been monitored by HPLC. The non-toxicity of the pro-drugs and their ability to rescue the proteotoxic stress of Aβ oligomers have been also tested by using the same cellular system.

To assess the mechanisms by with the studied compounds exert their cytoprotective effects, their ability to rescue the proteostatic balance has been addressed. First, the antioxidant capacity of both drugs and pro-drugs has been established by using the TEAC assay. Next, we have investigated the ability of both Sil A and Sil B to modulate the UPS. In particular, their ability to activate the yeast and human 20S proteasome has been proved and the molecular mechanism by which the activation takes place has been described by molecular docking. The ability of both silybin-phospho-trehalose conjugates to maintain the properties as activators of the 20S proteasome has been verified. Then, the effect of silybins and silybins derivatives in interfering with the ubiquitination cascade has been also studied.

The anti-amyloidogenic properties of silybins and silybin derivatives have been profiled. First, we have studied the effect of both Sil A and Sil B in Aβ aggregation in the presence of neuronal model membranes and their ability to interfere with the amyloid-induced lipidic membrane damage. Second, we have addressed the effects of the two compounds in interfering with hIAPP aggregation in aqueous media or the presence of pancreatic model membranes. Next, the ability of both Sil A and Sil B to protect lipid membranes from the amyloid-induced damage has been investigated for both amyloidogenic peptides Aβ or IAPP by using dye-leakage assays also unveiling the molecular mechanisms involved in the membrane damage process. The effect of silybin derivatives on Aβ and IAPP aggregation has been studied in both aqueous media and in

the presence of neuronal or pancreatic model membranes, respectively, and their ability to protect neuronal/pancreatic membranes from amyloid-induced toxicity has been investigated.

To unveil the atomistic details of the molecular mechanism by which the compounds exert the anti-amyloidogenic properties, the interaction between both poorly soluble ligands, Sil A and Sil B, and the peptide hIAPP has been investigated by MD simulations. Finally, the molecular mechanism by which silybin glycoconjugates interact with Aβ monomers and oligomers has been determined by NMR experiments.

Chapter 3. Results and Discussion

3.1. The cytoprotective properties of Silybins: strengths and weaknesses

Due to the previously reported promising results, silybins are highly attractive candidates in the research against AD and T2DM with potential cytoprotective properties against the proteotoxic stress. However, their scarce solubility and bioavailability make it necessary to design a reliable delivery system that allows the administration of these potential drugs. Thus, in this chapter, we face both issues: i) cytoprotective properties of silybins against the proteotoxic stress induced by Aβ oligomers; ii) the design and synthesis of a pro-drug to overcome the poor bioavailability limitations.

3.1.1. Protective effects of silybins from proteotoxic stress on neuronal cell lines

In order to evaluate the possible toxic effects of silybins, the cell viability of neuroblastoma SH-SY5Y cells was monitored in presence of both Sil A and Sil B (2 - 10 μM) using MTT assays in collaboration with Dr. M.L. Giuffrida and Dr. S. Zimbone in our lab. The human cell line SH-SY5Y can be differentiated with retinoic acid, from the neuroblast-like state into mature neuron-like cells, giving rise to a reliable cellular model to assess the neuroprotective properties of the drug candidate.[277] As shown in figure 23, natural silybins were not toxic in the used cell system.

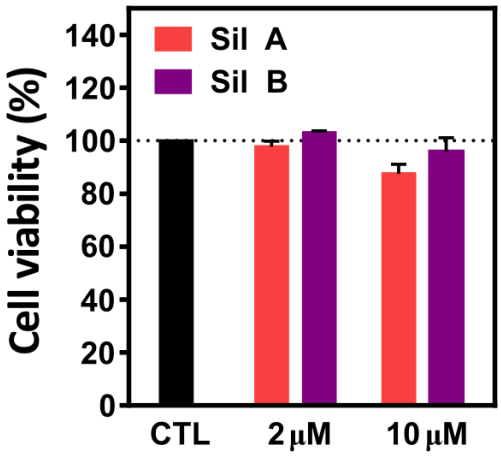

Figure 23 – Non-cytotoxicity of silybins. Cytotoxicity of Sil A (red bars), Sil B (purple bars) at 2 µM and 10 µM tested in differentiated SH-SY5Y neuroblastoma cells after 48 h treatments and quantified by the MTT assay. Results are reported as the normalized percentage of cell viability (± SEM) of 5 independent experiments**.**

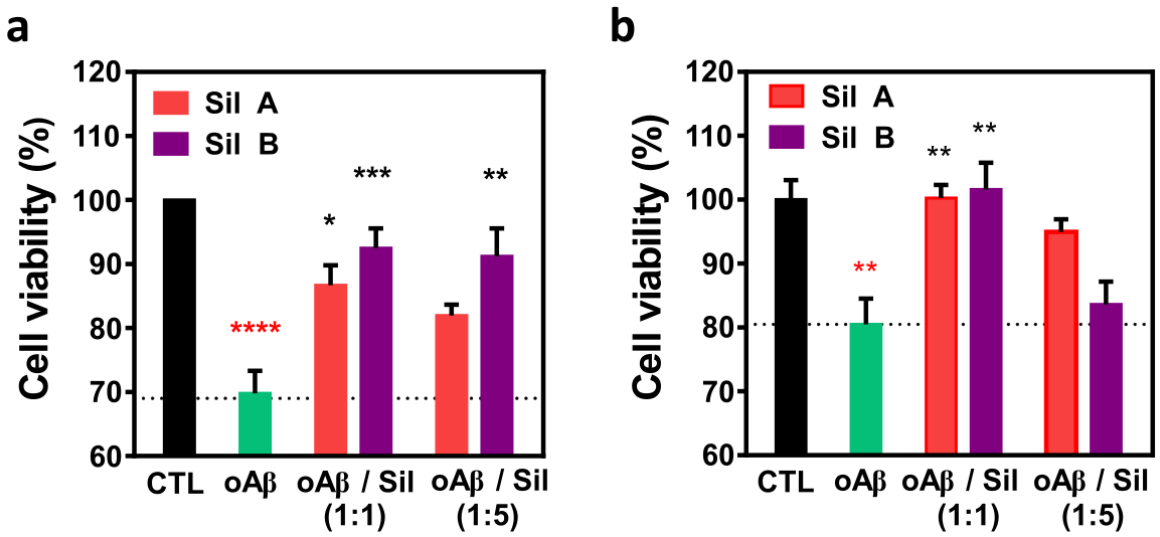

Figure 24 – Reduction of Aβ oligomers cytotoxicity by silybins. **(a)** Cytotoxicity of preformed Aβ oligomers (oAβ) in the absence (green bar) and presence of Sil A (red bars) or Sil B (purple bars) at oAβ/ligand 1:1 and 1:5 molar ratios, tested in differentiated SH-SY5Y neuroblastoma cells and quantified by an MTT assay. Results are reported as normalized percentage of cell viability (± SEM) of 6 independent experiments; analysis of variance has been performed by One-way ANOVA followed by statistical Tukey's test (*p < 0.05; **p < 0.01; ***p < 0.001; ****p<0.0001; red starts (*): significance vs Control; black stars (*): significance vs. oAβ). **(b)** Rescue of the cytotoxicity of preformed Aβ oligomers (oAβ) administered to cells 3 h before the addition of Sil A (red bars) or Sil B (purple bars) at oAβ/ligand molar ratios 1:1 and 1:5, tested in differentiated SH-SY5Y neuroblastoma cells and quantified by an MTT assay. Results are reported as the normalized percentage of cell viability (± SEM) of 3 independent experiments; analysis of variance has been performed by One-way ANOVA followed by statistical Tukey's test (**p < 0.01; red stars (*): significance vs Control; black stars (*): significance vs. oAβ).

Next, we evaluated if these compounds were able to counteract $A\beta_{42}$-induced proteotoxic stress. To this aim, $A\beta_{42}$ oligomers (oAβ) were prepared by incubating $A\beta_{42}$ (2 μM) during 48 h at 4 ºC, in the presence of silybins (Aβ/ligand ratios 1:1 and 1:5). Subsequently, the preformed oAβs were administered to cells. MTT assays performed after 48 h (see figure 24-a) showed that oAβs promoted a reduction of cell viability of around 30% compared to control; however, this toxicity was reduced by both silybins. The higher efficiency of Sil B reconciles with experiments previously reported.[260]

Finally, we studied the ability of the studied compounds to rescue the proteotoxic stress of oAβ previously added to differentiated neuroblastoma SH-SY5Y cells. Preformed oligomers were incubated with cells and, after 3 hours, silybins were added. After 48h, MTT assays (see figure 24-b) were carried out showing, as expected, a reduction of viability of about 20% caused by oAβs. The toxicity was totally rescued in presence of both silybins in a peptide/ligand molar ratio 1:1. At the higher tested ratio 1:5, these effects were slightly lower for Sil A while Sil B presented a more reduced protective activity.

3.1.2. Enhancing silybins solubility and bioavailability: silybin-phospho-trehalose conjugates

Although both Sil A and Sil B have shown very promising effects in terms of the protection against proteotoxic stress induced by Aβ, their low solubility in aqueous solution and poor bioavailability prevent their possible use in effective therapeutic treatments. Moreover, the low solubility of the molecules hinders a complete chemical characterization of the molecular mechanisms underlying their anti-aggregating properties. A plausible strategy to overcome this limitation relies on the chemical modification of the compounds, introducing a hydrophilic moiety in the structure without modifying the properties of the lead compound. Here, in collaboration with Prof. G. Di Fabio (University of Naples Federico II), we set out to conjugate the natural compounds Sil A and Sil B with trehalose (TH), a non-reducing disaccharide thought a phosphate linker (see figure 25; synthesis procedure described in the methodology chapter 4.2). This choice could potentially represent a win-win strategy since TH by itself is known as an antiaggregant molecule able to cross the BBB. Both phosphate and trehalose motifs will increase the solubility and viability of the parent

compounds. Furthermore, the phosphate linker will permit the hydrolysis of silybin glycoconjugates by the endogenous phosphatases and the progressive release of the silybins with an increase of their pharmacokinetics and bioavailability.

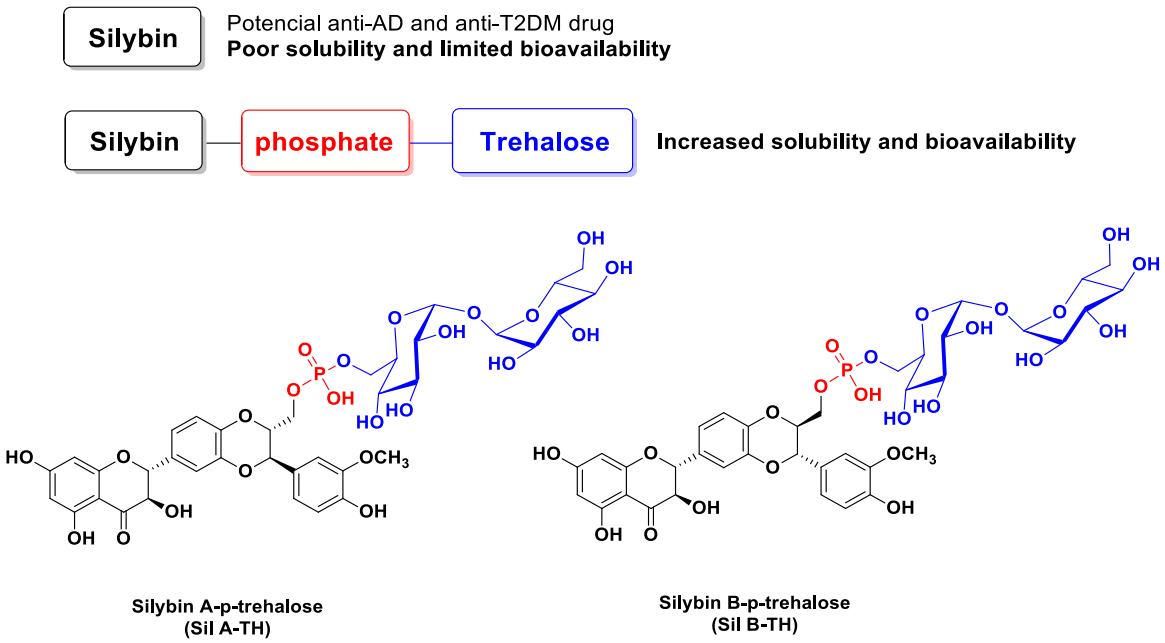

Figure 25. Structure of Sil A and B and their phospho-trehalose glycoconjugates.

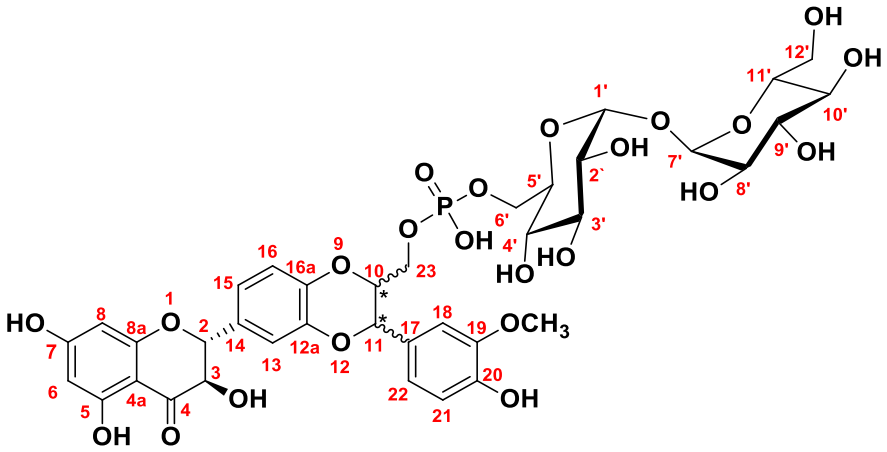

Figure 26. Nomenclature followed for silybin-phospho-trehalose conjugates.

3.1.2.1. Solubility of Sil A/B-phospho-trehalose conjugates

Dynamic Light Scattering (DLS) is the most common technique used to analyze the particle size in the nm range and to determine the particle size distribution. This technique is based on the detection of the scattered light intensity due to the presence of particles in solution. The characterization of particles size is possible thanks to the existent correlation

between the Brownian movements of particles and their hydrodynamic size, which is calculated by using the Stokes-Einstein equation.[278]

To confirm the increase in solubility of silybin glycoconjugates in comparison with the parental silybins, the solubility in water of silybins and silybin glycoconjugates was analyzed by Dynamics Light Scattering (DLS) measurements. Figure 27 shows the plots of the autocorrelation coefficient versus the delay time of silybins and silybin glycoconjugates solutions at different concentrations, allowing the identification of aggregates and the characterization of their size. DLS data indicate that particles in suspension were present at 10 µM for Sil A and at 5 µM for Sil B, both containing two differently sized populations around 40-60 nm and 200-250 nm. Silybin glycoconjugates were analyzed up to 200 µM without exhibiting the presence of particles in solution, verifying their higher solubility (see figure 27).

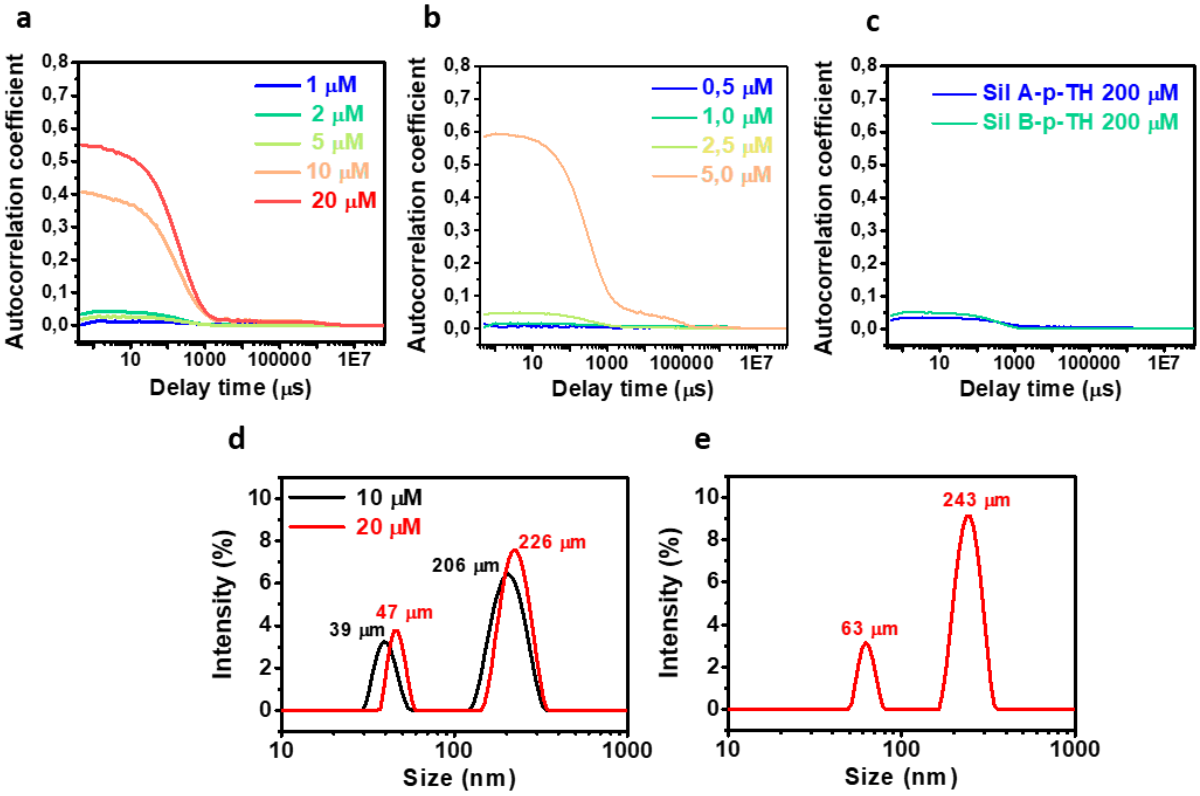

Figure 27 – Dynamic Light Scattering (DLS). (a) The decay of autocorrelation function with time obtained from DLS for aqueous Sil A solutions at increasing concentrations (from 1 µM to 20 µM). **(b)** as (a) except for Sil B (from 0.5 µM to 5 µM). **(c)** as (a) except for Sil A-p-TH and Sil B-p-TH at 200µM. **(d)** Particle size distribution curves (intensity vs. particle diameter) of Sil A (10 µM and 20 µM) obtained from (a). **(e)** As (a) except for Sil B 5 µM obtained from (b).

3.1.2.2. Stability of Sil A/B-p-TH in Human Serum

Due to the presence of endogenous phosphodiesterase enzymes in the blood, human serum represents a reliable model to estimate the stability of silybin-trehalose phosphodiester conjugates *in vivo*. Thus, the serum stabilities of both Sil A-p-TH and Sil B-p-TH were evaluated at 37 °C. To this aim, the hydrolysis rate of the silybin derivatives was monitored by HPLC (see figure 28). The Sil A-p-TH and Sil B-p-TH half-life in serum obtained under these conditions were $t_{1/2}$ = 93 h and $t_{1/2}$ = 88 h, respectively.

These data confirm the progressive release, in a time-scale of days, of the bioactive silybins and hence, the potential use of their trehalose conjugates in a pro-drug approach. Conclusively, glycoconjugation allows overcoming the limitations associated with the low solubility and bioavailability of silybins. The increased solubility of silybin-glycoconjugates allows the administration of higher amounts of the pro-drug, which in turn, is stable for days and releases progressively the less bioavailable active silybin.

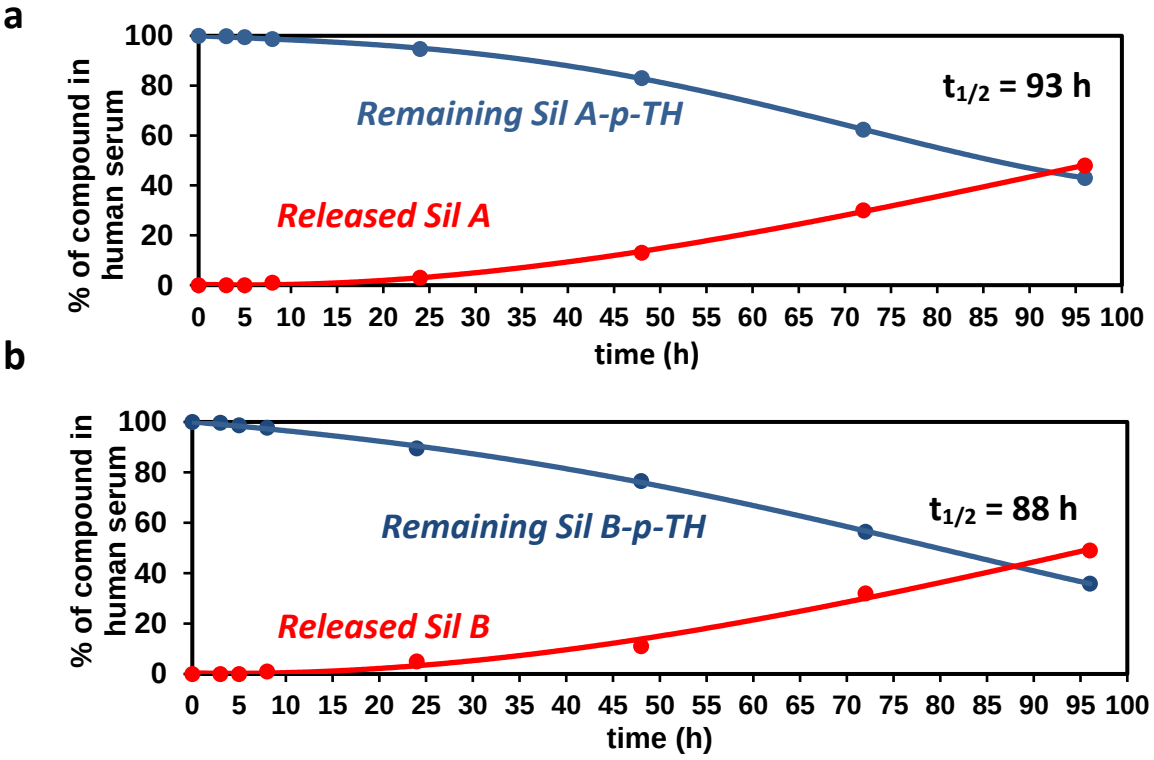

Figure 28 – Stability in human serum of Sil A-p-TH and Sil B-p-TH. (a) Percentage of Sil A-p-TH (red curve) and Sil A (blue curve) over time in human serum. The amount of both molecules released over time has been quantified by the change in the integration of the corresponding HPLC peaks. **(b)** As (a) except for Sil B-p-TH and Sil B.

3.1.3. Protective effects of silybins derivatives from proteotoxic stress on neuronal cell lines

The possible toxic effect of silybin derivatives and trehalose was evaluated following the procedures already used to test the natural silybins. As shown in figure 29, silybin-conjugates and trehalose were not toxic in the used cell line.

Next, cell viability studies were carried out after the co-administration of $A\beta_{42}$ oligomers (oAβ) and the ligands. All the tested compounds, i.e. Sil A-p-TH, Sil B-p-TH, and TH, were able to counteract oAβ-induced proteotoxic stress (see figure 30-a) but, interestingly, natural silybins were significantly more effective than the silybin derivatives or TH. When the ligands were added 3 h after the administration of the preformed oAβ, the toxicity was totally rescued in presence of both silybin derivatives in a peptide/ligand molar ratio 1:1, while at 1:5 molar ratio, Sil B-p-TH, as its parental compound, presented a reduced efficacy (see figure 30-b).

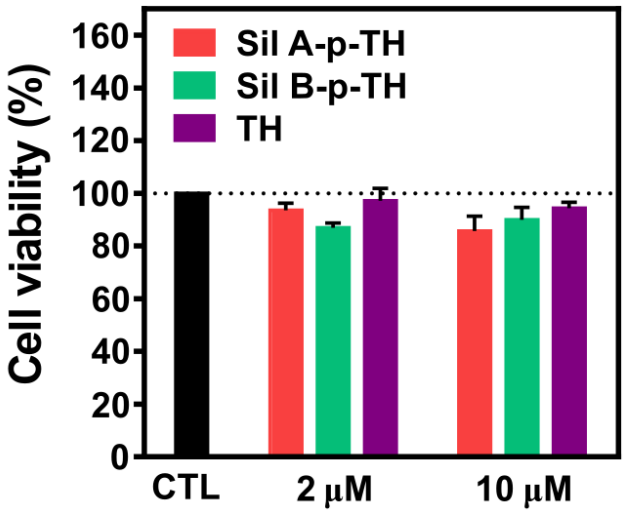

Figure 29 – Non-cytotoxicity of silybin derivatives and trehalose. Cytotoxicity of Sil A-p-TH (red bars), Sil B-p-TH (green bars), and TH (blue bars) at 2µM and 10µM tested in differentiated SH-SY5Y neuroblastoma cells after 48h treatments and quantified by MTT assay. Results are reported as the normalized percentage of cell viability (± SEM) of 5 independent experiments.

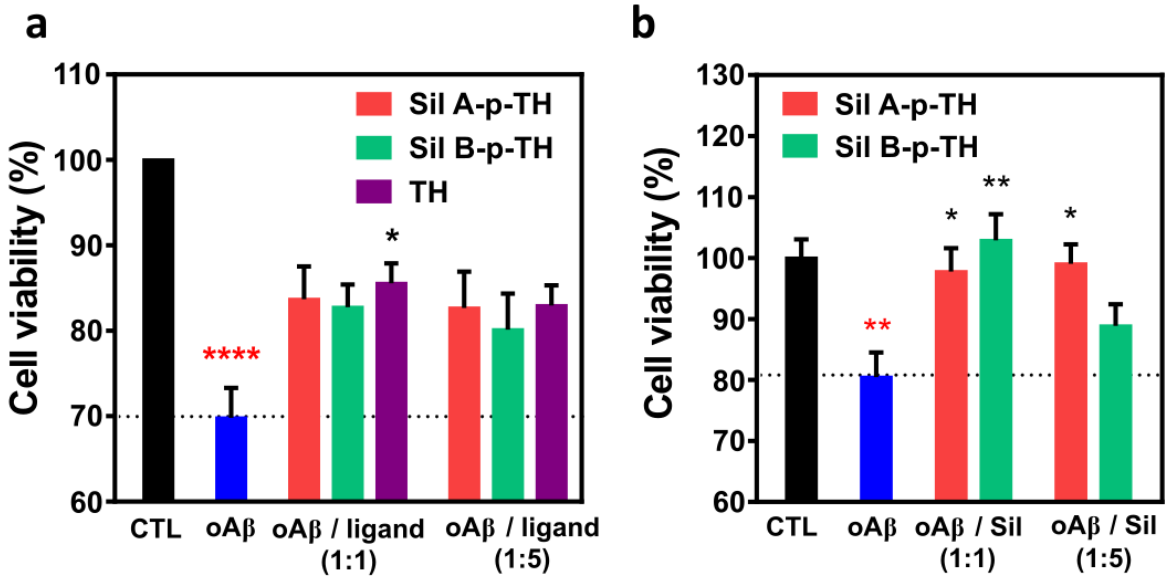

Figure 30 – Reduction of Aβ oligomers cytotoxicity by silybin derivatives and trehalose. **(a)** Cytotoxicity of preformed Aβ oligomers (oAβ) in the absence (blue bar) and presence of Sil A-p-TH (red bars), Sil B-p-TH (green bars), and TH (purple bars) at oAβ/ligand 1:1 and 1:5 molar ratios, tested in differentiated SH-SY5Y neuroblastoma cells and quantified by an MTT assay. Results are reported as the normalized percentage of cell viability (± SEM) of 6 independent experiments; analysis of variance has been performed by One-way ANOVA followed by statistical Tukey's test (*p < 0.05; ****p<0.0001; red starts (*): significance vs Control; black stars (*): significance vs. oAβ). **(b)** Rescue of the cytotoxicity of preformed Aβ oligomers (oAβ) administered to cells 3 h before the addition of Sil A-p-TH (red bars) or Sil B-p-TH (green bars) at oAβ/ligand molar ratios 1:1 and 1:5, tested in differentiated SH-SY5Y neuroblastoma cells and quantified by an MTT assay. Results are reported as the normalized percentage of cell viability (± SEM) of 3 independent experiments; analysis of variance has been performed by One-way ANOVA followed by statistical Tukey's test (*p < 0.05; **p < 0.01; red stars (*): significance vs Control; black stars (*): significance vs. oAβ).

3.1.4. Antioxidant capacity of Sil A, Sil B, Sil A-p-TH and Sil B-p-TH

It is known that neuroprotective effects of some small molecules mostly rely on their ability to counteract oxidative stress which occurs in pathological conditions. To study the antioxidant capacity of Sil A, Sil B, and their derivatives Sil A-p-TH and Sil B-p-TH, we used the Trolox Equivalent Antioxidant Capacity (TEAC) assay. This assay measures the ability of antioxidants to scavenge the stable radical cation $ABTS^{\bullet+}$ (2,2'-azinobis(3-ethylbenzothiazoline-6-sulfonic acid)), a blue-green chromophore with a maximum absorption band at 734 nm. The absorbance intensity decreases when the radical species

is reduced in the presence of antioxidants forming the colorless ABTS, with a decrease in absorbance proportional to the antioxidant capacity of the compound. In this assay, the results are expressed as equivalents of Trolox, a well-known antioxidant compound used as control which is a water-soluble analog of Vitamin E.

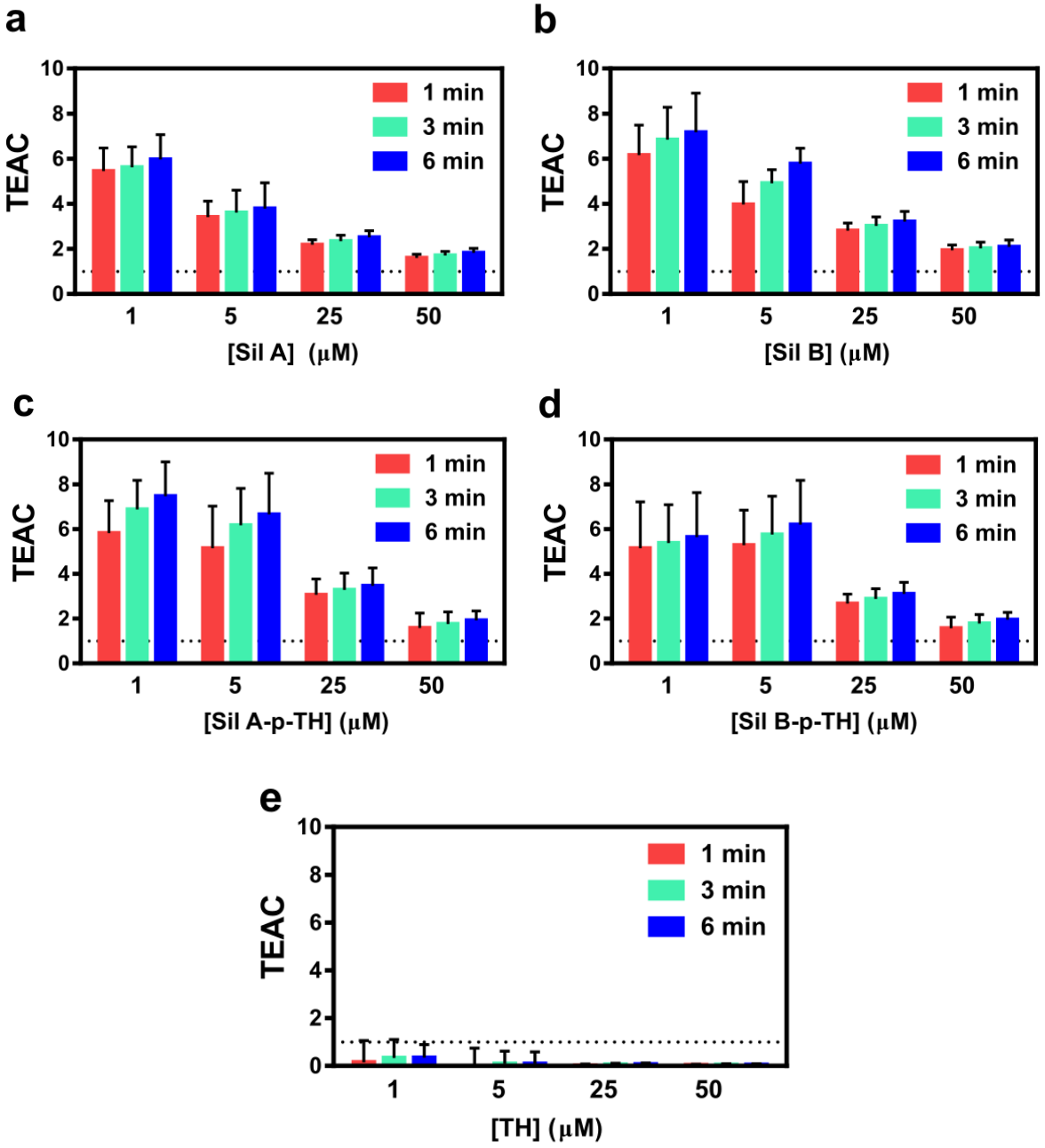

Figure 31 – Antioxidant capacity of silybins, silybin derivatives, and trehalose. (a) Trolox equivalent antioxidant capacity (TEAC) of Sil A measured at different concentrations (1 µM, 5 µM, 25µM, and 50 µM). Results are reported as the average of at least 6 different experiments (± SEM). **(b)** As (a) except for Sil B. **(c)** As (a) except for Sil A-p-TH. **(d)** As (a) except for Sil B-p-TH. **(e)** As (a) except for TH.

Silybins (Sil A and Sil B) and silybin derivatives (Sil A-p-TH and Sil B-p-TH) showed a similar (and high) antioxidant capacity, significatively superior to Trolox, which increased over time and decreased with the increase of concentration (see figure 31). Indeed, TEAC was around 6-7 in all the cases when were assayed at 1 µM concentration and decreased until around 1.5-2 at 50 µM. This behavior has been observed with other phenolic compounds: the stoichiometry of the process varies from one to another phenolic compound and it has been observed that, for phenols which present a large stoichiometry coefficient, it tends to decrease by increasing the phenol concentration.[279] The TEAC value increased with time because of the different kinetics profiles of the reaction of Trolox and silybins with the $ABTS^{\bullet+}$ radical (see figure 32). Indeed, Trolox exerts its antioxidant action very quickly, completing the reaction in the first seconds after its addition. On the contrary, silybins exert their antioxidant effect with significantly slower kinetics, and thus, their TEAC value increases with time. In fact, the reaction was not completed at the last reported measure (6 min). Complex kinetic profiles of this reaction have been observed for several polyphenols, associated with the different reactivity of the reactive centers of the compounds.[280] In particular flavonoids antioxidant reactions are characterized by two distinct phases with kinetics determined by the structure of the B ring.[281]

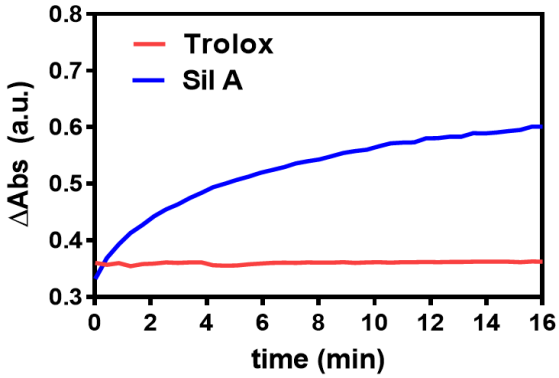

Figure 32. Reduction in the absorbance of the radical $ABTS^{\bullet+}$ with respect to control over time in presence of 50 µM Trolox (red) and 50 µM Sil A (blue).

TEAC was also measured for TH as a control in the same experimental conditions. As expected for a non-reducing sugar, trehalose does not show antioxidant activity. In conclusion, the high antioxidant capacity which makes silybins and silybin derivatives particularly good free radical scavengers is an additional value against AD and T2DM, where oxidative stress is present, triggering the pathologies.

3.2. Silybins as activators of proteostasis

The role of the amyloid clearance systems is fundamental in maintaining the proteostasis and the activation of these pathways represents a suitable strategy in the fight against PCDs when proteostasis is unbalanced leading to amyloid aggregation. Here we focus on evaluating the ability of natural silybins to regulate the main amyloid clearance pathway, i.e. the UPS. In particular, we evaluate how these compounds may i) regulate the process by with the incorrect or misfolded proteins are marked to be recognized by the proteolytic pathways, i.e. the ubiquitination cascade; ii) modulate the catalytic core of this system, i.e. the activity of the 20S proteasome.

3.2.1. Effects of silybins and their derivatives on the poly-ubiquitination pathway

As we have seen before, the UPS impairment could be related not only to proteasome failure but also to the ubiquitin conjugation machinery. It is difficult to single out the roles played by a single small molecule on each of the two UPS partners, i.e. ubiquitin or proteasome. Therefore, to exclude the cross-related effects with proteasome presents in the live cell, where an intricate network of cross-related effects may occur simultaneously, we ran specific tube test experiments. For this reason, to distinguish the effect of the parent drugs Sil A and Sil B and their glycoderivatives on the ubiquitination pathway, we performed dose-response ubiquitination assays in tube tests.

K48-linked polyubiquitination reactions were carried out in the presence of Sil A, Sil B, Sil A-p-TH, or Sil B-p-TH at a concentration ranging from 1 µM to 5 µM (see figure 33-a). Sil A, both 1 µM and 5 µM, showed a mild activation of the ubiquitination cascade increasing the total amount of polyubiquitinated species around 7% and 12%, respectively. In the case of Sil B, a bimodal behavior was observed: a mild activation up to 1 µM, (although higher than what was observed with Sil A) raising around 20% the total amount of polyubiquitinated species. However, at a higher concentration, inhibition of the process occurs, and the total number of formed polyubiquitinated species decreased by about 36% when compared to control (see figure 33-a and -c). Due to the low solubility of silybin, we

ascribe the inhibitory effect of Sil B at 5µM to the soluble small-sized assemblies of the ligand; however, the involvement of other possible mechanisms cannot be ruled out.

The ability of trehalose-conjugates to activate polyubiquitination reactions was significantly higher than for the natural compounds (see figure 33-b and -c). The quantity of poly-ubiquitinated species increases 70% and 100% in the presence of Sil A-p-TH 1 µM and 5 µM, respectively, in comparison with the control. Reactions in presence of Sil B-p-TH showed an increase of poly-ubiquitinated species of about 100% when its concentration was 1 µM but was 53% when the concentration was increased to 5 µM.

As mentioned previously (see chapter 1.2.5.3), the length of the polyubiquitinated chain is strongly correlated with the efficiency of substrate recognition by the proteolytic machinery and tetraubiquitin has been proposed as a minimum degradative signal to be recognized for the proteolytic pathways. For this reason, we ran a densitometric study of the revealed PAGE comparing the different polyubiquitinated species. This analysis revealed a slight increment in the quantity of all polyubiquitinated species (di-, tri-, and tetra- or higher-order ubiquitinated species) in the presence of Sil A (1µM and 5µM) and Sil B (1µM), but a decrease of all them (except for tri-ubiquitinated species) when Sil B 5µM was used (see figure 33-d, -e and -f). An increase in the number of diubiquitinated species was also observed after the incubation with Sil A-p-TH and Sil B-p-TH. This effect was even larger than in presence of natural compounds. Furthermore, a significant increment of levels of polyubiquitinated species of four or more Ub units was observed for Sil A-p-TH and Sil B-p-TH, at 1 µM. This effect was less pronounced in presence of silybin derivatives at 5 µM, particularly in the case of Sil B-p-TH (see figure 33-f). It should be noted that tri-ubiquitin was not considered in the densitometry analysis when the derivatives were used because of an overlap with the E2 band. The obtained pattern was similar to that obtained in the presence of Sil A and Sil B, but the activation was much more pronounced for the trehalose conjugates. (see figure 33-d).

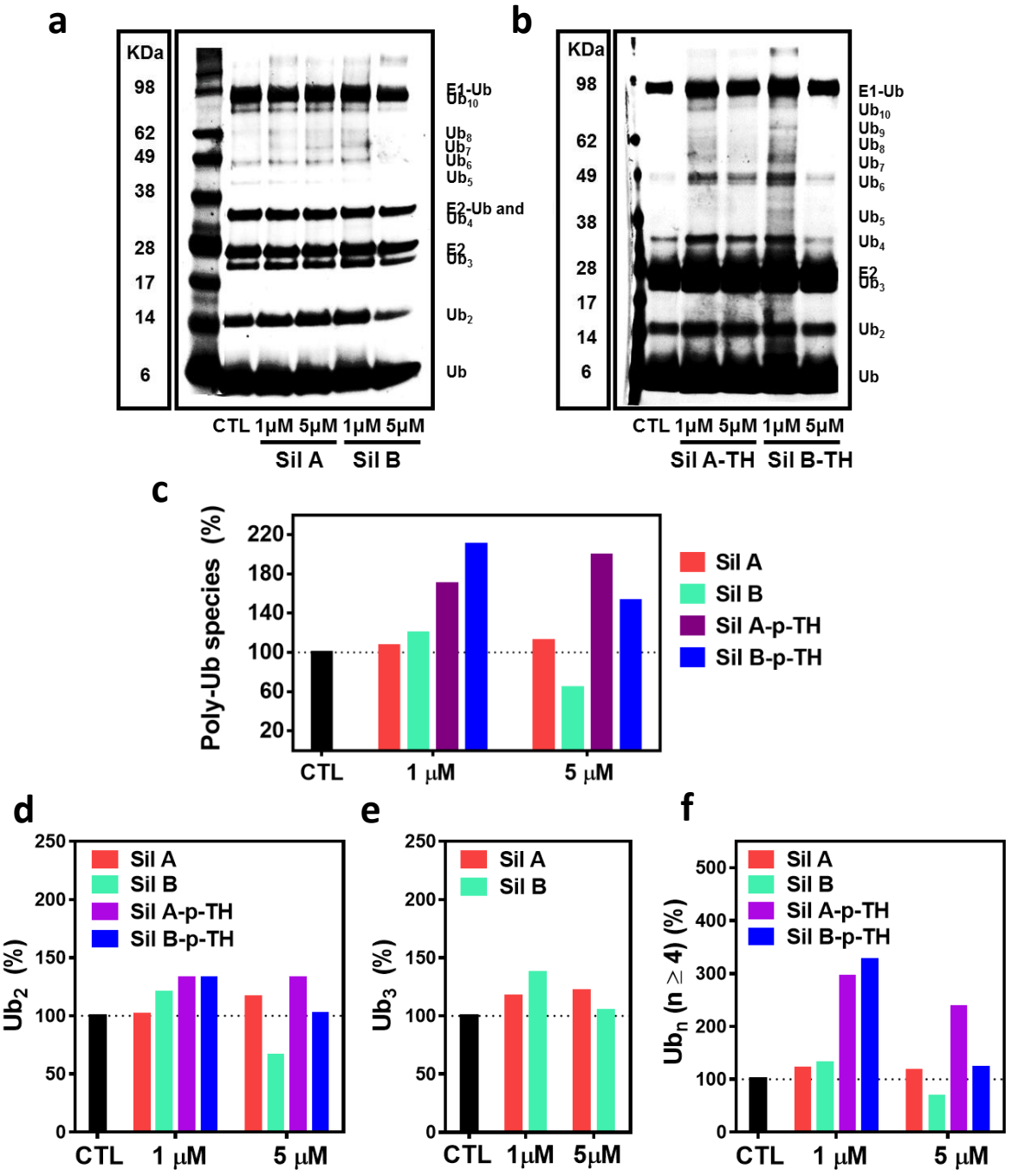

Figure 33 – Poly-ubiquitination pattern in the presence of Sil A, Sil B, Sil A-p-TH, and Sil B-p-TH. (a) WB analysis of K-48 linked ubiquitination reactions in the presence of the Sil A or Sil B, in ubiquitin/silybin ratios 20:1 and 4:1, revealed by Silver Staining. **(b)** As (a) except for Sil A-p-TH and Sil B-p-TH. **(c)** the total amount of polyubiquitinated species obtained by densitometry analysis of PAGE showed in (a) and (b). Results are reported as the normalized percentage of poly-ubiquitinated species with respect to the control. **(c)** Percentage of di-ubiquitinated species (Ub_2) obtained by densitometry analysis of the PAGE showed in (a) and (b). Results are reported as the normalized percentage of di-ubiquitinated species with respect to the control. **(d)** As (c) except for tri-ubiquitinated species (Ub_3). **(e)** As (c) except for tetra- or higher molecular weight ubiquitinated species (Ub_n with $n \geq 4$).

To shed light on the ubiquitin activation mechanism and to verify if silybins affect the Ub activation step by interfering with the interaction between ubiquitin and the E1 enzyme, the pyrophosphate (PPi or $P_2O_7^{2-}$) released in the first ATP-consuming step of the process was measured by using the molybdopyrophosphate assay. In this assay, the concentration of $P_2O_7^{2-}$ source anion produced in the enzymatic reaction mixture is determined spectrophotometrically by following the formation of blue molybdophosphate complex species. EDTA is added to the reaction mixture to preclude the Mg^{2+}-dependent enzymatic reaction. Then, the addition of $MoO4^{2-}$ to the ubiquitination reaction mixture which contains the $P_2O_7^{2-}$anion, in an acetonitrile-water acid reaction system, generates the formation of the yellow 18-molybdophosphate ($[(P_2O_7)Mo_{18}O_{54}]^{4-}$) anion according to:

$$P_2O_7^{4-} + 18\ MoO_4^{2-} + 36\ H^+ \longrightarrow [(P_2O_7)Mo_{18}O_{64}]^{4-} + 18\ H_2O$$

After adding ascorbic acid, the 18-molybdopyrophosphate anion is reduced and the concentration of pyrophosphate anion can be evaluated colorimetrically based on the formation of the blue molybdopyrophosphate complex species.[282]

Accordingly, cell-free Lys48-linked polyubiquitination reactions were carried out in the presence of increasing concentrations of Sil A, Sil B, Sil A-p-TH, Sil B-p-TH, and TH (see figure 34). The release of PPi during the polyubiquitination reaction in presence of 1 µM Sil A or Sil B was increased by about 13%. This value did not change by increasing Sil B concentration up to 5 µM but raised to about 20% in presence of 5 µM Sil A. These results suggest a silybin-mediated ATP-dependent Ub activation during the first step of the ubiquitination cascade. This dose-dependent activation was not observed with 5 µM Sil B likely due to ligand aggregation. Similar experiments carried out with trehalose-conjugates showed a slight increase in the amount of released PPi, yet smaller than what was observed for the parent molecules. This effect was dose-dependent for both Sil A-p-TH and Sil B-p-TH in the whole range of concentrations (from 1µM to 40µM). The release of PPi was also assayed, as a control, in the presence of TH, to establish if could contribute to the effect silybin derivatives, but we ascertain that it does not interfere in the ATP-dependent step of the polyubiquitination cascade.

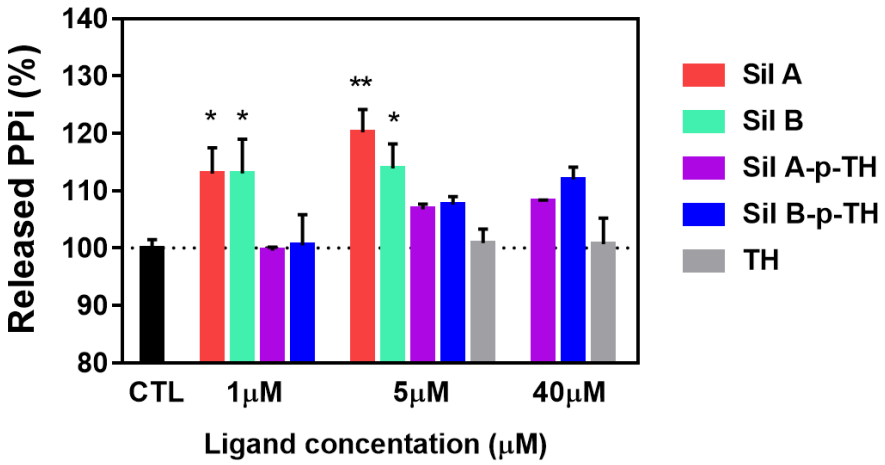

Figure 34. Released PPi during the Lys48-linked polyubiquitination reactions in the presence of different concentrations of Sil A (red bars) and Sil B (green bars), Sil A-p-TH (purple bars), Sil B-p-TH (blue bars), and TH (grey bars) quantified by the colorimetric molybdopyrophosphate assay**.** Results are reported as the normalized percentage of released PPi (± SEM) of at least 3 independent experiments; analysis of variance has been performed by One-way ANOVA followed by statistical Dunnett's test (*$p < 0.05$; **$p<0.01$).

3.2.2. Sil A and Sil B activate 20S proteasome activity

According to our previous experience,[283] the molecules order addition could be critical in the proteasome activity assay, especially when poorly soluble or aggregating molecules are used. This observation led us to carefully design and optimize the experimental conditions of the assay (see annexes and supplementary figure S1). Next, the ChT-L activity of y20S was assayed after the addition of increasing concentrations of both silybin diastereoisomers. The y20S proteasome was activated by about 20% by both Sil A and Sil B at 5µM (see figure 35). Proteasome activation showed a different dose-response profile for each silybin, suggesting a different molecular mechanism of interaction: the peptidase activity increased linearly with the concentration in the presence of Sil A, but raised abruptly at 0.5 µM when Sil B was used. It was not possible to determine the saturating concentration of proteasome activators (i.e. the concentration giving the maximum of activation), because of the poor solubility of the compounds.

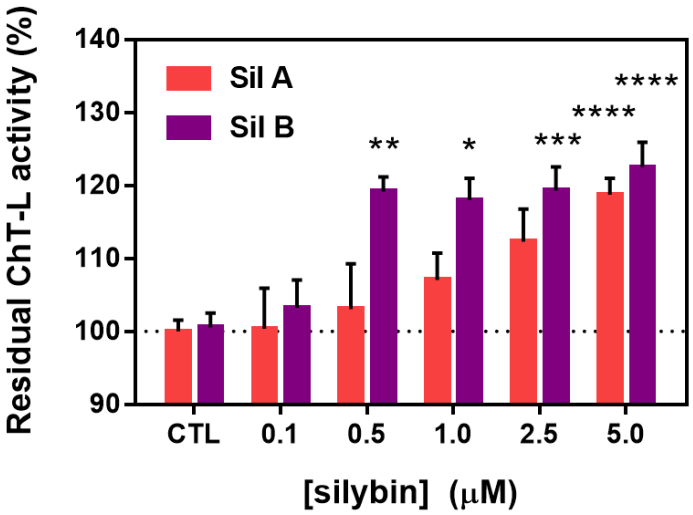

Figure 35. Residual ChT-L activity of yeast yCP measured at increasing concentrations of Sil A (red bars) and Sil B (purple bars). Assay buffer: 50 mM Tris buffer (pH 8), 37 °C. Results are reported as normalized percentage of residual activity (± SEM); analysis of variance has been performed by One-way ANOVA followed by statistical Tukey's test (*p < 0.05; **p < 0.01; ***p<0.001; ****p < 0.0001).

Next, we studied the effects of silybins on T-L and PGPH proteasome activities. Sil A and Sil B activated all the three ChT-L, T-L, and PGPH peptidase activities of y20S proteasome (see figure 36), albeit with slightly different dose-response effects. While Sil B already activated all the three activities at 1μM concentration, Sil A showed a barely detectable effect at this dose. However, at higher concentrations (2,5 - 5μM) the activation effects of Sil A on the ChT-L and PGPH-L activities became similar to those of Sil B, except for T-L activity which was higher for Sil B. Furthermore, PGPH activity was enhanced to a greater extent (around 65% for both Sil A and Sil B) than ChT-L (around 20% for both Sil A and Sil B) or the T-L activities (around 20% for Sil A and 35% for Sil B). The different behavior of both silybins could be ascribable to a different activation mechanism. We hypothesize that the different special disposition of both diastereoisomers could be responsible for different interactions with the proteasome trigging different activation profiles of some activities.

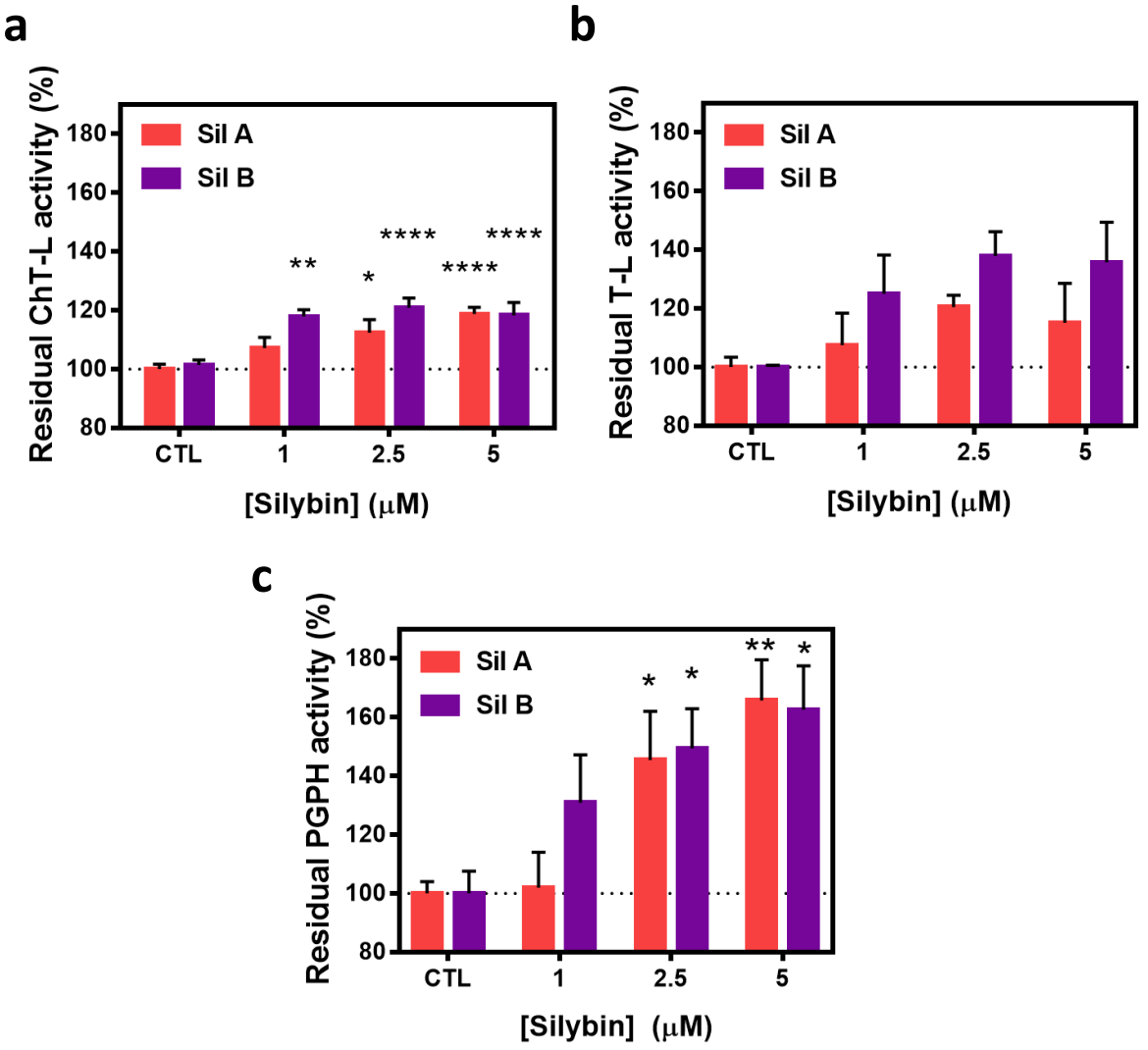

Figure 36. Residual ChT-L, T-L and, PGPH activities of yCP measured at increasing concentrations of Sil A (red bars) and Sil B (purple bars). Assay buffer: 50 mM Tris buffer (pH 8), 37°C. Results are reported as normalized percentage of residual activity (± SEM); analysis of variance has been performed by One-way ANOVA followed by statistical Dunnett's test (*$p < 0.05$; **$p < 0.01$; ****$p < 0.0001$).

The 20S proteasome may be activated according to two possible mechanisms: i) stabilization of the open-gate conformation of the alpha–ring that facilitates the entrance of substrate into the catalytic chamber; ii) allosteric regulation activating one or more of the peptidase activities of the proteasome. Small molecules which promote proteasome activity via these mechanisms are known as proteasome "gate-openers" and "stimulators", respectively.[184]

To gain insight into the silybin-mediated proteasome activation mechanism, the constitutively open-gate 20S α3ΔN yeast mutant was used; this proteasome mutant

presents the deletion of the α3-subunit tail responsible for the opening of the proteasome gate which permanently remains in a fully open conformation.[174] In contrast to the activation obtained in wild type y20S proteasome, silybins did not activate the α3ΔN mutant (see figure 37). Due to its mutation, the y20S α3ΔN can only be activated by stimulating allosterically its catalytic subunits because the activation via the gate opening is not possible. Thus, the absence of any activation effect of the α3ΔN mutant by silybins compared to their ability to activate the wild type y20S points to the role of silybins in stabilizing the open-gate conformation of y20S. Therefore, we postulate that silybins act on the alpha-ring of y20S, stabilizing its open conformation and mediating its activation; likely, allosteric movements may also come into play and differently influence the three catalytic sites obtaining different dose-response activation profiles.

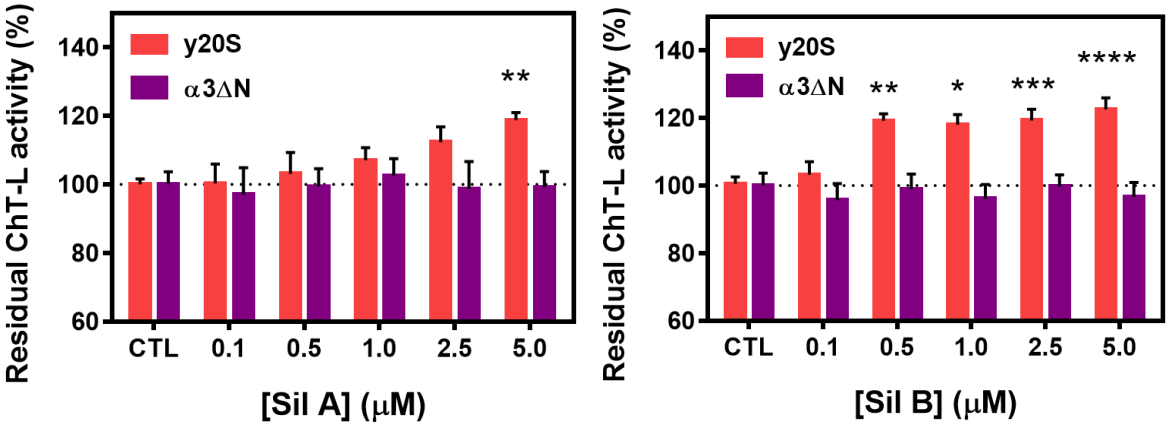

Figure 37. Residual ChT-L activity of wild type yeast CP (red bars) and the α3ΔN mutant (purple bars) measured at increasing concentrations of SilA or Sil B. Assay buffer: 50 mM Tris buffer (pH 8), 37°C. Results are reported as the normalized percentage of residual activity of the latent (yCP) and mutant (α3ΔN) proteasome, respectively (± SEM); analysis of variance has been performed by One-way ANOVA followed by statistical Tukey's test (*$p < 0.05$; **$p < 0.01$; ***$p < 0.001$; ****$p < 0.0001$).

Finally, human 20S activity (h20S) was also tested in the presence of both Sil A and Sil B. The ChT-L activity of h20S proteasome was activated around 40% by Sil A and 30% by Sil B. Interestingly, the different effects of the two silybins observed in ChT-L y20S activation were also confirmed when the h20S was used: a linear dose-dependent effect was observed for Sil A took place, while the activation profile increased abruptly at in the presence of 5 μM Sil B.

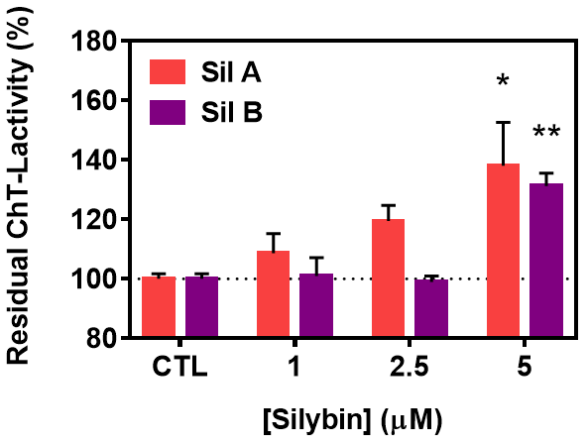

Figure 38. Residual ChT-L activity of hCP measured at increasing concentrations of Sil A (red bars) or Sil B (purple bars). Assay buffer: 50 mM Tris buffer (pH 8), 37 °C. Results are reported as the normalized percentage of residual activity of the hCP (± SEM); analysis of variance has been performed by One-way ANOVA followed by statistical Tukey's test (*p < 0.05; **p < 0.01).

3.2.3. Effect of Sil A-p-TH and Sil B-p-TH on the proteasome activity

Next, we evaluated the ability of Sil A-p-TH and Sil B-p-TH to activate the 20S proteasome. Similar to their parent molecules, both silybin derivatives were able to enhance dose-dependently the ChT-L activity of yeast 20S proteasome. In this case, the activation profile was similar for both glycoconjugates (see figure 39), differently than what was observed with the natural silybins (see figure 35). As mentioned above, the use of silybins is limited, due to their poor water solubility, to a range of concentrations not exceeding 5 µM. Despite the activity of both silybin trehalose-conjugates at 5 µM (activation of 12%) is slightly lower than natural compounds at the same concentration (activation of 20%), the conjugation with the sugar moiety allowed us to extend our investigations in a range of concentrations far beyond 5 µM. A dose-dependent enhancement of the y20S ChT-L activity was observed for both compounds, reaching an activation of 50% at a 50 µM ligand concentration (see figure 39).

Similar to what was observed in the presence of both silybins, the 20S α3ΔN mutant did not show changes in its activity in the presence of the silybin derivatives. Therefore, probably, silybin glycoconjugates are, as natural silybins, proteasome gate-openers. To exclude possible effects of the trehalose moiety of silybin derivatives on proteasome

activity, control experiments with TH were measured at two different concentrations (5 µM and 50 µM), showing no significant differences in the activity of y20S (see figure 40). Thus, the effects of the silybin conjugates on 20S proteasome can be ascribed to the silybin moiety. Moreover, despite glycoconjugation reduces the efficacy of proteasome activation, it allows the use of higher concentration achieving more significant effects on 20S proteasome.

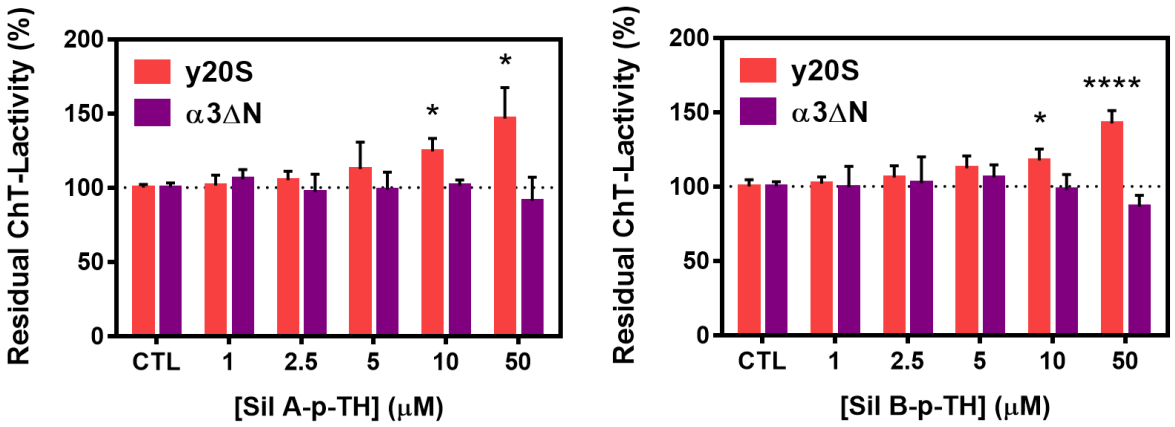

Figure 39. Residual ChT-L activity of wild type y20S (red bars) and the α3ΔN mutant (purple bars) measured at increasing concentrations of Sil A-p-TH or Sil B-p-TH. Assay buffer: 50 mM Tris buffer (pH 8), 37°C. Results are reported as the normalized percentage of residual activity of the latent (yCP) and mutant (α3ΔN) proteasome, respectively (± SEM); analysis of variance has been performed by One-way ANOVA followed by statistical Tukey's test (*p < 0.05; ****p < 0.0001).

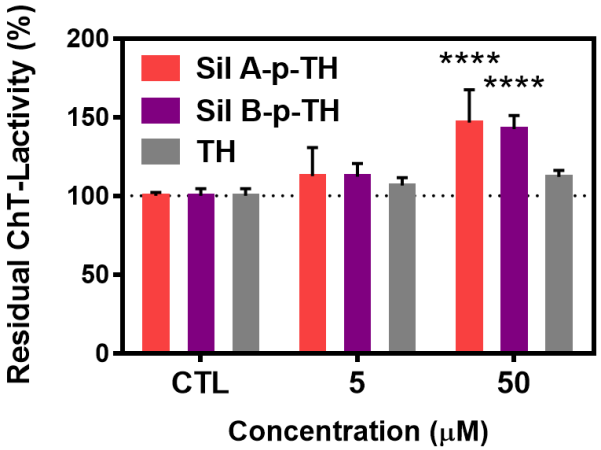

Figure 40. Normalized values of ChT-L residual activity of yeast 20S proteasome in presence of Sil A-p-TH (red bars), Sil B-p-TH (purple bars), or TH (grey bars) at different concentrations (5 µM and 50 µM). Assay buffer: 50 mM Tris buffer (pH 8), 37 °C. Results are reported as the normalized percentage of residual activity (± SEM); analysis of variance has been performed by One-way ANOVA followed by statistical Tukey's test (****p < 0.0001).

3.2.4. Molecular details on the silybin-mediated proteasome activation: dynamic docking studies

X-ray crystallography is one of the most widely used techniques in the compilation of structural information about the interaction of 20S proteasome with ligands.[284] However, the requirement of high ligand concentrations in soaking the protein crystal[175] restrains the use of this technique to gain insight into molecular details concerning the interaction between the CP proteasome and silybins, because of they tend to self-aggregate above 5 µM. Thus, computational studies become a suitable tool to reach our goal overcoming the practical limitations ascribable to the low water-solubility of the ligands.[283] Therefore, to obtain the molecular details of the mechanism of 20S proteasome activation by Sil A and Sil B, computational studies were carried out thanks to the collaboration with Prof. C. Fattorusso and Dr. M. Persico from the University of Naples "Federico II" (Italy).

Silybins structures were built in their anionic form, deprotonated in the hydroxyl group in position C(5), because of the prevalence of this protonation state at the pH adopted for proteasome activity assays (pH 8.0).[234] These structures were then subjected to a molecular mechanics (MM) energy minimization and each one of the obtained conformers was used as the starting structure for a subsequent conformational analysis by which several Sil A and Sil B conformations were randomly generated. Finally, after further MM energy minimization, the conformers generated were ranked by their potential energy values (i.e., ΔE from the energy global minimum (GM)), discarding conformers with differ in more than 5 kcal/mol from the GM.

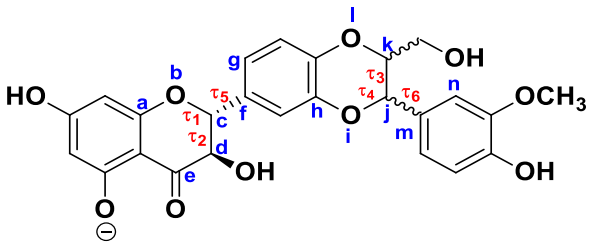

Figure 41. Torsional angles considered in the classification of both Sil A and Sil B conformers into families I-IV and subfamilies a or b. The torsional angles τ_1, τ_2, τ_3,τ_4, τ_5, and τ_6 are defined by the atoms indicated in the figure as abcd, bcde, ijkl, hijk, bcfg, and kjmn, respectively.

	Fam	ΔE_{GM}	% Fam	τ_1	τ_2	τ_3	τ_4	τ_5	τ_6
Sil A	**Ia**	0-1,17	8	53,84	-55,54	-60,26	44,77	114,67	-65,62
	Ib	0,03-1,07	2	53,64	-55,45	-60,25	44,83	-65,27	117,00
	IIb	1,67-3,81	15	53,71	-55,62	54,72	-38,06	-65,17	-51,17
	IIIb	2,00-4,71	15	-49,44	49,88	-60,28	44,79	-94,18	-65,12
	IIa	2,09-4,66	13	53,89	-55,56	55,36	-37,33	113,99	-53,34
	IIIa	2,46-4,10	8	-49,74	49,99	-60,31	44,49	82,36	-65,04
	IVa	3,32-4,57	19	-52,70	51,52	56,32	-39,54	69,90	-47,44
	IVb	4,13-4,98	20	-49,56	49,80	55,41	-36,64	-93,05	-52,56
Sil B	**Ib**	0-0,96	2	53,61	-55,45	60,01	-43,94	-65,22	65,92
	Ia	0,02-1,03	7	53,80	-55,53	60,26	-45,00	114,01	-117,05
	IIb	1,89-2,89	13	53,57	-55,57	-55,35	37,71	-65,42	53,25
	IIa	1,89-4,42	19	53,69	-55,48	-55,72	38,19	117,33	49,97
	IIIb	1,90-3,07	10	-49,52	49,88	60,16	-44,10	-94,11	64,40
	IIIa	2,43-3,50	7	-49,58	49,97	60,31	-44,71	82,42	65,21
	IVb	2,55-4,51	33	-54,19	50,54	-56,93	54,04	-99,74	-58,90
	IVa	4,47-4,82	9	-49,88	50,05	-55,26	36,61	82,06	54,21

Table 2. Classification of Sil A and Sil B conformers into sub-families according to the two conformations of the two bicyclic ring systems (determined by torsional angles τ_1-τ_4) and the torsional angle value between both bicyclic rings (determined by τ_5). The table indicates, from left to right, the silybin diastereoisomer, each one of the classified sub-families (Fam), the occurrence rates of each family (% Fam), the range of potential energy values from the energy global minimum (ΔE_{GM}) of each conformational sub-family and, finally, each one of the torsional angles which correspond with the selected energy minimum conformer for each group(τ_1-τ_6).

The selected conformers were classified into families (see table 2) according to the two possible conformations (pseudo-axial or pseudo-equatorial) of their two bicyclic ring systems, i.e. based on the torsional angles τ_1-τ_4 defined in figure 41. In particular, conformers were grouped in four families (families I-IV): family I includes those conformers with both bicyclic ring systems in pseudo-equatorial disposition; family II those where the first and the second bicyclic systems are in pseudo-equatorial and pseudo-axial disposition, respectively; conformers of family III correspond with just the opposite situation; and, finally, family IV comprises conformers with both bicyclic rings in pseudo-axial conformation. On one hand, for both silybins, the combination of a positive value of τ_1 and a negative value of τ_2 corresponds with a pseudo-equatorial disposition of the first bicycle, while the opposite combination (negative τ_1 and positive τ_2) indicates a pseudo-axial conformation of it. On the other hand, however, the different chirality of both diastereoisomers is responsible for an opposite conformation of the second bicyclic system

of Sil A and Sil B in conformers with the same combination of torsional τ_3/τ_4 values. Hence, the combination of positive/negative or negative/positive values of τ_3/τ_4 corresponds with a pseudo-axial or pseudo-equatorial disposition of the bicycle in Sil A, respectively. Conversely, these same combinations correspond with just the opposite conformational state for Sil B (pseudo-equatorial and pseudo-axial, respectively). Then, families were subgrouped into two subfamilies according to the torsional angle value between the two bicyclic rings: subfamily "a" comprises conformers with positive τ_5 values while subfamily "b" includes those with negative ones. Finally, the energy minimum conformers of each sub-family of Sil A and Sil B were selected for the definition of the putative starting complexes for the dynamic docking studies. Table 2 shows the occurrence rates and the range of ΔE_{GM} values of each conformational sub-family, as well as the torsional angles which correspond with the selected energy minimum conformer for each group.

As mentioned above (see chapter 1.2.5.2), the RPs trigger the proteasome gate opening by interacting with one or more α-grooves of the 20S proteasome. Furthermore, it has been reported that other peptides such as proline-rich (PR) peptides,[285] peptides Tat1 and Tat2 (fragments of the basic domain of HIV-1 Tat protein),[286] the Blm-10 analog Blm-pep,[185] as well as some small molecules as porphyrins[175,287] or pyrazolones[283] are able to modulate the CP activity by interacting with the α-surface, particularly with its α1-α2 and α5-α6 grooves. Besides, the effects of silybins resemble those shown by Blm10 and Blm-pep (triggering a higher activation of the PGPH activity than the other two ones), which interact with the 20S proteasome through the α5-α6 groove. Thus, the α5-α6 groove was selected as a starting point for CP/silybins docking studies. To this aim, a molecular model of h20S proteasome in the open conformation was built as reported in the experimental section; this model and a previously developed model of h20S in the closed conformation[287] (see figure 42) were used for dynamic docking studies with each one of the previously selected energy minimum silybins conformers, by using a docking methodology which considers all the systems flexible (i.e., ligand and protein) allowing the identification of the most probable binding modes. Therefore, the location of the C-terminal HbYX motif of the Rpt5 subunit (i.e., YYA) of 19S bound to the h20S proteasome in both open and closed conformation (PDB ID: 6MSB and 6MSK, respectively), was taken as a basis to place the selected silybin conformers. The interactions of the HbYX motif with the α5/α6-groove are

reported in figure 43. In particular, the centroid of the negatively charged group of silybins was superimposed on the centroid of the C-terminal carboxyl group of the Rpt5 and the centroid of the other two aromatic rings of silybins (i.e., the rings not presenting the negative charge) were superimposed on the centroids of the phenyl rings of the two tyrosine residues of the Rpt5 subunit. The conformations with the lowest potential energy that did not show significant steric overlap with the protein were selected as starting conformations for the docking calculations.

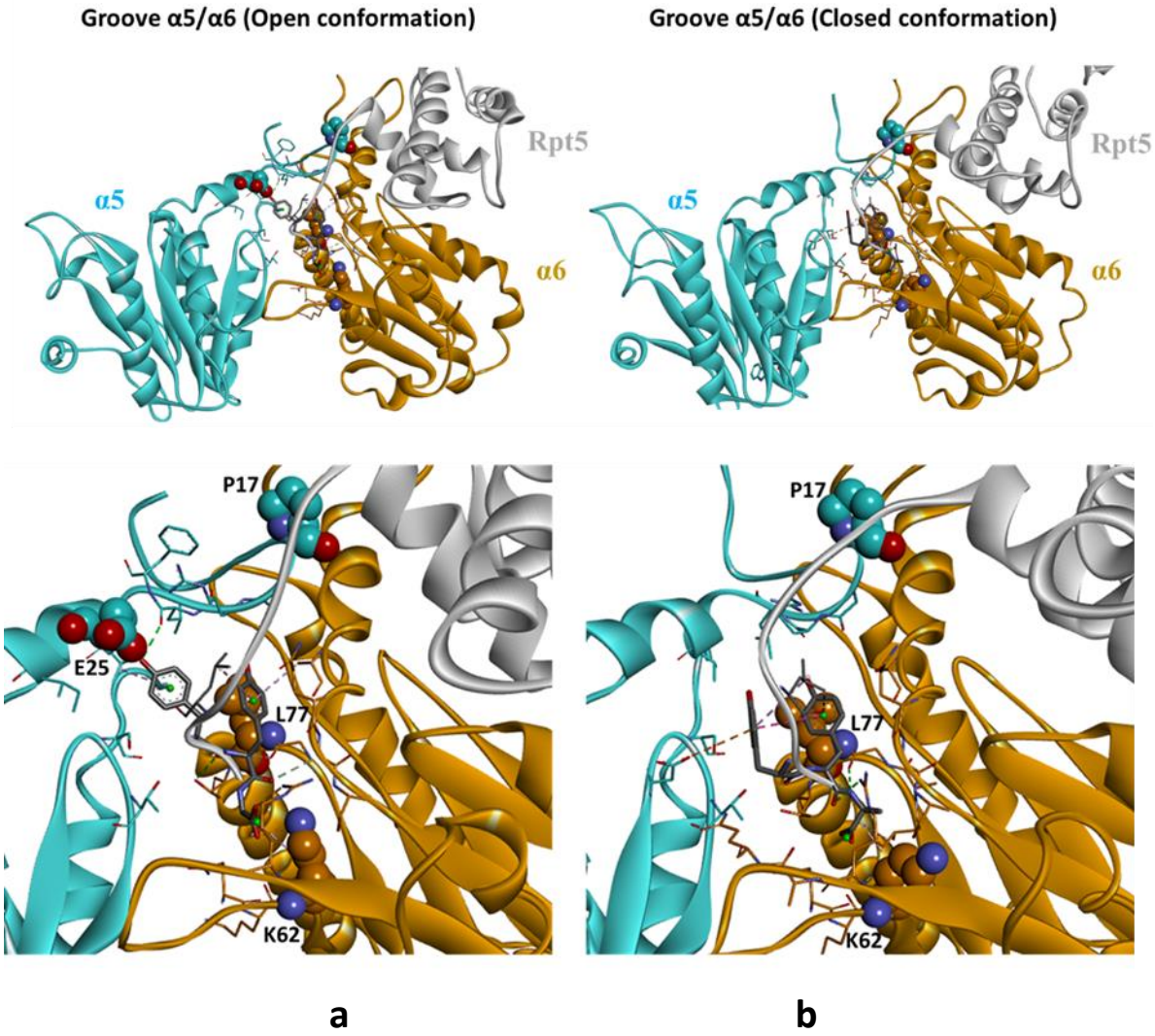

Figure 42. Groove α5/α6 in its open (a) and closed (b) conformational states of the h26S proteasome. α5 and α6 subunits of the CP are colored in blue and orange, respectively; the Rpt5 subunit of the 19S RP is colored in grey.

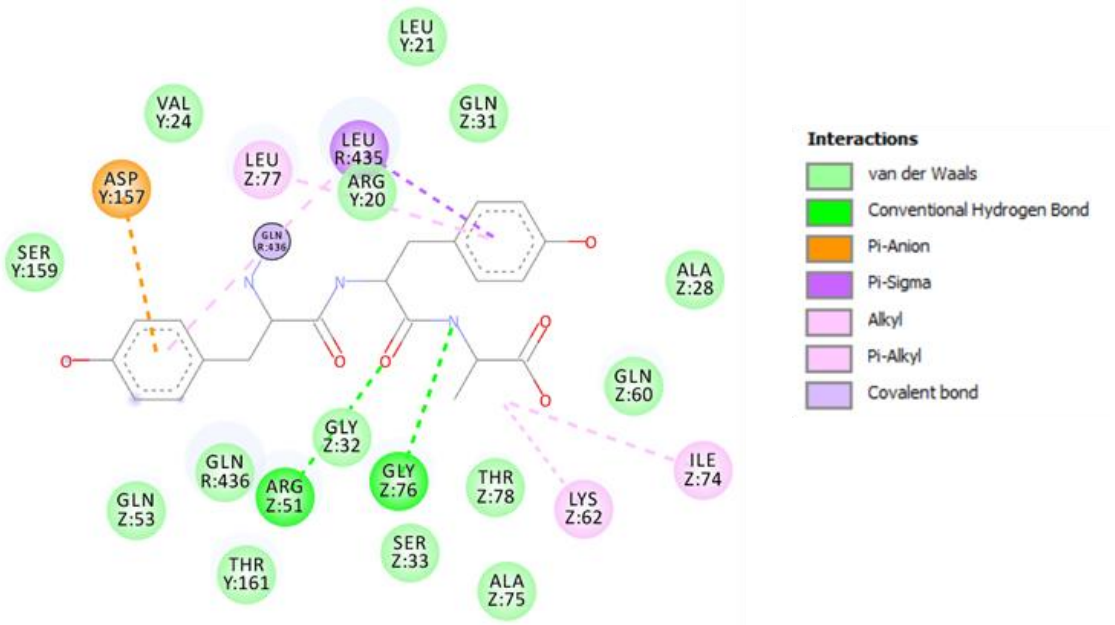

Figure 43. Interactions of the C-terminal HbYX motif (i.e., YYA) of the Rpt5 subunit with the α5/α6 in its closed conformation.

A stable interaction between both silybins and the α5/α6 groove was only obtained for docking simulations with the 20S proteasome in its open state. These results are indicative of the ability of both silybins to favor the h20S open-gate conformation and thus, are in accordance with our experimental data. In particular, based on the rank of non-bonded interaction energies obtained by Monte Carlo calculations, two complexes were selected for each ligand as the most probable binding modes. The most energetically favored complex (hereafter referred to complex SilA-1) involves Sil A as the ligand and is characterized by non-bonded interaction energy of -43.980 kcal/mol. The remaining three complexes, one for Sil A (complex SilA-2) and two for Sil B (complex Sil B-1 and complex Sil B-2), exhibit comparable non-bonded interaction energies (-37.398 kcal/mol, -38.559 kcal/mol, and -38.955 kcal/mol for complexes SilA-2, Sil B-1, and Sil B-2, respectively). Both complexes SilA-1 and SilB-1 resemble the RP tail location (see figures 44 and 45) much more than complexes SilA-2 and SilB-2. Furthermore, the binding mode of complex SilA-2, was totally different from the other complexes (up-side-down with regard to the other ones), with its negative charge toward the N-terminal region (see figure 44).

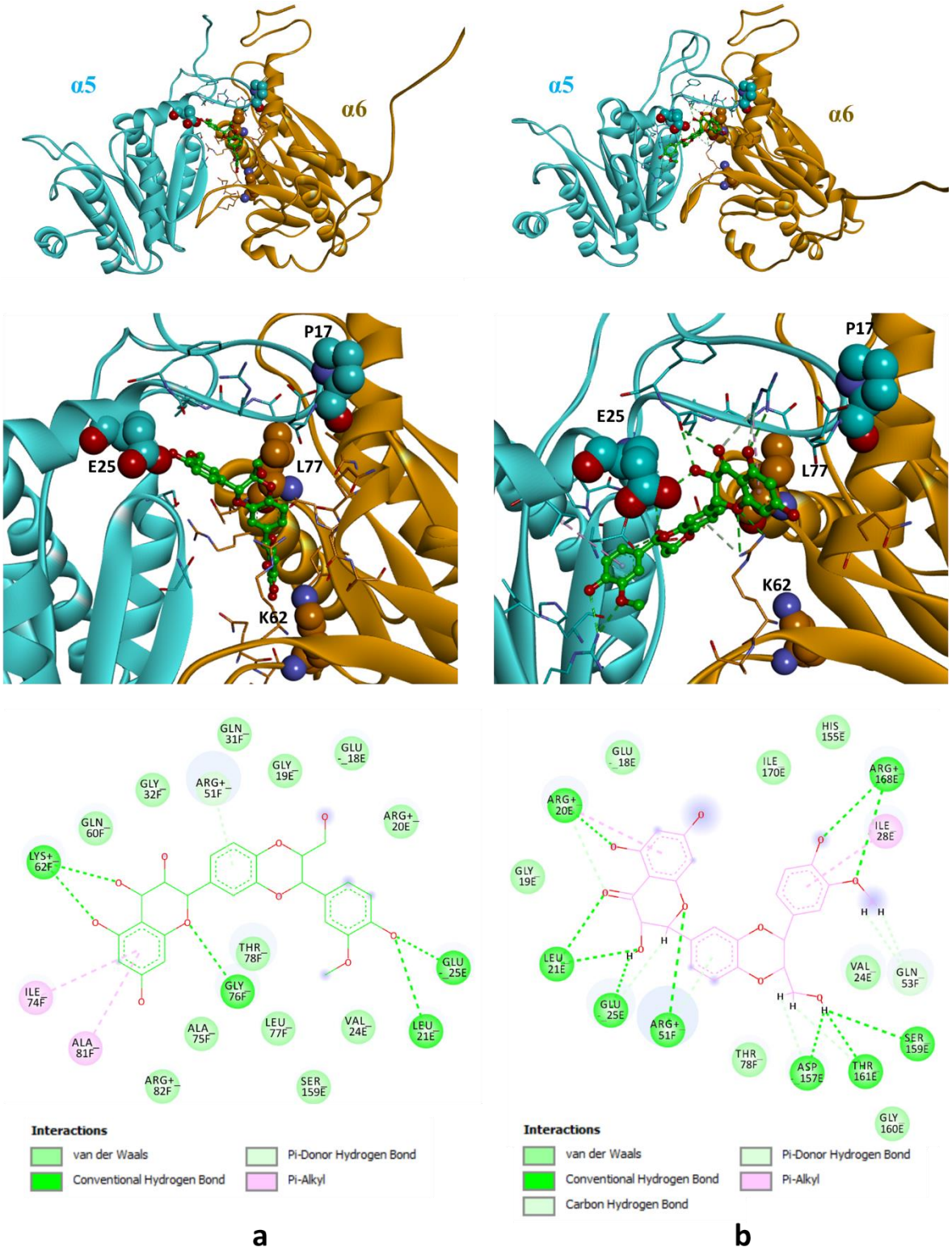

Figure 44 – Docking results of Sil A in the α5/α6 groove in the open conformation. (a) Complex Sil A-1 which corresponds with non-bonded interaction energy of -43.980 kcal/mol. **(b)** Complex Sil A-2 which corresponds with non-bonded interaction energy of -37.398 kcal/mol.

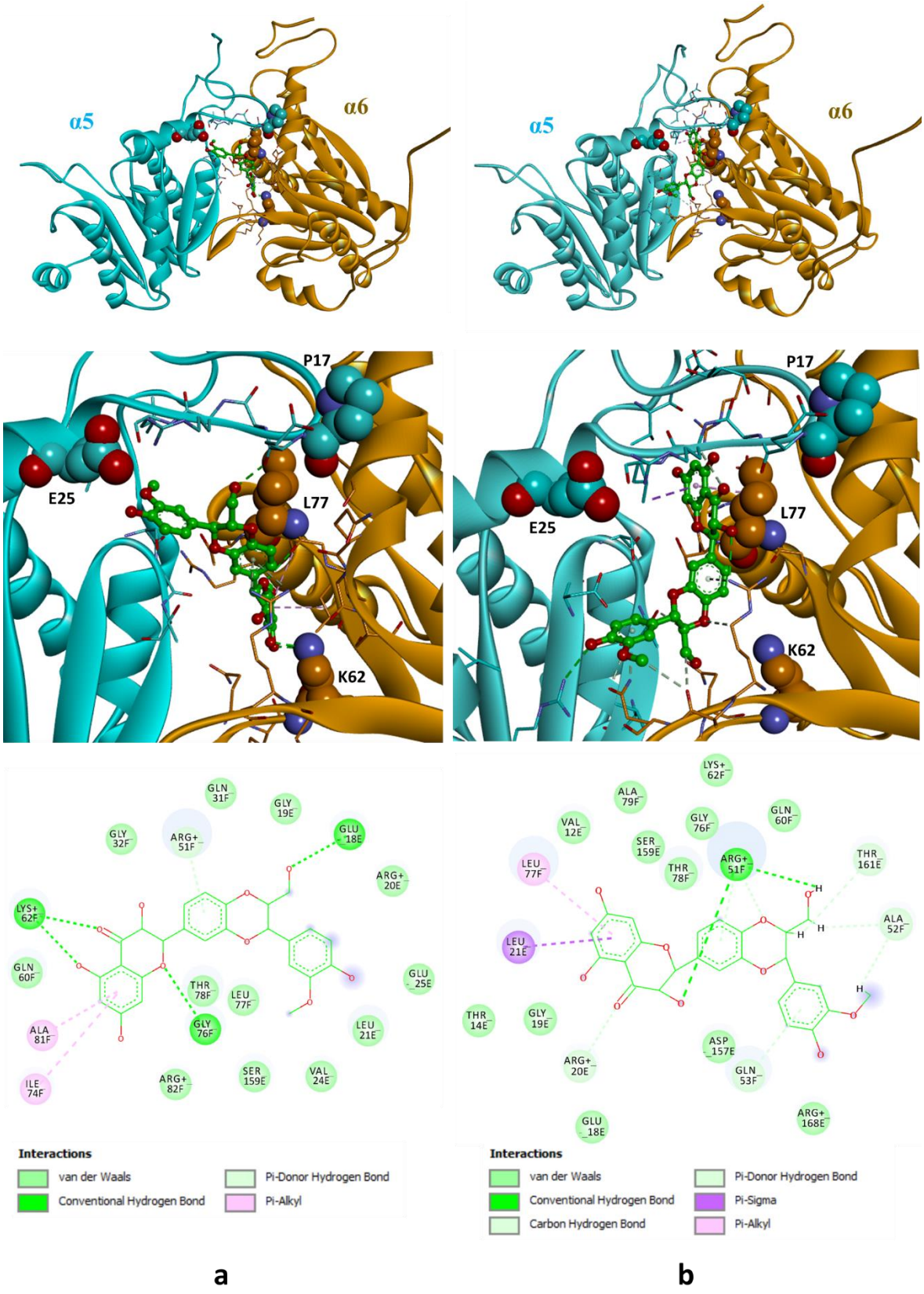

Figure 45 – Docking results of Sil B in the α5/α6 groove in the open conformation. (a) complex Sil B-1 which corresponds with non-bonded interaction energy of -38.559 kcal/mol. **(b)** complex Sil B-2 which corresponds with non-bonded interaction energy of -38.955 kcal/mol.

In complexes SilA-1 and SilB-1, both Sil A and Sil B share some binding modes with the α5/α6-groove. On one hand, both complexes show similar interactions between the ligand and the α6 subunit: the ring A of both ligands interacts through π-alkyl interactions with both I74 and A81 residues, the ring B form a π-donor hydrogen bond with R51, and the hydroxyl and carbonyl groups in positions C(5) and C(3), respectively, form hydrogen bonds with K62 and G76. Residues R51, K62, G76, and I74 are also involved in the binging of the terminal HbYX motif of Rpt5 with the α5/α6 groove (see figure 43), reinforcing the idea that silybins interact with the CP reproducing the location and some interactions of the RPs. On the other hand, in these complexes, the interactions of Sil A or Sil B with the α5 subunit were different because of the involvement of functional groups which are located in a different spatial disposition in both diastereoisomers due to the different configuration of its stereocenters. In particular, the 20-0H group of Sil A forms hydrogen bonds with L21 and E25 while Sil B forms a hydrogen bond with E18 through the 23-OH moiety.

Complexes SilA-2 and SilB-2 showed totally different interaction patterns. As reported in figure 44-b, in the complex Sil A-2, Sil A interacts with the α5 subunit through H-bonds with residues R20, L21, G25, T161, D157, S159, R168 (by means 5-OH/4-O, 3-OH/4-O, 3-OH/H-2, 23-OH/23-H, 23-OH/23-H, 23-OH and 20-OH/21-methoxy, respectively). Furthermore, R20 and I28 connect through π-alkyl interactions with the phenolic rings A and C, respectively. Finally, interactions with the α6 subunit take place thought a hydrogen bond between the 1-oxyl from the ligand and R51; additionally, this residue bonds with the B-phenolic ring of the ligand thought a π-donor hydrogen bond. Last, Q53 interacts with the methoxy group in position 19 through two carbon-hydrogen bonds. In the case of complex Sil B-2 (see figure 45-b), Sil B interacts with the α5 subunit through a π-sigma interaction between its phenolic ring A and L21 and forming carbon-hydrogen bonds between residues R20 and T161 with 4-O and 10-H, respectively. Interactions with the α6 subunit take place through hydrogen bonds between both 3-OH and 23-OH with the residue R51, which also forms a π-donor hydrogen bond with the phenolic ring B and a carbon-hydrogen bond with the oxo group in position 9. Furthermore, A52 interacts through carbon-hydrogen bonds with H-23 and the H from the methoxy group in position 19; ring A of Sil B bonds with L77 through a π-alkyl interaction between

L77, and a π-donor hydrogen bond between Q53 with the phenolic ring C is also present. The different binding modes observed between both Sil A and Sil B with the α5/α6 of the proteasome are in accordance with the experimental data.

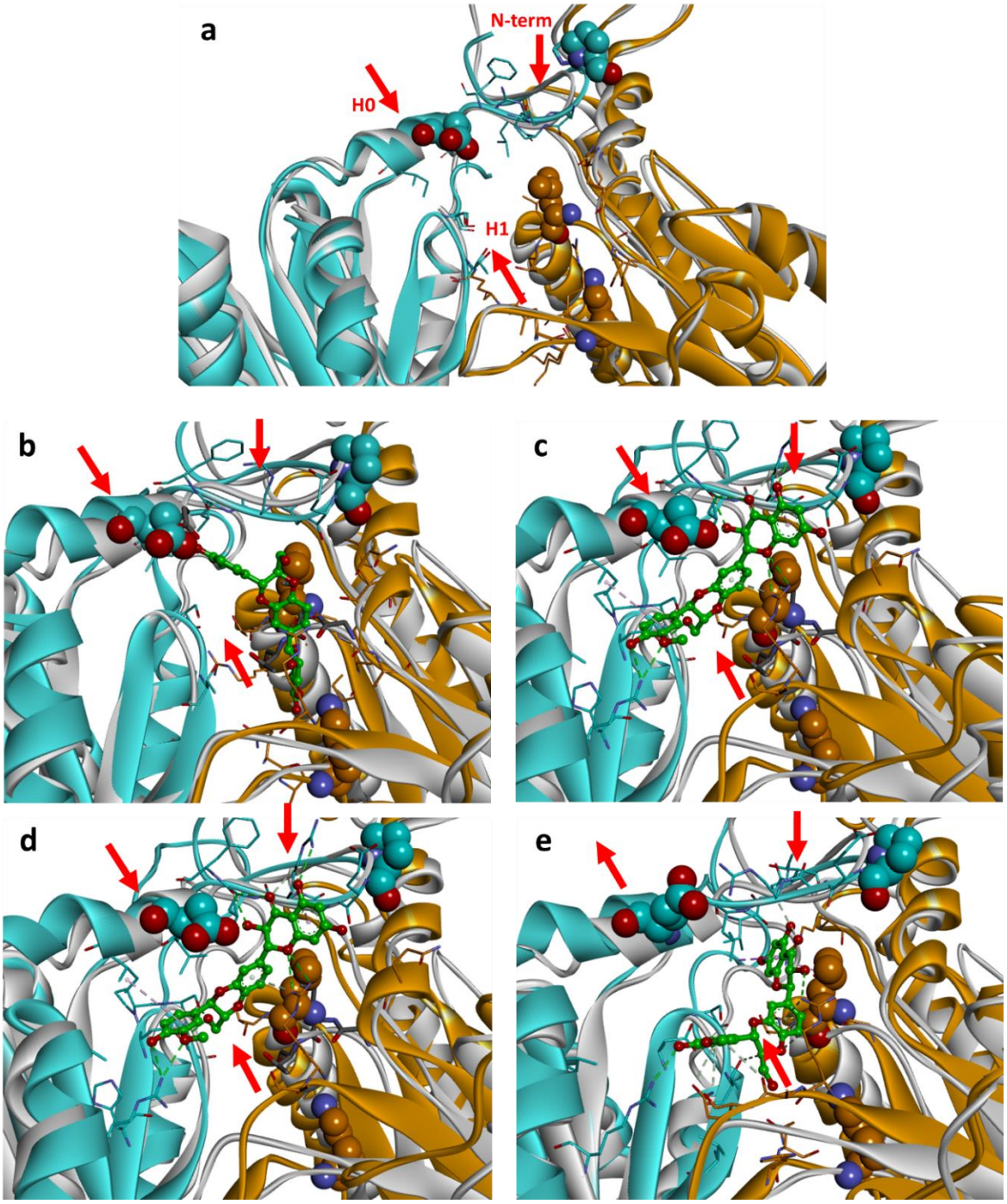

Figure 46. (a) Overlap of open (colored in white) and closed (α5 and α6 subunits colored in blue and orange, respectively) conformational states of the α5/α6 groove. The red arrows indicate the movement between both conformations; **(b)** and **(c)** as (a) except for the use of docking calculations in presence of Sil A in the open conformational state; complex 1 and 2, respectively; **(d)** and **(e)** as (b) and (c) except for Sil B.

The overlay of the h20S closed and open conformations allowed us to observe the more relevant conformational changes of the α5/α6 groove consequent to the CP gate opening. In particular, three conformational movements are related to the opening of the gate: the downward movements of the N-terminal region and the H0 helix (subunit α5) and the raising of the H1 helix (subunit α6). The analogy of these conformational changes with those observed in the presence of the ligands suggests that they are consistent with the dynamics of proteasome activation (see figure 46-a). Particularly, Sil A (in both complexes Sil A-1 and Sil A-2) and SilB (in complex Sil B-1) induced all the three movements related to the opening of the gate (see figure 46-b, -c, and -d). However, complex SilB-2 reproduced only the N-terminal region and the H1 helix (from subunit α5) movements, while induced an opposite movement of the H0 helix (from subunit α6) (see figure 46-e).

3.3. Profiling the anti-amyloidogenic potency of silybins: studies on Aβ and IAPP

On one hand, the activation of the UPS represents a desirable characteristic of a drug to restore proteostasis, promoting the hydrolysis of the misfolded amyloidogenic peptides. On the other hand, drugs with anti-amyloidogenic properties could halt the self-assemble of Aβ or hIAPP, contributing to mitigate the effect of these amyloids in the organism. Here, we profile the effect of Sil A, Sil B, and its trehalose-phospho-derivatives on Aβ and hIAPP amyloid growth in buffer solution as well as in the presence of membranes-mimicking systems. Furthermore, to evaluate the mechanisms by which silybins reduce the cytotoxicity of Aβ and hIAPP, we assess here how the ability of amyloid species to disrupt the cell membrane is modified in presence of these compounds.

3.3.1. Silybins catalyze Aβ growth in presence of neuronal model membranes but protect it from the amyloid-induced membrane damage

The inhibitory effect on $A\beta_{40}$ aggregation in aqueous solution of silybins, particularly Sil B, has been previously reported by our research group.[260] However, it is well known that amyloid peptides interact with lipidic membranes which, in turn, interfere with the amyloid aggregation pathway. Therefore, to assess the effect of Sil A and Sil B on Aβ aggregation in a milieu containing lipidic membranes, $A\beta_{40}$ (10μM) growth kinetics were monitored in the presence of neuronal model membranes and each one of the silybins, at increasing concentrations, by ThT assays. In parallel, dye leakage assays were also performed to study the protective effect of Sil A and Sil B versus amyloid-induced membrane disruption. Total Lipid Brain Extract (TLBE) was used in the preparation of lipid vesicles to mimic the lipid composition of neuronal cell membranes. The assayed peptide/ligand molar ratios were chosen based on the conditions of the previously reported experiments in aqueous solution, to make reliable comparisons between the effect of silybins in the absence and presence of the lipidic environment.

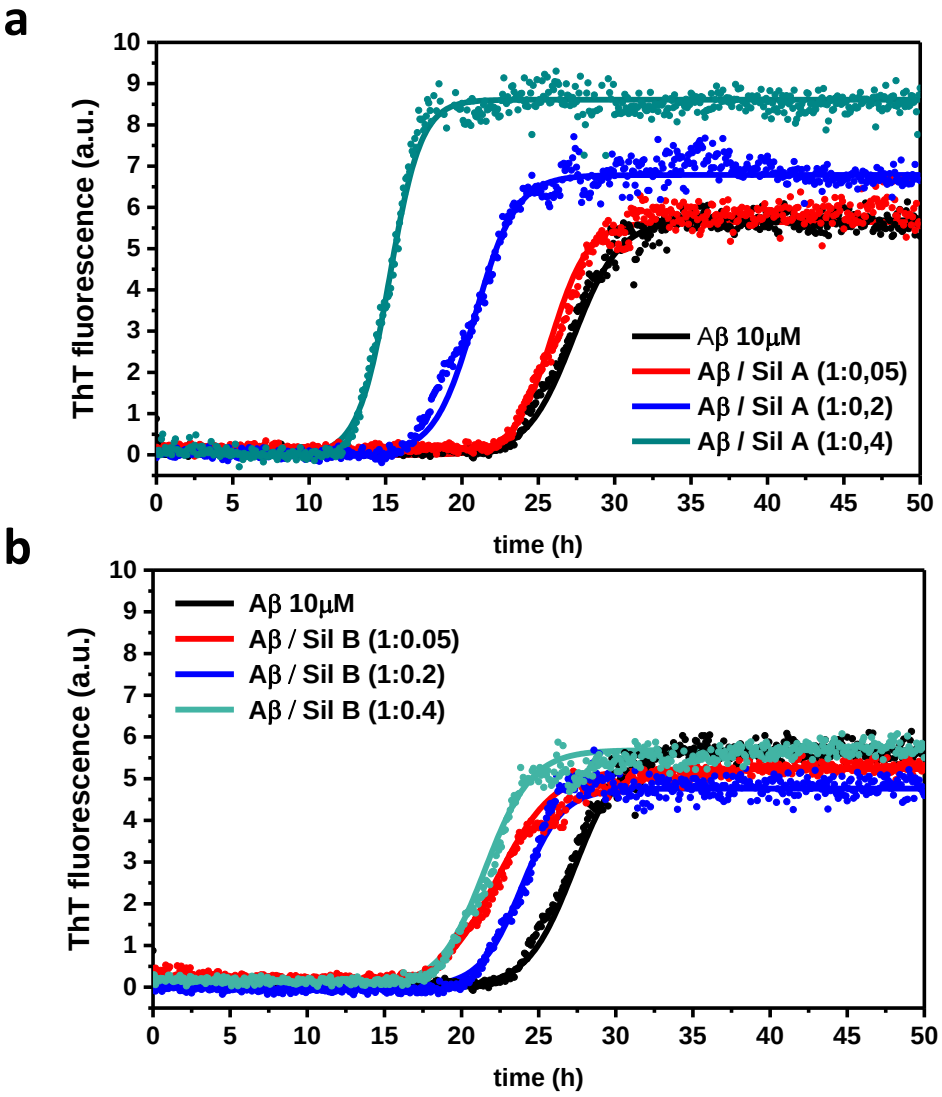

Figure 47 – Aβ aggregation kinetics in a milieu containing neuronal model membranes in the presence of different concentrations of Sil A or Sil B. (a) Amyloid fibrillation kinetics of $A\beta_{40}$ in the absence (black curve) and presence of Sil A in peptide/Sil A molar ratios 1:0.05 (red curve), 1:0.2 (blue curve), and 1:0.4 (turquoise curve). Dots represent experimental data; the continuous line is the fit of the kinetic obtained by averaging each one of the characteristic parameters of the kinetics of three different experiments. The characteristic kinetic parameters are reported in table 3. Experiments were carried out by using $A\beta_{40}$ 10 μM, TLBE LUVs 200 μg/ml, in phosphate buffer 10 mM NaCl 100 mM pH 7.4 at 37 °C. **(b)** As (a) except for Sil B.

Sil A catalyzed Aβ aggregation in presence of TLBE bilayers in a dose-dependent manner, increasing the amount of formed fibrils and reducing 12 h the $t_{1/2}$ at the higher tested concentration (peptide/ligand molar ratio 1:0.4) if compared to samples containing only Aβ. Differently, Sil B produced a much more moderate effect on Aβ aggregation kinetics (see figure 47-b and table 3). Surprisingly, despite silybins did not show anti-aggregating properties in presence of lipidic bilayers, Sil B protected membranes from the

damage induced by Aβ, reducing dye-leakage of neuronal model membranes. On the contrary, Sil A revealed a poor membrane-protective effect (see figure 48 and table 4). This behavior is likely due to the different effects of the two compounds in interfering with the mechanism of Aβ aggregation and is consistent with the higher cytoprotective effect of silybin B shown above (figure 24-a) in differentiated S5H5 neuroblastoma cells, as well as in vivo in studies in transgenic *C. elegans* strains expressing human Aβ, recently reported by our group.[260]

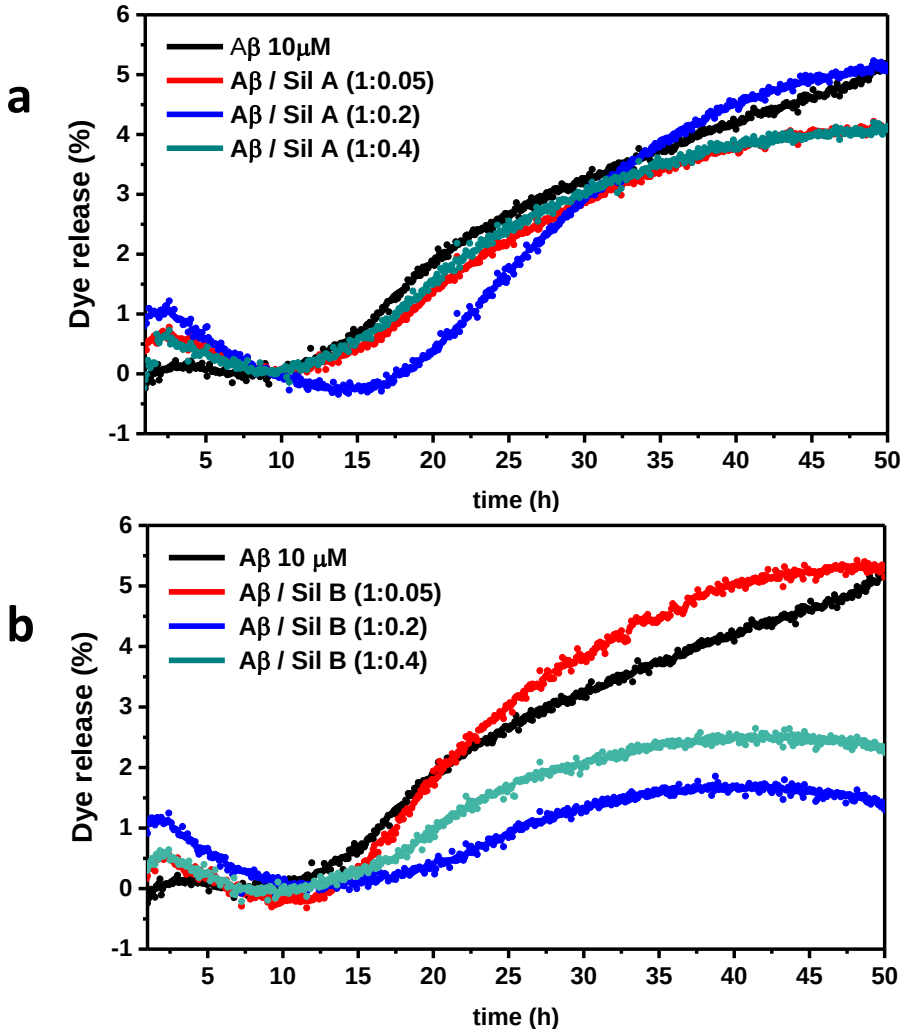

Figure 48 – Dye leakage assays of Aβ-mediated neuronal model membranes disruption in the presence of different concentrations of Sil A and Sil B. (a) Percentage of dye released from TLBE LUVs triggered by $A\beta_{40}$ in the absence (black curve) and presence of Sil A in peptide/Sil A molar ratios 1:0.1 (red curve), 1:0.4 (blue curve) and 1:0.8 (turquoise curve). Dots represent experimental data, being the average of three different experiments; the characteristic kinetic parameters are reported in table 4. Experiments were carried out by using $A\beta_{40}$ 10 μM, TLBE LUVs 200 μg/ml, in phosphate buffer 10 mM NaCl 100 mM pH 7.4 at 37 °C. **(b)** As (a) except for Sil B.

	$I_{max}(u.a.)$	$k\ (h^{-1})$	$t_{1/2}\ (h)$	$t_{lag}\ (h)$
$A\beta_{40}$ 10 µM	5.7 (0.9)	0.66 (0.02)	27.3 (0.5)	23.9 (0.4)
$A\beta_{40}$ /Sil A (1:0.05)	5.6 (0.6)	0.82 (0.09)	25.8 (6.5)	23.2 (6.3)
$A\beta_{40}$ /Sil A (1:0.2)	6.8 (1.4)	0.74 (0.44)	20.9 (11.5)	17.2 (11.4)
$A\beta_{40}$ /Sil A (1:0.4)	8.6 (2.4)	0.96 (0.16)	15.3 (1.5)	13.0 (1.8)
$A\beta_{40}$ /Sil B (1:0.05)	5.2 (1.2)	0.54 (0.09)	22.3 (2.9)	18.2 (2.2)
$A\beta_{40}$ /Sil B (1:0.2)	4.8 (1.9)	0.75 (0.05)	23.9 (7.6)	20.6 (8.1)
$A\beta_{40}$ /Sil B (1:0.4)	5.7 (0.1)	0.67 (0.25)	21.5 (8.6)	17.9 (7.3)

Table 3 – Characteristic parameters of Aβ aggregation kinetics in the presence of silybins in a neuronal membrane mimicking milieu. I_{max}, $t_{1/2}$, k, and t_{lag} kinetics parameters of $A\beta_{40}$ 10 µM fibrillation in a milieu containing TLBE LUVs in the presence and absence of Sil A or Sil B in peptide/ligand molar ratios 1:0.05, 1:0.2, and 1:0.4 plotted in figure 47. The kinetics has been fitted with the logarithmical equation $\boldsymbol{I = I_{max}/(1 + e^{-k(t-t_{1/2})})}$, where I_{max} represents the maximum intensity of fluorescence; k is the slope or rate of aggregation kinetics; lag phase (t_{lag}) and $t_{1/2}$ have been defined as the point in time where the signal reaches 10% and 50% of the amplitude of the transition, respectively. Results are reported as the mean of three experiments (± SD).

	$I_{max}(u.a.)$	$k\ (h^{-1})$	$t_{1/2}\ (h)$
$A\beta_{40}$ 10 µM	5.34 (0.13)	0.13 (0.01)	27.6 (1.7)
$A\beta_{40}$ /Sil A (1:0.05)	4.08 (0.19)	0.18 (0.01)	24.7 (0.4)
$A\beta_{40}$ /Sil A (1:0.2)	5.09 (0.77)	0.22 (0.02)	29.2 (0.8)
$A\beta_{40}$ /Sil A (1:0.4)	4.02 (0.81)	0.19(0.02)	23.3 (1.1)
$A\beta_{40}$ /Sil B (1:0.05)	5.20 (0.75)	0.22 (0.04)	24.1 (0.5)
$A\beta_{40}$ /Sil B (1:0.2)	1.26 (0.19)	0.45 (0.09)	24.9 (1.3)
$A\beta_{40}$ /Sil B (1:0.4)	2.38 (0.33)	0.28 (0.05)	21.8 (1.5)

Table 4 – Characteristic parameters of Aβ-mediated neuronal membranes disruption kinetics in the presence of silybins. I_0, I_{max}, $t_{1/2}$, and k kinetics parameters of the dye release from TLBE LUVs triggered by $A\beta_{40}$ 10 µM and in the absence or presence of Sil A or Sil B in peptide/ligand molar ratios 1:0.05, 1:0.2, and 1:0.4 plotted in figure 48. The kinetics have been fitted with the logarithmical equation $\boldsymbol{I = I_{max}/(1 + e^{-k\cdot(t-t_{1/2})})}$, where I_0 and I_{max} represent the initial and the maximum intensity of fluorescence; k is the slope or rate of aggregation kinetics; $t_{1/2}$ is the point in time where the signal reaches 50% of the amplitude of the transition. Results are reported as the mean of three experiments (± SD).

3.3.2. Silybin derivatives inhibit Aβ aggregation

Although silybins derivatives have been designed for their potential use as pro-drugs, it is important to evaluate whether they could actively interact with the studied targets. To this aim, ThT assays were first carried out to monitor $A\beta_{40}$ (20 µM) amyloid

growth in the presence of both silybin glycoconjugates. Both Sil A-p-TH and Sil B-p-TH showed a dose-dependent behavior in delaying aggregation kinetics: i.e. increasing lag phase and $t_{1/2}$ compared with samples containing only Aβ. Remarkably, some differences in the effects of both diastereoisomers in Aβ aggregation were observed: Sil A-p-TH was more effective than Sil B-p-TH when used in substoichiometric (peptide/ligand molar ratio 1:0.4) or stoichiometric concentrations; in particular, Sil A-p-TH led to a delay in $t_{1/2}$ of about 12 h and 16 h, in substoichiometric and stoichiometric conditions, respectively, (Sil B-p-TH delayed $t_{1/2}$ of about 3 h and 10 h in the same experimental conditions). However, in the presence of an excess of ligand (peptide/ligand molar ratio 1:5), the anti-aggregating effect of Sil B-p-TH was higher than Sil A-p-TH showing Aβ aggregation kinetics a $t_{1/2}$ of 44 h and 50 h in the presence of Sil A-p-TH and Sil B-p-TH, respectively, i.e. a delay of 18 h and 24 h with respect the amyloid aggregation in absence of the ligands (see figure 49 and table 5).

The effect of TH was also studied as control but, in this case, differences in the aggregation kinetics were not observed; henceforth, we could infer that the antiaggregant effect of glycoconjugates was due to the silybin structure and not to the TH moiety, which merely increased the solubility of the drug. These results, which underline the higher antiaggregant activity of Sil B-p-TH between both diastereoisomers, are in accordance with the already reported higher antiaggregant activity of its parental compound Sil B with respect to Sil A.[260] Therefore, we can conclude that conjugation of both Sil A and Sil B maintains the ability of the compound to interact with Aβ and to interfere with its aggregation pathway, delaying the formation of ThT-positive fibrils.

	$I_{max}(u.a.)$	$k(h^{-1})$	$t_{1/2}\ (h)$	$t_{lag}(h)$
$A\beta_{40}$ 20 µM	49 (9)	0.4 (0.2)	26 (10)	20 (8)
$A\beta_{40}$ / Sil A-p-TH (1:0.4)	47 (9)	0.5(0.3)	38 (6)	32 (9)
$A\beta_{40}$ / Sil A-p-TH (1:1)	40 (3)	0.4 (0.1)	42 (8)	36 (8)
$A\beta_{40}$ / Sil A-p-TH (1:5)	44 (2)	0.6 (0.2)	44 (11)	40 (10)
$A\beta_{40}$ / Sil B-p-TH (1:0.4)	40 (2)	0.5 (0.1)	29 (8)	24 (9)
$A\beta_{40}$ / Sil B-p-TH (1:1)	45 (3)	0.7 (0.3)	36 (9)	33 (8)
$A\beta_{40}$ / Sil B-p-TH (1:5)	44 (7)	0.5 (0.2)	50 (12)	38 (12)
$A\beta_{40}$ / TH (1:5)	48 (1)	0.5 (0.2)	27 (11)	23 (9)

Table 5 – Characteristic parameters of Aβ aggregation kinetics in the presence of silybin derivatives. I_{max}, $t_{1/2}$, k, and t_{lag} of $A\beta_{40}$ fibrillation kinetics in the presence and absence of Sil A-p-TH or Sil B-p-TH in peptide/ligand molar ratios 1:0.4, 1:1, and 1:5 and in the presence

of trehalose (TH) in a peptide/ligand molar ratio 1:5, plotted in figure 49**.** The kinetics have been fitted with the logarithmical equation $I = I_{max}/(1 + e^{-k(t-t_{1/2})})$, where I_{max} represents the maximum intensity of fluorescence; *k* is the slope or rate of aggregation kinetics; lag phase (t_{lag}) and $t_{1/2}$ have been defined as the point in time where the signal reaches 10% and 50% of the amplitude of the transition, respectively.

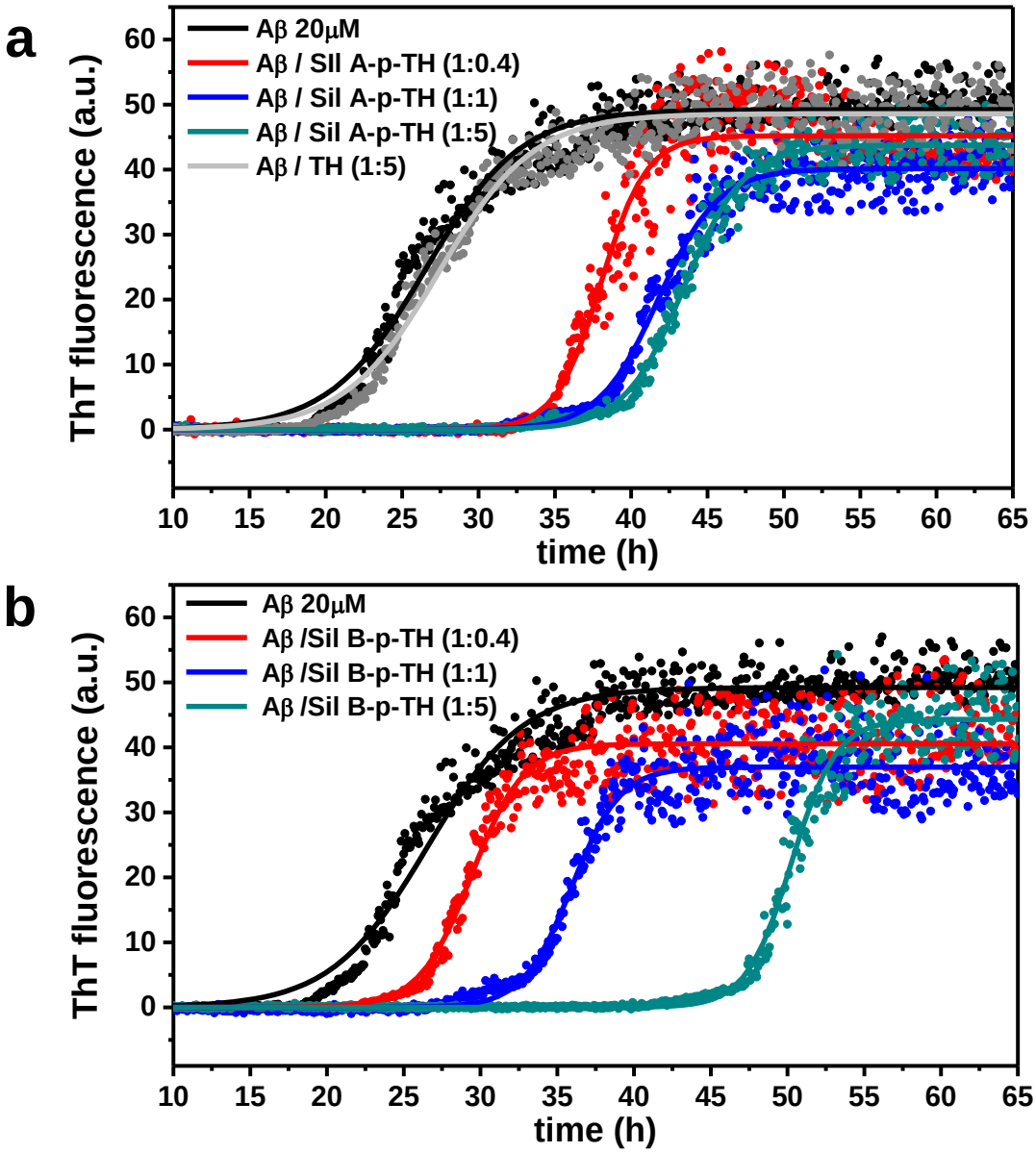

Figure 49 – Aβ fibrillation kinetics in the presence of different concentrations of Sil A-p-TH and Sil B-p-TH. (a) $A\beta_{40}$ growth kinetics in the absence and presence of Sil A-p-TH in peptide/Sil A-p-TH molar ratios 1:0.4 (red curve), 1:1 (blue curve), and 1:5 (turquoise curve) and TH in peptide/ligand molar ratio 1:5 (grey curve). Dots represent experimental data; the continuous line is the fit of the kinetic obtained by averaging each one of the characteristic parameters of the kinetics of three different experiments (reported in table 5). Experiments were carried out using $A\beta_{40}$ 20 μM at 37 °C in phosphate buffer 10 mM NaCl 100 mM pH 7.4. **(b)** As (a) except for Sil B-p-TH.

3.3.2.1. $A\beta_{40}$ fibrils morphology in the presence of Sil A/B-p-TH

To prove the presence of amyloid fibrils and study their morphology, different techniques which include transmission electron microscopy (TEM), scanning electron microscopy (SEM), and atomic force microscopy (AFM) are widely used in parallel to ThT studies.

Sample staining increases the contrast of TEM images and negative staining with aqueous uranyl acetate is the most common procedure used with this type of preparation, allowing better observation of the fibrils; in our case, TAAB EM Stain 336, an uranyl acetate alternative which instead contains a mixture of lanthanum, samarium and gadolinium salts has been used to avoid the use of radioactive substances in our procedure.[288]

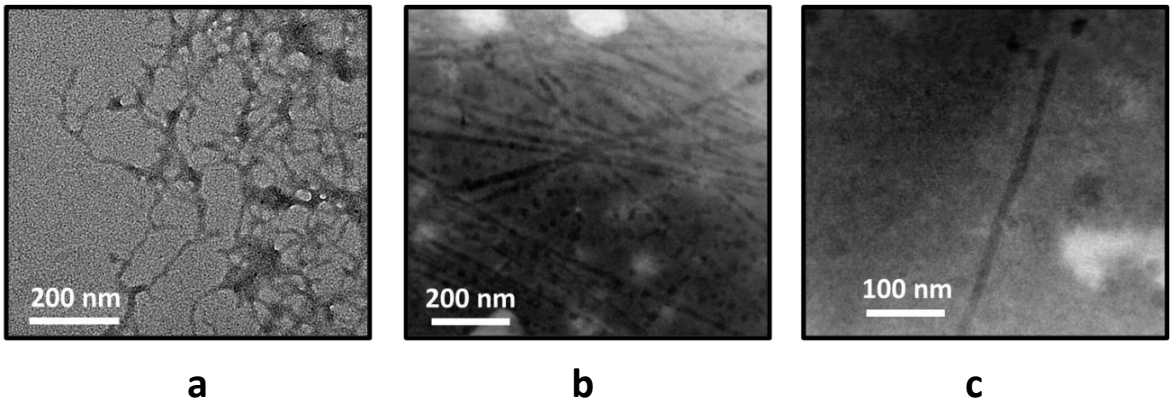

Figure 50. TEM images of different preparations of $A\beta_{40}$ fibrils.

In figure 50, various $A\beta_{40}$ fibrils samples observed by using different staining procedures are reported. We used Electron Energy Loss Spectroscopy (EELS) elemental analysis to assign Aβ fibrils correctly, discarding artifacts structures of non-proteinaceous nature (see figure 51). In particular, the presence of nitrogen has been used to monitor the presence of amyloid because of the lack of this element in the studied silybin-phospho-trehalose conjugates. As shown in figure 51-b, the nitrogen profile permits to measure the width of fibrils.

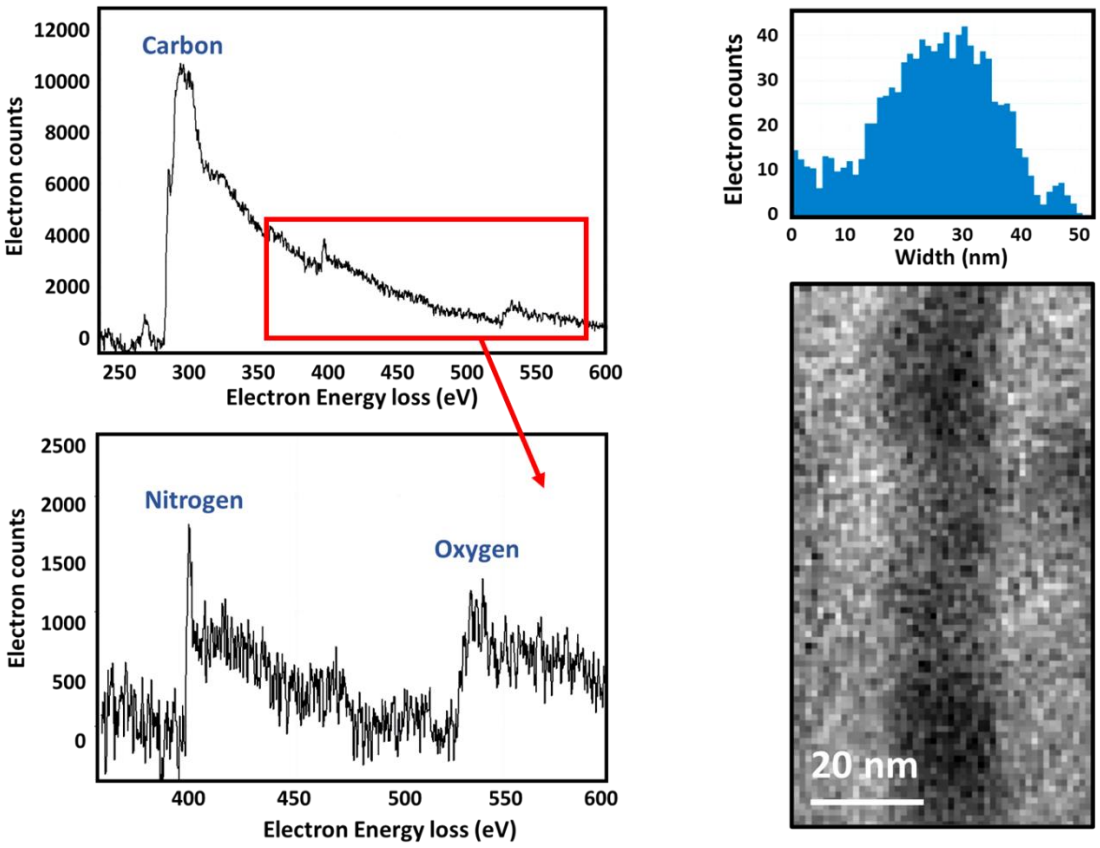

Figure 51. (a) EELS spectrum of the fibril showed in figure 50-c. **(b)** The upper plot represents the nitrogen profile of the fibril shown just below, which correspond to a zoomed picture of the fibril showed in figure 50-c.

To study the morphology of $A\beta_{40}$ fibrils formed in the presence of silybin glycoconjugates, $A\beta_{40}$ monomer was incubated for 3 days at 37 ºC in the presence or absence of Sil A-p-TH or Sil B-p-TH (peptide/ligand molar ratio 1:2.5) and observed by TEM. In the control sample, a high number of amyloid fibrils were observed with a diameter of about 7 nm and, in less proportion, fibrils with 14 nm of diameter (see figure 52-a). However, surprisingly, evident fibrils were not identified in samples that contain the ligand Sil A-p-TH or Sil B-p-TH (see figures 52-b and 52-c, respectively), despite their formation was confirmed previously by ThT assays; therefore, we concluded that ThT-positive fibrils formed in presence of silybin derivatives are smaller in size than those formed in absence of ligand, probably protofibrils, that are not discernible due to the resolution limits of this technique. Furthermore, for the same reason, it was not possible to quantitatively assign

differences in the anti-aggregatory efficiency of both diastereoisomers by using TEM alone. However, despite the challenges in the characterization of amyloid fibrils formed in the presence of silybin glycoconjugates, this finding further supports the ability of silybin glycoconjugates to interfere with the on-pathway amyloid aggregation previously described by ThT assays.

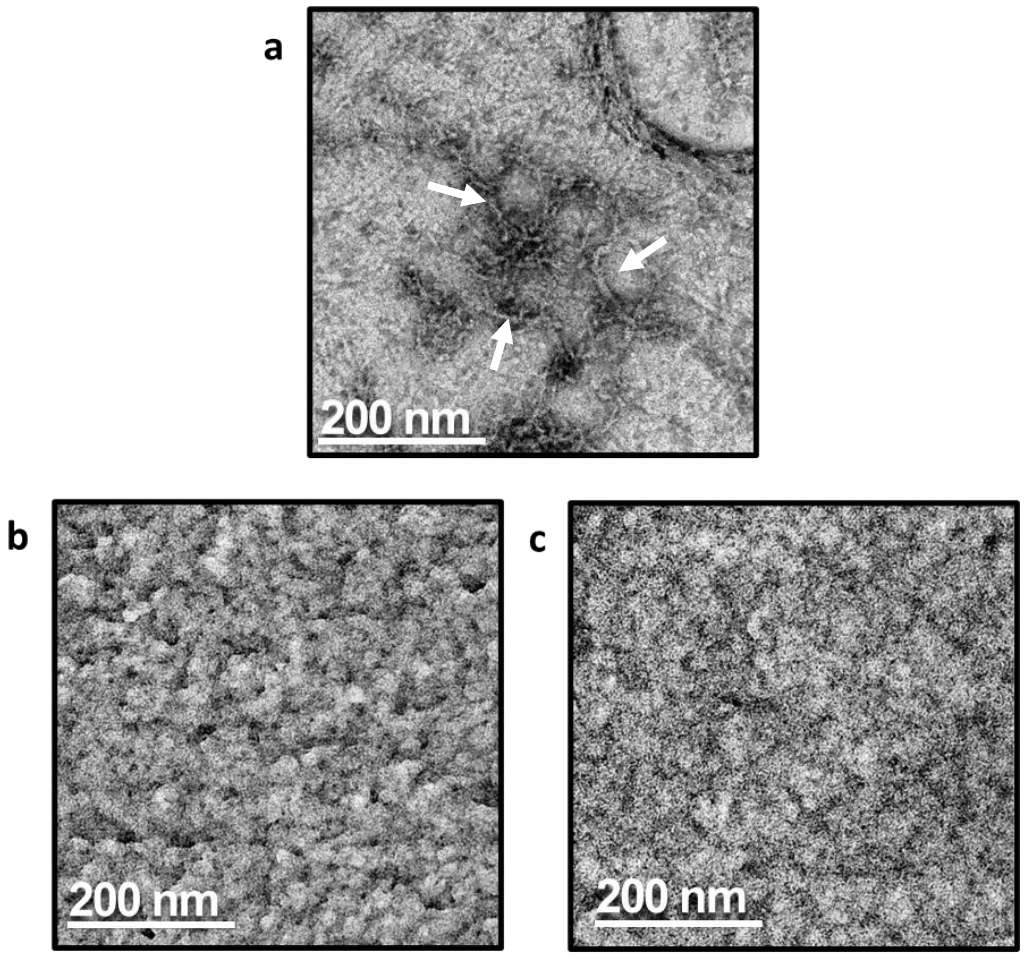

Figure 52– TEM images. (a) $A\beta_{40}$ amyloid fibrils (100 µM); **(b)** $A\beta_{40}$ (100 µM) incubated in presence of Sil A-p-TH; peptide/ligand molar ratio 1:2.5; **(c)** as (b) except for Sil B-p-TH.

3.3.2.2. Conformational analysis of Aβ in presence of SilA/B-p-TH by Circular Dichroism

Circular dichroism is largely adopted to study the conformation of peptides and proteins in aqueous solution. Amide groups of peptide backbone are chromophores in the far-UV region (between 180 nm and 260 nm) which are aligned in different patterns depending on the secondary structure; each structure has a characteristic circular

dichroism spectrum due to a different absorbance of the right-handed and left-handed circular polarized light.[289]

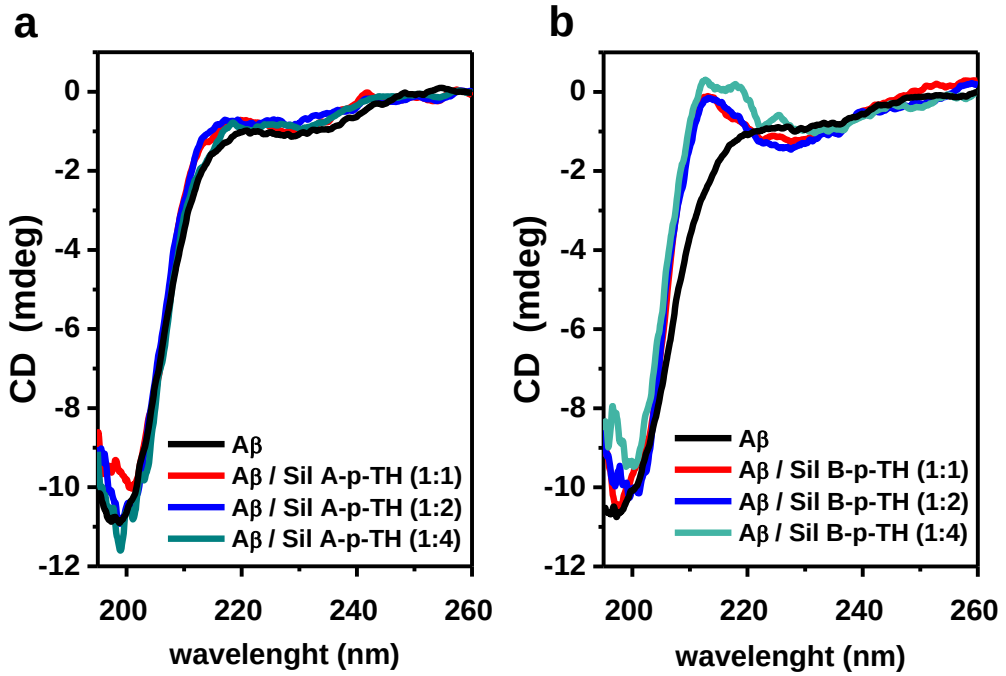

Figure 53. (a) CD spectra of $A\beta_{40}$ (2 µM) in the presence of Sil A-p-TH at peptide/ligand molar ratios 1:1 (red), 1:2 (blue) and 1:4 (turquoise). Data have been registered at 4 °C in 10 mM phosphate buffer pH 7.4. **(b)** as (a) except for Sil B-p-TH.

Based on ThT assays, we expect that the two silybin derivatives could interact with the amyloid peptide *via* different binding modes. To single out the ligand-induced $A\beta_{40}$ conformational changes for the two derivatives, we recorded circular dichroism (CD) spectra of the peptide in the presence and absence of different concentrations of Sil A-p-TH and Sil B-p-TH. CD spectra of both ligands were recorded in the same experimental conditions and subtracted from the curves related to the ligand/peptide mixtures. Differently from Sil A-p-TH, which was almost inactive, the difference spectra of $A\beta_{40}$ containing increasing amounts of Sil B-p-TH show a negative band at 197 nm and a weak positive one at 214 nm (see figure 53). Although it may be difficult to deconvolute these CD spectra which likely reflects a complex mixture of slightly different conformations, this spectral signature is typical of a poly-L-proline II (PPII) helix structure.[290] PPII structure has been reported as indicative of the physiological/functional state of amyloidogenic proteins, since as it reduces the aggregation propensity of amyloidogenic peptides.[291] CD analysis reconciles with ThT experiments and suggests that the major anti-aggregating effect of Sil B-p-TH is related to its effect on the conformational preferences of $A\beta_{40}$.

3.3.3. Silybins inhibit hIAPP amyloid growth

To investigate the ability of Sil A and Sil B to inhibit hIAPP aggregation, ThT assays were performed in the presence of increasing concentrations of each compound at peptide/ligand molar ratios 1:0.1, 1:0.4, and 1:0.8. Sample concentrations were optimized to allow a detectable amyloid growth and prevent ligand precipitation. Both compounds reduced the maximum ThT intensity compared to control in a dose-dependent manner and thus decreased the amount of the formed fibrils. Furthermore, both Sil A and Sil B dose-dependently slowed down the aggregation kinetics presenting higher values of $t_{1/2}$ than the control.

At a peptide/ligand molar ratio 1:0.1, Sil A showed an inhibitory action on hIAPP aggregation while Sil B did not show any effect. However, by increasing the dose, the inhibitory effects on hIAPP aggregation of Sil B became more evident. In fact, Sil A reduced the amount of fibrils formed around 49% when it was added in a peptide/ligand molar ratio 1:0.8, while the reduction in the presence of Sil B in the same conditions was around 57% (see figure 54). These results reconcile with the previously reported effects of the two compounds in inhibiting Aβ aggregation.[260]

	$I_{max}(u.a.)$	$k\ (min^{-1})$	$t_{1/2}\ (min)$
hIAPP 5 µM	1.48 (0.01)	$7.4{\cdot}10^{-3}(0.5{\cdot}10^{-3})$	364 (37)
hIAPP/Sil A (1:0.1)	1.14 (0.09)	$5.8{\cdot}10^{-3}\,(1.2{\cdot}10^{-3})$	400 (166)
hIAPP/Sil A (1:0.4)	0.80 (0.19)	$5.1{\cdot}10^{-3}\,(2.9{\cdot}10^{-3})$	467 (130)
hIAPP/Sil A (1:0.8)	0.76 (0.14)	$4.9{\cdot}10^{-3}\,(3.2{\cdot}10^{-3})$	540 (242)
hIAPP/Sil B (1:0.1)	1.51 (0.49)	$6.6{\cdot}10^{-3}\,(2.5{\cdot}10^{-3})$	367 (154)
hIAPP/Sil B (1:0.4)	1.14 (0.19)	$4.3{\cdot}10^{-3}\,(1.5{\cdot}10^{-3})$	432 (166)
hIAPP/Sil B (1:0.8)	0.64 (0.08)	$3.4{\cdot}10^{-3}\,(0.5{\cdot}10^{-3})$	597 (270)

Table 6 – Characteristic parameters of hIAPP aggregation kinetics in the presence of Sil A or Sil B. I_{max}, k, and $t_{1/2}$ of hIAPP fibrillation kinetics in the presence of Sil A and Sil B in peptide/ligand ratios 1:0.1, 1:0.4, and 1:0.8 plotted in figure 54. The kinetics have been fitted with the logarithmic equation $\boldsymbol{I = I_{max}/(1 + e^{-k(t-t_{1/2})})}$, where I_{max} represents the maximum intensity of fluorescence, k is the slope or rate of aggregation kinetics, and $t_{1/2}$ has been defined as the point in time where the signal reaches 50% of the amplitude of the transition. Results are reported as the mean of three experiments (± SD).

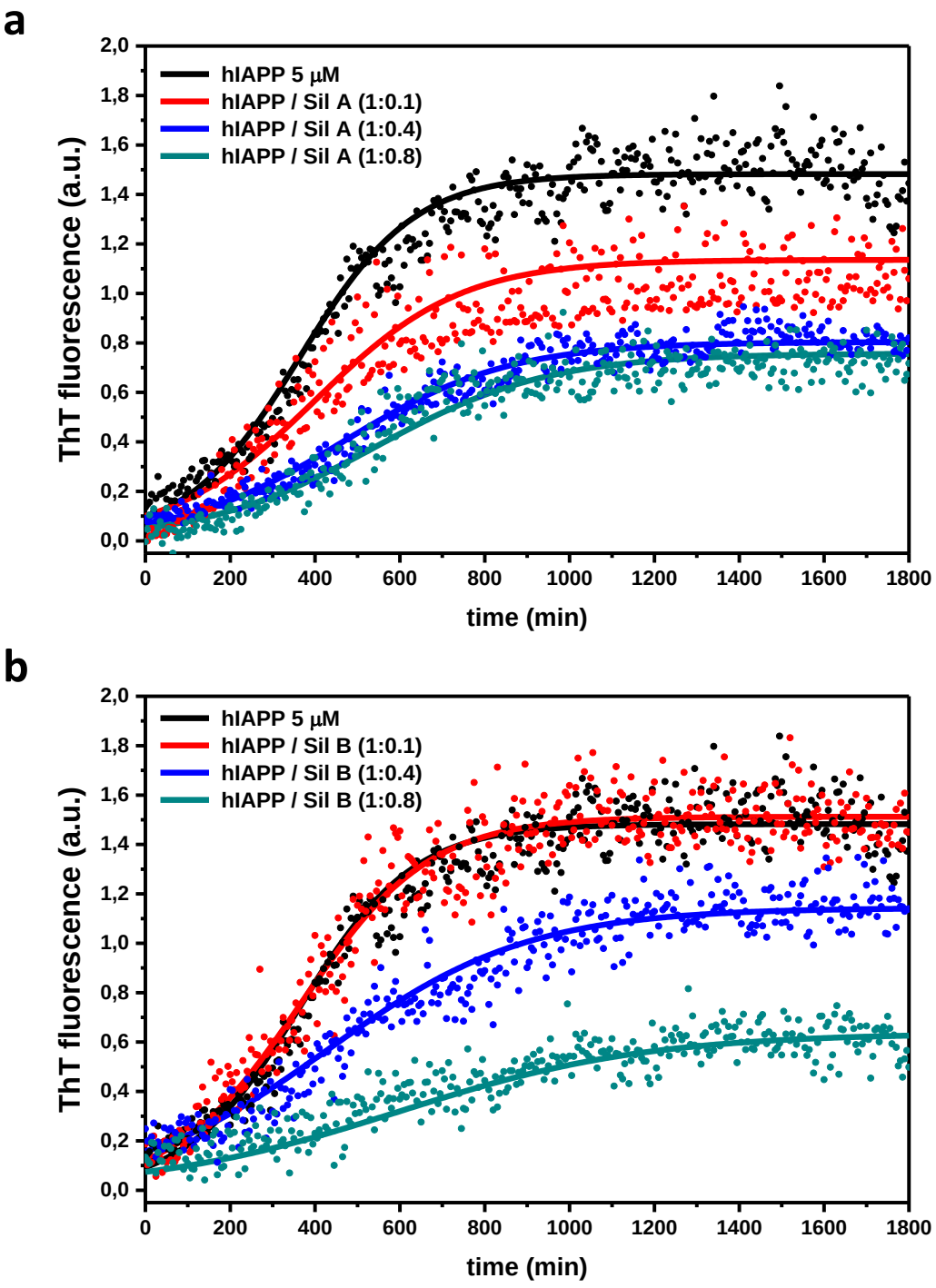

Figure 54 – hIAPP aggregation kinetics of in presence of Sil A and Sil B. (a) Amyloid fibrillation kinetics of hIAPP in the absence (black curve) and presence of Sil A in peptide/Sil A molar ratios 1:0.1 (red curve), 1:0.4 (blue curve), and 1:0.8 (turquoise curve). Dots represent experimental data; the continuous line is the fit of the kinetic obtained by averaging each one of the characteristic parameters of the kinetics of three different experiments (see table 6). Experiments were carried out using hIAPP 5 µM at 25 °C in phosphate buffer 10 mM NaCl 100 mM pH 7.4. **(b)** As (a) except for Sil B.

3.3.4. Silybins catalyze hIAPP amyloid growth in a membrane-mimicking environment but protect the membrane integrity from the amyloid-induced damage

As previously described, amyloid oligomers and fibrils are able to interact with cell membranes by different mechanisms inducing the disruption of the lipid bilayer and eliciting toxicity to the cell. To study if Sil A and Sil B may counteract hIAPP aggregation in a pancreatic membrane-emulating environment, ThT and dye leakage assays were carried out in parallel by using model membranes mimicking the lipid composition of pancreatic islet cell membranes. In particular, a mixture of the zwitterionic phopsphatidylcholine (POPC) and the anionic phospatidylserine (POPS) lipids at a molar ratio 7:3 was used.[65,292,293]

First, membrane-bound hIAPP amyloid growth kinetics were monitored in the presence of Sil A or Sil B at different peptide/ligand molar ratios (1:0.1, 1:0.4, and 1:0.8). Second, dye leakage assays were also run to study the protective effect of both silybins against membrane disruption induced by hIAPP oligomers and fibrils.

In striking contrast to what was observed in aqueous solution, both Sil A and Sil B catalyzed the formation of amyloid fibrils, increasing their amount and reducing both lag phase and the $t_{1/2}$ with respect to control (see figure 55). However, despite the increase in hIAPP aggregation kinetics induced by both Sil A and Sil B, dye leakage assays showed, in the presence of silybins, a significant reduction in hIAPP-induced membrane damage. As shown in figure 56, dye leakage kinetics are the sum of two different processes. The first one occurs within the first 200 min, before the formation of ThT-detectable species; hence it may be associated with a disruptive phenomenon initiated by soluble, membrane-active amyloid oligomers through a poration mechanism. On the contrary, the second one starts when ThT-positive species, i.e. amyloid protofibrils, are already detectable: therefore it may be ascribed to a detergent-like mechanism (for more details about both mechanisms see chapter 1.2.4.1).

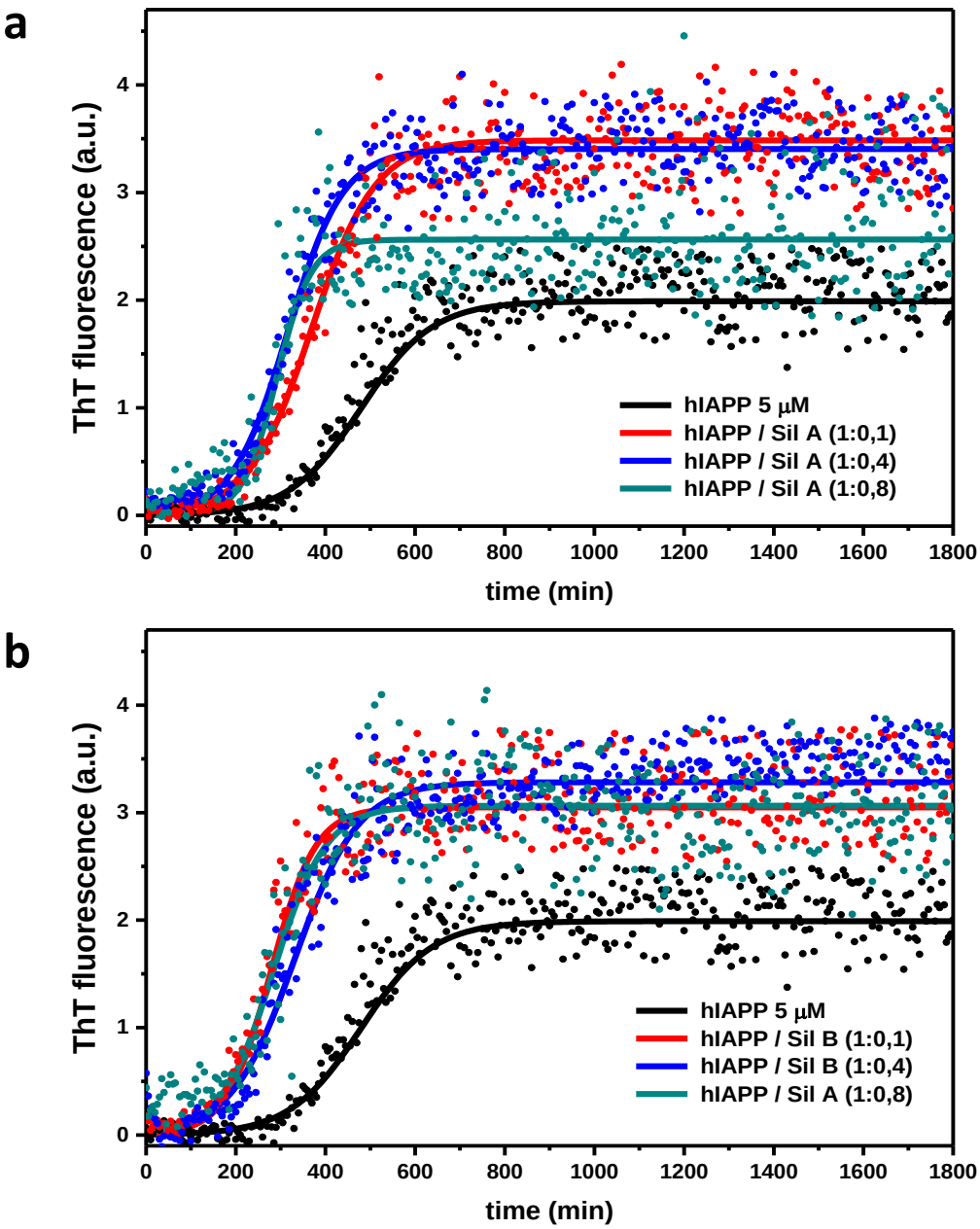

Figure 55 – hIAPP fibrillation kinetics in a milieu containing pancreatic model membranes in the presence of different concentrations of Sil A or Sil B. (a) Amyloid fibrillation kinetics of hIAPP in the absence (black curve) and presence of Sil A in peptide/Sil A molar ratios 1:0.1 (red curve), 1:0.4 (blue curve), and 1:0.8 (turquoise curve). Dots represent experimental data; the continuous line is the fit of kinetics obtained by averaging each of the characteristic parameters of the kinetics of three different experiments (reported in table 7). Experiments were carried out by using hIAPP 5 μM, POPC:POPC 7:3 LUVs 100μM, in phosphate buffer 10 mM NaCl 100 mM pH 7.4 at 25°C. **(b)** As (a) except for Sil B.

Sil A and Sil B inhibited both pore-like and detergent-like mechanisms involved in hIAPP-induced membrane damage. A dose-dependent effect, however, was observed only for the detergent-like mechanism. The two diastereoisomers showed different effects

being Sil B more efficient than Sil A against both disruptive phenomena. While Sil A showed a reduction of the hIAPP-induced membrane poration of about ~ 80%, Sil B inhibited this phenomenon almost completely (~90%). Differences between both diastereoisomers were also evidenced in membrane damage occurring via the detergent-like mechanism. Sil A and Sil B showed a decrease in the amount of dye released of about 11% and 26%, respectively, when they were assayed in peptide/ligand molar ratios 1:01 and 1:04. Furthermore, both Sil A and Sil B significantly delayed dye leakage at a peptide/ligand molar ratio 1:0.4; but Sil B was more efficient (which $t_{1/2}$ values that showed a delay of about 156 min for Sil A and 1080 min for Sil B). The delay in leakage was maintained when Sil A was added at a peptide/ligand molar ratio 1:0.8 albeit showing a significant decrease (of about 76%) in the amount of dye released. Importantly, Sil B was able to fully abolish membrane damage when it was used at the same conditions. Thus, we can conclude that Sil B is more efficient than Sil A in inhibiting both hIAPP-induced membrane damage events, i.e. poration and detergent-like mechanisms.

	$I_{max}(u.a.)$	$k\ (min^{-1})$	$t_{1/2}\ (min)$	$t_{lag}(min)$
hIAPP 5 µM	1.99 (0.22)	$1.25{\cdot}10^{-2}$ ($0.36{\cdot}10^{-2}$)	479 (58)	295 (32)
hIAPP/Sil A (1:0.1)	3.49 (0.22)	$1.14{\cdot}10^{-2}$ ($0.49{\cdot}10^{-2}$)	370 (64)	201 (63)
hIAPP/Sil A (1:0.4)	3.40 (0.47)	$1.62{\cdot}10^{-2}$($0.45{\cdot}10^{-2}$)	316 (52)	171 (34)
hIAPP/Sil A (1:0.8)	2.56 (0.19)	$2.59{\cdot}10^{-2}$ ($0.57{\cdot}10^{-2}$)	291 (4)	187 (33)
hIAPP/Sil B (1:0.1)	3.05 (0.70)	$2.02{\cdot}10^{-2}$ (($0.74{\cdot}10^{-2}$)	278 (59)	160 (52)
hIAPP/Sil B (1:0.4)	3.28 (0.85)	$1.40{\cdot}10^{-2}$ ($0.34{\cdot}10^{-2}$)	332 (15)	167 (57)
hIAPP/Sil B (1:0.8)	3.06 (0.51)	$1.69{\cdot}10^{-2}$ ($0.62{\cdot}10^{-2}$)	284 (49)	144 (35)

Table 7 – Characteristic parameters of hIAPP aggregation kinetics in the presence of silybins in a pancreatic membrane mimicking milieu. I_{max}, $t_{1/2}$, k, and t_{lag} kinetics parameters of 5 µM hIAPP fibrillation in the presence of POPC:POPS (7:3) LUVs with or without Sil A or Sil B at peptide/ligand molar ratios 1:0.1, 1:0.4, and 1:0.8 (reported in figure 55). Aggregation kinetics were fitted by the equation $I = I_{max}/(1 + e^{-k(t-t_{1/2})})$, where I_{max} represents the maximum intensity of fluorescence; k is the slope or rate of aggregation kinetics; $t_{1/2}$ and lag phase (t_{lag}) have been defined as the point in time where the signal reaches 50% and 10% of the amplitude of the transition, respectively. Results are reported as the average of three experiments (± SD).

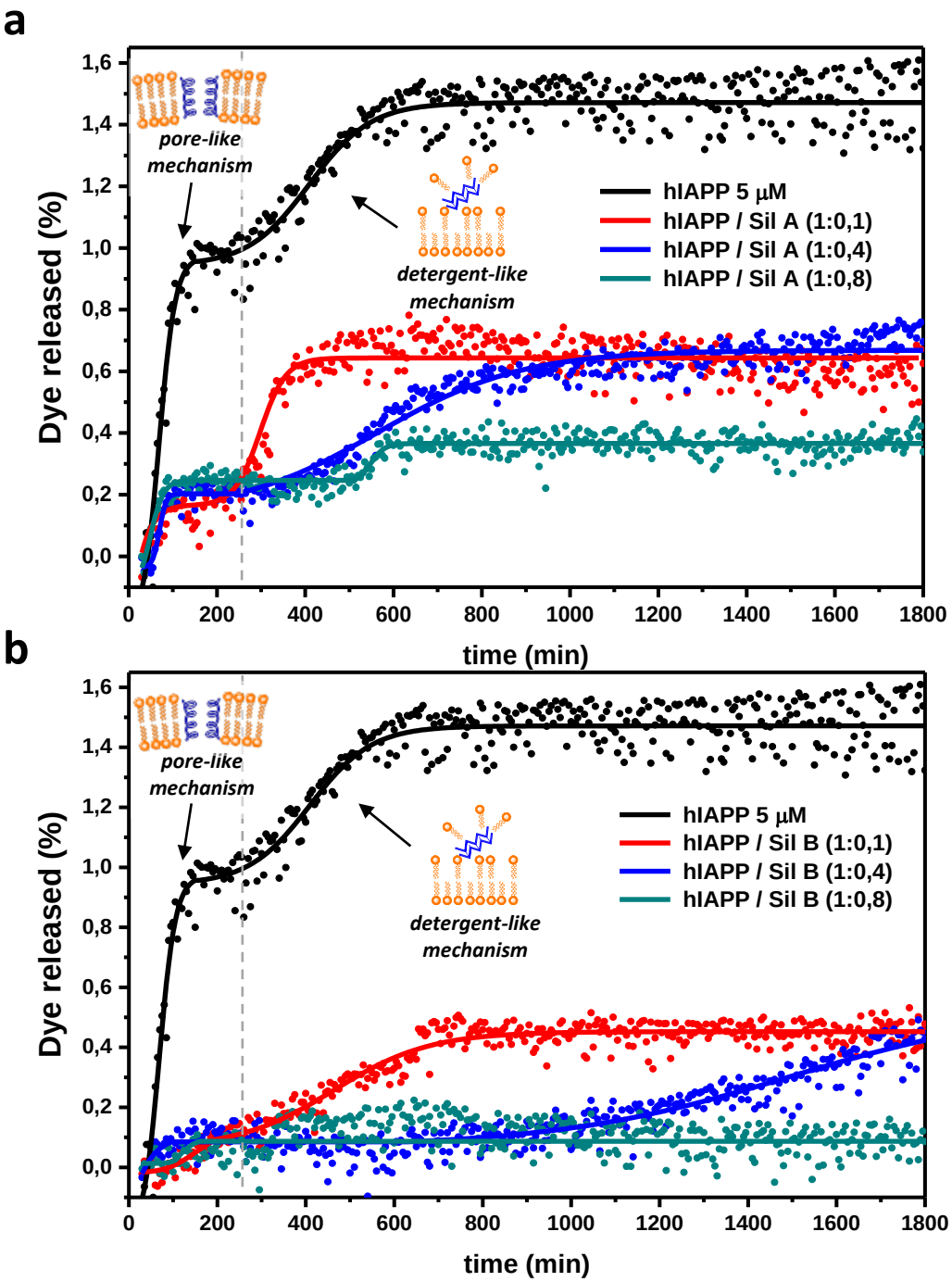

Figure 56 – Dye leakage assays of hIAPP-mediated pancreatic model membranes disruption in the presence of different concentrations of Sil A and Sil B. (a) Percentage of dye released from POPC:POPS (7:3) LUVs triggered by hIAPP in the absence (black curve) and presence of Sil A in peptide/SilA molar ratios 1:0.1 (red curve), 1:0.4 (blue curve), and 1:0.8 (turquoise curve). Dots represent experimental data; the continuous line is the fit of the kinetic obtained by averaging each one of the characteristic kinetic parameters of three different experiments (reported in table 8); dashed line indicates the start of the growth phase, and henceforth, the limit between pore-like and detergent-like mechanisms. Experiments were carried out by using hIAPP 5 µM, POPC:POPC 7:3 LUVs 100 µM, in phosphate buffer 10 mM NaCl 100 mM pH 7.4 at 25 °C. **(b)** As (a) except for Sil B.

First dye release phenomenon				
	I_0 $(u.a.)$	I_{max} $(u.a.)$	$t_{1/2}$ (min)	τ (min)
hIAPP 5µM	-0,23 (0.12)	0,97 (0,02)	69 (5)	18.2 (3.3)
hIAPP / Sil A (1:0.1)	-0.02 (0.04)	0.17 (0.01)	370 (64)	17.3 (8.5)
hIAPP / Sil A (1:0.4)	-0.02 (0.01)	0.20 (0.01)	316 (52)	6.8 (1.7)
hIAPP / Sil A (1:0.8)	-0.06 (0.03)	0.25 (0.01)	291 (4)	12.9 (2.2)
hIAPP / Sil B (1:0.1)	-0.02 (0.02)	0.10 (0.04)	138 (23)	28.7 (22.0)
hIAPP / Sil B (1:0.4)	0.00 (0.05)	0.10 (0.01)	49 (18)	18.6 (10.6)
hIAPP / Sil B (1:0.8)	0.02 (0.02)	0.104 (0.002)	208 (63)	63.2 (29.6)
Second dye release phenomenon				
	I_0 $(u.a.)$	I_{max} $(u.a.)$	$t_{1/2}$ (min)	τ (min)
hIAPP 5µM	0.95 (0.03)	1.482 (0,004)	415 (9)	74 (9)
hIAPP / Sil A (1:0.1)	0.16 (0.01)	0.643 (0.003)	312 (5)	29 (4)
hIAPP / Sil A (1:0.4)	0.19 (0.01)	0.672 (0.004)	571 (8)	112 (7)
hIAPP / Sil A (1:0.8)	0.236 (0.004)	0.366 (0.002)	548 (6)	16 (5)
hIAPP / Sil B (1:0.1)	0.06 (0.02)	0.452 (0.002)	463 (13)	108 (8)
hIAPP / Sil B (1:0.4)	0.07 (0.01)	0.54 (0.06)	1495 (68)	267 (34)
hIAPP / Sil B (1:0.8)	----	----	----	----

Table 8 – Characteristic parameters of hIAPP-mediated pancreatic model membranes disruption kinetics in the presence of silybins. I_0, I_{max}, $t_{1/2}$ and τ kinetic parameters of the dye release from POPC:POPS (7:3) LUVs induced by 5µM hIAPP and in the absence or presence of Sil A or Sil B (peptide/ligand molar ratios 1:0.1, 1:0.4 and 1:0.8) as plotted in figure 56. The kinetics have been fitted with the logarithmical equation $\boldsymbol{I = (I_0 - I_{max})/(1 + e^{(t-t_{1/2})/\tau}) + I_{max}}$, where I_0 and I_{max} represent the initial and the maximum intensity of fluorescence, $\boldsymbol{\tau}$ is the time constant, and $t_{1/2}$ is the point in time where the signal reaches 50% of the amplitude of the transition. Results are reported as the mean of three experiments (± SD).

3.3.5. Conformational analysis of hIAPP in the presence of Sil A/B by Circular Dichroism

CD experiments have been carried out to study the secondary structure of monomeric hIAPP in the presence of Sil A and Sil B. The CD spectrum of 2.5 µM hIAPP did show a random coil structure. Then, we registered CD spectra of the peptide in the presence of Sil A and Sil B at a peptide/ligand molar ratios 1:1 and 1:2. All CD spectra in the presence of the ligands exhibited a positive peak at 210 nm, characteristic of a polyproline II helix (PPII) structure (see figure 57). The intensity of this band was similar in both spectra in the presence of Sil A at different molar ratio (1:1 and 1:2) while a dose-dependent effect was observed in the presence of Sil B, with a more intense band at 1:2 peptide/ligand ratio, indicating a larger conformational change induced by Sil B than Sil A. A shift in hIAPP conformation, stabilizing a PPII structure could be related to the anti-aggregating effects

observed in ThT experiments, where a higher anti-fibrillogenic effect of Sil B was evidenced; an aspect that reconciles with the conformational changes monitored by CD experiments.

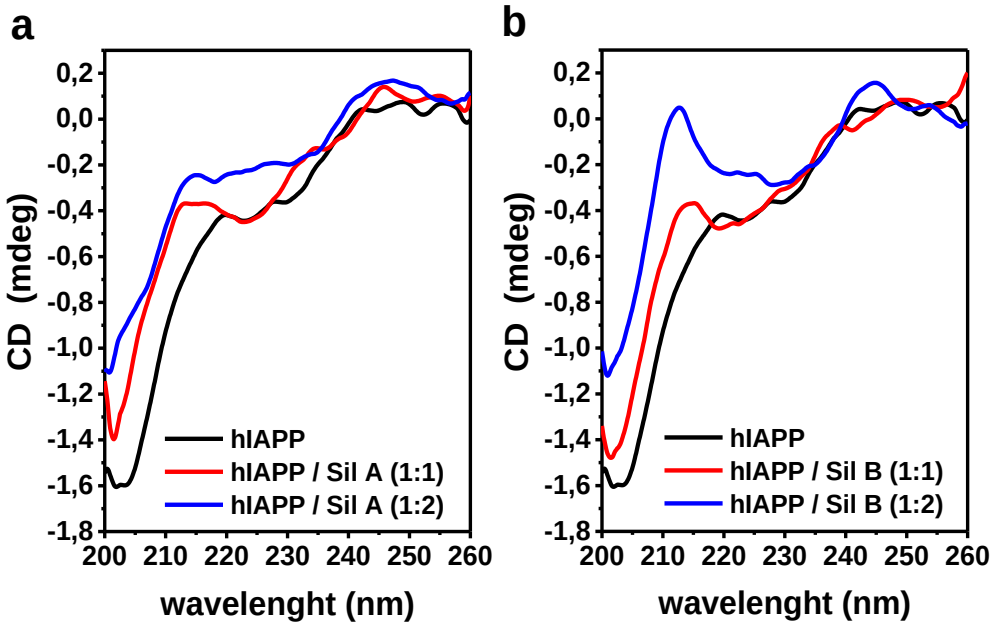

Figure 57 – CD spectra. (a) Circular Dichroism spectrum of hIAPP in the absence (black line) and presence of Sil A in a peptide/ligand ratio 1:1 (red line) and 1:2 (blue line). CD curves have been registered at 4 °C in 10 mM phosphate buffer pH 7.4, using a peptide concentration of 2.5 µM. **(b)** As (a) except for Sil B instead of Sil A.

However, it is important to remind that, as most of the experimental methods used in the characterization of proteins, CD may provide only structural-average information. This, together with the conformational heterogeneity of IDPs severely complicates their structural characterization being this one of the major challenges in the study of this group of proteins[294] and, therefore, other techniques should be used to obtain a detailed description of conformational equilibriums and to unveil the molecular details of ligand-peptide interactions. This topic is analyzed in-depth in chapter 3.4.

3.3.6. Silybin derivatives inhibit hIAPP amyloid growth

To evaluate whether the hIAPP antiaggregant properties of silybins are maintained in their trehalose conjugates, ThT assays have been performed. To this aim, hIAPP fibrillation kinetics have been monitored in presence of increasing concentrations of both Sil A-p-TH and Sil B-p-TH, in particular, in peptide/ligand ratios 1:0.4, 1:1, and 1:5. Both compounds induced a slight delay in aggregation kinetics as well as a significant dose-dependent decrease of the amount of ThT-positive fibrils formed, as shown in figure 58.

A decline in the ThT signal was observed after achieving the maximum ThT fluorescence in samples containing silybin derivatives, but not in the control. A ThT signal decline, usually, may be ascribable to a precipitation of the formed fibrils. However, glass beds are added in our experiments which, together with a 10 s shaking preceding each measure, avoid fibril precipitation. Furthermore, it has been a very reproducible phenomenon occurring just in samples containing Sil A-p-TH or Sil B-p-TH. Thus, we hypothesize that: i) ligands induce the formation of a different type of fibrils, with a higher tendency to precipitate or ii) ligands induce a structural change in the formed fibrils leading to structures that fail to bond with ThT or produce another binding mode which involves a less fluorescent signal.

Typical sigmoidal increase of fluorescence

	$\boldsymbol{I_{max}}\ (u.a.)$	$\boldsymbol{k}\ (min^{-1})$	$\boldsymbol{t_{1/2}}\ (min)$	$\boldsymbol{t_{lag}}\ (min)$
hIAPP 5 µM	17.0 (0.5)	0.029 (0.015)	281 (59)	188 (32)
hIAPP / Sil A-p-TH (1:0.4)	13.2 (0.5)	0.035 (0.020)	292 (48)	214 (82)
hIAPP / Sil A-p-TH (1:1)	12.9 (1.3)	0.046 (0.005)	290 (23)	242 (24)
hIAPP / Sil A-p-TH (1:5)	3.9 (0.6)	0.031 (0.007)	289 (22)	216 (8)
hIAPP / Sil B-p-TH (1:0.4)	15.0 (3.0)	0.048 (0.009)	287 (8)	240 (17)
hIAPP / Sil B-p-TH (1:1)	9.8 (2.2)	0.037 (0.015)	329 (10)	262 (14)
hIAPP / Sil B-p-TH (1:5)	4.4 (0.5)	0.044 (0.019)	309 (17)	254 (15)

Fluorescence dropped – 2nd order polynomial

	$\boldsymbol{A}\ (u.a.)$	$\boldsymbol{B}\ (u.a.\cdot h^{-1})$	$\boldsymbol{C}\ (u.a.\cdot h^{-2})$
hIAPP 5 µM	--	--	--
hIAPP / Sil A-p-TH (1:0.4)	14,3 (5,7)	$-0.4\cdot10^{-2}$ ($1.8\cdot10^{-2}$)	$-0.3\cdot10^{-6}$ ($8.6\cdot10^{-6}$)
hIAPP / Sil A-p-TH (1:1)	18.7 (5.2)	$-2.1\cdot10^{-2}$ ($0.3\cdot10^{-2}$)	$-8.3\cdot10^{-6}$ ($3.0\cdot10^{-6}$)
hIAPP / Sil A-p-TH (1:5)	4.8 (1.0)	$-0.3\cdot10^{-2}$ ($0.3\cdot10^{-2}$)	$-1.1\cdot10^{-6}$ ($1.4\cdot10^{-6}$)
hIAPP / Sil B-p-TH (1:0.4)	24.1 (4.5)	$-2.9\cdot10^{-2}$ ($0.6\cdot10^{-2}$)	$-1.2\cdot10^{-5}$ ($2.9\cdot10^{-6}$)
hIAPP / Sil B-p-TH (1:1)	15.5 (3.6)	$-1.4\cdot10^{-2}$ ($0.6\cdot10^{-2}$)	$-5.4\cdot10^{-6}$ ($2.8\cdot10^{-6}$)
hIAPP / Sil B-p-TH (1:5)	8.2 (1.7)	$-1.0\cdot10^{-2}$ ($0.4\cdot10^{-2}$)	$-4.6\cdot10^{-6}$ ($2.2\cdot10^{-6}$)

Table 9 – Sigmoidal fit equation and characteristic parameters of aggregation kinetic. I_{max}, $t_{1/2}$, k, and t_{lag} of hIAPP fibrillation kinetics in the presence of Sil A-p-TH and Sil B-p-TH in peptide/ligand molar ratios 1:0.1, 1:0.4, and 1:0.8 plotted in figure 58. The first part of the kinetics have been fitted with the logarithmical equation $\boldsymbol{I = I_{max}/(1 + e^{-k(t-t_{1/2})})}$, where I_{max} represents the maximum intensity of fluorescence; k is the slope or rate of aggregation kinetics; $t_{1/2}$ and lag phase (t_{lag}) and have been defined as the point in time where the signal reaches 50% and 10% of the amplitude of the transition, respectively. The fluorescence dropped has been fitted with a second-order polynomial equation $\boldsymbol{I = A + t \cdot B + t^2 \cdot C}$.

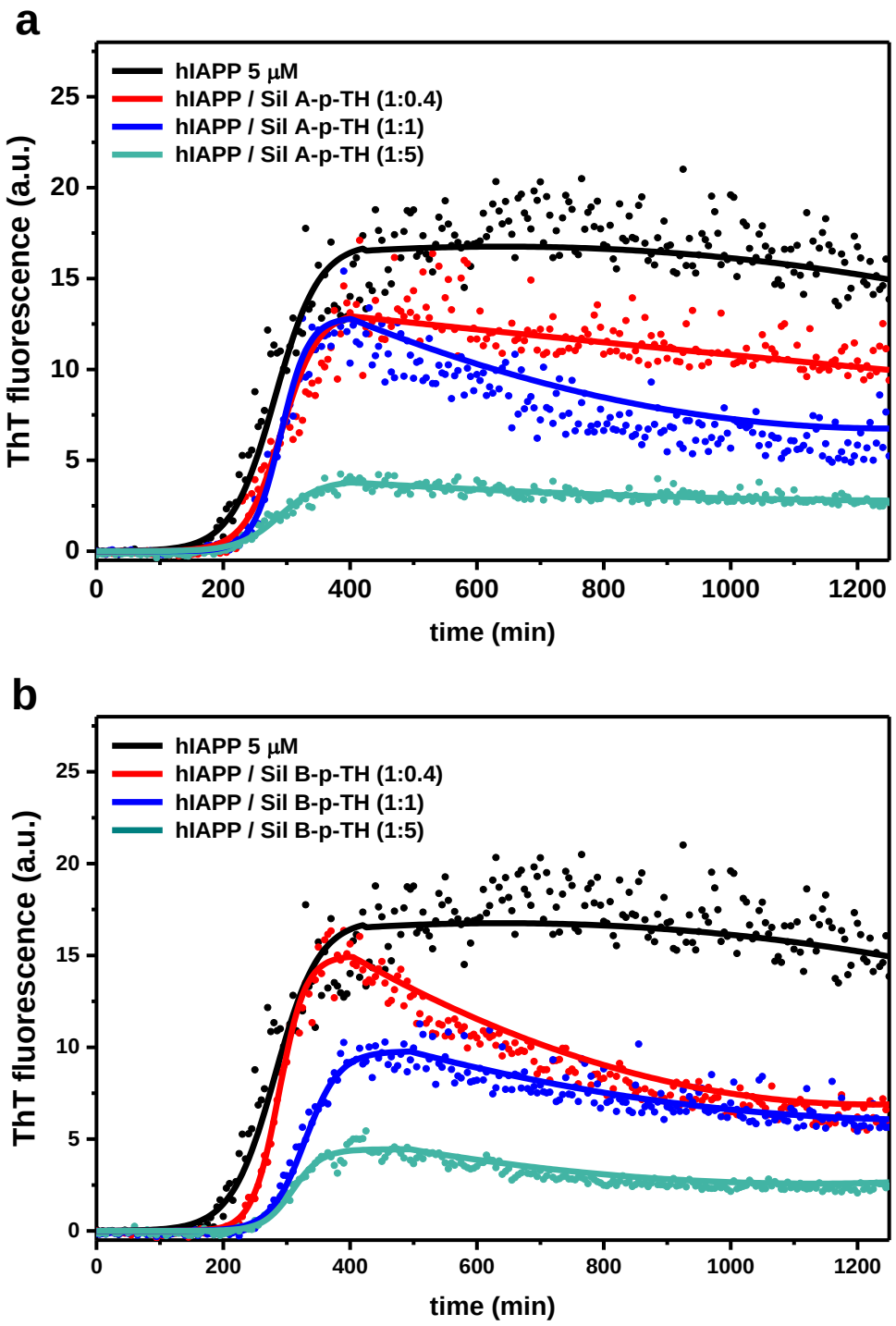

Figure 58 – hIAPP aggregation kinetics of in presence of Sil A-p-TH and Sil B-p-TH.(a) Amyloid fibrillation kinetics of hIAPP in the absence (black curve) and presence of Sil A-p-TH in peptide/Sil A-p-TH molar ratios 1:0.4 (red curve), 1:1 (blue curve), and 1:5 (turquoise curve). Dots represent experimental data; the continuous line is the fit of the kinetics obtained by averaging each one of the characteristic parameters of the kinetics of three different experiments (reported in table 9). Experiments were carried out using hIAPP 5 μM at 25 °C in phosphate buffer 10 mM NaCl 100 mM pH 7.4. **(b)** As (a) except for Sil B.

3.3.7. Silybin derivatives inhibit hIAPP amyloid growth in a membrane-mimicking environment and protect the membrane integrity from the amyloid-induced damage

ThT assays were carried out to assess the effect of silybin derivatives on hIAPP amyloid growth in presence of pancreatic model membranes. When silybin derivatives were tested at substoichiometric (hIAPP/ligand molar ratio 1:0.4) and stoichiometric conditions, no significant differences were observed in the kinetics of aggregation. However, in excess of ligand (hIAPP/ligand molar ratio 1:5), the maximum intensity of fluorescence, and thus the amount of amyloid fibrils, was decreased in presence of each one of the glycoconjugates by about 45% (see figure 59).

Dye release experiments performed at increased concentrations (peptide/ligand ratios 1:0.4, 1:1, and 1:5) of Sil A-p-TH and Sil B-p-TH allowed evaluating their effect on modulating the membrane disruption processes mediated by hIAPP (see figure 60). As observed in the same experiment performed in presence of the parent molecules, two disruptive processes were identified. The first is ascribable to oligomeric IAPP species, and thus, to a pore-like mechanism. The second one, occurs later, when fibril formation has already started, and therefore it is associated with fibrillar hIAPP species acting through a detergent-like mechanism.

Both membrane damage mechanisms are partially inhibited by Sil A-p-TH and Sil B-p-TH although with some differences. On one hand, the pore-like mechanism is inhibited by both compounds in all experimental conditions showing a decrease of dye release of around 62% in the presence of the highest dose (peptide/ligand ratio 1:5) for both compounds. On the other hand, the detergent-like mechanism was inhibited to a lesser extent (around 16%) by both compounds. However, differently from Sil A-p-TH, Sil B-p-TH delayed the process in a concentration-dependent manner. Therefore, we can conclude that both compounds may protect membranes from hIAPP damage, although, Sil B-p-TH was more effective.

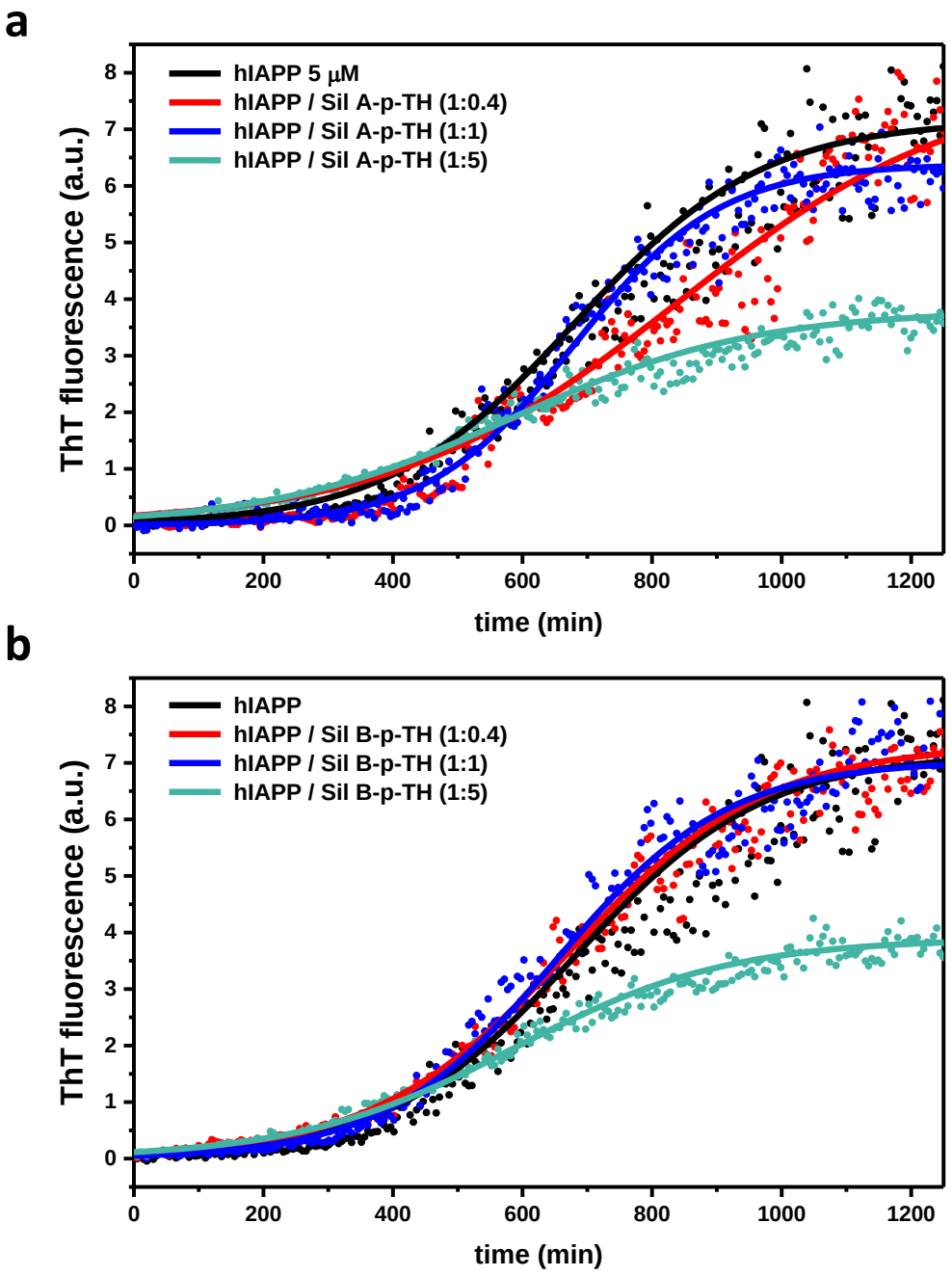

Figure 59 – hIAPP fibrillation kinetics in a milieu containing pancreatic model membranes in the presence of different concentrations of Sil A-p-TH or Sil B-p-TH. (a) Amyloid fibrillation kinetics of hIAPP in the absence (black curve) and presence of Sil A in peptide/Sil A-p-TH molar ratios 1:0.1 (red curve), 1:0.4 (blue curve), and 1:0.8 (turquoise curve). Dots represent experimental data; the continuous line is the fit of kinetics obtained by averaging each of the characteristic parameters of the kinetics of three different experiments (reported in table 10). Experiments were carried out by using hIAPP 5 µM, POPC:POPC 7:3 LUVs 100 µM, in phosphate buffer 10 mM NaCl 100 mM pH 7.4 at 25 °C. **(b)** As (a) except for Sil B.

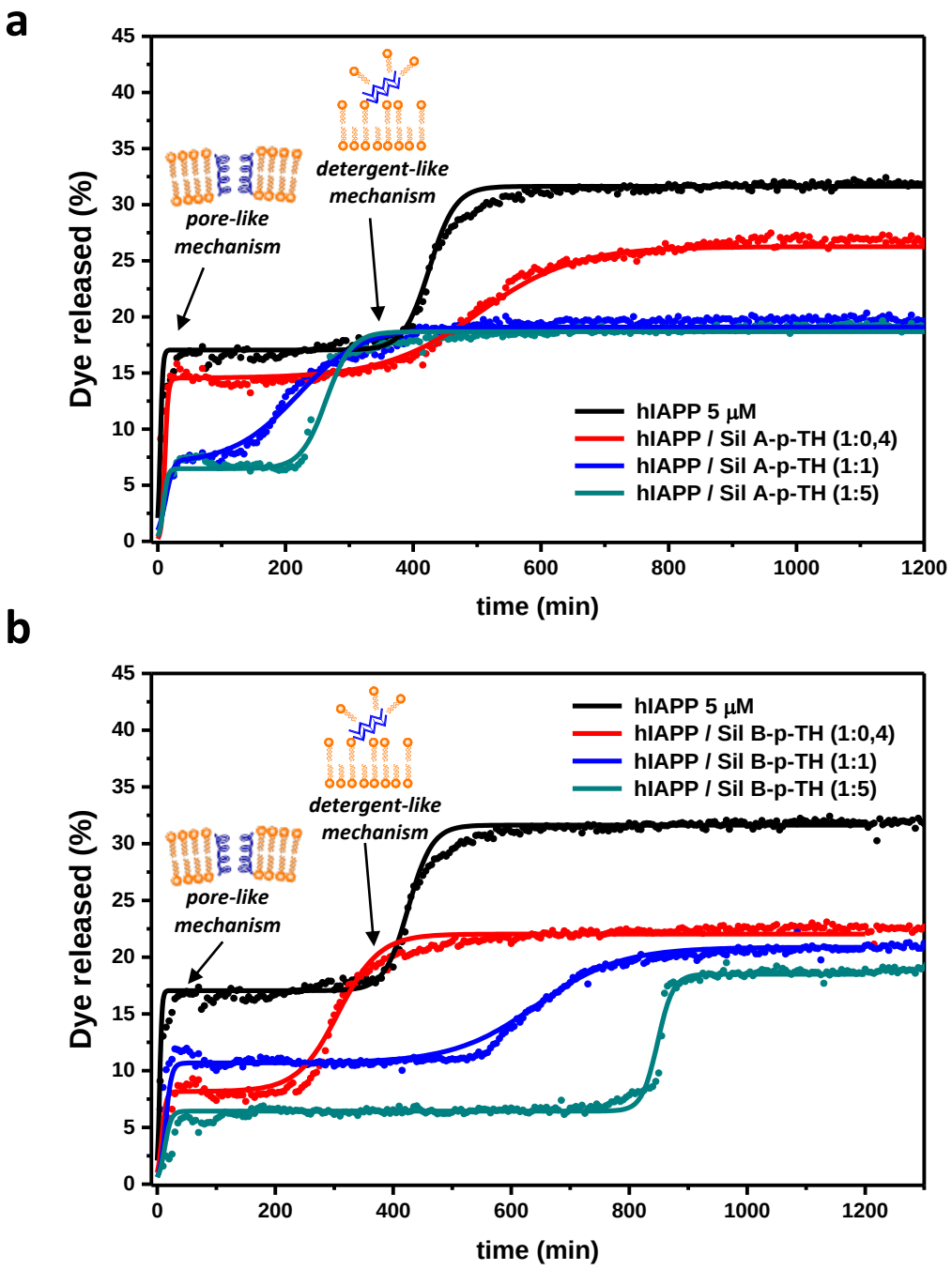

Figure 60 – Dye leakage assays of hIAPP-mediated pancreatic model membranes disruption in the presence of different of Sil A-p-TH and Sil B-p-TH. (a) Percentage of dye released from POPC:POPS (7:3) LUVs triggered by hIAPP in the absence (black curve) and presence of Sil A-p-TH in peptide/ligand molar ratios 1:0.1 (red curve), 1:0.4 (blue curve), and 1:0.8 (turquoise curve). Dots represent experimental data; the continuous line is the fit of the kinetic obtained by averaging each one of the characteristic kinetic parameters of three different experiments (reported in table 11); the dashed line indicates the start of the growth phase, and henceforth, the limit between pore-like and detergent-like mechanisms. Experiments were carried out by using hIAPP 5 µM, POPC:POPC 7:3 LUVs 100 µM, in phosphate buffer 10 mM NaCl 100 mM pH 7.4 at 25 °C.

	$I_{max}(u.a.)$	$k\ (min^{-1})$	$t_{1/2}\ (min)$	$t_{lag}\ (min)$
hIAPP	7.2 (0.9)	$6.8{\cdot}10^{-3}$ ($4.4{\cdot}10^{-3}$)	681 (121)	209 (22)
hIAPP / Sil A-p-TH (1:0.4)	7.9 (0.4)	$4.5{\cdot}10^{-3}$ ($1.1{\cdot}10^{-3}$)	840 (18)	219 (23)
hIAPP / Sil A-p-TH (1:1)	6.4(1.2)	$8.8{\cdot}10^{-3}$ ($2.1{\cdot}10^{-3}$)	680 (106)	225 (22)
hIAPP / Sil A-p-TH (1:5)	3.8 (1.9)	$5.4{\cdot}10^{-3}$ ($1.5{\cdot}10^{-3}$)	584 (141)	214 (37)
hIAPP / Sil B-p-TH (1:0.4)	7.3 (3.5)	$6.5{\cdot}10^{-3}$ ($1.6{\cdot}10^{-3}$)	672 (173)	198 (23)
hIAPP / Sil B-p-TH (1:1)	7.0 (2.6)	$7.5{\cdot}10^{-3}$ ($2.6{\cdot}10^{-3}$)	652 (62)	242 (5)
hIAPP / Sil B-p-TH (1:5)	3.9 (0.7)	$6.0{\cdot}10^{-3}$ ($1.6{\cdot}10^{-3}$)	586 (146)	226 (33)

Table 10 – Characteristic parameters of hIAPP aggregation kinetics in the presence of silybin derivatives in a pancreatic membrane mimicking milieu. I_{max}, $t_{1/2}$, k, and t_{lag} kinetics parameters of 5 µM hIAPP fibrillation in the presence of POPC:POPS (7:3) LUVs with or without Sil A-p-TH or Sil B-p-TH at peptide/ligand molar ratios 1:0.4, 1:1, and 1:5 (reported in figure 59). Aggregation kinetics were fitted by the equation $\boldsymbol{I = I_{max}/(1 + e^{-k(t-t_{1/2})})}$, where I_{max} represents the maximum intensity of fluorescence; k is the slope or rate of aggregation kinetics; $t_{1/2}$ and lag phase (t_{lag}) has been defined as the points in time where the signal reaches 50% and 10% of the amplitude of the transition, respectively. Results are reported as the average of three experiments (± SD).

First release

	$I_{max}(u.a.)$	$k(h^{-1})$	$t_{1/2}\ (h)$
hIAPP 5µM	17.0 (1.7)	0.50 (0.24)	4.0 (0.7)
hIAPP / Sil A (1:0.4)	14.5 (1.9)	0.38 (0.33)	11.0 (7.4)
hIAPP / Sil A (1:1)	7.4 (1.2)	0.16 (0.02)	12.0 (0.9)
hIAPP / Sil A (1:5)	6.5 (0.5)	0.30 (0.11)	8.8 (1.0)
hIAPP / Sil B (1:0.4)	8.3 (1.4)	0.26 (0.10)	7.5 (1.6)
hIAPP / Sil B (1:1)	10.7 (4.5)	0.20 (0.10)	14.1 (5.1)
hIAPP / Sil B (1:5)	6.4 (0.4)	0.18 (0.15)	12.5 (11.3)

Second release

	$I_0(u.a.)$	$I_{max}(u.a.)$	$k(h^{-1})$	$t_{1/2}\ (h)$
hIAPP 5µM	17.0 (1.7)	14.6 (2.2)	0.049 (0.050)	425 (215)
hIAPP / Sil A (1:0.4)	14.5 (1.9)	11.7 (1.8)	0.013 (0.004)	503 (74)
hIAPP / Sil A (1:1)	7.4 (1.2)	12.2 (1.3)	0.020 (0.005)	219 (17)
hIAPP / Sil A (1:5)	6.5 (0.5)	12.2 (2.3)	0.051 (0.041)	264 (24)
hIAPP / Sil B (1:0.4)	8.3 (1.4)	13.9 (2.3)	0.029 (0.010)	307 (17)
hIAPP / Sil B (1:1)	10.7 (4.5)	10.2 (1.6)	0.014 (0.010)	643 (61)
hIAPP / Sil B (1:5)	6.4 (0.4)	12.1 (4.9)	0.076 (0.039)	848 (126)

Table 11 – Characteristic parameters of hIAPP-mediated pancreatic model membranes disruption kinetics in the presence of silybin derivatives. I_0, I_{max}, $t_{1/2}$, and k kinetics parameters of the dye release from POPC:POPS (7:3) LUVs triggered by hIAPP 5µM and in the absence or presence of Sil A-p-TH or Sil B-p-TH in peptide/ligand molar ratios 1:0.1, 1:0.4, and 1:0.8 plotted in figure 60. First and second release kinetics have been fitted with the equations $\boldsymbol{I = I_{max}/(1 + e^{-k(t-t_{1/2})})}$ and $\boldsymbol{I = I_0 + (I_{max}/(1 + e^{-k(t-t_{1/2})}))}$, respectively, where I_0 and I_{max} represent the initial and the maximum intensity of fluorescence; k is the time constant; $t_{1/2}$ is the point in time where the signal reaches 50% of the amplitude of the transition. Results are reported as the mean of three experiments (± SD).

3.4. High-resolution structures of silybin/amyloid complexes

3.4.1. Study of the Aβ and Sil A/B-p-TH interaction by NMR

Nuclear Magnetic Resonance (NMR) is as a powerful tool to study protein-ligand interactions in solution; in particular, NMR methods could be applied to i) evaluate the protein/ligand binding affinity, ii) identify the binding epitopes on both ligand and protein, and iii) monitor the structural changes induced in the protein by ligand binding.[295] Unfortunately, the ability of this technique to generate a detailed molecular description of the complexes is counterbalanced by the need for large amounts of water-soluble samples. For this reason, the interaction of proteins with poorly soluble compounds as silybins cannot be analyzed with this technique. By contrast, highly soluble ligands as silybin-phospho-trehalose conjugates may be conveniently investigated by NMR. Thus, to understand the mechanism of action of the soluble glycoconjugates Sil A-p-TH and Sil B-p-TH against Aβ aggregation, different NMR experiments (i.e. STD, ^{1}H-^{1}H NOESY, and ^{1}H-^{15}H HSQC NMR experiments) have been carried out in collaboration with prof. G. Melacini and Dr. R. Ahmed from McMaster University, Hamilton (Canada).

Saturation Transfer Difference (STD) experiments are used to estimate the binding epitope of ligands, that is, the groups of the ligand that are important for the recognition by the protein. In these experiments, a protein frequency-selective pulse is applied to some protons of the protein and the magnetic saturation is transferred to all the protein and at the protons of the ligand that are interacting with it, being the transferring of saturation to the ligand protons proportional to their proximity to the protein. The mentioned spectrum or “on-resonance” spectrum is subtracted from a reference spectrum or “off-resonance” spectrum of the ligand alone, permitting to establish the binding epitope of the ligand. Finally, STD experiments can be cumulated at different concentrations to obtain a titration curve used to calculate the dissociation constant (K_d) for the ligand-protein interaction. Consequently, STD NMR titration using different concentrations of silybin glycoconjugates (from 0 to 1000 μM) was carried out to establish

the affinity constants of the silybin derivatives and preformed $A\beta_{40}$ oligomers, i.e. to determine whether the anti-aggregation potency of the glycoconjugates resulting from the binding with $A\beta_{40}$ oligomers. Both compounds Sil A-p-TH and Sil B-p-TH showed similar affinities for the oligomers (see figure 61) with K_D = 396 ± 88 µM and K_D = 333 ± 62 µM, respectively.

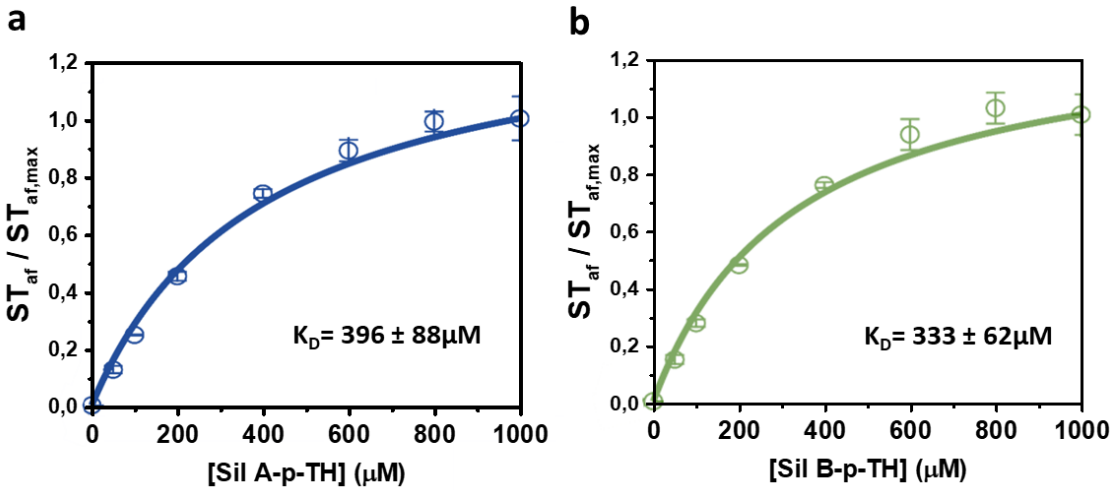

Figure 61 – Binding affinities between silybin derivatives and $A\beta_{40}$ oligomers. (a) Binding isotherm for the titration of Sil A-p-TH into $A\beta_{40}$ oligomers monitored through the STD amplification factor (STD_{af}) and normalized to the maximum STD value. STD_{af} values represent the average of two different aromatic protons and are indicated as mean (± SD). Sil A-p-TH/$A\beta_{40}$ oligomer dissociation constant (K_D) is indicated in the figure. **(b)** As (a) except for Sil B-p-TH.

STD:STR ratios of the previously shown STD-NMR spectra at the end of the titration were used to build the binding epitopes maps of the silybin glycoconjugates (see figure 62), showing different binding regions with $A\beta_{40}$ oligomers. Protons that belong to the phenolic ring A showed the largest STD signal, indicating that it encloses the predominant binding sites with $A\beta_{40}$ oligomers. The protons of the trehalose and the methoxy group exhibited a small saturation signal and, therefore, their contribution to the interaction with the oligomers is negligible. Finally, phenolic rings C and E, exhibited a significant saturation transfer, although to a lesser extent than ring A. Differences between binding epitopes of SilA-p-TH and Sil B-p-TH diastereoisomers were only observed for the protons belonging to the rings C and E (i.e. peaks form $H_{13,15,18,22}$ and $H_{16,21}$), where SilA-p-TH showed a slightly higher STD signal.

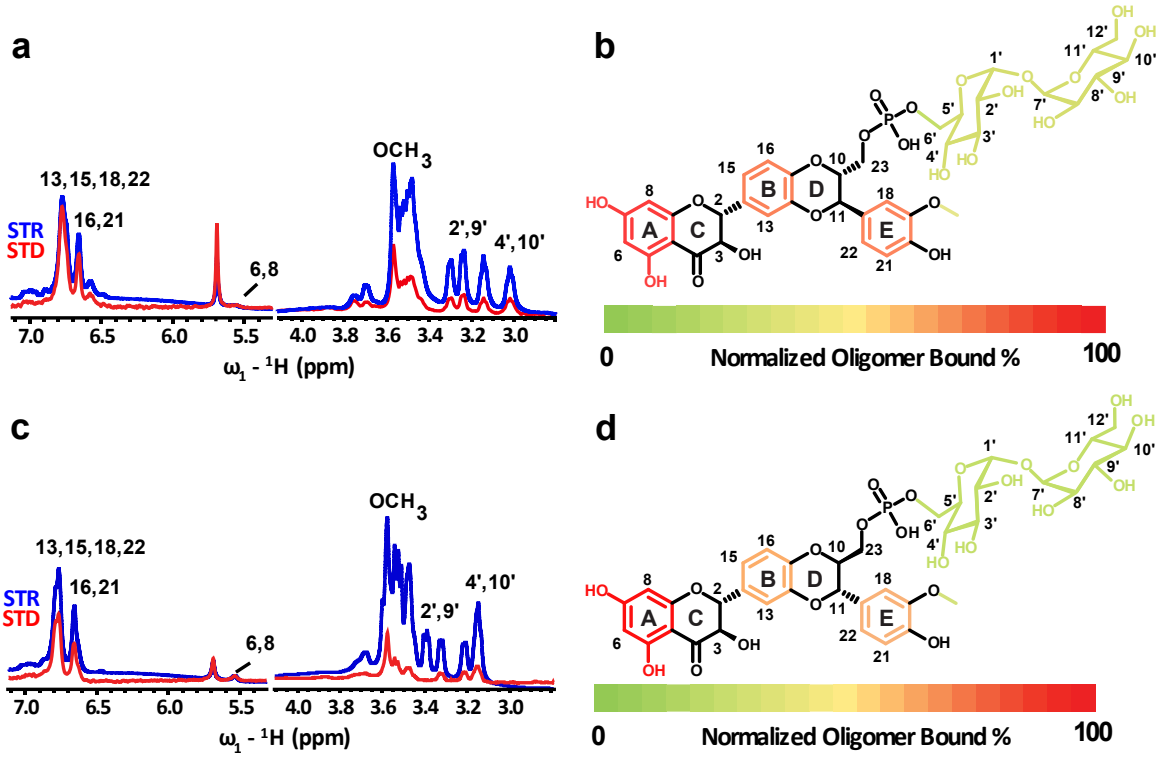

Figure 62 – Binding epitopes of Sil A-p-TH and SilB-p-TH as bound to Aβ$_{40}$ oligomers. (a) Saturation transfer difference (STD, red) and reference (STR, black) spectra of Aβ$_{40}$ (90 μM) in presence of 1mM Sil A-p-TH. Spectra are normalized with respect to the highest STD:STR peak ratio, i.e. H$_{6,8}$. **(b)** Binding epitopes of Sil A-p-TH based on the STD:STR ratios shown in (a). **(c)** As (a) except for Sil-B-p-TH. **(d)** As (c) except for Sil B-p-TH.

To study the conformational changes in silybin glycoconjugates ensued from the interaction with Aβ$_{40}$ oligomers, 2D - NOESY experiments were performed (see figure 63). These experiments are widely used to study conformational changes in the ligand when it binds to the protein thanks to the arisen changes in Nuclear Overhauser Effects (NOEs) called transferred-NOEs (tr-NOEs). In our case, additional NOE signals appeared in the spectra in presence of Aβ$_{40}$ oligomers (oAβ) compared with the spectra of the free ligand in solution. In particular, in both diastereoisomers appeared a cross-peak signal (H$_{13,15,18,22}$ vs. H$_{9',2'}$) indicating an approaching between some protons from the rings B/E and the trehalose moiety when silybin conjugates interact with oAβ. Moreover, the spectrum of oAβ-bounded Sil B-p-TH showed two additional cross-peaks (H$_{16,21}$vs. H$_{11}$ and H$_{6,8}$ vs. H$_{11}$) that were not verifiable for Sil A-p-TH because of the presence of residual water signal which conceals the potential ligand signal. These cross-peaks allowed us to hypothesize that: i) the re-orientation of the ring E, rotating about the single bond with the D ring, getting the H$_{18}$ closer to the H$_{15}$ and ii) the re-orientation of ring A-C through the rotation of this moiety

across the single bond with ring B, allowing the positioning of the H_6 and/or H_8 from the ring A in the vicinity of the H_{11} from the ring D. Thus, the interaction of silybin conjugates with oAβ leads ligands to assume a more compact conformation.

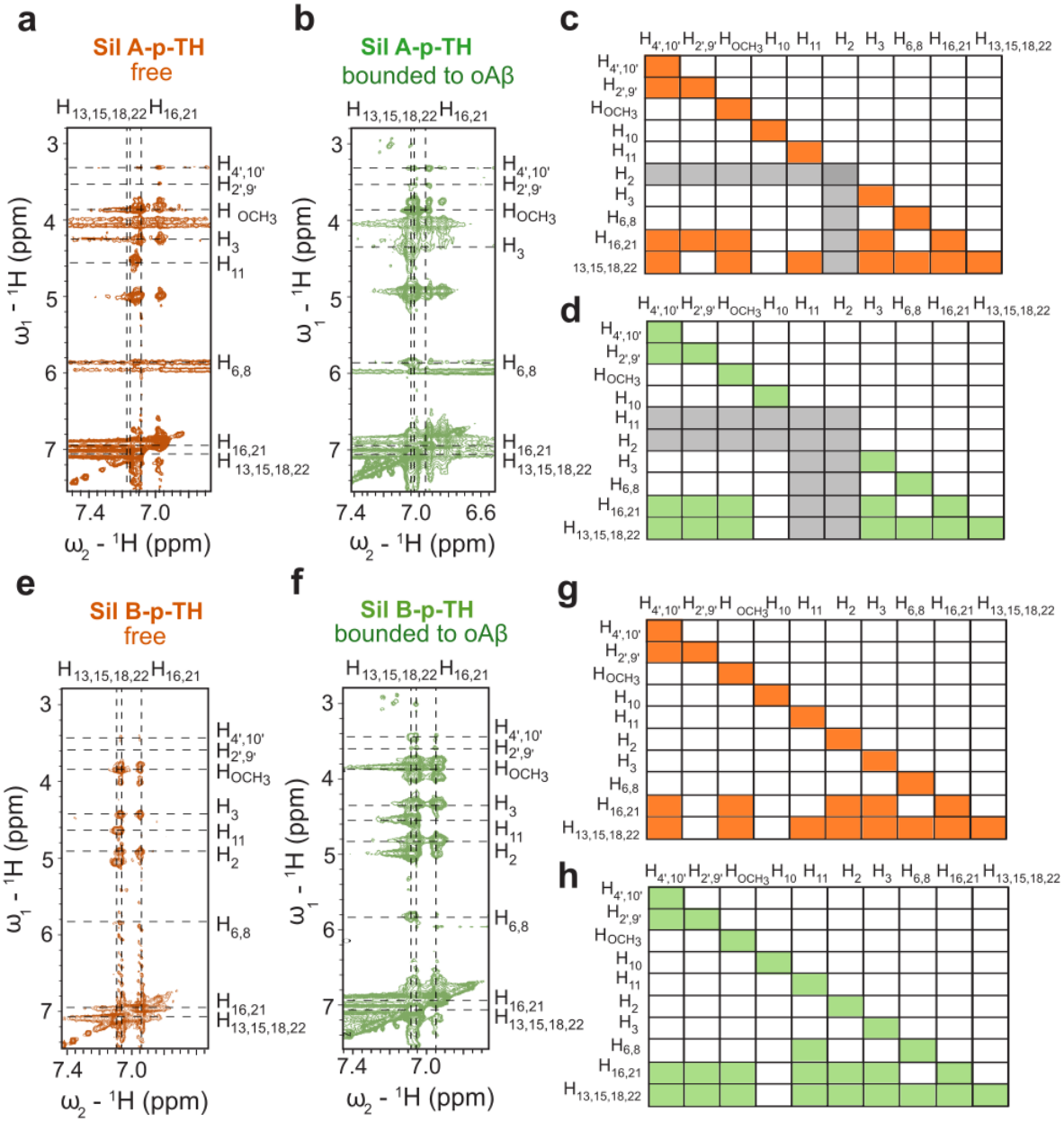

Figure 63 – ^{1}H-^{1}H NOESY of Sil A-p-TH and Sil B-p-TH in the absence and presence of Aβ$_{40}$ oligomer. (a) Enlarged ^{1}H-^{1}H NOESY spectra of 500 µM Sil A-p-TH. **(b)** Enlarged ^{1}H-^{1}H NOESY spectra of 100 µM Sil A-p-TH in presence of 90 µM Aβ$_{40}$. **(c)** Schematic map of the intramolecular NOEs showed in (a). Grey zones indicate the residual H_2O signal which conceals the potential ligand resonances. **(d)** As (c) except for intramolecular NOEs showed in (b). **(e)** As (a) except for Sil B-p-TH**. (f)** As (b) except for Sil B-p-TH. **(g)** As (c) except for intramolecular NOEs showed in (e). **(h)** As (c) except for intramolecular NOEs showed in (f).

To measure the Sil A-p-TH and Sil B-p-TH binding affinity to $A\beta_{40}$ monomers, $^{1}H–^{15}N$ Heteronuclear Single Quantum Coherence (HSQC) experiments were carried out. The heterocorrelation between the ^{15}N and ^{1}H from the amide bonds generates one peak for each residue of the protein (except for proline) as well as additional peaks due to the amides present in the peptide side chain. Chemical shifts produced by the binding with the ligand permit to map the binding site of the ligand on the protein. $A\beta_{40}$ monomers were titrated with both ligands (from 50 to 1000 μM) and residue-specific chemical shift changes (ΔCCS) and residue-specific intensity changes in HSQC spectra were plotted (see figures 64a -b and 65a-b, for Sil A-p-TH and Sil B-p-TH binding affinities, respectively). The presence of both Sil A-p-TH and Sil B-p-TH produced shift and intensity changes in a dose-dependent way, indicating a significant affinity of the compounds to the monomers. A linear correlation between average ΔCCS and intensity changes was observed in both cases.

The largest shift change was observed in residue R5, followed by Q15 and N27 in presence of both Sil A-p-TH and Sil B-p-TH; this last one also prompted a big shift in residue A28 with was not present for Sil A-p-TH. Arginine is an amino acid with a positive charge, and as hypothesized in the study of hIAPP/silybins interactions (see chapter 3.4.2), binding with the monomer could be directed by electrostatic interactions of residue R5 with the deprotonated hydroxyl group in position 5. Furthermore, this scenario is supported by previous studies of binding epitopes of Sil A-p-TH and Sil B-p-TH to oAβ (see figures 62-b and 62-d) where we observed ring A as the most strongly interacting group of both ligands, which is the group which contains the 5-OH moiety. By averaging the changes in the chemical shift of each one of the peptide regions (i.e. N-terminal, CHC, and C-terminal; black horizontal lines in figures 64-a and 65-a), it was observed that the biggest chemical shift changes correspond with the N-terminus, followed by the CHC and the C-terminus. Both CHC and N-terminus have been recently identified as toxic surface regions[296] of Aβ; the chemical shifts observed in residues which belong to these regions pointed to their involvement in the interaction with silybins and, thus, the antiaggregant effect of both silybins could be ascribable to these specific interactions. Furthermore, these changes were more evident in the presence of Sil B-p-TH, in accordance with the higher antiaggregant activity of this diastereoisomer.

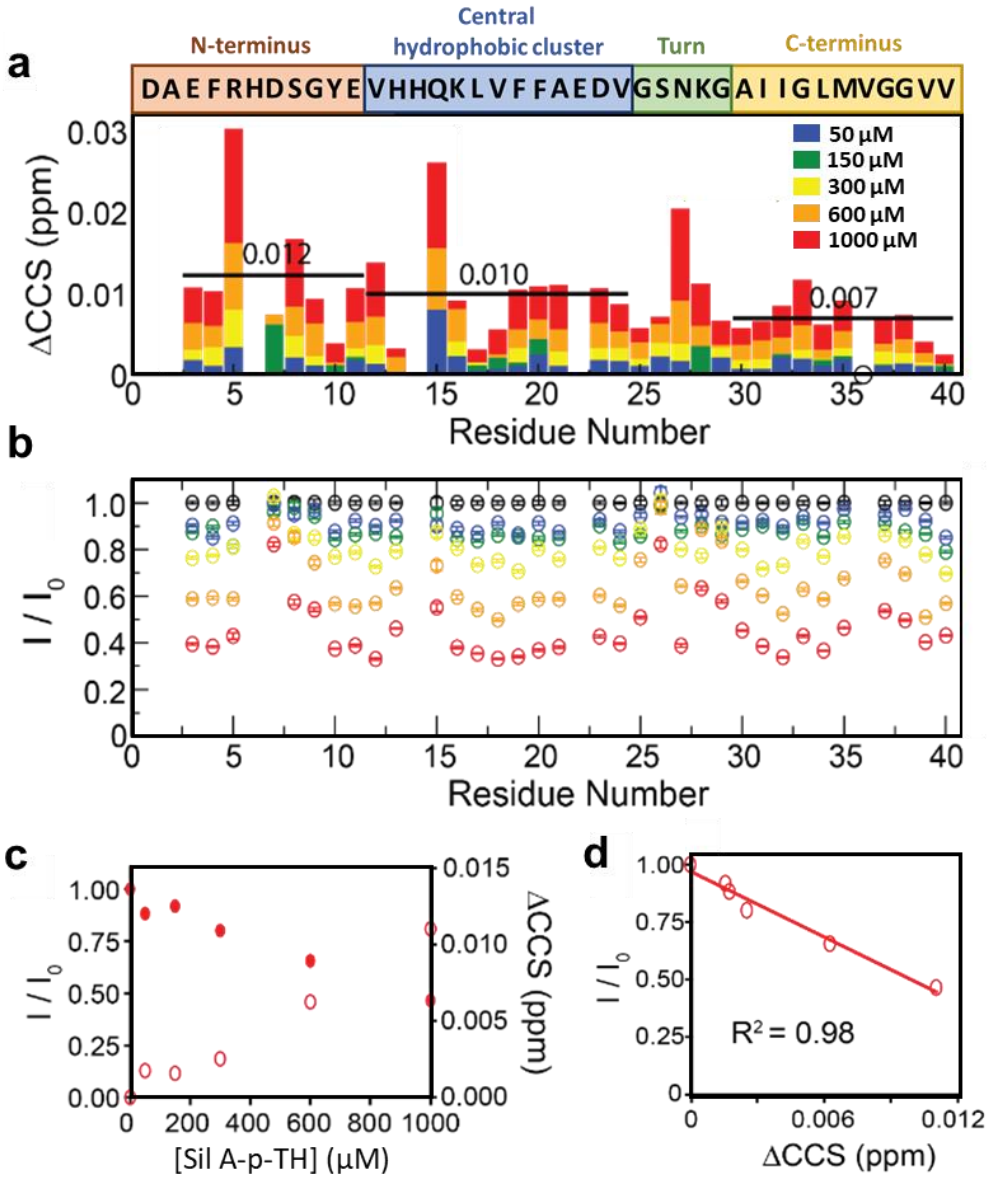

Figure 64 – ^{1}H-^{15}N HSQC chemical shifts and intensity changes on $A\beta_{40}$ monomer induced by Sil A-p-TH. (a) $A\beta_{40}$ monomer residue-specific ^{1}H and ^{15}N combined chemical shift changes (ΔCCS) induced by Sil A-p-TH at increasing concentrations (50 µM (blue), 150 µM (green), 300 µM (yellow), 600 µM (orange), and 1000 µM (red)). N-terminal, CHC, and C-terminal regions are indicated over the chart and average ΔCCS of each region are specified with a black line. The peak corresponding to residue 36 could not be resolved due to resonance overlap and is indicated with a hollow black circle. **(b)** $A\beta_{40}$ monomer residue-specific intensity changes induced by Sil A-p-TH at increasing concentrations; the color code has been maintained from (a). Data are normalized to the intensity in absence of ligand (I_0). **(c)** Average combined chemical shift (*hollow red circles*) and intensity (*solid red circles*) changes of $A\beta_{40}$ monomers with respect to the added Sil A-p-TH concentration. **(d)** Correlation between average ΔCCS and intensity changes.

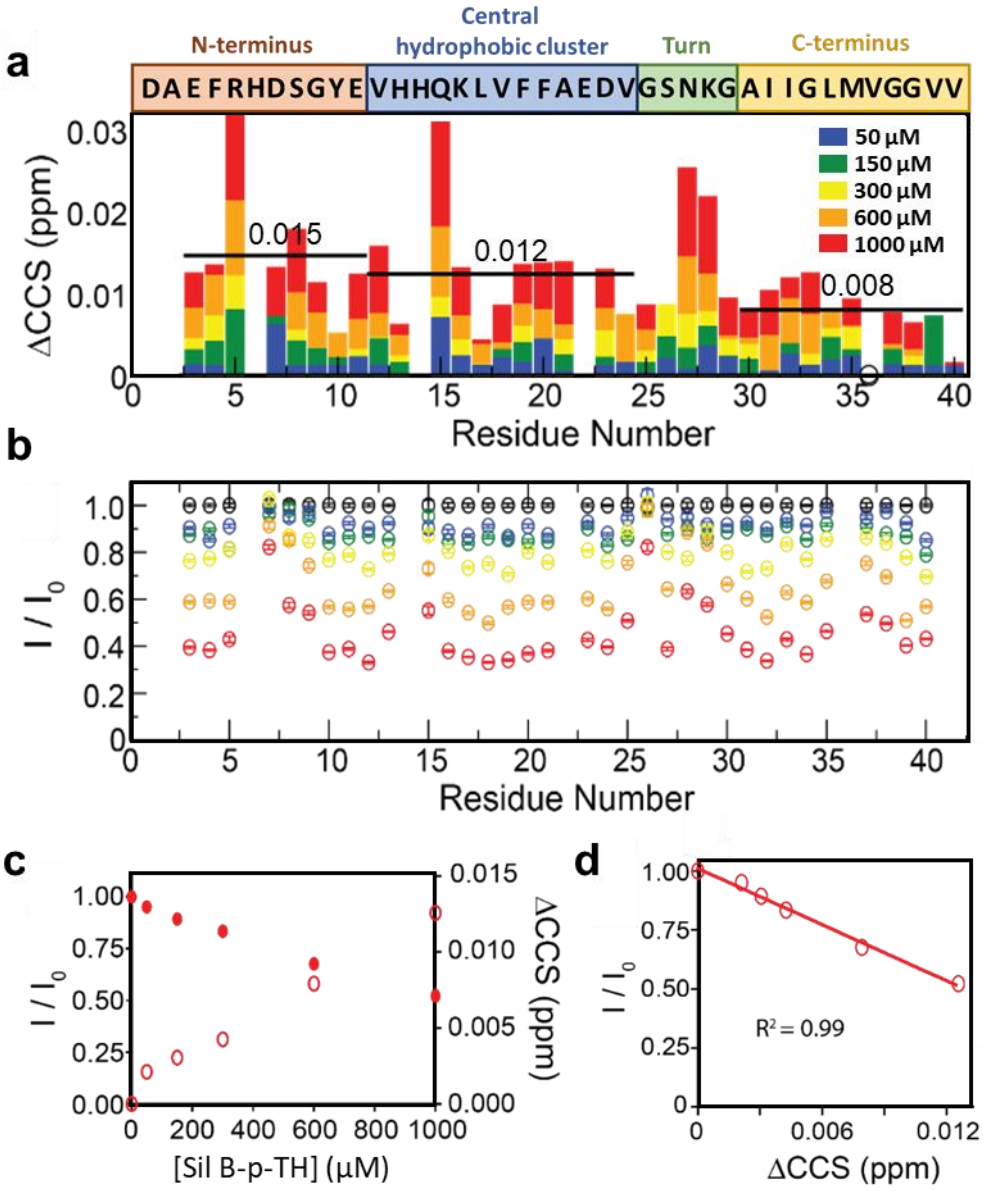

Figure 65 – ^{1}H-^{15}N HSQC chemical shifts and intensity changes on $A\beta_{40}$ monomer induced by Sil B-p-TH. (a) $A\beta_{40}$ monomer residue-specific ^{1}H and ^{15}N combined chemical shift changes (ΔCCS) induced by Sil B-p-TH at increasing concentrations (50 µM (blue), 150 µM (green), 300 µM (yellow), 600 µM (orange), and 1000 µM (red)). N-terminal, CHC, and C-terminal regions are indicated over the chart and average ΔCCS of each region are specified with a black line. The peak corresponding to residue 36 could not be resolved due to resonance overlap and is indicated with a hollow black circle. **(b)** $A\beta_{40}$ monomer residue-specific intensity changes induced by Sil A-p-TH at increasing concentrations; the color code has been maintained from (a). Data are normalized to the intensity in absence of ligand (I_0). **(c)** Average combined chemical shift (*hollow red circles*) and intensity (*solid red circles*) changes of $A\beta_{40}$ monomers with respect to the added Sil B-p-TH concentration. **(d)** Correlation between average ΔCCS and intensity changes.

3.4.2. Investigation of hIAPP and Sil A/B interaction by Molecular Dynamics

Due to the low water solubility of Sil A and Sil B, it is not possible to analyze ligand-peptide complexes by conventional experimental techniques such as NMR because of the high ligand concentrations required for each experiment. Therefore, to gain molecular details about the mechanism of interaction between hIAPP and silybins, molecular dynamic simulations were carried out during a 3-months research stage in the laboratories headed by prof. A. Caflisch (University of Zurich, Switzerland). Molecular dynamics (MD) simulations are widely used to simulate the behavior of several biological processes, e.g. protein folding or ligand binding, at an atomistic detail. The theoretical approach is based on the use of the classical Newton's equation of motion to simulate the dynamics of a group of atoms over time.

First, the 3D structures of Sil A and Sil B were obtained from pdb files also considering their protonation states in position C(5) at neutral pH. Next, preliminary explicit solvent MD simulations were carried out for both ligands at different protonation states evidencing that the protonated molecules sampled very similar states to the monodeprotonated molecules in position 5-OH (see supplementary figures S2 and S3). Based on these observations and combined with experimental evidence, which indicates the prevalence of the monodeprotonated species at pH 7.4,[234] we decided to use these in the production simulations. Thus, henceforth, mentions of silybins will refer only to the monodeprotonated compounds.

Due to the lack of a reported PDB structure of hIAPP in the studied conditions (it is only registered stabilized by an SDS environment or in its fibrillary state), seven independent amylin structures were randomly generated from the human peptide sequence (including the C_2-C_7 disulfide bridge which is essential for the biological function of the peptide) and used as starting structures. The system was prepared as reported in the experimental section and MDs were produced by each one of the hIAPP structures. From a total cumulated sampling of about 6000 ns of simulation, we extracted 5 representative snapshots of hIAPP visited along multiple trajectories, that were posteriorly used as protein starting structures in hIAPP/silybins MDs.

To identify these representative snapshots, we used the SAPPHIRE (States And Pathways Projected with High REsolution) analysis. This computational method allows ordering all the sampled states of an intricate system, assigning their statistical weight and the recurrence with which are visited along one or multiple trajectories.[297] Basically, in SAPPHIRE analysis a geometric parameter is given as input and, according to the similarities that each one of the sampled states present in regard to this parameter, all the snapshots are ordered and defined by a progress index. The construction of the called "cut function" by counting the transitions along the entire simulation which present similarities according to the input, permits the partition of the entire sampling into a set of free energy basins which group the similar snapshots. Thus, the local minima of the cut function correspond with the highly populated states while the local maxima are barriers, i.e. conformational stated visited sporadically. Furthermore, several geometric variables (e.g. the secondary structure assignment per residue) can be added to facilitate the visual characterization of the states.

In the present case, we defined the metric input for the analysis as the RMSD of the ψ-angles of the residues at the core of the peptide, i.e. T9-S28 excluding residues H18, S19, S20, N21, N22, F23, and G24. The rest of the residues (H18- G24, K1-A8, and S29-V37) were not considered because of their scarce structuration and thus their lack of discriminatory contribution to the analysis. The statistical weight of the different metastable states of hIAPP was identified thanks to the cut function in the SAPPHIRE analysis (black line in figure 66). From all the identified basins, only a few of them, that were visited with recurrence in several of the individual simulations (recurrence is indicated with red dots in the central part of figure 66), were selected as starting configurations for the subsequent amylin-silybin MDs. They are indicated with green stars in figure 66 and their configuration is represented in figure 67.

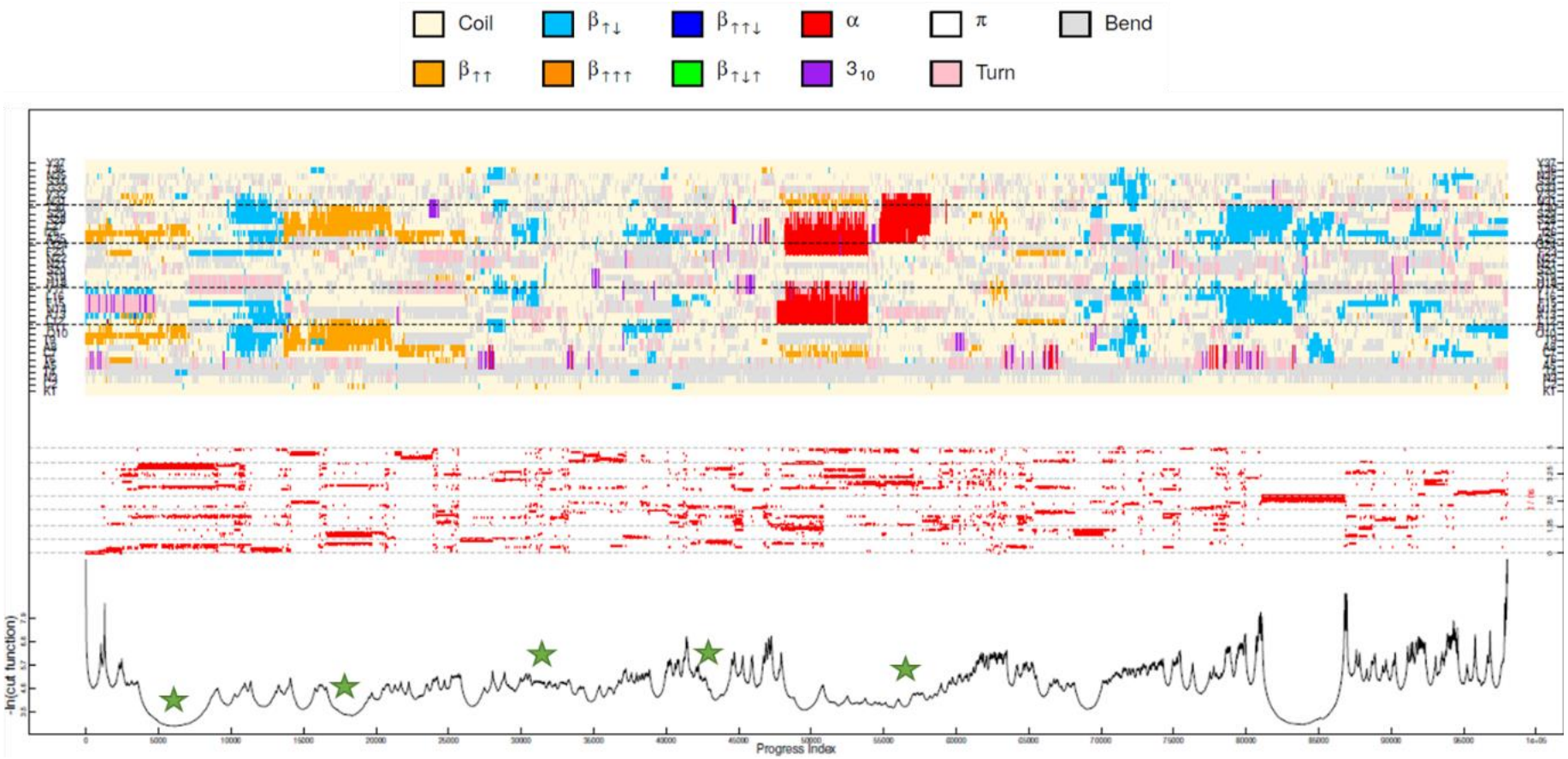

Figure 66 – SAPPHIRE analysis plot of hIAPP simulation. The cut function (black line) throughout the progress index is accompanied by the dynamic trace (red dots) which allows the identification of the recurrence of each conformation through the time-scale and in each one of the individual runs (delimited by the horizontal gray dashed lines). The secondary structure assignment (DSSP) per residue along the sequence (upper part of the plot; legend in the top) is included to facilitate the identification of the states. Green stars indicate the selected representative states used as starting configurations for the subsequent amylin-silybin MDs

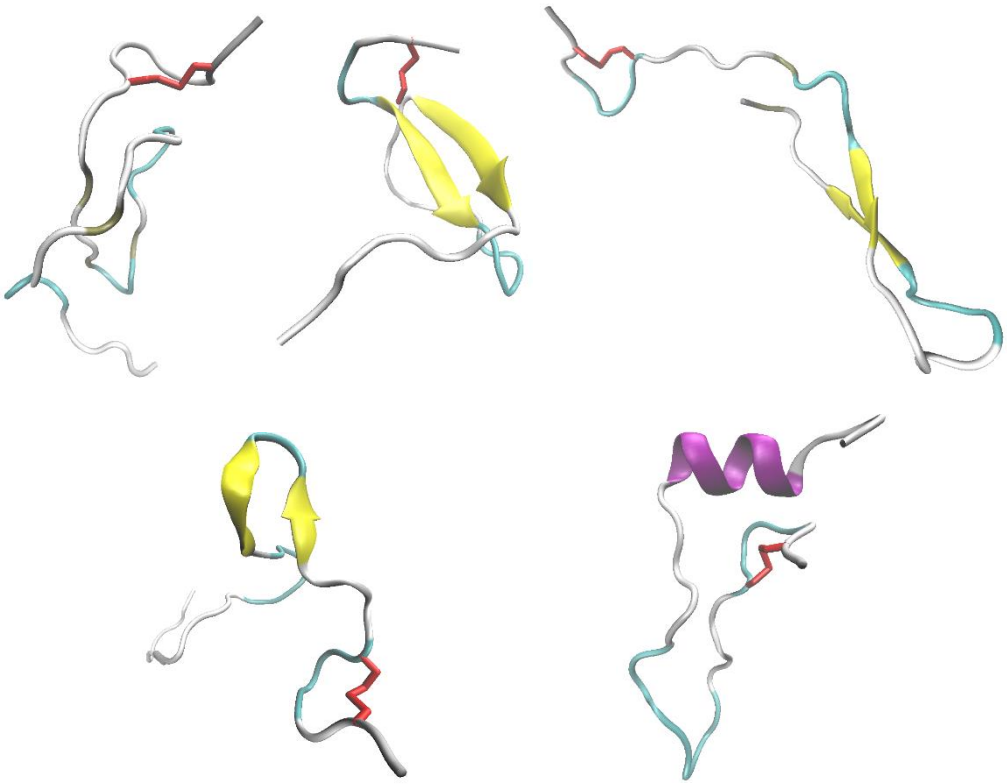

Figure 67 – Snapshots of the representative structures of hIAPP selected from the SAPPHIRE analysis. The structures have been selected from the SAPPHIRE analysis (green starts in figure 66). The red stick symbolizes the C_2-C_7 disulfide bridge.

These five selected amylin conformations, together with the previously generated Sil A and Sil B structures, were used to generate the structure and topology of hIAPP-Sil A and hIAPP-Sil B complexes at the peptide/ligand ratios 1:1 and 1:2. The systems were prepared as reported in the materials and methods section. Ten different MD simulations (2 for each one of the selected hIAPP structures) were produced for each one of the studied systems, obtaining a total simulating time of around 6-7 μs in each case (secondary structure assignments – DSSP – to the amino acids of the protein throughout the concatenated simulations are reported in supplementary figures S4-S8).

The analysis of the trajectories of the performed simulations indicated differences in the time of interaction along the entire sampling between hIAPP and each one of the silybin diastereoisomers. While Sil A interacted with hIAPP around 35% of the simulated time in both the assessed peptide/ligand ratios (1:1 and 1:2), Sil B showed a dose-dependent effect. The time of interaction of Sil B with hIAPP was around 30% in a 1:1 ratio and was doubled (about 60%) when the 1:2 ratio was simulated. This behavior was also observed in the average number of hIAPP-silybin interactions per frame: both

Sil A and Sil B presented, on average, 3.5 interaction per frame in simulations performed in a 1:1 peptide/ligand ratio; when the ratio was increased to 1:2, this value showed a slight increase (average of 3.7 interactions per frame) for Sil A, while, for Sil B, the increase was substantial (average of 10 interactions per frame) (see figure 68). This behavior could explain the higher antiaggregant activity of Sil B than Sil A previously observed by ThT assays (see figure 54).

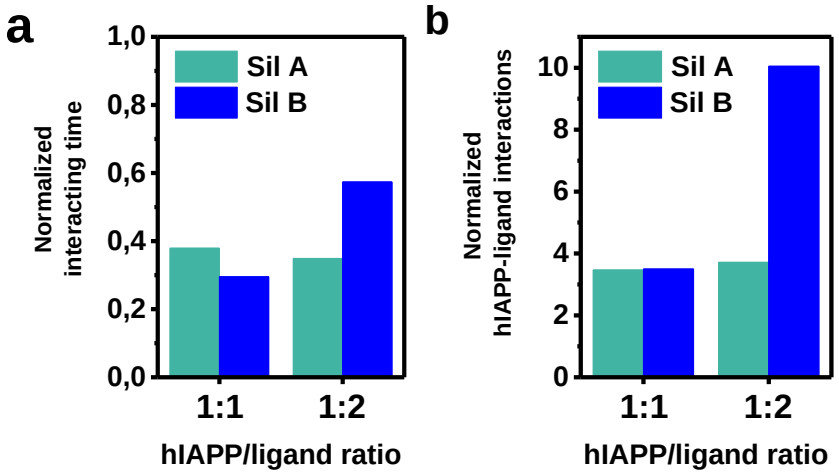

Figure 68. (a) Normalized interacting time between hIAPP and Sil A (turquoise bars) and Sil B (blue bars) in a peptide/ligand ratio 1:1 and 1:2. Interacting time has been calculated considering the frames where one or more atoms from the protein are near any atom of the ligand, considering a threshold distance of 5 Å, and normalizing to the total number of frames. **(b)** Average number of hIAPP-silybin interactions per frame for systems containing Sil A (turquoise bars) and Sil B (blue bars)in a peptide/ligand ratio 1:1 and 1:2. Data have been calculated by considering any pair of atoms from hIAPP and the ligand with a minimum distance below a threshold of 5 Å during the entire sampled time and normalizing by the total number of frames.

As evidenced in the hIAPP contact maps reported in figure 69, silybins produced significant changes in the pattern of hIAPP inter-peptide interactions. On one hand, in all the studied systems in the presence of silybins, interactions between the stretches T9-A13 and N14-S19 from the N-terminal region (N-term) were increased if compared with the simulations of hIAPP lacking ligands. On the other hand, a remodeling of the inter-peptide interactions between the amyloidogenic core (AC) and the N-term was observed. In particular, interactions between stretches I26-V32 (A.C and N-term) and F15-S20 (N-term) were increased in all systems containing silybin. Furthermore, the

interactions between the stretches N21-L27 (A.C.) and T6-Q10 (N-term) increased, at the expense of a decrease in the interactions between this same AC stretch and the T6-Q10 from the N-terminal region.

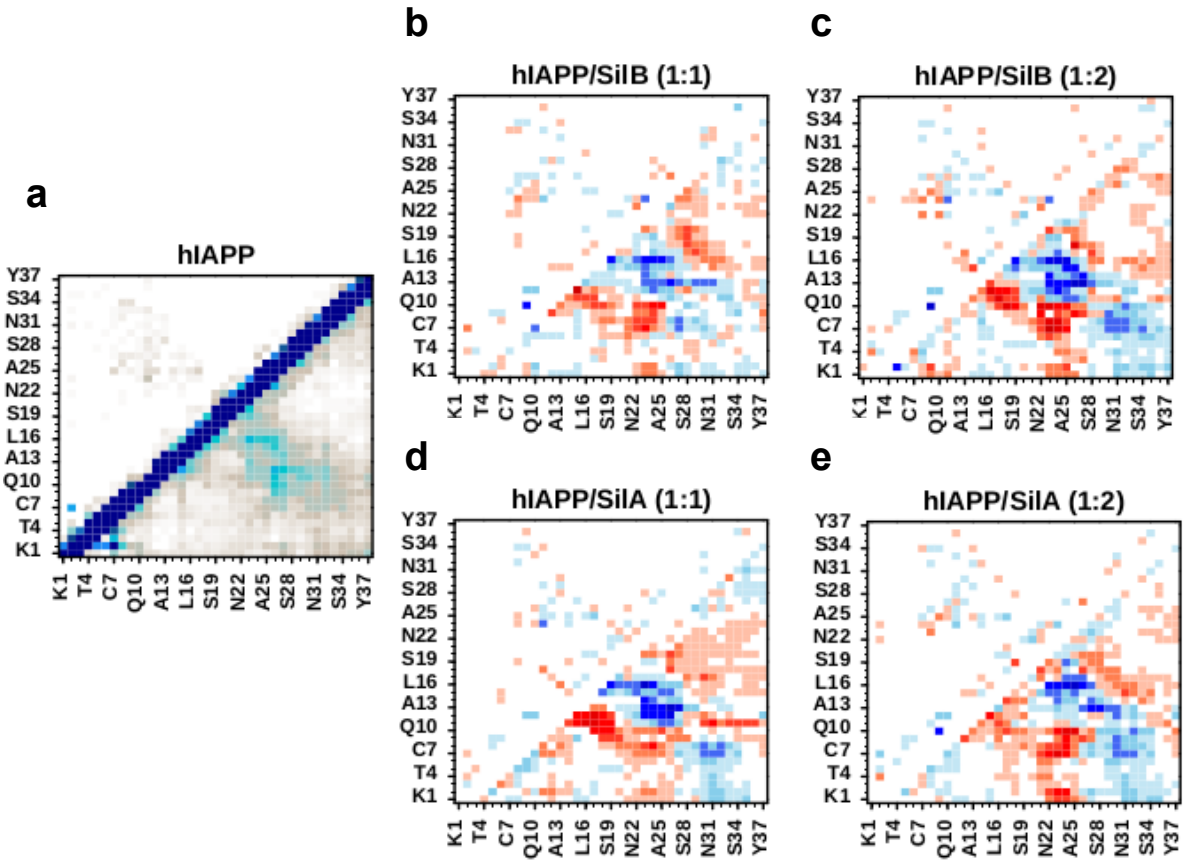

Figure 69 – Contact maps. (a) Probability of contact between all possible residues pairs of hIAPP in absence of ligand. Data has been obtained considering the minimum distance between all the residues during all the simulation and using a threshold distance of 5 Å. The upper-left portion of the plot considers the center of mass of the residues in the calculation while the lower-right portion considers the minimum atomic distance. **(b)** Qualitative changes in the probability of contact between all possible residues pairs of hIAPP in presence of Sil A in a peptide/ligand 1:1. Red and blue dots represent an increase or decrease in the probability, respectively. Data have been calculated by subtracting the contact map of hIAPP in presence of the ligand (in the specified condition and calculated as previously reported) and the contact map of the protein alone showed in (a). **(c)** As (b) except for a protein/ligand ratio 1:2. **(d)** As (b) except for Sil B. **(e)** As (c) except for Sil A.

The radius of gyration (Rg) of freely joined chains and the asphericity (δ) are parameters widely used in the characterization of proteins shape and packing. The first one is directly related to the compactness of the peptide while the second one is an indication of the asymmetry in its shape. The presence of Sil A and or Sil B in 1:1

peptide/ligand ratio induced a narrower probability distribution of the Rg of hIAPP. This effect was more evident in the presence of Sil B at a peptide/ligand ratio 1:2, differently from Sil A which induced a distribution insensitive to the molar ratio (see figures 70-a and -b). A shift in the asphericity distribution to higher values was observed in simulations containing silybins, indicating the predominance of more extended protein states when the protein interact with the ligands (see figures 70-c and -d).

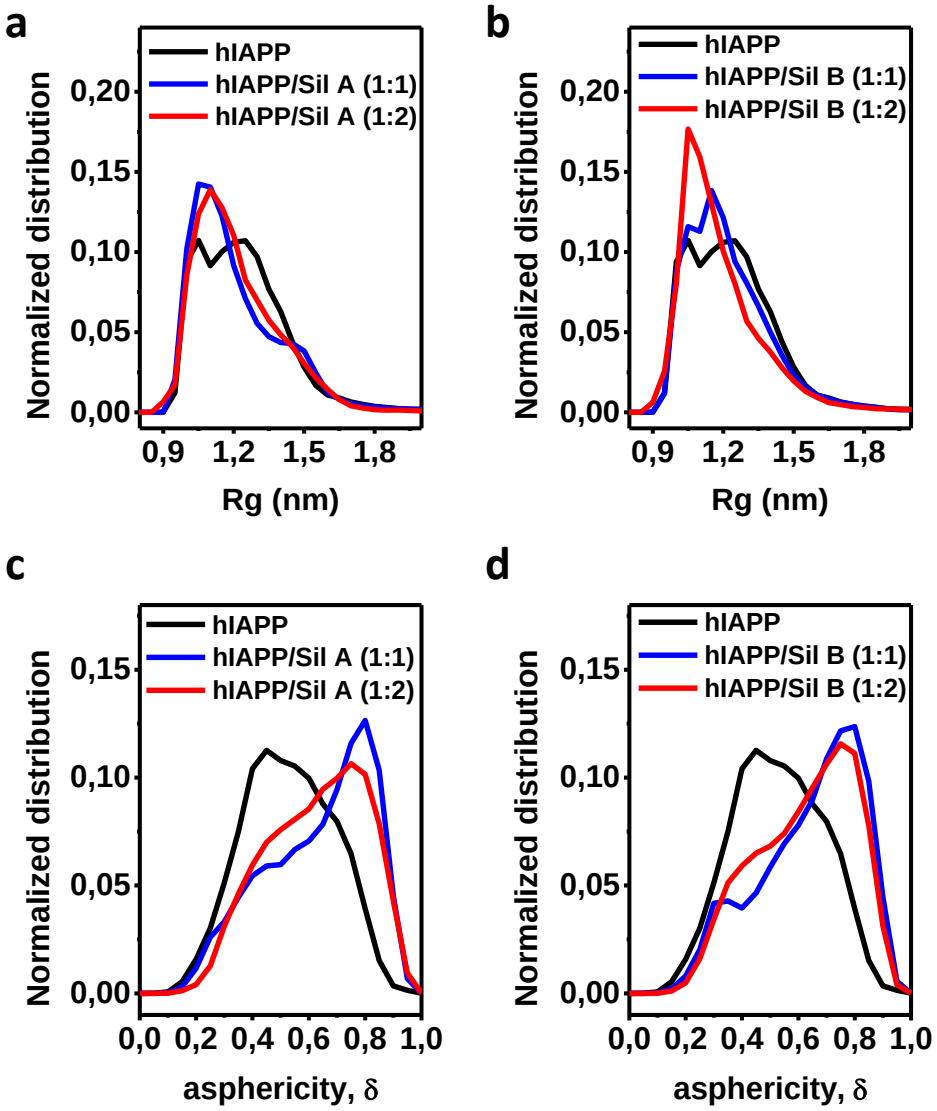

Figure 70. **(a)** Probability distribution of the radius of gyration (Rg) of freely joined chains of hIAPP (black line), in the presence of SilA in peptide/ligand ratio 1:1 (blue line) and 1:2 (red line). **(b)** As (a) except for Sil B. **(c)** Probability distribution of asphericity (δ) of hIAPP in the presence of Sil A in peptide/ligand ratio 1:1 (blue lines) and 1:2 (red line). **(d)** As (a) except for Sil B.

The presence of silybins produced modifications in the fluctuations over the peptide conformations. Both Sil A and B induced a decrease of the root-mean-square-fluctuation (RMSF) along the α-C of the amylin stretch I26-G33 that could be ascribable to the aforementioned increase in inter-peptide interactions involving residues F15-S20. Conversely, the fluctuation along the α-C of stretches K1-C7, R11-A25, and S34-Y37 increased in simulations including silybins (see figure 71).

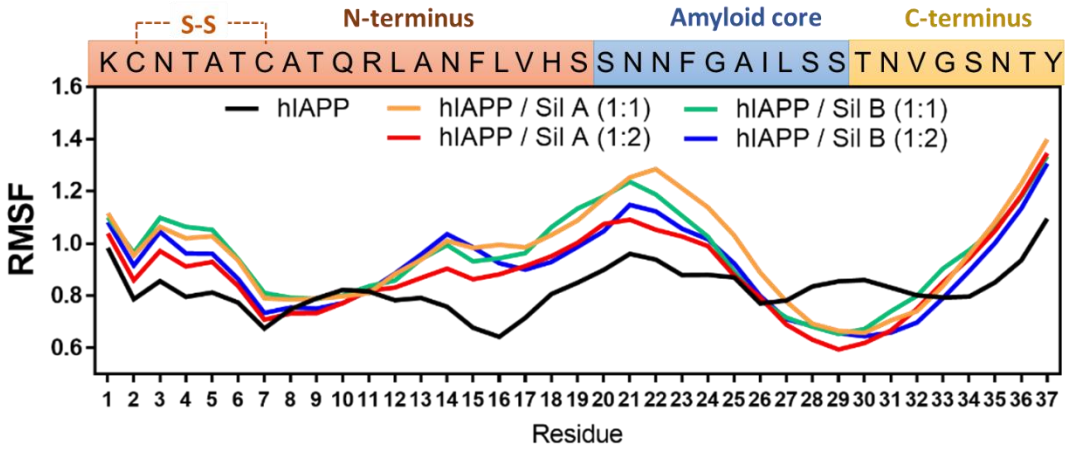

Figure 71 – Root-mean-square fluctuation (RMSF). RMSF calculated along the α-C of hIAPP in the absence (black) and presence of Sil A in a peptide ligand ratio 1:1 (orange) and 1:2 (red), and of Sil B in a peptide ligand ratio 1:1 (green) and 1:2 (blue).

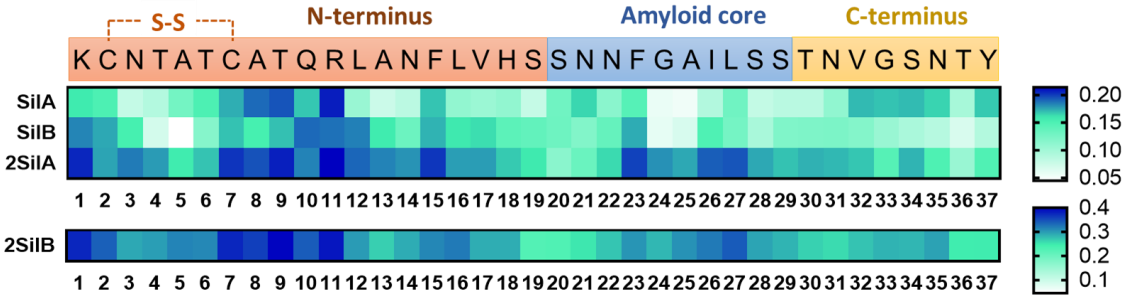

Figure 72 – Binding sites of silybins on hIAPP monomers. Intensity mapping of binding sites of Sil A and Sil B on hIAPP in simulations performed at peptide/ligand ratios 1:1 and 1:2. Interactions have been calculated considering the minimum distance between any pair of atoms from each residue and the ligand, applying a threshold distance of 5 Å and normalizing to the total number of frames in each system.

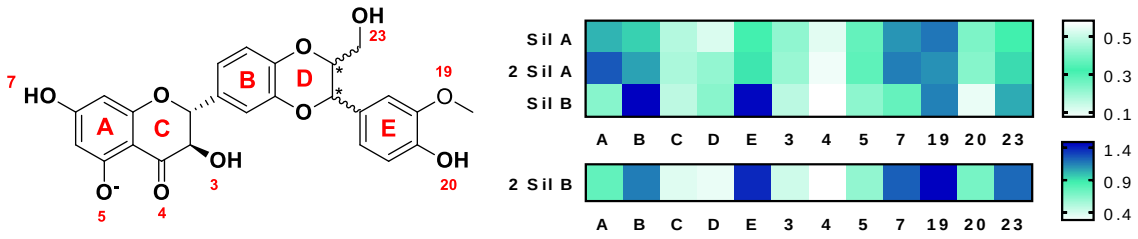

Figure 73 – Silybin binding sites on hIAPP. Sil A and Sil B binding regions on hIAPP monomer in peptide/ligand ratios 1:1 and 1:2. Intensity mapping was obtained considering all the interactions along the entire sampling and normalizing to the total number of frames. Interactions have been calculated considering the minimum distance between any pair of atoms from the protein and each binding region of the ligand (threshold distance of 5 Å). The nomenclature used to design the different silybin binding regions are indicated in the structural representation on the left.

The interactions between hIAPP and Sil A or Sil B were studied by examining the most recurrent contacts between the protein and each one of the ligands in all the studied systems (peptide/ligand ratios 1:1 and 1:2). Highly recurrent interactions between the deprotonated hydroxyl in position C-5 of both silybins and the cationic residues K1 and R11 were observed in all the assessed conditions, indicating the interaction of the peptide with both Sil A and Sil B thought electrostatic forces (see figures 72 and 74).

Due to the well-known key role played by phenolic motifs in inhibiting the aggregation of amyloidogenic peptides,[298–300] the interactions of the peptide with the aromatic rings A, B, and C of each one of the diastereoisomers were carefully evaluated. This analysis evidenced for Sil B a higher recurrence of interactions with the peptide and a larger involvement of rings B and E in these interactions, differently from Sil A which shows predominant interactions with ring A and B (see figure 73). In particular, aromatic ring A of Sil A was involved in interactions with residues F15 and B32. The same peptide regions results also involved, albeit to a lesser extent, to ring B, at both the simulated peptide/ligand ratios (1:1 and 1:2) (see figure 74). When 2 Sil A molecules were simulated, additional recurrent contacts were observed with these two aromatic rings, in particular with residues A8, L16, F23, I26, and A25. Sil B interacted with amylin by means of both rings B and E, involving a higher number of residues, i.e. A8, L12, F15,

L16, F23, I26, L27, and V32. Furthermore, interactions with residues A5, V17, and A25 were also evidenced in MD simulations with 2 molecules of Sil B. The interactions with Sil B by ring E that were not present with Sil A, are ascribable to the different chirality of the stereocenter located in C-11.

Moreover, other remarkable differences between the two diastereoisomers were observed. The hydroxyl and the methoxy groups in positions C-7 and C-19, respectively, evidenced significant interactions with hIAPP for both diastereoisomers (see figure 73). However, interactions with the hydroxyl group in position 23 were significant only for Sil B. Once again, the different chirality of Sil A and Sil B leads to a different geometry of this group, and thus, these interactions were favored only for Sil B.

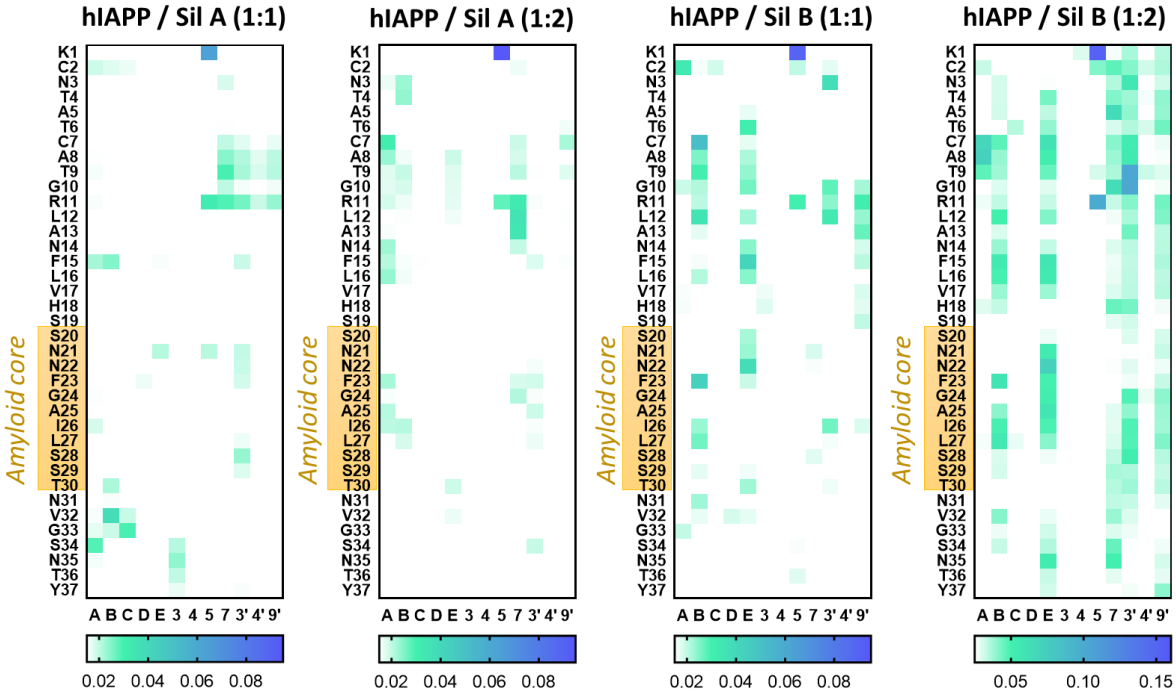

Figure 74 – Distribution of silybin-hIAPP interactions. Sil A and Sil B binding regions on hIAPP vs. hIAPP residues involved in the interactions in peptide/ligand ratios 1:1 and 1:2. Interactions have been obtained considering the minimum distance between any pair of atoms from each residue and each binding region of silybin has been considered (threshold distance of 5 Å).

Due to the importance of the amyloid core in the fibrillation process, the interactions between Sil A and Sil B with this stretch were analyzed in detail. This domain

exhibited more highly recurrent interactions with Sil B. These interactions resulted increased in simulations performed at a peptide/ligand 1:2 ratio. In addition to hydrophobic interactions, H-bonds between Sil B, and the hIAPP stretches N21-G24 (A.C.) and S28-N35 (A.C. and C-term) plays a major role in driving the interactions between Sil B and the peptide (see figure 75). The stronger interactions of Sil B with the hIAPP amyloid reconciles with its higher antiaggregant efficiency observed in ThT assays.

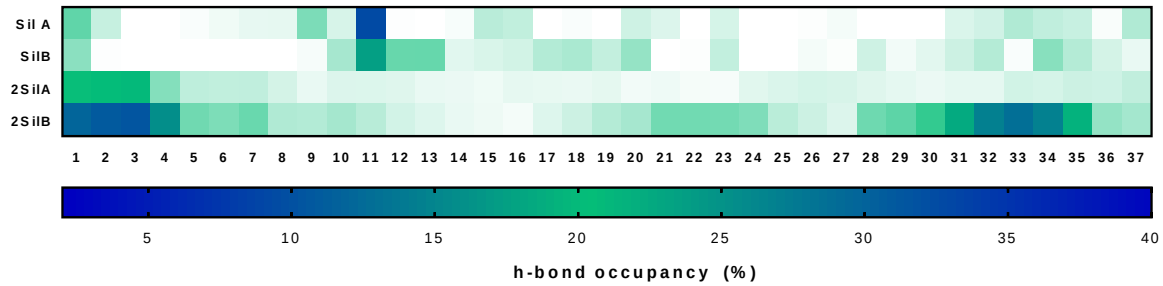

Figure 75 – Hydrogen bonds occupancy between the residues of hIAPP and silybins. H-bond occupancy of hIAPP residues with Sil A or Sil B in a peptide/ligand ratio 1:1 and 1:2. H-bonds have been calculated considering a cut-off distance of 4 Å and a cut-off angle of 30°.

To assess the conformational changes induced by silybins into every single residue, the difference between the Ramachandran probability distribution of simulations in the presence and absence of each one of the ligands were plotted (see supplementary figures S9-S13). In particular, the most common conformational changes, observed in several residues, were a decrease of β-sheet structure (ϕ ~ -150°; Ψ ~ 150°), an increase in PPII structure (ϕ ~ -60°; Ψ ~ 150°), or changes (increase or decrease) of α_L(ϕ ~ -60°; Ψ ~ -60°) or α_R (ϕ~ 80°; Ψ ~ 0°) structures. Following the same procedure, the differences in the global Ramachandran probability distributions allowed to evaluate the global conformational changes resulted in the peptide due to the presence of Sil A and Sil B (see figure 76). Both ligands, Sil A and Sil B, induced an increase in the probability of PPII and α_L structures and a decrease in the probability of α_R structure. The decrease in α_R structure was more evident for simulations performed at an equimolar ratio than in those performed in the presence of two ligand molecules. Furthermore, the presence of Sil B in a peptide/ligand ratio 1:2 induced an additional decrease of β-sheet structures. Notably, the observed increase in PPII content reconciles

with CD studies. Moreover, the decrease in the content of β-sheet structure in presence of Sil B is in accordance with the higher antiaggregant ability of this diastereoisomer.

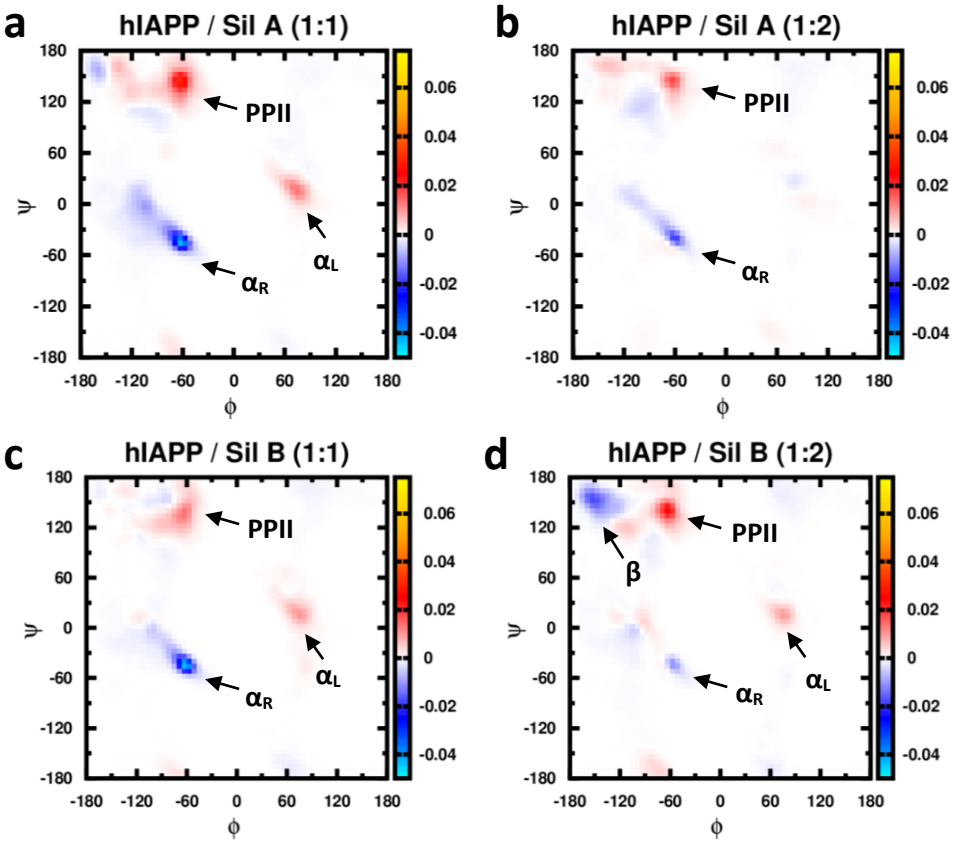

Figure 76 – Changes in the probability distribution of backbone dihedral angles (Ramachandran plots). (a) Changes in the probability distribution of backbone dihedral angles of hIAPP induced by the presence of SilA in a peptide/ligand ratio 1:1. The plot has been obtained by subtracting the Ramachandran probability distribution of hIAPP alone from that one in the presence of Sil A in the specified conditions. Red and blue regions in the plot correspond with positive and negative values, respectively, and thus, with an increase or decrease in the probability of these dihedral angles. **(b)** As (a) except for 1:2 ratio. **(c)** As (a) except for Sil B. **(d)** As (b) except for Sil B.

Chapter 4. Conclusions

The lack of effective treatments for AD and T2DM is to a large extent due to their multifactorial nature and highly complex pathogenic mechanisms. Accordingly, the failure in clinical trials of all the drugs designed so far for their treatment is clear evidence of the limitation of the classical one-drug - one-target approach in this field. Therefore, given the interconnections between these two maladies which share common pathogenic mechanisms, we propose here a new, multi-target strategy against both diseases, to profile small molecules for their potential to be used as Aβ/hIAPP proteostasis rescuers for the treatment of AD and T2DM.

To accomplish this ambitious goal, we have investigated the cytoprotective effect of two natural compounds (Silybin A and Silybin B) extracted from the plant *Silybum marianum* and described how they may i) inhibit Aβ/hIAPP aggregation in aqueous solution or in the presence of model membranes; ii) counteract amyloid-mediated membrane disruption, iii) enhance 20S proteasome activity, iv) foster ubiquitin signaling and v) protect from oxidative stress (see figure 77). The elucidation of the molecular mechanisms by which silybins exert their action against the mentioned targets was carried out by using several techniques. We next evidenced the important role of the stereochemistry in these processes and designed and synthesized silybin derivatives able to overcome the limitations in the use of these compounds, i.e. their low water solubility and bioavailability. The conjugation of silybins to a trehalose moiety through a phosphodiester linker, following a pro-drug approach, notably increases solubility and bioavailability. This approach allows the administration of higher amounts of pro-drug, which in turn, will progressively release, in a time-scale of days, the less bioavailable but active silybin. In addition, the synthesized pro-drugs are not devoided of activity but, rather, partially maintain or, in some cases, even increase the ability of silybins against the studied targets. The activity of the pro-drugs represents an

additional advantage, addressing not only the solubility related problem and permitting the delivery of the drug, but furthermore, being a part of the whole drug system where both drug and pro-drug present desirable activities in restoring proteostasis. In fact, the ability to halt and rescue the cytotoxicity of Aβ oligomers by both silybins and silybins derivatives has been validated in a neuron-like cell system. Finally, high-resolution analysis of peptide/ligand complexes allowed us to fully uncover to an unprecedented level of accuracy the molecular reasons that entail the cytoprotective effect of silybins against the proteotoxic stress induced by Aβ and IAPP, and which makes Sil B more effective than Sil A.

We hope that our multi-target strategy to rescue both Aβ and hIAPP proteostasis could pave the way to future studies aimed at treating these important pathologies, also including other targets with the objective of totally counteract the proteostasis imbalance responsible of the progress of both AD and T2DM.

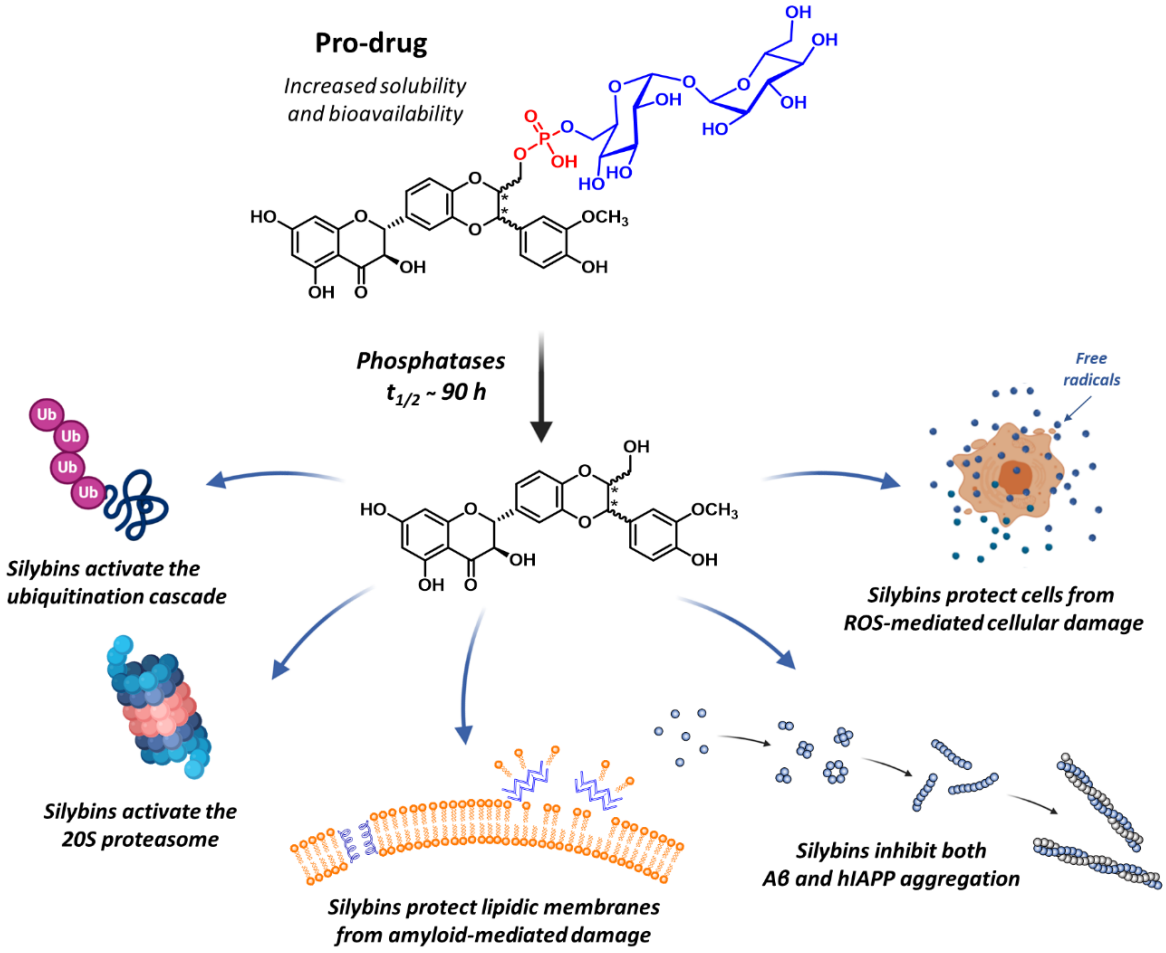

Figure 77. Release of silybins following the pro-drug approach and silybins' targets that entail their cytoprotective effect.

Chapter 5. Materials and methods

5.1. Chemicals

Silibinin was purchased from Sigma-Aldrich. $A\beta_{40}$ and hIAPP were purchased from GenScript. $A\beta_{42}$ was purchased from Bachem. Unlabeled $A\beta_{40}$ and uniformly labeled ^{15}N-Aβ40 used in NMR experiments were purchased from EZBiolab and rPeptide, respectively. 1-Palmitolyl-2-oleoyl-sn-glycero-3-phosphatidylcholine (POPC), 1-palmitoyl-2-oleoyl-sn-glycero-3-phospho-L-serine (POPS), and total lipid brain extract (TLBE) were purchased from Avanti Polar Lipids. Hexafluoro-isopropanol (HFIP) and HPLC-grade acetonitrile (ACN) were obtained from Carlo Erba. Purified human 20S proteasome and the fluorogenic substrates Suc-Leu-Leu-Val-Tyr-AMC, Z-Leu-Leu-Glu-AMC, and Ac-Arg-Leu-Arg-AMC, used to assay the ChT-L, T-L, and C-L activities, were obtained from Boston Biochem. Purified yeast 20S and α3ΔN yeast 20S mutant were a generous gift of Prof. Michael Groll (Technical University of Munich). Trolox was purchased from Acros Organic. 2,2'-azinobis(3-ethylbenzothiazoline-6-sulfonic acid) (ABTS) was obtained from Aeser. Thioflavin T (ThT), ammonium molybdate heptahydrate, sodium pyrophosphate, CH_3OH, dithiothreitol (DTT), sodium dodecylsulphate (SDS), Tris buffer, ATP, ascorbic acid, NaOH and $MgCl_2$, and all-trans-retinoic acid (RA) were purchased from Sigma-Aldrich. Ub from bovine red cells was obtained from Sigma Aldrich and purified by extensive dialysis against pure water for 24 h at 48 °C. Ub concentration in pure water was routinely measured by UV (ε 280 = 1280 M^{-1} cm^{-1}). Human recombinant Ub activating enzyme (UBA1), and human recombinant Ub conjugating enzyme UbcH1 were purchased from Boston Biochem. DMEM-F12 fetal calf serum, penicillin and streptomycin were purchased from Gibco, Thermofisher. TAAB EM Stain 336 was obtained from Taab Laboratories Equipment . All water solutions were prepared with ultrapure Milli Q water.

5.2. Synthesis of Sil A-TH and Sil B-TH

Using a selective and orthogonal approach,[301] we started from Sil A (or B), previously obtained by RP-HPLC separation from silibinin,[302] and the α,α-trehalose. We initially converted Sil A (or B) into 9''-ODMT ether with DMT-chloride (DMTCl) in pyridine, and after exhaustive acetylation with excess isobutyryl anhydride, successive treatment with 5% formic acid in CH_2Cl_2 allowed the removal of the DMT protecting group and to led **2a** (or **2b**) in 63% yield (67% for **2b**). Intermediate **2a** (or **2b**) was reacted with 2-cyanoethyl-N,N-diisopropylamino-chlorophosphoramidite and DIEA in anhydrous CH_2Cl_2. After purification, the identity of compounds **3a** (61%) and **3b** (65%) were confirmed by NMR (^1H, ^{13}C, and ^{31}P) and ESI-MS data.

The same approach was used to synthesize hepta-O-acetyl-trehalose (**4**). We converted α,α-trehalose into 6-ODMT-ethers and then fully acetylated by treatment with excess acetyl anhydride in pyridine. Treatment with 5% formic acid in CH_2Cl_2 allowed the removal of the DMT protecting group leading to 2,3,4,6,2',3',4'-hepta-O-acetyl-α,α-trehalose in good yields (60%).[303]

Trehalose derivative **4** was coupled with silibinin phosphoramidite **3a** (or **3b**) using 0.45 M 4,5-dicyanoimidazole (DCI) to 1h. After treatment with 5.5 M tert-butyl hydroperoxide (TBHP) solution in decane (30 min), the crude material was purified by flash chromatography and then treated with conc. aq. ammonia and CH_3OH (1:1, v:v) at 50 °C, which allowed full cleavage of the acyl and cyanoethyl (CE) protecting groups. The crude materials were subjected to reverse-phase analysis and purification leading to the desired phosphodiester derivatives **5** and **6**. Both compounds were then converted into the corresponding sodium salts by cation exchange on a DOWEX (Na^+ form) resin to obtain crystalline compounds (43% and 46% yields respectively).

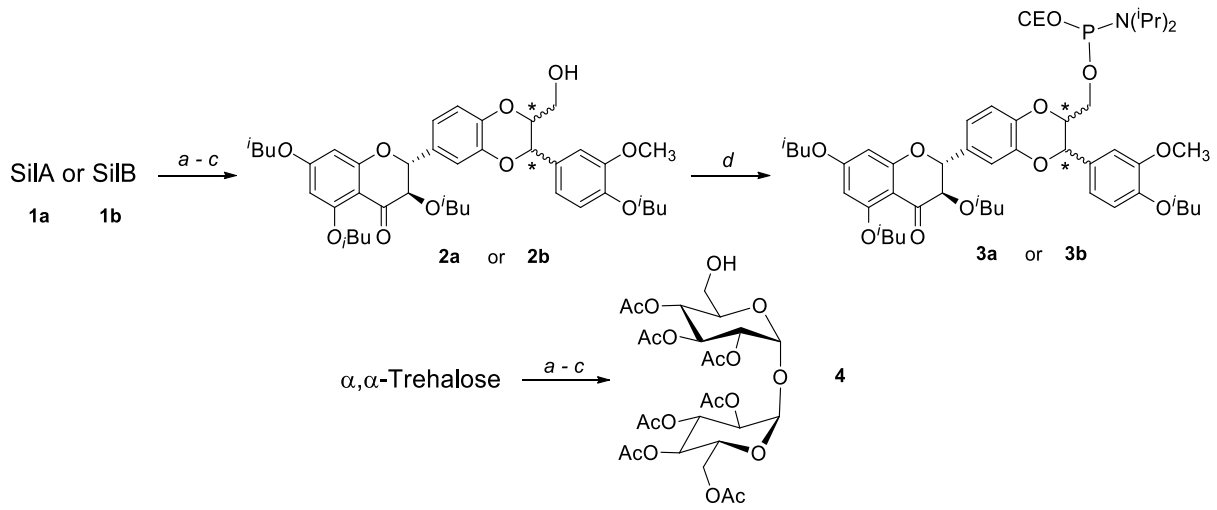

Scheme 1. Synthesis of silibinin phosphoramidites **3a** and **3b** and trehalose derivative 4. Reagents and conditions: (a) DMTCl, pyridine, r.t.;(b) isobutyl anhydride, pyridine; (c) 5% formic acid in CH_2Cl_2; (d) 2-cyanoethyl-N,N-diisopropylamino-chlorophosphoramidite, DIEA, CH_2Cl_2.

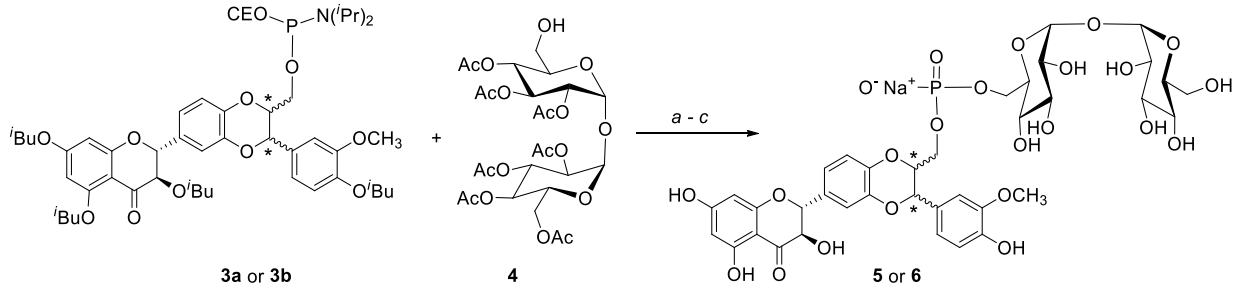

Scheme 2. Synthesis of **5** and **6**. Reagents and conditions: (a) 0.45 M DCI in THF, r.t.; (b) 0.02 M I_2 in THF, r.t.; (c) 28% NH_4OH aq. 50 °C.

5.3. MTT assays

Oligomers preparation. To prepare the $A\beta_{42}$ oligomers, 1 mg of $A\beta_{42}$ (HFIP-treated) was firstly dissolved in 5 mM DMSO. A solution of 10 µM $A\beta_{42}$ in ice-cold DMEM F-12 w/o Phenol Red, was prepared and allowed to oligomerize for 48 h at 4 °C according to the Lambert protocol[87] and our research group previously described method.[304] Cells were treated with a 2 µM final concentration of oligomers.

Cell Culture. The neuroblastoma (NB) cell lines, SH-SY5Y, were cultured in DMEM-F12, supplemented with 10% heat-inactivated (HI) fetal calf serum, 100 mg/mL penicillin and streptomycin, and 2 mM L-glutamine at 37 °C, 5% CO_2. Two weeks before experiments, $5 \cdot 10^3$ cells were plated on 96 multi-well plates in DMEM-F12 with 5% HI

fetal calf serum. The percentage of serum was gradually decreased until 1% of total. Five micromolar of all-trans-retinoic acid (RA) was used to promote neuronal differentiation and medium-containing RA was changed every 3 days. Treatments were performed on fully differentiated cells. In order to evaluate the ability of Sil A, Sil B, and their trehalose conjugates to inhibit toxic Aβ oligomerization, samples of $A\beta_{42}$ (10 µM) were incubated in the presence or absence of Sil A, Sil B, Sil A-p-TH, or Sil B-p-TH compounds (Aβ/ligand ratios 1:1, 1:5). The natural compounds' stock solutions were dissolved in DMSO, keeping the final DMSO concentration under 0.4%. After 48 h incubation, Aβ/ligand mixtures were applied to the differentiated SH-SY5Y cells at the final concentration of 2 µM Aβ. After 48 h treatment, MTT assay was performed to assess cell viability.

MTT assay. To assess the effect of Sil A, Sil B, and their trehalose conjugates, cell viability of differentiated SH-SY5Y was assessed by the 3-[4,5-dimethylthioazol-2-yl]-2,5-diphenyl tetrazolium bromide (MTT) assay, after 48nh treatment. Cultures were incubated with MTT (0.5 mg/mL) for 2 h at 37 °C, then lysed with DMSO for 15 min at 37 °C. Formazan production was evaluated in a plate reader (λ = 570 nm).

5.4. Dynamic Light Scattering (DLS)

Samples were prepared in milli Q water with increasing concentrations of Sil A and Sil B (up to 20µM) and Sil A-p-TH or Sil B-p-TH (up to 200 µM) from 1mM stocks solutions (in DMSO or water for silybins and trehalose-conjugates, respectively). Stock solutions were previously filtered with a cellulose or PTFE filter (for water or DMSO solutions, respectively; pore size 0.2 µm). DLS measurements were carried out with a Zetasizer Nano ZS (Malvern Instruments, UK) equipped for backscattering at 173 with a 633 nm He–Ne laser. Each DLS measurement was run using automated, optimal measurement times, and laser attenuation settings. A measurement of 10 runs was carried out for each concentration. The recorded correlation functions were converted into size distributions by using Dispersion Technology Software (DTS).

5.5. Stability in human serum

An appropriate amount of compound was dissolved in one volume (e.g., 100 µL) of Tris-HCl buffer (50 mM, pH 7.4) at 37 °C. Height volumes (e.g., 800 µL) of preheated

human serum were added, and the solutions were kept in a water bath at 37 °C (initial concentrations were 0.6 - 0.7 mM). At appropriate intervals (t_i, i = 0, 1, 3, 5, 24, 48, 72, 96 hours), 100 µL samples were withdrawn and "deproteinized" adding 450 µL of methanol/tetrahydrofuran (4:0.5 v/v). After mixing and centrifugation, the supernatants were filtered on syringe filters regenerated cellulose membrane (diam. 4 mm, pore size 0.2 µm) and then 100 µL were injected into the HPLC. HPLC analysis was performed with an LC-9A HPLC system (Shimadzu, Milan, Italy) equipped with a Shimadzu SPD-6A detector using an RP8 column (LUNA, Phenomenex, 5µm particle size, C8 (2) 100 Å, 250×4.60 mm i.d.) eluted with ammonium acetate 50mM (pH = 7.4) and ACN, following the gradient: 5% ACN for 5 min, and then 5–100% ACN in 30 min (flow = 1.0 mL/min) and monitored at 288 nm.

5.6. Total antioxidant capacity – TEAC assay

A solution of ABTS 7mM with the oxidant reactant potassium persulfate 2.45 mM was prepared; the solution was incubated at room temperature overnight in darkness to generate the stable radical $ABTS^{\bullet+}$. A definite quantity (to obtain an absorbance of around 0.8 a.u., λ=734 nm) of the freshly radical solution was added to a solution of the studied molecule (from 1µ to 50 µM; final concentration) in 10 mM phosphate buffer pH 7.4. The absorbance at 734 nm was monitored at 1 min, 3 min, and 6 min. The same protocol was used to determine the antioxidant capacity of Trolox; results were reported as Trolox equivalents.

5.7. Poly-ubiquitination assay

Polyubiquitination reactions were carried out in buffer Tris 10 mM, in the presence of our compound (1 µM, 5 µM), ubiquitin 20 µM, ATP 2 mM, $MgCl_2$ 5 mM as a cofactor, DTT 11 µM as a reducing agent, ubiquitin-activation enzyme (UBA1) 100nM and the E2 ubiquitin-conjugating enzyme UbcH1 (750 nM) which can catalyze the formation of K48-linked ubiquitin chains in the absence of E3 ligase. The reactions were analyzed by SDS-PAGE and silver staining. Densitometric analysis of SDS-PAGE was carried out using the software Image J; data were expressed as relative

polyubiquitinated species ($I_{polyubiquitinated\ specie}/I_{ubiquitin}$) and normalized by considering the sum of all the polyubiquitinated species of the control as 100%.

5.8. Molybdopyrophosphate assay

Lys48-linked polyubiquitination reactions were performed in the presence and absence of Sil A, Sil B, Sil A-p-TH, and Sil B-p-TH (1 µM and 5 µM) in 10 µL of ligation buffer (50 mM Tris–HCl, 30 mM $MgCl_2$, 650 µM DTT, and 2.6 mM ATP) containing Ub (80 mM), ubiquitin-activation enzyme (UBA1) 100 nM and the E2 ubiquitin-conjugating enzyme UbcH1 (300 nM) at 37 °C during 1 h. The reaction mixtures were collected in a 96 well plate. In each well, 10 µL of a 400 mM EDTA solution was used to quench all reactions. 20 µL of a freshly prepared ammonium heptamolybdate $(NH_4)_6Mo_7O_{24}$ solution (20 mM, 0.6 M HCl, in H_2O/ACN (60:40)) was added to form the 18-molybdopyrophosphate and, after 10 min, it was reduced by adding 80 µL of a freshly prepared solution of ascorbic acid (500mM, 2M HCl, in H_2O/ACN (60:40)). The pyrophosphate concentration was determined colorimetrically at 790 nm by using a Varioskan plate reader (ThermoFisher, Waltham, MA).[282]

5.9. 20S Proteasome activity assays

Due to the high homology levels between yeast and human 20S (y20S and h20S, respectively) proteasomes[174] and because of the larger availability of y20S in our laboratory, we used it as a screening model and to optimize the experimental conditions. We monitored the ChT-L activity in this preliminary phase because is generally considered the rate-limiting of proteasome activity.[305] However, it has seen that the relevance of each one of the hydrolytic activities of the CP depends on the degraded protein, and, in mammalians, the role of PGPH and T-L activities are not negligible;[172] for this reason, the ability of silybins to modulate the other two activities was also posteriorly tested. The chymotrypsin-like (ChT-L), trypsin-like (T-L), and caspase-like (C-L) peptidase activities of the proteasome were assayed by using 7-amino-4-methylcoumarin (AMC) labeled peptides, i.e., fluorogenic substrates (Suc-LLVY-AMC, Z-LLG-AMC, and Ac-RLR-AMC, respectively). In the experiments, purified human or yeast 20S (1 nM) were used in Tris buffer 50 mM at pH 8.0. Sil A, Sil B (solved in DMSO), Sil A-

p-TH, or Sil B-p-TH (solved in H_2O) were added and incubated 30 min at 37°C in presence of proteasome. Sequentially, the peptide-AMC (100µM) was added. At this moment, the reaction started, and proteasome activity was monitored by measuring AMC fluorescence at 440 nm (λ_{exc}= 360nm) using a fluorescence plate reader (Multiskan, Thermo) in a 384 multiwell black plate. Fluorescent substrate cleavage by the 20S proteasome was linear during this incubation time frame. Each experiment was carried out at least three times, in triplicate. Data are expressed as normalized percentages of residual activity considering the slope of the control (fluorogenic peptide/proteasome in the absence of molecules) as 100% of proteasome activity.

5.10. Monomerization of hIAPP and Aβ

hIAPP or Aβ peptides were solubilized in HFIP (1 mg/mL), aliquoted (100 µL/aliquot), frozen at -80 ºC and lyophilized. Quantification of aliquots was done by solving hIAPP or Aβ aliquots in 20 µL of DMSO or NaOH 1mM, respectively, adding it to 180 µL of buffer (phosphate 10 mM, pH 7.4) and checking the absorbance at 280 nm (ε_{hIAPP} = 1615 $M^{-1}\,cm^{-1}$; $\varepsilon_{A\beta}$ = 1450 $M^{-1}\,cm^{-1}$).

5.11. Amyloid aggregation - ThT assays

Samples were prepared by adding 1 µL of the studied molecule stock solutions (Sil A and Sil B in H_2O, Sil A-p-TH and Sil B-p-TH in DMSO) to 100 µL of ThT 20 µM in PBS (phosphate 10 mM, pH 7.4, 100 mM NaCl) with or without LUVs (POPC:POPS (7:3) 100-200 µM or TLBE 100-200 mg/mL) (see LUVs preparation procedure 5.12). Experiments were carried out in 384-well plates. Immediately after the addition of hIAPP or Aβ (previously monomerized by the above-described protocol; 5 µM, 10 µM, or 20 µM final concentration) time traces were recorded using a Varioskan plate reader (ThermoFisher, Waltham, MA) with λ_{exc} 440 nm and λ_{em} 480 nm at 25 °C or 37 °C.

5.12. Preparation of lipid vesicles

Lipid solution (7:3 POPC/POPS or TLBE) in chloroform was vortexed under warm air flow; the lipid mixture was left at room temperature overnight to achieve the complete evaporation of the solvent. The lipid film was rehydrated with PBS (phosphate

10 mM, NaCl 0.1 M, pH 7.4) to obtain multilamellar vesicles (MLVs) and extruded 23 times with a 100 nm polycarbonate Nucleopore membrane filter (Whatman) mounted on a mini-extruder to obtain large unilamellar vesicles (LUVs) (100 nm, average diameter). The final lipid concentration was measured by the Stewart assay.[306]

5.13. Membrane integrity - Dye leakage assays

To mimic neuronal and pancreatic cells, total lipid brain extract (TLBE) and POPC:POPS (7:3 molar ratio), respectively, were used. Large unilamellar vesicles (LUVs) filled with 6-carboxyfluorescein were prepared and the fluorescence changes in the presence of Aβ or IAPP and our molecules were measured. Dye-filled LUVs were obtained hydrating the lipid film with 6-carboxyfluorescein 80 mM aqueous solution. The formed MLVs were extruded as reported above (see preparation of lipid vesicles - chapter 5.8.). Sephadex G50 size exclusion column was used to eliminate the non-encapsulated dye. The final lipid concentration was measured by the Stewart assay. Samples were prepared by adding 1 µL of the studied molecule solutions to 500 µL of LUVs (POPC:POPS (7:3) 100-200 µM or TLBE 100-200 mg/mL) in buffer (phosphate 10 mM, pH 7.4, NaCl 100 mM). Experiments were carried out in 384-well plates. hIAPP or Aβ (previously monomerized by the above-described protocol) was added (5-20 µM, final concentration) and time traces were recorded using a Varioskan plate reader (ThermoFisher, Waltham, MA) with λ_{exc} 494 nm and λ_{em} 520 nm at 25°C or 37°C.

5.14. Transmission Electronic Microscopy (TEM)

Fresh solutions of $A\beta_{1-40}$ (previously monomerized by the above-described protocol) in milli-Q water (previously filtered with a 0.2 µm filter), were prepared and Sil A-TH or Sil B-TH solutions were added (final concentrations, Aβ 100 µM, ligand 250 µM). The control solution was prepared in the same way by adding water instead of the ligand stock solution. Samples were incubated for 3 days at 37 °C. 3 µL of each solution were deposited in a Holey Ultra-Thin Carbon grid and re-incubated 24 hours in a humidity chamber at 37°C. 3 µL of TAAB EM Stain 336 (Uranyl acetate alternative) diluted 1:16 was added and samples were, again, incubated 1h in the humidity chamber. Grids were washed with milli-Q water removing the excess, carefully, with a filter paper.

TEM analysis was performed with a Jeol JEM 2010 electron microscope placed in the STMicroelectronics plant of Catania, operating at 200 kV accelerating voltage and equipped with an Oxford energy dispersive X-ray spectrometer (EDXS).

5.15. Circular Dichroism (CD)

CD measurements were performed by using a Jasco J-810 spectropolarimeter using quartz cuvettes with an optical path of 1 cm, at 4 °C, from 260 nm to 200 nm. 2.5 μM $A\beta_{40}$ or hIAPP solutions were freshly prepared in 100 mM phosphate buffer pH 7.4, from freshly prepared peptide aliquots monomerized according to the above-mentioned protocol. CD spectra were recovered after adding increasing concentrations of Sil A, Sil B, Sil A-p-TH, or Sil B-p-TH from aqueous 1 mM stock solution. The pH of Sil A and Sil B stock solutions was previously fixed to 10.2 to avoid their aggregation. Reported spectra were obtained by routinely subtracting the ligand spectrum at the same concentration.

5.16. 20S proteasome computational studies

Molecular modeling. Molecular modeling calculations were performed on E4 Server Twin 2 x Dual Xeon 5520, equipped with two nodes. Each node: 2 x Intel Xeon QuadCore E5520, 2,26Ghz, 36 GB RAM.

Conformational analysis of Silybin A and B. The compounds were considered in their anionic form in all calculations performed according to the experimental data published by Bai et Al.[234] The compounds were built using the Small Molecule tool of Discovery Studio 2017 (Dassault Systèmes BIOVIA, San Diego). Then, the compounds were subjected to molecular mechanic (MM) energy minimization (ε = 80*r) until the maximum RMS derivative was less than 0.001 kcal/Å, using the Conjugate Gradient[307] as minimization algorithm. Atomic potentials and charges were assigned using the CFF force field.[308] The conformers obtained for each compound were used as the starting structure for the subsequent conformational analysis (Search Small Molecule Conformations; Discovery Studio 2017). The conformational space of the compounds was sampled using the stochastic conformation search algorithm BEST for the random

generation of a maximum of 300 conformations. Finally, to ensure a wide variance of the input structures to be fully minimized, an energy threshold value of 10^6 kcal/mol was used as selection criteria. The generated structures were then subjected to MM energy minimization until the maximum RMS derivative was less than 0.001 kcal/Å, using Conjugate Gradient as minimization algorithm. Finally, the resulting conformers were ranked by their potential energy values (i.e., ΔE from the energy global minimum (GM)). The conformers within 5 kcal/mol from the GM, were firstly classified into families according to the two conformations of the two bicyclic ring systems. Then, each family was grouped into two subfamilies according to the torsional angle value between the two bicyclic rings that is, having a positive or negative value. The occurrence rates and the range of ΔE_{GM} values of each conformational sub-family were calculated. The energy minimum conformers of each sub-family of Silybin A and B were selected for the definition of the putative starting complexes for the dynamic docking studies.

Modeling of human 20S proteasome in the open conformation. The molecular model of human 20S proteasome in the open conformation was built starting from the experimentally determined structure of human 20S proteasome (PDB ID: 6MSK), which lacks the N-terminal regions (α1: aa1-5; α2: aa1-4; α3: aa1-3; α4: aa1; α5: aa1-7; α6: aa1-3; α7: aa1-5), C-terminal regions (α1: aa245-246; α3: aa252-261; α4: aa241-248; α6: aa242-263; α7: aa246-255; β1: aa192-205; β2: aa221-234; β4: aa200-201; β5: aa202-204; β7: aa216-219), one loop region (α5: aa128-133), and the side chains of several residues (α1: aa45, 46, 55, 59, 63, 146, 181,186-188, 196, 223; α2: aa18, 36, 52-55, 60, 139-141, 143, 163, 176-178, 184, 193, 195, 196, 199, 200, 202, 226, 227, 230, and 233; α3: aa13, 37, 51, 52, 54, 177, 184, 194, 201, 205, 210, 222, 229-231, 250, and 251; α4: aa27, 40, 42, 46-50, 53, 136-138, 141, 157, 163, 166, 169, 170, 174, 181-183, 185, 187, 189, 192, 193, 195-199, 204, 207, 208, 212-213, 216, 218, 223, 225-227, 229, 232-237, 239 and 240; α5: 8, 86, 187, 192, 208, 209, and 231; α6: aa208, 217, 218, 237, 238, and 241; α7: aa110, 144, 204, 206, 208, and 224; β2: aa9, 180, 206, and 214; β3: aa47; β4: aa41, 95, 109, 185, 198, and 199; β5: aa106, 150, and 185; β6: aa45, 161, 166, and 200; β7: aa44, 156, and 195). The sequence of 6MSK was aligned with the sequences of human 20S proteasome downloaded from the UniProtKB/Swiss-Prot Data Bank (http://www.uniprot.org; entry P60900 (α1); P25787 (α2); P25789 (α3); O14818 (α4);

P28066 (α5); P25786 (α6); P25788 (α7); P28072 (β1); Q99436 (β2); P49720 (β3); P49721 (β4); P28074 (β5); P20618 (β6), and P28070 (β7)) by using the Multiple_Alignment algorithm (Homology module, Accelrys, San Diego). Subsequently, the secondary structural prediction of human 20S proteasome was performed using the Structure Prediction and Sequence Analysis server PredictProtein (http://www.predictprotein.org/). The coordinates of the structurally conserved regions (α1: aa6-244; α2: aa5-234; α3: aa4-251; α4: aa2-240; α5: aa8-127, 134-241; α6: aa4-241; α7: aa6-245; β1: aa1-191; β2: aa1-220; β3: aa1-204; β4: aa1-199; β5: aa1-201; β6: aa1-213; β7: aa1-215) were accordingly assigned by the Structurally Conserved Regions (SCRs)-AssignCoords procedure (Homology Module, Insight 2005) using 6MSK as template structure. The lacking loop segment in the α5 subunit (aa128-133) was inserted by using the Generate Loops procedure. With the Generate Loops procedure, a peptide backbone chain is built between two conserved peptide segments using randomly generated values for all the loops' ϕ's and ψ's. The chain was defined starting from the N-terminal end of the loop being built; the Start and Stop Residues were defined as the SCR residues of the model protein at either end of the loop itself. The geometry about the base was described by the four distances between Cα and N-termini of the Start residue and the Cα and C-termini of the Stop Residues. In the process of closing the loop, the values for the generated ϕ's and ψ's are adjusted until the four distance criteria are met. Specifically, a function was defined for the distances in terms of the dihedral angles (Scale Torsions: 60). The differences between the desired distances and their current values were minimized using a linearized Lagrange multiplier method. After a series of 1000 iterations, the loop was closed, except in the case where the distances between the ends of the loop were not respected (Convergence = 0.05). The geometry at the base of the loop is then checked for proper chirality. Finally, the loops were screened on the basis of steric overlap violations. All loops that are found to have unacceptable contacts were rejected. Since successive calculations can correct some bad contacts, a fairly large overlap factor was used (Internal and External overlap = 0.6). A bump check of the 10 generated loops together with the evaluation of their conformational energy were used as selection criteria. The lowest conformational energy loop presenting no steric overlap with the rest of the protein was selected. Finally, the coordinates of the lacking N-terminal and C-terminal amino acids were

assigned using the EndRepair command (Homology Module, Insight 2005). The obtained homology model was completed inserting the missing residue side chains by using the Replace command (Biopolymer module, Accelrys, San Diego). The obtained homology model was then subjected to a full energy minimization within Insight 2005 Discover_3 module (Steepest Descent algorithm, maximum RMS derivative = 0.5 kcal/Å; ε = 80*r). During the minimization, only the whole disordered N- and C- terminals and the SCRs side chains were left free to move, whereas the SCRs backbone were fixed to avoid unrealistic results. Each step of the refining procedure was followed by a structural check by using the Struct_Check command of the ProStat pulldown in the Homology module to verify the correctness of the geometry optimization procedure before moving to the next step. Checks included ϕ, ψ, χ1, χ2, χ3, and ω dihedral angles, Cα virtual torsions, and Kabsch and Sander main chain H-bond energy evaluation. The quality of the resulting complexes was then checked using Molprobity structure evaluator software[309] and compared to that of the reference PDB structure. The obtained homology model was used for successive dynamic docking studies.

Docking studies on human 20S proteasome. According to the experimental data [185,188]and our bioinformatics/structural analysis, we selected the α5-α6 groove as the starting point for the docking studies. In order to define the putative starting complexes for the dynamic docking studies, the energy minimum conformers of each sub-family of Silybin A and B were placed in the α5-α6 groove taking into account the positioning of the side chains of the C-terminal HbYX activating motif of Rpt5 (i.e., YYA) both in the closed and open conformational state (PDB ID: 6MSB and 6MSK). In particular, the centroid of the negatively charged group of silybins was superimposed on the centroid of the C-terminal carboxyl group of Rpt5 as well as the centroid of the other two rings of silybins (i.e., the rings not presenting the negative charge) on the centroids of the phenyl rings of the two tyrosine residues. The conformations with the lowest potential energy that did not show significant steric overlap with protein were selected as starting conformations for the docking calculations.

Docking calculations were performed by using our previously developed atomic model of human 20S in the closed conformational state[287] and the newly developed atomic model of human 20S in the open state. The starting complexes were then

subjected to dynamic docking studies (Affinity, SA_Docking; Insight2005, Accelrys, San Diego). In particular, a docking methodology, which considers all the systems flexible (i.e., ligand and protein), was used. Flexible docking was achieved using the Affinity module in the Insight 2005 suite, setting the SA_Docking procedure[310] and using the Cell Multipole method for non-bonded interactions.[311] The binding domain area was defined as a subset including all residues of human 20S proteasome. Thus, all proteasome atoms were left free to move during the entire course of docking calculations, whereas, in order to avoid unrealistic results, a tethering restraint was applied on the SCRs of the protein (see below).

To identify SCRs, the human 20S proteasome sequences were analyzed using the Structure Prediction and Sequence Analysis server PredictProtein (http://www.predictprotein. org/). In α1 subunits, 6 α-helix and 10 β-sheet secondary structures were predicted to be highly conserved (α1, aa23−33; α2, aa85−104; α3, aa111−128; α4, aa172−183; α5, aa191−207; α6, aa232−243; β1, aa13−16; β2, aa38−43; β3, aa48−53; β4, aa68−72; β5, aa76−80; β6, aa135-143; β7, aa150-154; β8, aa160-168; β9, aa215-222; β10, aa226-229). In α2 subunits, 6 α-helix and 10 β-sheet secondary structures were predicted to be highly conserved (α1, aa20−30; α2, aa81−100; α3, aa107−124; α4, aa167−178; α5, aa184−198; α6, aa223−231; β1, aa9−13; β2, aa34−39; β3, aa44−49; β4, aa66−68; β5, aa72−76; β6, aa131-139; β7, aa145-149; β8, aa155-163; β9, aa208-214; β10, aa219-220). In α3 subunits, 6 α-helix and 10 β-sheet secondary structures were predicted to be highly conserved (α1, aa18−29; α2, aa80−100; α3, aa107−124; α4, aa168−178; α5, aa186−200; α6, aa230−248; β1, aa10−12; β2, aa33−38; β3, aa43−48; β4, aa66−68; β5, aa72−76; β6, aa131-139; β7, aa146-150; β8, aa157-164; β9, aa211-217; β10, aa224-227). In α4 subunits, 6 α-helix and 10 β-sheet secondary structures were predicted to be highly conserved (α1, aa17−27; α2, aa78−97; α3, aa104−121; α4, aa165−176; α5, aa183−198; α6, aa222−243; β1, aa6−10; β2, aa31−36; β3, aa41−46; β4, aa62−65; β5, aa69−73; β6, aa128-136; β7, aa143-147; β8, aa154-161; β9, aa206-212; β10, aa217-219). In α5 subunits, 6 α-helix and 10 β-sheet secondary structures were predicted to be highly conserved (α1, aa22−32; α2, aa83−102; α3, aa109−120; α4, aa174−185; α5, aa191−206; α6, aa231−240; β1, aa11−15; β2, aa36−41; β3, aa46−51; β4, aa66−70; β5, aa74−78; β6, aa138-146; β7, aa152-156; β8, aa162-170; β9, aa215-221; β10, aa226-228). In α6 subunits, 6 α-helix and 10 β-sheet secondary

structures were predicted to be highly conserved (α1, aa19−30; α2, aa79−98; α3, aa105−122; α4, aa165−176; α5, aa184−199; α6, aa226−236; β1, aa10−13; β2, aa35−39; β3, aa45−49; β4, aa62−66; β5, aa70−74; β6, aa129-137; β7, aa143-147; β8, aa154-161; β9, aa210-216; β10, aa221-223). In α7 subunits, 6 α-helix and 10 β-sheet secondary structures were predicted to be highly conserved (α1, aa22−32; α2, aa83−102; α3, aa109−124; α4, aa170−180; α5, aa187−202; α6, aa229−245; β1, aa13−15; β2, aa36−41; β3, aa46−51; β4, aa67−70; β5, aa74−78; β6, aa133-141; β7, aa148-152; β8, aa160-166; β9, aa212-219; β10, aa224-227). In β1 subunits, 5 α-helix and 11 β-sheet secondary structures were predicted to be highly conserved (α1, aa52−69; α2, aa76−90; α3, aa132-143; α4, aa149−166; α5, aa191−200; β1, aa2−8; β2, aa12−16; β3, aa25−27; β4, aa34−37; β5, aa41−45; β6, aa95-103; β7, aa110-114; β8, aa120-122; β9, aa124-128; β10, aa174-180; β11, aa185-189). In β2 subunits, 5 α-helix and 12 β-sheet secondary structures were predicted to be highly conserved (α1, aa52−67; α2, aa76−90; α3, aa131-142; α4, aa148−165; α5, aa194−201; β1, aa2−8; β2, aa12−17; β3, aa25−27; β4, aa33−37; β5, aa41−45; β6, aa95-103; β7, aa109-113; β8, aa123-127; β9, aa173-179; β10, aa184-186; β11, aa210-213; β12, aa215-225). In β3 subunits, 4 α-helix and 10 β-sheet secondary structures were predicted to be highly conserved (α1, aa56−76; α2, aa83−97; α3, aa142-152; α4, aa159−175; β1, aa9−14; β2, aa18−24; β3, aa32−34; β4, aa41−44; β5, aa48−52; β6, aa103-111; β7, aa119-123; β8, aa134-138; β9, aa184-190; β10, aa194-199). In β4 subunits, 5 α-helix and 10 β-sheet secondary structures were predicted to be highly conserved (α1, aa32−35; α2, aa50−70; α3, aa77−93; α4, aa136-147; α5, aa153−170; β1, aa3−8; β2, aa12−17; β3, aa26−27; β4, aa36−38; β5, aa42−46; β6, aa99-107; β7, aa114-118; β8, aa129-132; β9, aa178-184; β10, aa189-190). In β5 subunits, 6 α-helix and 11 β-sheet secondary structures were predicted to be highly conserved (α1, aa31−34; α2, aa49−69; α3, aa76−91; α4, aa132-143; α5, aa149−166; α6, aa189−200; β1, aa2−8; β2, aa12−16; β3, aa25−26; β4, aa35−37; β5, aa41−45; β6, aa96-104; β7, aa110-114; β8, aa120-122; β9, aa124-128; β10, aa174-180; β11, aa185-186). In β6 subunits, 4 α-helix and 11 β-sheet secondary structures were predicted to be highly conserved (α1, aa58−77; α2, aa85−99; α3, aa142-152; α4, aa168−184; β1, aa5−6; β2, aa11−16; β3, aa20−26; β4, aa34−36; β5, aa42−46; β6, aa50-54; β7, aa105-113; β8, aa120-124; β9, aa134-138; β10, aa193-199; β11, aa203-210). In β7 subunits, 6 α-helix and 10 β-sheet secondary structures were predicted to be highly conserved (α1, aa39−41; α2, aa57−77;

α3, aa85-100; α4, aa143−154; α5, aa162−179; α6, aa207−216; β1, aa10−16; β2, aa20−25; β3, aa33−35; β4, aa42−45; β5, aa49−53; β6, aa107-115; β7, aa121-125; β8, aa136-139; β9, aa187-193; β10, aa198-199).

Within the identified SCRs, the distance between backbone hydrogen bond donors and acceptors in the alpha-helices was restrained within 2.5 Å. On the other hand, the ϕ and ψ torsional angles of the beta-sheets were restrained to -119° and +113°, or -139° and +135°, respectively, according to the presence of a parallel or anti-parallel structure. According to the reliability index values obtained from the secondary structure prediction analysis, we applied restraints with a quadratic form and the following set of force constants: i) 1 kcal/mol/Å^2 (maximum force: 10 kcal/mol/Å^2) for reliability index values from 0 to 3, ii) 10 kcal/mol/Å^2 (maximum force: 100 kcal/mol/Å^2) for reliability index values from 4 to 6, and iii) 100 kcal/mol/Å^2 (maximum force: 1000 kcal/mol/Å^2) for reliability index values from 7 to 9.

The docking protocol included a Monte Carlo based conformational search of the ligand within the obtained homology models of human 20S proteasome (i.e., closed and open conformation) for the random generation of a maximum of 20 acceptable complexes. During the first step, in the starting structures, the ligand was moved by a random combination of translation, rotation, and torsional changes to sample both the conformational space of the ligand and its orientation with respect to the protein (MxRChange = 3 Å; MxAngChange = 180°). During this step, van der Waals (vdW) and Coulombic terms were scaled to a factor of 0.1 to avoid very severe divergences in the vdW and Coulombic energies. If the energy of a complex structure resulting from random moves of the ligand was higher by the energy tolerance parameter than the energy of the last accepted structure, it was not accepted for minimization. To ensure a wide variance of the input structures to be successively minimized, an energy tolerance value of 10^6 kcal/mol from the previous structure was used. After the energy minimization step (conjugate gradient; 2500 iterations; ε = 1), the energy test, with an energy range of 50 kcal/mol, and a structure similarity check (RMS tolerance = 0.3 kcal/Å) was applied to select the 20 acceptable structures. Each subsequent structure was generated from the last accepted structure. Following this procedure, the resulting docked structures were ranked by their conformational energy and were analyzed

considering the non-bonded interaction energies between the ligand and the enzyme (vdW and electrostatic energy contribution; Group-Based method[312]; CUT_OFF = 100; ε = 2*r; Discover_3 Module of Insight2005). The complexes with the best non-bonded interaction energies obtained by Monte Carlo calculations were selected as the structures representing the most probable binding modes.

5.17. NMR spectroscopy

Peptide stock solutions were prepared by dissolving 1 mg of the unlabeled-peptide in 1 mL of 10 mM NaOH. The resulting mixture was sonicated twice for 2 min with a 2 min incubation period on ice in between. After sonication, the samples were divided into 100 µL aliquots, lyophilized, and frozen at −20 °C. Two aliquots were dissolved in 500 µL of 20 mM sodium phosphate buffer (pH 6.8), 100% D_2O, 0.05% NaN_3. The resulting mixture was sonicated twice for 2 min with a 2 min incubation period on ice in between. The final concentration, assessed by absorbance measurements at 280 nm, was approximately 90 µM. Ligand stock solutions were prepared by dissolving the powder in 20 mM sodium phosphate buffer, 100% D_2O, 0.05% NaN_3, to match the peptide conditions. NMR spectra were recorded at 10 °C, using either a Bruker AV 700 spectrometer equipped with a TCI cryoprobe or a Bruker 850 HD spectrometer equipped with a TXI probe. All spectra were analyzed with TopSpin 3.2.1 and Sparky.50.

Saturation Transfer Difference (STD) NMR Experiments. Unlabeled 90 µM $A\beta_{40}$, was titrated with increasing concentrations of Sil A-p-TH or Sil B-p-TH up to 1000 µM, and after each addition of ligand, 1D STD NMR spectra were acquired with 1024 scans, 32K complex points, and a spectral width of 15.98 ppm. Selective saturation of $A\beta_{40}$ oligomers was implemented through methyl irradiation, using a train of 20 Gaussian-shaped pulses of 50 ms, separated by a 1 ms interpulse delay. A 30 ms spin lock was also employed to suppress peptide signals that overlap Sil A-p-TH or Sil B-p-TH resonances. Subtraction of on-resonance vs off-resonance intensities was completed through phase cycling. Saturation transfer reference (STR) spectra were recorded with 256 scans, 32K complex points, and a spectral width of 15.98 ppm. A binding isotherm was created through modeling the STD amplification factors (STD_{af}) at each Sil A-p-TH or Sil B-p-TH concentration using two different aromatic proton peaks. The STD_{af} was calculated as:

$$STD_{af} \propto ((I_0 - I_{sat})/I_0) \cdot L_{tot}$$

where $I_0 - I_{sat}$ represents the signal intensity in the STD spectrum, I_0 is the intensity in the STR spectrum, and L_{tot} is the total Sil A-p-TH or Sil B-p-TH concentration. The Sil A-p-TH or SilB-p-TH epitopes for binding to the $A\beta_{40}$ oligomers were determined through the STD vs. STR ratio of each SilA-p-TH or SilB-p-TH proton resonance at ligand concentrations where the protein is nearly saturated (1000 µM). For epitope mapping, the STD vs. STR ratios were then normalized to the highest ratio, in this case H_6 and H_8 from ring A, which was set to 100%.

^{1}H–^{15}N Heteronuclear Single Quantum Coherence (HSQC) Experiments. Uniformly labeled 30 µM $A\beta_{40}$, prepared as described above, was titrated with SilA-p-TH or SilB-p-TH up to 1000 µM and monitored by sensitivity-enhanced ^{1}H–^{15}N HSQC spectra. The HSQC spectra were recorded with 64 scans, a recycle delay of 1.0 s, 256 (t_1) and 2048 (t_2) complex points, and spectral widths of 31.82 and 14.06 ppm for the ^{15}N and ^{1}H dimensions, respectively. The ^{1}H and ^{15}N carrier frequencies were set at the water resonance and the center of the amide region, respectively.

Ligand-Based Transfer Nuclear Overhauser Effect Spectroscopy (TrNOESY). Unlabeled 90 µM $A\beta_{40}$ was incubated with 1000 µM *SilA-p-TH* or *SilB-p-TH* and probed by TrNOESY NMR with a WATERGATE suppression scheme. The TrNOESY spectrum was recorded with 64 scans, a recycle delay of 1.20 s, 512 (t_1) and 2048 (t_2) complex points, and spectral widths of 11.98 ppm for each ^{1}H dimension. A NOE buildup was generated using NOESY mixing times ranging from 60 to 300 ms. The shortest mixing of 60 ms was used to measure the NOEs.

5.18. hIAPP Molecular dynamics (MDs)

Five random amylin structures were generated by using Monte Carlo sampling and the CAMPARI simulation package. Topologies were obtained, cubic boxes (12.8 nm length) were generated, systems were solvated with water molecules, and 150 mM of Na^+Cl^- ions were added adjusting the system to neutrality. Energy minimization of the systems was carried out. Then, structures were relaxed through *NPT* equilibration at 310

K for 1 ns. Finally, molecular dynamic simulations were run at constant *NVT* with snapshots saved every 50 ps over a total run length of around 6000 ns.

SAPPHIRE analysis was used to identify the metastable states, their statistical weight, and to extract five representative amylin configurations. Ligand structures of Sil A and Sil B were obtained from PDB files; protonation states were adjusted and the CHARMM General Force Field (CgenFF) was used to generate the partial charges. These and amylin parameters previously obtained were used to create the structure and the topology of the complexes with both *Sil A* and *Sil B* in 1:1 and 1:2 peptide/ligand ratios. The previously described MD procedure used in amylin simulations was used with the hIAPP/silybin complexes.

All the simulations were carried out using the GROMACS 2018.3 version, the all-atom additive CHARMM36m force field,[313] and the TIP3P water model. Velocity-rescaling thermostat and Berendsen barostat were used to maintain the system at constant temperature (310K) and pressure (1 bar) during the simulations. Temperature and pressure coupling times were fixed to 0,1ps and 2ps, respectively. LJ and Coulomb potential were shifted to zero using the Verlet list cut-off scheme. All the short-range neighbor-list van der Waals and electrostatic cut-off distances were fixed to 1.2 nm. Due to the use of a cut-off, long-range dispersion corrections were applied for pressure and energy. To treat the system outside the cut-off distance (long-range electrostatic interactions), the Particle Mesh Ewald (PME) method with a cubic interpolation order and a grid spacing for Fast Fourier Transform (FFT) of 0.16 nm were applied. To constrain all-bonds length the LINCS algorithm (fourth-order, 2 iterations) was used. The time step of simulations was fixed to 2 fs and Three-dimensional Periodic Boundary Conditions (3D-PBC) were used for approximating a large system. All productive MD simulations were performed in the Piz Daint supercomputer from the Swiss National Supercomputing Centre (CSCS).

Contributions and collaborations

In this PhD program all external collaborations were arranged and organized to fully exploit the triple "i" dimension (inter- national mobility, inter-sectoral exposure, and inter-disciplinarity) of H2020 – Marie Curie Sklodowska Actions.

International mobility: The international mobility has been achieved at different levels. First, although the author of this PhD dissertation has spent most of the training in the CNR laboratories, she has been embedded in an international scientific environment and has been involved in existing networks of international collaborations. Second, she had the opportunity to go abroad on secondment to academia for a period of 3 months, in order to acquire specific sets of skills.

Inter-sectoral exposure: This PhD program has been highly committed to effectively cross the boundaries among different sectors. In this frame, the author has been exposed to a non-academic environment: indeed, the CNR institute has several on-going projects in collaboration with industry.

Inter-disciplinarity: The CNR institute that hosted this PhD program covers a wide spectrum of expertise, spanning from biology, medicine, chemistry, physics, and computer science. This has represented per se a valuable inter-disciplinary environment for the author, which had the opportunity to discuss with researchers from different areas and to address the same biological question from different perspectives.

The author carried out, analyzed and interpreted the results of all the kinetical studies of hIAPP and Aβ amyloid aggregation, amyloid-mediated model membranes disruption, experimental proteasome assays, experimental ubiquitination assays, studies of antioxidant capacity, circular dichroism (CD) experiments and dynamic light scattering (DLS) measures.

Computational studies of the interaction between hIAPP and silybins have been carried out and analyzed by the author in a research stage in the Prof. Amedeo Caflisch's group (University of Zurich, Switzerland) under the supervision of Dr. Ioana Ilie (1st May 2019 – 31st July 2019).

The author has been in charge of the optimization of the procedure and the preparation of all the samples for Transmission Electron Microscopy (TEM) experiments. The TEM images of amyloid fibrils have been collected in collaboration with Dr. Clelia Galati, Dr. Natalia Spinella (STMicroelectronics) and Dr. Corrado Bongiorno (IMM CNR).

The purification of the natural Sil A and Sil B, the synthesis of their trehalose-conjugates and the serum stability studies has been carried out by Dr. Valeria Romanucci, Dr. Armando Zarelli, and Prof. Dr. Giovani di Fabio (University Federico II of Naples, Italy).

NMR experiments to study the interaction between Aβ and silybin-glycoconjugates have been carried out in collaboration with Dr. Rashik Ahmed and Prof. Dr. Giuseppe Melacini (McMaster University, Canada).

Docking simulations between proteasome and silybins has been performed thanks to the collaboration with Dr. Marco Persico and Prof. Dr. Caterina Fattorusso (University of Naples, Italy).

In cell studies of Aβ toxicity in the presence of silybin glycoconjugates have been carried out by Dr. Stefania Zimbone and Dr. Maria Laura Giuffrida (CNR IC Catania, Italy).

Scientific contributions

This PhD program has allowed the author to contribute to the production of several publications and to the dissemination of the results in some congresses, some of them containing part of the research of this PhD thesis. All of them are listed below.

Publications:

1. Ubiquitin binds the Amyloid β peptide and interferes with its clearance pathways.
   F. Bellia, V. Lanza, **S. García-Viñuales**, I. M. M. Ahmed, A. Pietropaolo, C. Iacobucci, G. Malgieri, G. D'Abrosca, R. Fattorusso, V. G. Nicoletti, D. Sbardella, G. R. Tundo, M. Coletta, D. Calcagno, G. Grasso, D. Milardi
   Chemical Sciences, **2019**, *10*, 2732-2742.
   https://doi.org/10.1039/C8SC03394C

2. Site directed mutagenesis of insulin-degrading enzyme allows to single out the molecular basis of peptidase versus E1-like activity: the role of metal ions. F. Bellia, V. Lanza, I. Ahmed, **S. García-Viñuales**; E. Veiss, M. Arizzi, D. Calcagno, D. Milardi; G. Grasso
   Metallomics, **2019**, *11*, 278-281.
   https://doi.org/10.1039/C8MT00288F

3. Pyrazolones activate proteasome by gating mechanisms and protect neuronal cells from Aβ amyloid toxicity.
   M. Santoro, V.Lanza, F. Bellia, D. Sbardella, G. R. Tundo, A. Cannizzo, G. Grasso, M. Arizzi, V. G. Nicoletti, S. Alcaro, G. Costa, A. Pietropaolo; G. Malgieri, G. D'Abrosca, R. Fattorusso, **S. García-Viñuales**, I. M. M. Ahmed, M. Coletta; D. Milardi.
   ChemMedChem, **2020**, 15(3), 302-316.
   https://doi.org/10.1002/cmdc.201900612

4. Endogenous and artificial miRNAs explore a rich variety of conformations: a potential relationship between secondary structure and biological functionality.
   C. M. A. Gangemi, S. Alaimo, A. Pulvirenti, **S. Garcia-Viñuales**, D. Milardi, A. P. Falanga,d M. E. Fragalà, G. Oliviero, G. Piccialli, N. Borbone, A. Ferro, A. D'Urso, C.M. Croce, R. Purrello.
   Scientific Reports, **2020**,10, 453.
   https://doi.org/10.1038/s41598-019-57289-8

5. The Ionophoric Activity of a Pro-Apoptotic VEGF 165 Fragment on HUVEC Cells.
   S. Zimbone, A.M. Santoro, D. La Mendola, C. Giacomelli, M.L. Trincavelli, M.F. Tomasello, D. Milardi, **S. García-Viñuales**, M.F. M. Sciacca, C. Martini, and G. Grasso.
   International Journal of Molecular Sciences, **2020**, 21(8), 2866.
   https://doi.org/10.3390/ijms21082866.

6. The Lipid-Chaperon Hypothesis: A Common Molecular Mechanism of Membrane Disruption by Intrinsically Disordered Proteins.
   M.F.M. Sciacca, F. Lolicato, C. Tempra, F. Scollo, B.R. Sahoo, M.D. Watson, **S. García-Viñuales**, D. Milardi, A. Raudino, J.C. Lee, A. Ramamoorthy, C. La Rosa.
   ChemRxiv, **2020.** Preprint.
   https://doi.org/10.26434/chemrxiv.12770504.v1
7. Trehalose Conjugates of Silybin as Prodrugs for Targeting Toxic Aβ Aggregates.
   S. García-Viñuales, R. Ahmed, M. F. M. Sciacca, V. Lanza, M. L. Giuffrida, S. Zimbone, V. Romanucci, A. Zarrelli, C. Bongiorno, N. Spinella, C. Galati, G. Di Fabio, G. Melacini, D. Milardi.
   ACS Chemical Neuroscience, **2020,** 11(17), 2566–2576.
   https://doi.org/10.1021/acschemneuro.0c00232

8. Modulating Aβ aggregation by tyrosol-based ligands: The crucial role of the catechol moiety.
   V. Romanucci, **S. García-Viñuales**, C. Tempra, R. Bernini, A. Zarrelli, F. Lolicato, D. Milardi, G. Di Fabio.
   Biophysical Chemistry, **2020**, 265, 106434.
   https://doi.org/10.1016/j.bpc.2020.106434

9. Substitution of the Native Zn(II) with Cd(II), Co(II) and Ni(II) Changes the Downhill Unfolding Mechanism of Ros87 to a Completely Different Scenario.
   R. Grazioso, **S. García-Viñuales**, L. Russo, G. D'Abrosca, S. Esposito, L. Zaccaro, R. Iacovino, D. Milardi, R. Fattorusso, G. Malgieri, C. Isernia.
   International Journal of Molecular Sciences, **2020**, 21(21), 8285.
   https://doi.org/10.3390/ijms21218285

10. The interplay between lipid and Aβ amyloid homeostasis in Alzheimer's Disease: risk factors and therapeutic opportunities.
    S. García-Viñuales, M.F.M. Sciacca, V. Lanza, A.M. Santoro, G. Grasso, G.R. Tundo, D. Sbardella, M. Coletta, G. Grasso, C. La Rosa, D. Milardi. *Chemistry and Physics of Lipids*, **2020** (submitted).

11. Different buffer same folding scenario: the change of conditions does not affect Ros87 downhill mechanism.
    R. Grazioso, **S. García-Viñuales**, G. D'Abrosca, I. Baglivo, P. V. Pedone, D. Milardi, R. Fattorusso, C. Isernia, L. Russo, G. Malgieri.
    Scientific Reports, **2020** (submitted)

12. Tyrosol-based Phosphodiester Dimers as new pharmacological agents: synthesis and effect on amyloid β aggregation and metal chelation.
    V. Romanucci, M. Giordano, G. De Tommaso, M. Iuliano, R. Bernini, M. Clemente, **S. García-Viñuales**, D. Milardi, A. Zarrelli and G. Di Fabio.
    (manuscript in preparation)

13. Inhibition of hIAPP amyloid growth and protection from amyloid-mediated membrane disruption by silybins.
    S. García-Viñuales, I. Illie, A. Santoro, M. F. M. Sciacca, V. Lanza, A. Caflisch, D. Milardi.
    (manuscript in preparation)

14. Silybins activate the ubiquitination cascade and the 20S proteasome by interacting with its α5/α6 groove.
    S. García-Viñuales, V. Lanza, A.M. Santoro, M. Persico, C. Fattorusso, D. Milardi.
    (manuscript in preparation)

Scientific contributions in congresses:

1. Multi-target strategy in Alzheimer's Disease and Type II Diabetes Mellitus.
   S. García-Viñuales, M. F.M Sciacca, V. Lanza, A. Maria Santoro, V. Romanucci, A. Zarrelli, G. Di Fabio, D. Milardi.
   National Congress of the division of chemistry of biological systems (DSCB 2018 – Caserta, 26-28 September 2018). Poster contribution.

2. Aβ competitively binds Ubiquitin and inhibits polyubiquitination: a new paradigm for amyloid toxicity.
   D. Milardi, F. Bellia, Valeria Lanza, **S. García-Viñuales**, A. Pietropaolo, C. Iacobucci, G. Malgieri, G. D'Abrosca, R. Fattorusso, V. G. Nicoletti, D. Sbardella, G. R. Tundo, M. Coletta, D. Calcagnoe, G. Grasso.
   National Congress of the division of chemistry of biological systems (DSCB 2018 – Caserta, 26-28 September 2018). Poster contribution.

3. Structure vs sequences: miRNAs a rich variety of conformations.
   D'Urso, C. M. A. Gangemi, S. Alaimo, A. Pulvirenti, **S. Garcia-Viñuales**, D. Milardi, G. Oliviero, A. Ferro, C. M. Croce, R. Purrello.
   National Congress of the division of chemistry of biological systems (DSCB 2018 – Caserta, 26-28 September 2018). Poster contribution.

4. Aβ binds Ubiquitin and inhibits polyubiquitination: alternative mechanisms for amyloid toxicity.
   F. Bellia, V. Lanza, **S. García-Viñuales**, I.M.M. Ahmed, A. Pietropaolo, C. Iacobucci, G. Malgieri, G. D'Abrosca, R. Fattorusso, V. G. Nicoletti, D. Sbardella, G.R. Tundo, M. Coletta, D. Calcagno, G. Grasso, D. Milardi.
   International Symposium on Pathomechanisms of Amyloid Diseases (20-21 December 2018, Miami, Florida, USA). Oral contribution.

5. Trehalose phosphodiester conjugates of silybins protect neuronal cells from Aβ toxicity by multiple pathways.
   S. García-Viñuales, V. Lanza, M.F.M. Sciacca, A. M. Santoro, S. Zimbone, M. L. Giuffrida, V. Romanucci, A. Zarrelli, G. Di Fabio, D. Milardi.
   14th International Conference on Alzheimer's & Parkinson's Diseases (AD/PD 2019™, March 2019, Lisbon, Portugal). Poster contribution.

6. Site directed mutagenesis of insulin-degrading enzyme allows singling out the molecular basis of peptidase versus E1-like activity: the role of metal ions.
   G. Grasso, F. Bellia, V. Lanza, I.M.M. Ahmed, **S. Garcia-Viñuales**, M. Arizzi, D. Calcagno, D. Milardi. Poster contribution.
   7th International Symposium on Metallomics (30 June -3 July 2019, Warsaw, Poland).

7. New Phosphate-Linked Tyrosol Dimers: Synthesis, antioxidant activity, metal chelating capacity and effect on Aβ aggregation.
   M. Giordano, V. Romanucci, R. Bernini, M. Clemente, **S. García-Viñuales**, D. Milardi, M. Iuliano, G. De Tommaso, A. Zarrelli, G. Di Fabio.
   XXXIX National Convention of the Division of Organic Chemistry of the Italian Chemical Society (CDCO, September 2019, Turin, Italy). Poster contribution.

8. Endogenous and artificial miRNAs: a rich variety of conformations.
   C.M.A. Gangemi, S. Alaimo, A. Pulvirenti, **S. García-Viñuales**, D. Milardi, A. P. Falanga, M. E. Fragalà, G. Oliviero, G. Piccialli, N. Borbone, A. Ferro, A. D'Urso, C. M. Croce & R. Purrello.
   Workshop Italian Chemical Society (SCI) Sicily 2020 (28 February, Messina, Italy). Poster contribution.

Acknowledgements

This PhD fellowship has been possible thanks to the financial support from European Union funding (H2020 – Marie Sklodowska Curie Actions; grant agreement INCIPIT n. 665403) and the National Research Council (CNR).

I would like first to thanks my tutors, Dr. Danilo Milardi and Prof. Roberto Purrello, for giving me the opportunity to accomplish my goals, taking part in this project, and for their support during the course of producing my research and PhD dissertation. My deep gratitude to Dr. Danilo Milardi, who expertly guided me through the development of my research, encouraging me to face each one of the encountered challenges; I could not have imagined having a better mentor for my PhD thesis. I would like to express my sincere gratitude to Dr. Ana Maria Santoro, Dr. Valeria Lanza, and Dr. Michelle Sciacca for all they have taught me, the stimulating discussions, and their immense support and advice from the minute one of my research.

I would like to thank prof. Amedeo Caflisch for hosting me in his group during a three months research stay, allowing me to introduce myself in the computational field, and Dr. Ioana Ilie for all her dedication and supervision during this period. This dissertation could not be possible without the collaboration end expertise of Prof. Giovani Di Fabio, Dr. Valeria Romanucci, Dr. Armando Zarelli, Dr. Stefania Zimbone, Dr. Maria Laura Giuffrida, Prof. Giusseppe Melacine, Dr. Rashik Ahmed, Prof. Caterina Fattoruso, Dr. Marco Persico, Dr. Clelia Galati, Dr. Natalia Spinella, and Dr. Corrado Buongiorno. Thank all of you to participate in this project; collaborate with you has been an immeasurable pleasure.

A special appreciation to all my CNR colleagues who have made me feel so at home, for giving me this unforgettable experience. Ikhlas, I feel grateful to have traversed this challenging road together.

Thank you Conchi and Claudia for your trust and support now and always. Finally, a special thanks to Luis, who prompted me to face this challenge; I can never forget that you have been present in each one of the difficult moments.

References

1. Chiti, F. & Dobson, C. M. Protein Misfolding, Amyloid Formation, and Human Disease: A Summary of Progress Over the Last Decade. *Annu Rev Biochem* **86**, 27–68 (2017).
2. Klaips, C. L., Jayaraj, G. G. & Hartl, F. U. Pathways of cellular proteostasis in aging and disease. *J Cell Biol* **217**, 51–63 (2018).
3. de la Monte, S. M. & Wands, J. R. Alzheimer's Disease Is Type 3 Diabetes–Evidence Reviewed. *J Diabetes Sci Technol* **2**, 1101–1113 (2008).
4. Walker, L. C. & LeVine, H. Corruption and Spread of Pathogenic Proteins in Neurodegenerative Diseases. *J Biol Chem* **287**, 33109–33115 (2012).
5. Hartl, F. U. Protein Misfolding Diseases. *Annual Review of Biochemistry* **86**, 21–26 (2017).
6. Geschwind, M. D. Prion Diseases. *Continuum (Minneap Minn)* **21**, 1612–1638 (2015).
7. Gao, Y.-L. *et al.* Tau in neurodegenerative disease. *Ann Transl Med* **6**, 175 (2018).
8. Hatters, D. M. Protein misfolding inside cells: the case of huntingtin and Huntington's disease. *IUBMB Life* **60**, 724–728 (2008).
9. Palsdottir, A., Snorradottir, A. O. & Thorsteinsson, L. Hereditary cystatin C amyloid angiopathy: genetic, clinical, and pathological aspects. *Brain Pathol.* **16**, 55–59 (2006).
10. Towards a dementia plan: a WHO guide. Geneva: World Health Organization; 2018. Licence: CC BY-NC-SA 3.0 IGO.
11. 2015 Alzheimer's disease facts and figures. *Alzheimers Dement* **11**, 332–384 (2015).
12. El-Hayek, Y. H. *et al.* Tip of the Iceberg: Assessing the Global Socioeconomic Costs of Alzheimer's Disease and Related Dementias and Strategic Implications for Stakeholders. *J. Alzheimers Dis.* **70**, 323–341 (2019).
13. Brothers, H. M., Gosztyla, M. L. & Robinson, S. R. The Physiological Roles of Amyloid-β Peptide Hint at New Ways to Treat Alzheimer's Disease. *Frontiers in Aging Neuroscience* **10**, 118 (2018).

14. Gong, C.-X. & Iqbal, K. Hyperphosphorylation of Microtubule-Associated Protein Tau: A Promising Therapeutic Target for Alzheimer Disease. *Curr Med Chem* **15**, 2321–2328 (2008).
15. Köpke, E. *et al.* Microtubule-associated protein tau. Abnormal phosphorylation of a non-paired helical filament pool in Alzheimer disease. *J. Biol. Chem.* **268**, 24374–24384 (1993).
16. Kuret, J. *et al.* Evaluating triggers and enhancers of tau fibrillization. *Microsc. Res. Tech.* **67**, 141–155 (2005).
17. De Strooper, B. & Karran, E. The Cellular Phase of Alzheimer's Disease. *Cell* **164**, 603–615 (2016).
18. Mormino, E. C. & Papp, K. V. Amyloid accumulation and cognitive decline in clinically normal older individuals: implications for aging and early Alzheimer's disease. *J Alzheimers Dis* **64**, S633–S646 (2018).
19. Ewers, M., Sperling, R. A., Klunk, W. E., Weiner, M. W. & Hampel, H. Neuroimaging markers for the prediction and early diagnosis of Alzheimer's disease dementia. *Trends Neurosci* **34**, 430–442 (2011).
20. American Diabetes Association. Diagnosis and Classification of Diabetes Mellitus. *Diabetes Care* **32**, S62–S67 (2009).
21. Blair, M. Diabetes Mellitus Review. *Urol Nurs* **36**, 27–36 (2016).
22. Fernandez, M. S. Human IAPP amyloidogenic properties and pancreatic beta-cell death. *Cell Calcium* **56**, 416–427 (2014).
23. Goyal, R. & Jialal, I. Diabetes Mellitus Type 2. in *StatPearls* (StatPearls Publishing, 2020).
24. International Diabetes Federation. IDF Diabetes Atlas, 9th edn. Brussels, Belgium: 2019. (2019).
25. Ott, A. *et al.* Diabetes mellitus and the risk of dementia: The Rotterdam Study. *Neurology* **53**, 1937–1942 (1999).

26. Cheng, G., Huang, C., Deng, H. & Wang, H. Diabetes as a risk factor for dementia and mild cognitive impairment: a meta-analysis of longitudinal studies. *Intern Med J* **42**, 484–491 (2012).

27. Wang, J.-H., Wu, Y.-J., Tee, B. L. & Lo, R. Y. Medical Comorbidity in Alzheimer's Disease: A Nested Case-Control Study. *J. Alzheimers Dis.* **63**, 773–781 (2018).

28. Duran-Aniotz, C. & Hetz, C. Glucose Metabolism: A Sweet Relief of Alzheimer's Disease. *Current Biology* **26**, R806–R809 (2016).

29. Jackson, K. *et al.* Amylin deposition in the brain: A second amyloid in Alzheimer disease? *Ann Neurol* **74**, 517–526 (2013).

30. Martinez-Valbuena, I. *et al.* Amylin as a potential link between type 2 diabetes and alzheimer disease. *Ann. Neurol.* **86**, 539–551 (2019).

31. Labbadia, J. & Morimoto, R. I. The biology of proteostasis in aging and disease. *Annu Rev Biochem* **84**, 435–464 (2015).

32. Hipp, M. S., Kasturi, P. & Hartl, F. U. The proteostasis network and its decline in ageing. *Nat Rev Mol Cell Biol* **20**, 421–435 (2019).

33. Labbadia, J. & Morimoto, R. I. Repression of the heat shock response is a programmed event at the onset of reproduction. *Mol Cell* **59**, 639–650 (2015).

34. Maklakov, A. A. & Immler, S. The Expensive Germline and the Evolution of Ageing. *Current Biology* **26**, R577–R586 (2016).

35. Chen, B., Retzlaff, M., Roos, T. & Frydman, J. Cellular Strategies of Protein Quality Control. *Cold Spring Harb Perspect Biol* **3**, a004374 (2011).

36. Dikic, I. Proteasomal and Autophagic Degradation Systems. *Annu Rev Biochem* **86**, 193–224 (2017).

37. Gadhave, K. *et al.* The ubiquitin proteasomal system: a potential target for the management of Alzheimer's disease. *J Cell Mol Med* **20**, 1392–1407 (2016).

38. Liu, J. & Li, L. Targeting Autophagy for the Treatment of Alzheimer's Disease: Challenges and Opportunities. *Front Mol Neurosci* **12**, 203 (2019).

39. Mputhia, Z. *et al.* Autophagy Modulation as a Treatment of Amyloid Diseases. *Molecules* **24**, 3372 (2019).

40. Cummings, J. L., Morstorf, T. & Zhong, K. Alzheimer's disease drug-development pipeline: few candidates, frequent failures. *Alzheimers Res Ther* **6**, 37 (2014).

41. Yiannopoulou, K. G. & Papageorgiou, S. G. Current and Future Treatments in Alzheimer Disease: An Update. *J Cent Nerv Syst Dis* **12**, 1179573520907397 (2020).

42. Stimulus package. *Nature Medicine* **24**, 247 (2018).

43. Uversky, V. N. Intrinsically Disordered Proteins and Their "Mysterious" (Meta)Physics. *Frontiers in Physics* **7**, 10 (2019).

44. Oldfield, C. J. & Dunker, A. K. Intrinsically Disordered Proteins and Intrinsically Disordered Protein Regions. *Annu. Rev. Biochem.* **83**, 553–584 (2014).

45. Burger, V. M., Gurry, T. & Stultz, C. M. Intrinsically Disordered Proteins: Where Computation Meets Experiment. *Polymers* **6**, 2684–2719 (2014).

46. Iljina, M. *et al.* Quantitative analysis of co-oligomer formation by amyloid-beta peptide isoforms. *Sci Rep* **6**, 28658 (2016).

47. LaFerla, F. M., Green, K. N. & Oddo, S. Intracellular amyloid-β in Alzheimer's disease. *Nature Reviews Neuroscience* **8**, 499–509 (2007).

48. Clifford, P. M. *et al.* Aβ peptides can enter the brain through a defective blood–brain barrier and bind selectively to neurons. *Brain Research* **1142**, 223–236 (2007).

49. Hiltunen, M., van Groen, T. & Jolkkonen, J. Functional roles of amyloid-beta protein precursor and amyloid-beta peptides: evidence from experimental studies. *J Alzheimers Dis* **18**, 401–412 (2009).

50. Pearson, H. A. & Peers, C. Physiological roles for amyloid β peptides. *J Physiol* **575**, 5–10 (2006).

51. Kumar, R., Nordberg, A. & Darreh-Shori, T. Amyloid-β peptides act as allosteric modulators of cholinergic signalling through formation of soluble BAβACs. *Brain* **139**, 174–192 (2016).

52. Petkova, A. T. *et al.* A structural model for Alzheimer's β-amyloid fibrils based on experimental constraints from solid state NMR. *Proceedings of the National Academy of Sciences* **99**, 16742–16747 (2002).

53. Jarrett, J. T., Berger, E. P. & Lansbury, P. T. The carboxy terminus of the beta amyloid protein is critical for the seeding of amyloid formation: implications for the pathogenesis of Alzheimer's disease. *Biochemistry* **32**, 4693–4697 (1993).

54. Zhang, X.-X., Pan, Y.-H., Huang, Y.-M. & Zhao, H.-L. Neuroendocrine hormone amylin in diabetes. *World J Diabetes* **7**, 189–197 (2016).

55. Press, M., Jung, T., König, J., Grune, T. & Höhn, A. Protein aggregates and proteostasis in aging: Amylin and β-cell function. *Mech. Ageing Dev.* **177**, 46–54 (2019).

56. Visa, M. *et al.* Islet amyloid polypeptide exerts a novel autocrine action in β-cell signaling and proliferation. *FASEB J.* **29**, 2970–2979 (2015).

57. Braun, M., Ramracheya, R. & Rorsman, P. Autocrine regulation of insulin secretion. *Diabetes Obes Metab* **14 Suppl 3**, 143–151 (2012).

58. Rushing, P. A., Hagan, M. M., Seeley, R. J., Lutz, T. A. & Woods, S. C. Amylin: a novel action in the brain to reduce body weight. *Endocrinology* **141**, 850–853 (2000).

59. Akter, R. *et al.* Islet Amyloid Polypeptide: Structure, Function, and Pathophysiology. *Journal of Diabetes Research* **2016**, 2798269 (2015).

60. Liang, G., Zhao, J., Yu, X. & Zheng, J. Comparative Molecular Dynamics Study of Human Islet Amyloid Polypeptide (IAPP) and Rat IAPP Oligomers. *Biochemistry* **52**, 1089–1100 (2013).

61. Cao, P., Meng, F., Abedini, A. & Raleigh, D. P. The Ability of Rodent Islet Amyloid Polypeptide to Inhibit Amyloid Formation by Human Islet Amyloid Polypeptide Has Important Implications For the Mechanism of Amyloid Formation and the Design of Inhibitors. *Biochemistry* **49**, 872–881 (2010).

62. Westermark, P., Engström, U., Johnson, K. H., Westermark, G. T. & Betsholtz, C. Islet amyloid polypeptide: pinpointing amino acid residues linked to amyloid fibril formation. *Proc Natl Acad Sci U S A* **87**, 5036–5040 (1990).

63. Chiu, C., Singh, S. & de Pablo, J. J. Effect of Proline Mutations on the Monomer Conformations of Amylin. *Biophysical Journal* **105**, 1227–1235 (2013).

64. Nilsson, M. R. & Raleigh, D. P. Analysis of amylin cleavage products provides new insights into the amyloidogenic region of human amylin1 1Edited by P. E. Wright. *Journal of Molecular Biology* **294**, 1375–1385 (1999).

65. Khemtémourian, L., Engel, M. F. M., Liskamp, R. M. J., Höppener, J. W. M. & Killian, J. A. The N-terminal fragment of human islet amyloid polypeptide is non-fibrillogenic in the presence of membranes and does not cause leakage of bilayers of physiologically relevant lipid composition. *Biochimica et Biophysica Acta (BBA) - Biomembranes* **1798**, 1805–1811 (2010).

66. Nanga, R. P. R., Brender, J. R., Xu, J., Veglia, G. & Ramamoorthy, A. Structures of rat and human islet amyloid polypeptide IAPP(1-19) in micelles by NMR spectroscopy. *Biochemistry* **47**, 12689–12697 (2008).

67. Gilead, S. & Gazit, E. The Role of the 14–20 Domain of the Islet Amyloid Polypeptide in Amyloid Formation. *Exp Diabetes Res* **2008**, 256954 (2008).

68. Koo, B. W. & Miranker, A. D. Contribution of the intrinsic disulfide to the assembly mechanism of islet amyloid. *Protein Science* **14**, 231–239 (2005).

69. Brännström, K. *et al.* Scanning electron microscopy as a tool for evaluating morphology of amyloid structures formed on surface plasmon resonance chips. *Data in Brief* **19**, 1166–1170 (2018).

70. Paravastu, A. K., Leapman, R. D., Yau, W.-M. & Tycko, R. Molecular structural basis for polymorphism in Alzheimer's β-amyloid fibrils. *PNAS* **105**, 18349–18354 (2008).

71. Wälti, M. A. *et al.* Atomic-resolution structure of a disease-relevant Aβ(1–42) amyloid fibril. *Proc Natl Acad Sci USA* **113**, E4976 (2016).

72. Kollmer, M. *et al.* Cryo-EM structure and polymorphism of Aβ amyloid fibrils purified from Alzheimer's brain tissue. *Nature Communications* **10**, 1–8 (2019).

73. Dubnovitsky, A. *et al.* Amyloid-β Protofibrils: Size, Morphology and Synaptotoxicity of an Engineered Mimic. *PLoS One* **8**, e66101 (2013).

74. Gremer, L. *et al.* Fibril structure of amyloid-β(1–42) by cryo–electron microscopy. *Science* **358**, 116–119 (2017).

75. Sunde, M. & Blake, C. The Structure of Amyloid Fibrils by Electron Microscopy and X-Ray Diffraction. in *Advances in Protein Chemistry* (eds. Richards, F. M., Eisenberg, D. S. & Kim, P. S.) vol. 50 123–159 (Academic Press, 1997).

76. Sgourakis, N. G., Yau, W.-M. & Qiang, W. Modeling an In-Register, Parallel "Iowa" Aβ Fibril Structure Using Solid-State NMR Data from Labeled Samples with Rosetta. *Structure* **23**, 216–227 (2015).

77. Salahuddin, P., Fatima, M. T., Abdelhameed, A. S., Nusrat, S. & Khan, R. H. Structure of amyloid oligomers and their mechanisms of toxicities: Targeting amyloid oligomers using novel therapeutic approaches. *European Journal of Medicinal Chemistry* **114**, 41–58 (2016).

78. Xue, C., Lin, T. Y., Chang, D. & Guo, Z. Thioflavin T as an amyloid dye: fibril quantification, optimal concentration and effect on aggregation. *R Soc Open Sci* **4**, 160696 (2017).

79. Chatani, E. & Yamamoto, N. Recent progress on understanding the mechanisms of amyloid nucleation. *Biophys Rev* **10**, 527–534 (2017).

80. Crespo, R., Rocha, F. A., Damas, A. M. & Martins, P. M. A Generic Crystallization-like Model That Describes the Kinetics of Amyloid Fibril Formation. *J. Biol. Chem.* **287**, 30585–30594 (2012).

81. Cohen, S. I. A. *et al.* Proliferation of amyloid-β42 aggregates occurs through a secondary nucleation mechanism. *Proc. Natl. Acad. Sci. U.S.A.* **110**, 9758–9763 (2013).

82. Alzheimer, A. Ueber eine eigenartige Erkrankung der Hirnrinde. Allgem. Zeit. *Psychiatrie Psychisch-Gerichtliche Med* **64**, 146–148 (1907).

83. Strassnig, M. & Ganguli, M. About a Peculiar Disease of the Cerebral Cortex. *Psychiatry (Edgmont)* **2**, 30–33 (2005).

84. Masters, C. L. *et al.* Amyloid plaque core protein in Alzheimer disease and Down syndrome. *Proc Natl Acad Sci U S A* **82**, 4245–4249 (1985).

85. Glenner, G. G. & Wong, C. W. Alzheimer's disease: initial report of the purification and characterization of a novel cerebrovascular amyloid protein. *Biochem. Biophys. Res. Commun.* **120**, 885–890 (1984).

86. Hardy, J. A. & Higgins, G. A. Alzheimer's disease: the amyloid cascade hypothesis. *Science* **256**, 184–185 (1992).

87. Lambert, M. P. *et al.* Diffusible, nonfibrillar ligands derived from Aβ1–42 are potent central nervous system neurotoxins. *Proc Natl Acad Sci U S A* **95**, 6448–6453 (1998).

88. Shankar, G. M. *et al.* Amyloid-β protein dimers isolated directly from Alzheimer's brains impair synaptic plasticity and memory. *Nature Medicine* **14**, 837–842 (2008).

89. Townsend, M., Shankar, G. M., Mehta, T., Walsh, D. M. & Selkoe, D. J. Effects of secreted oligomers of amyloid beta-protein on hippocampal synaptic plasticity: a potent role for trimers. *J. Physiol. (Lond.)* **572**, 477–492 (2006).

90. Müller-Schiffmann, A. *et al.* Amyloid-β dimers in the absence of plaque pathology impair learning and synaptic plasticity. *Brain* **139**, 509–525 (2016).

91. Ono, K., Condron, M. M. & Teplow, D. B. Structure–neurotoxicity relationships of amyloid β-protein oligomers. *Proc Natl Acad Sci U S A* **106**, 14745–14750 (2009).

92. Bernstein, S. L. *et al.* Amyloid-β protein oligomerization and the importance of tetramers and dodecamers in the aetiology of Alzheimer's disease. *Nat Chem* **1**, 326–331 (2009).

93. Bitan, G. *et al.* Amyloid β-protein (Aβ) assembly: Aβ40 and Aβ42 oligomerize through distinct pathways. *Proc Natl Acad Sci U S A* **100**, 330–335 (2003).

94. O'Nuallain, B. *et al.* Amyloid beta-protein dimers rapidly form stable synaptotoxic protofibrils. *J. Neurosci.* **30**, 14411–14419 (2010).

95. Lesné, S. *et al.* A specific amyloid-beta protein assembly in the brain impairs memory. *Nature* **440**, 352–357 (2006).

96. Economou, N. J. *et al.* Amyloid β-Protein Assembly and Alzheimer's Disease: Dodecamers of Aβ42, but Not of Aβ40, Seed Fibril Formation. *J. Am. Chem. Soc.* **138**, 1772–1775 (2016).

97. Gong, Y. *et al.* Alzheimer's disease-affected brain: Presence of oligomeric Aβ ligands (ADDLs) suggests a molecular basis for reversible memory loss. *Proc Natl Acad Sci U S A* **100**, 10417–10422 (2003).

98. Kumar, A. *et al.* Specific Soluble Oligomers of Amyloid-β Peptide Undergo Replication and Form Non-fibrillar Aggregates in Interfacial Environments. *J Biol Chem* **287**, 21253–21264 (2012).

99. Breydo, L. & Uversky, V. N. Structural, morphological, and functional diversity of amyloid oligomers. *FEBS Letters* **589**, 2640–2648 (2015).

100. Benilova, I., Karran, E. & De Strooper, B. The toxic Aβ oligomer and Alzheimer's disease: an emperor in need of clothes. *Nature Neuroscience* **15**, 349–357 (2012).

101. Aisenbrey, C. *et al.* How is protein aggregation in amyloidogenic diseases modulated by biological membranes? *Eur. Biophys. J.* **37**, 247–255 (2008).

102. Hu, X. *et al.* Amyloid seeds formed by cellular uptake, concentration, and aggregation of the amyloid-beta peptide. *Proc Natl Acad Sci U S A* **106**, 20324–20329 (2009).

103. Ion, L., Ciobanu, C. I., Murariu, M., Gradinaru, V.-R. & Drochioiu, G. SDS-induced Peptide Conformational Changes: From Triglycyl-glycine to Amyloid-β Oligomers Associated with Alzheimer's Disease. *Int J Pept Res Ther* **22**, 45–55 (2016).

104. Hepler, R. W. *et al.* Solution state characterization of amyloid beta-derived diffusible ligands. *Biochemistry* **45**, 15157–15167 (2006).

105. Watt, A. D. *et al.* Oligomers, fact or artefact? SDS-PAGE induces dimerization of β-amyloid in human brain samples. *Acta Neuropathol* **125**, 549–564 (2013).

106. Bitan, G., Fradinger, E. A., Spring, S. M. & Teplow, D. B. Neurotoxic protein oligomers — what you see is not always what you get. *Amyloid* **12**, 88–95 (2005).

107. Chen, Y.-R. & Glabe, C. G. Distinct Early Folding and Aggregation Properties of Alzheimer Amyloid-β Peptides Aβ40 and Aβ42. *J. Biol. Chem.* **281**, 24414–24422 (2006).

108. Côté, S., Laghaei, R., Derreumaux, P. & Mousseau, N. Distinct Dimerization for Various Alloforms of the Amyloid-Beta Protein: Aβ1–40, Aβ1–42, and Aβ1–40(D23N). *J. Phys. Chem. B* **116**, 4043–4055 (2012).

109. Johnson, R. D. *et al.* Single-Molecule Imaging Reveals Aβ42:Aβ40 Ratio-Dependent Oligomer Growth on Neuronal Processes. *Biophys J* **104**, 894–903 (2013).

110. Chang, Y.-J. & Chen, Y.-R. The coexistence of an equal amount of Alzheimer's amyloid-β 40 and 42 forms structurally stable and toxic oligomers through a distinct pathway. *FEBS J.* **281**, 2674–2687 (2014).

111. Dumurgier, J. *et al.* Cerebrospinal fluid amyloid-β 42/40 ratio in clinical setting of memory centers: a multicentric study. *Alzheimer's Research & Therapy* **7**, 30 (2015).

112. Kokubo, H. *et al.* Amyloid Beta Annular Protofibrils in Cell Processes and Synapses Accumulate with Aging and Alzheimer-Associated Genetic Modification. *Int J Alzheimers Dis* **2009**, 689285 (2009).

113. Kayed, R. *et al.* Annular Protofibrils Are a Structurally and Functionally Distinct Type of Amyloid Oligomer. *J Biol Chem* **284**, 4230–4237 (2009).

114. Quist, A. *et al.* Amyloid ion channels: A common structural link for protein-misfolding disease. *PNAS* **102**, 10427–10432 (2005).

115. Evangelisti, E. *et al.* Membrane lipid composition and its physicochemical properties define cell vulnerability to aberrant protein oligomers. *J. Cell. Sci.* **125**, 2416–2427 (2012).

116. Mirzabekov, T. A., Lin, M. & Kagan, B. L. Pore Formation by the Cytotoxic Islet Amyloid Peptide Amylin. *J. Biol. Chem.* **271**, 1988–1992 (1996).

117. Sciacca, M. F. M. *et al.* The Role of Cholesterol in Driving IAPP-Membrane Interactions. *Biophys J* **111**, 140–151 (2016).

118. Ahyayauch, H. *et al.* Binding of β-Amyloid (1–42) Peptide to Negatively Charged Phospholipid Membranes in the Liquid-Ordered State: Modeling and Experimental Studies. *Biophys J* **103**, 453–463 (2012).

119. Wakabayashi, M. & Matsuzaki, K. Ganglioside-induced amyloid formation by human islet amyloid polypeptide in lipid rafts. *FEBS Lett.* **583**, 2854–2858 (2009).

120. Lai, A. Y. & McLaurin, J. Mechanisms of amyloid-Beta Peptide uptake by neurons: the role of lipid rafts and lipid raft-associated proteins. *Int J Alzheimers Dis* **2011**, 548380 (2010).

121. Williamson, R., Usardi, A., Hanger, D. P. & Anderton, B. H. Membrane-bound β-amyloid oligomers are recruited into lipid rafts by a fyn-dependent mechanism. *The FASEB Journal* **22**, 1552–1559 (2008).

122. Pike, L. J. Lipid rafts bringing order to chaos. *J. Lipid Res.* **44**, 655–667 (2003).

123. Sonnino, S., Prinetti, A., Mauri, L., Chigorno, V. & Tettamanti, G. Dynamic and Structural Properties of Sphingolipids as Driving Forces for the Formation of Membrane Domains. *Chem. Rev.* **106**, 2111–2125 (2006).

124. Kurganov, B., Doh, M. & Arispe, N. Aggregation of liposomes induced by the toxic peptides Alzheimer's Abetas, human amylin and prion (106-126): facilitation by membrane-bound GM1 ganglioside. *Peptides* **25**, 217–232 (2004).

125. Choo-Smith, L. P., Garzon-Rodriguez, W., Glabe, C. G. & Surewicz, W. K. Acceleration of amyloid fibril formation by specific binding of Abeta-(1-40) peptide to ganglioside-containing membrane vesicles. *J. Biol. Chem.* **272**, 22987–22990 (1997).

126. Hong, S. *et al.* Soluble Aβ oligomers are rapidly sequestered from brain ISF in vivo and bind GM1 ganglioside on cellular membranes. *Neuron* **82**, 308–319 (2014).

127. Fernández-Pérez, E. J., Sepúlveda, F. J., Peoples, R. & Aguayo, L. G. Role of membrane GM1 on early neuronal membrane actions of Aβ during onset of Alzheimer's disease. *Biochim Biophys Acta Mol Basis Dis* **1863**, 3105–3116 (2017).

128. Lin, M.-S., Chen, L.-Y., Wang, S. S. S., Chang, Y. & Chen, W.-Y. Examining the levels of ganglioside and cholesterol in cell membrane on attenuation the cytotoxicity of beta-amyloid peptide. *Colloids and Surfaces B: Biointerfaces* **65**, 172–177 (2008).

129. Kakio, A., Nishimoto, S., Yanagisawa, K., Kozutsumi, Y. & Matsuzaki, K. Cholesterol-dependent Formation of GM1 Ganglioside-bound Amyloid β-Protein, an Endogenous Seed for Alzheimer Amyloid. *J. Biol. Chem.* **276**, 24985–24990 (2001).

130. Fantini, J., Yahi, N. & Garmy, N. Cholesterol accelerates the binding of Alzheimer's β-amyloid peptide to ganglioside GM1 through a universal hydrogen-bond-dependent sterol tuning of glycolipid conformation. *Front. Physiol.* **4**, 120 (2013).

131. Butterfield, S. M. & Lashuel, H. A. Amyloidogenic protein-membrane interactions: mechanistic insight from model systems. *Angew Chem Int Ed Engl* **49**, 5628–5654 (2010).

132. Sciacca, M. F. M. *et al.* Cations as switches of amyloid-mediated membrane disruption mechanisms: calcium and IAPP. *Biophys J* **104**, 173–184 (2013).

133. Sciacca, M. F. M. *et al.* Two-step mechanism of membrane disruption by Aβ through membrane fragmentation and pore formation. *Biophys. J.* **103**, 702–710 (2012).

134. Di Scala, C. *et al.* Common molecular mechanism of amyloid pore formation by Alzheimer's beta-amyloid peptide and alpha-synuclein. *Sci Rep* **6**, 28781 (2016).

135. Kawahara, M., Kuroda, Y., Arispe, N. & Rojas, E. Alzheimer's beta-amyloid, human islet amylin, and prion protein fragment evoke intracellular free calcium elevations by a common mechanism in a hypothalamic GnRH neuronal cell line. *J Biol Chem* **275**, 14077–14083 (2000).

136. Hebda, J. A. & Miranker, A. D. The interplay of catalysis and toxicity by amyloid intermediates on lipid bilayers: insights from type II diabetes. *Annu Rev Biophys* **38**, 125–152 (2009).

137. Williams, T. L. & Serpell, L. C. Membrane and surface interactions of Alzheimer's Aβ peptide – insights into the mechanism of cytotoxicity. *The FEBS Journal* **278**, 3905–3917 (2011).

138. Brender, J. R. *et al.* Biphasic Effects of Insulin on Islet Amyloid Polypeptide Membrane Disruption. *Biophys J* **100**, 685–692 (2011).

139. Di Meo, S., Reed, T. T., Venditti, P. & Victor, V. M. Role of ROS and RNS Sources in Physiological and Pathological Conditions. *Oxid Med Cell Longev* **2016**, 1245049 (2016).

140. Jain, V., Langham, M. C. & Wehrli, F. W. MRI estimation of global brain oxygen consumption rate. *J Cereb Blood Flow Metab* **30**, 1598–1607 (2010).

141. Halliwell, B. Oxidative stress and neurodegeneration: where are we now? *J. Neurochem.* **97**, 1634–1658 (2006).

142. Chen, Z. & Zhong, C. Oxidative stress in Alzheimer's disease. *Neurosci Bull* **30**, 271–281 (2014).

143. Bikkad, M. D., Somwanshi, S. D., S, Ghuge, eep H. & Nagane, N. S. Oxidative Stress in Type II Diabetes Mellitus. *Biomedical Research* **25**, 84–87 (2014).

144. Cai, Z., Zhao, B. & Ratka, A. Oxidative Stress and β-Amyloid Protein in Alzheimer's Disease. *NeuroMolecular Medicine* **13**, 223–250 (2011).

145. Cheignon, C. *et al.* Oxidative stress and the amyloid beta peptide in Alzheimer's disease. *Redox Biol* **14**, 450–464 (2018).

146. Rehman, K. & Akash, M. S. H. Mechanism of Generation of Oxidative Stress and Pathophysiology of Type 2 Diabetes Mellitus: How Are They Interlinked? *J. Cell. Biochem.* **118**, 3577–3585 (2017).

147. Kohnert, K.-D., Freyse, E.-J. & Salzsieder, E. Glycaemic variability and pancreatic β-cell dysfunction. *Curr Diabetes Rev* **8**, 345–354 (2012).

148. Miraee-Nedjad, S., Sims, P. F. G., Schwartz, J.-M. & Doig, A. J. Effect of IAPP on the proteome of cultured Rin-5F cells. *BMC Biochemistry* **19**, 9 (2018).

149. Baram, M., Gilead, S., Gazit, E. & Miller, Y. Mechanistic perspective and functional activity of insulin in amylin aggregation. *Chem Sci* **9**, 4244–4252 (2018).

150. Susa, A. C. *et al.* Defining the Molecular Basis of Amyloid Inhibitors: Human Islet Amyloid Polypeptide–Insulin Interactions. *J Am Chem Soc* **136**, 12912–12919 (2014).

151. Kawahito, S., Kitahata, H. & Oshita, S. Problems associated with glucose toxicity: role of hyperglycemia-induced oxidative stress. *World J Gastroenterol* **15**, 4137–4142 (2009).

152. Pérez-Matute, P., Zulet, M. A. & Martínez, J. A. Reactive species and diabetes: counteracting oxidative stress to improve health. *Curr Opin Pharmacol* **9**, 771–779 (2009).

153. Masad, A. *et al.* Copper-mediated formation of hydrogen peroxide from the amylin peptide: a novel mechanism for degeneration of islet cells in type-2 diabetes mellitus? *FEBS Lett.* **581**, 3489–3493 (2007).

154. Tabner, B. J. *et al.* Hydrogen peroxide is generated during the very early stages of aggregation of the amyloid peptides implicated in Alzheimer disease and familial British dementia. *J. Biol. Chem.* **280**, 35789–35792 (2005).

155. Beshgetoor, D. & Hambidge, M. Clinical conditions altering copper metabolism in humans. *Am. J. Clin. Nutr.* **67**, 1017S-1021S (1998).

156. Zenaro, E., Piacentino, G. & Constantin, G. The blood-brain barrier in Alzheimer's disease. *Neurobiol Dis* **107**, 41–56 (2017).

157. Daneman, R. & Prat, A. The blood-brain barrier. *Cold Spring Harb Perspect Biol* **7**, a020412–a020412 (2015).

158. Bazan, N. G., Halabi, A., Ertel, M. & Petasis, N. A. Chapter 34 - Neuroinflammation. in *Basic Neurochemistry* (eds. Brady, S. T., Siegel, G. J., Albers, R. W. & Price, D. L.) 610–620 (Academic Press, 2012). doi:10.1016/B978-0-12-374947-5.00034-1.

159. Harry, G. J. & Kraft, A. D. Neuroinflammation and Microglia: Considerations and approaches for neurotoxicity assessment. *Expert Opin Drug Metab Toxicol* **4**, 1265–1277 (2008).

160. Streit, W. J., Mrak, R. E. & Griffin, W. S. T. Microglia and neuroinflammation: a pathological perspective. *J Neuroinflammation* **1**, 14 (2004).

161. Guest, C. B., Park, M. J., Johnson, D. R. & Freund, G. G. The implication of proinflammatory cytokines in type 2 diabetes. *Front. Biosci.* **13**, 5187–5194 (2008).

162. Su, F., Bai, F. & Zhang, Z. Inflammatory Cytokines and Alzheimer's Disease: A Review from the Perspective of Genetic Polymorphisms. *Neurosci Bull* **32**, 469–480 (2016).

163. Volpe, C. M. O., Villar-Delfino, P. H., dos Anjos, P. M. F. & Nogueira-Machado, J. A. Cellular death, reactive oxygen species (ROS) and diabetic complications. *Cell Death & Disease* **9**, 1–9 (2018).

164. Morawe, T., Hiebel, C., Kern, A. & Behl, C. Protein homeostasis, aging and Alzheimer's disease. *Mol. Neurobiol.* **46**, 41–54 (2012).

165. Yerbury, J. J. *et al.* Walking the tightrope: proteostasis and neurodegenerative disease. *J. Neurochem.* **137**, 489–505 (2016).

166. Whitley, D., Goldberg, S. P. & Jordan, W. D. Heat shock proteins: A review of the molecular chaperones. *Journal of Vascular Surgery* **29**, 748–751 (1999).

167. Brehme, M. *et al.* A Chaperome Subnetwork Safeguards Proteostasis in Aging and Neurodegenerative Disease. *Cell Reports* **9**, 1135–1150 (2014).

168. Casas, S. *et al.* Impairment of the Ubiquitin-Proteasome Pathway Is a Downstream Endoplasmic Reticulum Stress Response Induced by Extracellular Human Islet Amyloid Polypeptide and Contributes to Pancreatic β-Cell Apoptosis. *Diabetes* **56**, 2284–2294 (2007).

169. Wang, J. & Maldonado, M. A. The ubiquitin-proteasome system and its role in inflammatory and autoimmune diseases. *Cell. Mol. Immunol.* **3**, 255–261 (2006).

170. Tundo, G. R. *et al.* The proteasome as a druggable target with multiple therapeutic potentialities: Cutting and non-cutting edges. *Pharmacology & Therapeutics* **213**, 107579 (2020).

171. Yu, Z. *et al.* Allosteric coupling between α-rings of the 20S proteasome. *bioRxiv* 832113 (2019) doi:10.1101/832113.

172. Kisselev, A. F., Callard, A. & Goldberg, A. L. Importance of the Different Proteolytic Sites of the Proteasome and the Efficacy of Inhibitors Varies with the Protein Substrate. *J. Biol. Chem.* **281**, 8582–8590 (2006).

173. Latham, M. P., Sekhar, A. & Kay, L. E. Understanding the mechanism of proteasome 20S core particle gating. *Proc Natl Acad Sci USA* **111**, 5532 (2014).

174. Groll, M. *et al.* A gated channel into the proteasome core particle. *Nat. Struct. Biol.* **7**, 1062–1067 (2000).

175. Santoro, A. M. *et al.* Cationic porphyrins are tunable gatekeepers of the 20S proteasome. *Chem. Sci.* **7**, 1286–1297 (2016).

176. Stadtmueller, B. M. & Hill, C. P. Proteasome Activators. *Mol Cell* **41**, 8–19 (2011).

177. Saeki, Y. Ubiquitin recognition by the proteasome. *J Biochem* **161**, 113–124 (2017).

178. Unverdorben, P. *et al.* Deep classification of a large cryo-EM dataset defines the conformational landscape of the 26S proteasome. *Proc Natl Acad Sci U S A* **111**, 5544–5549 (2014).

179. Bar-Nun, S. & Glickman, M. H. Proteasomal AAA-ATPases: Structure and function. *Biochimica et Biophysica Acta (BBA) - Molecular Cell Research* **1823**, 67–82 (2012).

180. Santoro, A. M. *et al.* Cationic Porphyrins Are Reversible Proteasome Inhibitors. *J. Am. Chem. Soc.* **134**, 10451–10457 (2012).

181. Ustrell, V., Hoffman, L., Pratt, G. & Rechsteiner, M. PA200, a nuclear proteasome activator involved in DNA repair. *EMBO J* **21**, 3516–3525 (2002).

182. Soza, A. *et al.* Expression and subcellular localization of mouse 20S proteasome activator complex PA28. *FEBS Lett.* **413**, 27–34 (1997).

183. Saeki, Y. & Tanaka, K. Unlocking the Proteasome Door. *Molecular Cell* **27**, 865–867 (2007).

184. Njomen, E. & Tepe, J. J. Proteasome Activation as a New Therapeutic Approach To Target Proteotoxic Disorders. *J Med Chem* **62**, 6469–6481 (2019).

185. Witkowska, J. *et al.* Crystal structure of a low molecular weight activator Blm-pep with yeast 20S proteasome – insights into the enzyme activation mechanism. *Sci Rep* **7**, 6177 (2017).

186. Förster, A., Whitby, F. G. & Hill, C. P. The pore of activated 20S proteasomes has an ordered 7-fold symmetric conformation. *EMBO J* **22**, 4356–4364 (2003).

187. Förster, A., Masters, E. I., Whitby, F. G., Robinson, H. & Hill, C. P. The 1.9 A structure of a proteasome-11S activator complex and implications for proteasome-PAN/PA700 interactions. *Mol. Cell* **18**, 589–599 (2005).

188. Sadre-Bazzaz, K., Whitby, F. G., Robinson, H., Formosa, T. & Hill, C. P. Structure of a Blm10 complex reveals common mechanisms for proteasome binding and gate opening. *Mol Cell* **37**, 728–735 (2010).

189. Ben-Nissan, G. & Sharon, M. Regulating the 20S proteasome ubiquitin-independent degradation pathway. *Biomolecules* **4**, 862–884 (2014).

190. Mishto, M. *et al.* Immunoproteasome and LMP2 polymorphism in aged and Alzheimer's disease brains. *Neurobiol. Aging* **27**, 54–66 (2006).

191. Ferrington, D. A. & Gregerson, D. S. Immunoproteasomes: Structure, Function, and Antigen Presentation. *Prog Mol Biol Transl Sci* **109**, 75–112 (2012).

192. Nathan, J. A. *et al.* Immuno- and Constitutive Proteasomes Do Not Differ in Their Abilities to Degrade Ubiquitinated Proteins. *Cell* **152**, 1184–1194 (2013).

193. Ciechanover, A. & Brundin, P. The ubiquitin proteasome system in neurodegenerative diseases: sometimes the chicken, sometimes the egg. *Neuron* **40**, 427–446 (2003).

194. Oddo, S. The ubiquitin-proteasome system in Alzheimer's disease. *J Cell Mol Med* **12**, 363–373 (2008).

195. Marfella, R. *et al.* The possible role of the ubiquitin proteasome system in the development of atherosclerosis in diabetes. *Cardiovasc Diabetol* **6**, 35 (2007).

196. Broca, C. *et al.* Proteasome Dysfunction Mediates High Glucose-Induced Apoptosis in Rodent Beta Cells and Human Islets. *PLOS ONE* **9**, e92066 (2014).

197. Choi, J. *et al.* Oxidative modifications and down-regulation of ubiquitin carboxyl-terminal hydrolase L1 associated with idiopathic Parkinson's and Alzheimer's diseases. *J. Biol. Chem.* **279**, 13256–13264 (2004).

198. Zhao, X. & Yang, J. Amyloid-β Peptide Is a Substrate of the Human 20S Proteasome. *ACS Chem. Neurosci.* **1**, 655–660 (2010).

199. David, D. C. *et al.* Proteasomal degradation of tau protein. *J. Neurochem.* **83**, 176–185 (2002).

200. Singh, S., Trikha, S., Sarkar, A. & Jeremic, A. M. Proteasome regulates turnover of toxic human amylin in pancreatic cells. *Biochem J* **473**, 2655–2670 (2016).

201. Keck, S., Nitsch, R., Grune, T. & Ullrich, O. Proteasome inhibition by paired helical filament-tau in brains of patients with Alzheimer's disease. *J. Neurochem.* **85**, 115–122 (2003).

202. Thibaudeau, T. A., Anderson, R. T. & Smith, D. M. A common mechanism of proteasome impairment by neurodegenerative disease-associated oligomers. *Nature Communications* **9**, 1097 (2018).

203. Tseng, B. P., Green, K. N., Chan, J. L., Blurton-Jones, M. & LaFerla, F. M. Aβ inhibits the proteasome and enhances amyloid and tau accumulation. *Neurobiol Aging* **29**, 1607–1618 (2008).

204. Fushman, D. & Wilkinson, K. D. Structure and recognition of polyubiquitin chains of different lengths and linkage. *F1000 Biol Rep* **3**, 26 (2011).

205. Bustamante, H. A. *et al.* Interplay Between the Autophagy-Lysosomal Pathway and the Ubiquitin-Proteasome System: A Target for Therapeutic Development in Alzheimer's Disease. *Front Cell Neurosci* **12**, 126 (2018).

206. Lutz, J., Höllmüller, E., Scheffner, M., Marx, A. & Stengel, F. The Length of a Ubiquitin Chain: A General Factor for Selective Recognition by Ubiquitin-Binding Proteins. *Angewandte Chemie International Edition* **59**, 12371–12375.

207. Thrower, J. S., Hoffman, L., Rechsteiner, M. & Pickart, C. M. Recognition of the polyubiquitin proteolytic signal. *EMBO J.* **19**, 94–102 (2000).

208. Shabek, N. *et al.* The size of the proteasomal substrate determines whether its degradation will be mediated by mono- or polyubiquitylation. *Mol. Cell* **48**, 87–97 (2012).

209. López Salon, M., Morelli, L., Castaño, E. M., Soto, E. F. & Pasquini, J. M. Defective ubiquitination of cerebral proteins in Alzheimer's disease. *J. Neurosci. Res.* **62**, 302–310 (2000).

210. Bellia, F. *et al.* Ubiquitin binds the amyloid β peptide and interferes with its clearance pathways. *Chem. Sci.* **10**, 2732–2742 (2019).

211. Lamark, T. & Johansen, T. Aggrephagy: Selective Disposal of Protein Aggregates by Macroautophagy. *International Journal of Cell Biology* **2012**, 736905 (2012).

212. Rahman, M. A. & Rhim, H. Therapeutic implication of autophagy in neurodegenerative diseases. *BMB Rep* **50**, 345–354 (2017).

213. Li, L., Zhang, X. & Le, W. Autophagy dysfunction in Alzheimer's disease. *Neurodegener Dis* **7**, 265–271 (2010).

214. Xin, S.-H., Tan, L., Cao, X., Yu, J.-T. & Tan, L. Clearance of Amyloid Beta and Tau in Alzheimer's Disease: from Mechanisms to Therapy. *Neurotoxicity Research* **34**, 733–748 (2018).

215. Hulse, R. E., Ralat, L. A. & Tang, W.-J. Structure, Function, and Regulation of Insulin-Degrading Enzyme. *Vitam Horm* **80**, 635–648 (2009).

216. Farris, W. *et al.* Insulin-degrading enzyme regulates the levels of insulin, amyloid β-protein, and the β-amyloid precursor protein intracellular domain in vivo. *PNAS* **100**, 4162–4167 (2003).

217. Hersh, L. B. & Rodgers, D. W. Neprilysin and amyloid beta peptide degradation. *Curr Alzheimer Res* **5**, 225–231 (2008).

218. Guan, H., Chow, K. M., Shah, R., Rhodes, C. J. & Hersh, L. B. Degradation of Islet Amyloid Polypeptide by Neprilysin. *Diabetologia* **55**, 2989–2998 (2012).

219. Grasso, G. *et al.* The insulin degrading enzyme activates ubiquitin and promotes the formation of K48 and K63 diubiquitin. *Chem Commun (Camb)* **51**, 15724–15727 (2015).

220. Kochkina, E. G. *et al.* Effects of ageing and experimental diabetes on insulin-degrading enzyme expression in male rat tissues. *Biogerontology* **16**, 473–484 (2015).

221. Hellström-Lindahl, E., Ravid, R. & Nordberg, A. Age-dependent decline of neprilysin in Alzheimer's disease and normal brain: Inverse correlation with Aβ levels. *Neurobiology of Aging* **29**, 210–221 (2008).

222. Wang, D.-S., Iwata, N., Hama, E., Saido, T. C. & Dickson, D. W. Oxidized neprilysin in aging and Alzheimer's disease brains. *Biochemical and Biophysical Research Communications* **310**, 236–241 (2003).

223. Newman, D. J. & Cragg, G. M. Natural Products as Sources of New Drugs from 1981 to 2014. *J. Nat. Prod.* **79**, 629–661 (2016).

224. Allegra, M. Antioxidant and Anti-Inflammatory Properties of Plants Extract. *Antioxidants (Basel)* **8**, 549 (2019).

225. Isah, T. Stress and defense responses in plant secondary metabolites production. *Biol Res* **52**, (2019).

226. Murakami, A. Modulation of protein quality control systems by food phytochemicals. *Journal of Clinical Biochemistry and Nutrition* **52**, 215–227 (2013).

227. Harvey, A. L. Natural products in drug discovery. *Drug Discovery Today* **13**, 894–901 (2008).

228. Power, R., Prado-Cabrero, A., Mulcahy, R., Howard, A. & Nolan, J. M. The Role of Nutrition for the Aging Population: Implications for Cognition and Alzheimer's Disease. *Annual Review of Food Science and Technology* **10**, 619–639 (2019).

229. Scarmeas, N., Stern, Y., Tang, M.-X., Mayeux, R. & Luchsinger, J. A. Mediterranean diet and risk for Alzheimer's disease. *Ann. Neurol.* **59**, 912–921 (2006).

230. Trichopoulou, A. *et al.* Mediterranean diet and cognitive decline over time in an elderly Mediterranean population. *Eur J Nutr* **54**, 1311–1321 (2015).

231. McEvoy, C. T., Guyer, H., Langa, K. M. & Yaffe, K. Neuroprotective diets are associated with better cognitive function: the Health and Retirement Study. *J Am Geriatr Soc* **65**, 1857–1862 (2017).

232. Lourida, I. *et al.* Mediterranean Diet, Cognitive Function, and Dementia: A Systematic Review. *Epidemiology* **24**, 479–489 (2013).

233. Bijak, M. Silybin, a Major Bioactive Component of Milk Thistle (Silybum marianum L. Gaernt.)-Chemistry, Bioavailability, and Metabolism. *Molecules* **22**, (2017).

234. Bai, T.-C., Zhu, J.-J., Hu, J., Zhang, H.-L. & Huang, C.-G. Solubility of silybin in aqueous hydrochloric acid solution. *Fluid Phase Equilibria* **254**, 204–210 (2007).

235. Saller, R., Brignoli, R., Melzer, J. & Meier, R. An updated systematic review with meta-analysis for the clinical evidence of silymarin. *Forsch Komplementmed* **15**, 9–20 (2008).

236. Wu, J.-W., Lin, L.-C. & Tsai, T.-H. Drug-drug interactions of silymarin on the perspective of pharmacokinetics. *J Ethnopharmacol* **121**, 185–193 (2009).

237. Abenavoli, L., Capasso, R., Milic, N. & Capasso, F. Milk thistle in liver diseases: past, present, future. *Phytother Res* **24**, 1423–1432 (2010).

238. Javed, S., Kohli, K. & Ali, M. Reassessing bioavailability of silymarin. *Altern Med Rev* **16**, 239–249 (2011).

239. Han, Y. H. *et al.* Stereoselective metabolism of silybin diastereoisomers in the glucuronidation process. *J Pharm Biomed Anal* **34**, 1071–1078 (2004).

240. Vargas-Mendoza, N. *et al.* Hepatoprotective effect of silymarin. *World J Hepatol* **6**, 144–149 (2014).

241. Fraschini, F., Demartini, G. & Esposti, D. Pharmacology of Silymarin. *Clinical Drug Investigation* **22**, 51–65 (2002).

242. Soleimani, V., Delghandi, P. S., Moallem, S. A. & Karimi, G. Safety and toxicity of silymarin, the major constituent of milk thistle extract: An updated review. *Phytother Res* **33**, 1627–1638 (2019).

243. Surai, P. F. Silymarin as a Natural Antioxidant: An Overview of the Current Evidence and Perspectives. *Antioxidants (Basel)* **4**, 204–247 (2015).

244. Trappoliere, M. *et al.* Silybin, a component of sylimarin, exerts anti-inflammatory and anti-fibrogenic effects on human hepatic stellate cells. *J. Hepatol.* **50**, 1102–1111 (2009).

245. Lovelace, E. S. *et al.* Silymarin Suppresses Cellular Inflammation By Inducing Reparative Stress Signaling. *J. Nat. Prod.* **78**, 1990–2000 (2015).

246. Oliyarnyk, O. *et al.* Comparative effect of silymarin and silybin treatment on inflammation and oxidative stress in transgenic spontaneously hypertensive rats overexpressing human C-reactive protein. *Atherosclerosis* **252**, e220 (2016).

247. Gupta, O. P. *et al.* Anti-inflammatory and anti-arthritic activities of silymarin acting through inhibition of 5-lipoxygenase. *Phytomedicine* **7**, 21–24 (2000).

248. Devi, K. P., Malar, D. S., Braidy, N., Nabavi, S. M. & Nabavi, S. F. A Mini Review on the Chemistry and Neuroprotective Effects of Silymarin. *Curr Drug Targets* **18**, 1529–1536 (2017).

249. Narayanamurthy, U., Santhakumari, A. S. & Nirmala, P. Nephroprotective effect of silymarin in hyperglycemia-induced oxidative stress in rats. *International Journal of Basic & Clinical Pharmacology* **3**, 1030–1035 (2017).

250. Zholobenko, A. & Modriansky, M. Silymarin and its constituents in cardiac preconditioning. *Fitoterapia* **97**, 122–132 (2014).

251. Kim, S.-H. *et al.* Silymarin induces inhibition of growth and apoptosis through modulation of the MAPK signaling pathway in AGS human gastric cancer cells. *Oncology Reports* **42**, 1904–1914 (2019).

252. Agarwal, C. *et al.* Anti-cancer efficacy of silybin derivatives -- a structure-activity relationship. *PLoS ONE* **8**, e60074 (2013).

253. Ramasamy, K. & Agarwal, R. Multitargeted therapy of cancer by silymarin. *Cancer Lett* **269**, 352–362 (2008).

254. Pushpakom, S. *et al.* Drug repurposing: progress, challenges and recommendations. *Nat Rev Drug Discov* **18**, 41–58 (2019).

255. Duan, S. *et al.* Silibinin inhibits acetylcholinesterase activity and amyloid beta peptide aggregation: a dual-target drug for the treatment of Alzheimer's disease. *Neurobiol Aging* **36**, 1792–1807 (2015).

256. Lu, P. *et al.* Silibinin prevents amyloid beta peptide-induced memory impairment and oxidative stress in mice. *Br J Pharmacol* **157**, 1270–1277 (2009).

257. Yin, F. *et al.* Silibinin: a novel inhibitor of Aβ aggregation. *Neurochem. Int.* **58**, 399–403 (2011).

258. Yaghmaei, P., Azarfar, K., Dezfulian, M. & Ebrahim-Habibi, A. Silymarin effect on amyloid-β plaque accumulation and gene expression of APP in an Alzheimer's disease rat model. *Daru* **22**, 24 (2014).

259. Guo, H. *et al.* Silymarin's Inhibition and Treatment Effects for Alzheimer's Disease. *Molecules* **24**, 1748 (2019).

260. Sciacca, M. F. M. *et al.* Inhibition of Abeta Amyloid Growth and Toxicity by Silybins: The Crucial Role of Stereochemistry. *ACS Chem Neurosci* **8**, 1767–1778 (2017).

261. Young, L. M., Cao, P., Raleigh, D. P., Ashcroft, A. E. & Radford, S. E. Ion Mobility Spectrometry–Mass Spectrometry Defines the Oligomeric Intermediates in Amylin Amyloid Formation and the Mode of Action of Inhibitors. *J. Am. Chem. Soc.* **136**, 660–670 (2014).

262. Cheng, B. *et al.* Silibinin inhibits the toxic aggregation of human islet amyloid polypeptide. *Biochem Biophys Res Commun* **419**, 495–499 (2012).

263. Chu, C. *et al.* Role of silibinin in the management of diabetes mellitus and its complications. *Arch. Pharm. Res.* **41**, 785–796 (2018).

264. Najjar, A. & Karaman, R. The prodrug approach in the era of drug design. *Expert Opinion on Drug Delivery* **16**, 1–5 (2019).

265. Rautio, J., Meanwell, N. A., Di, L. & Hageman, M. J. The expanding role of prodrugs in contemporary drug design and development. *Nature Reviews Drug Discovery* **17**, 559–587 (2018).

266. Wadhwa, M. S. & Rice, K. G. Receptor mediated glycotargeting. *J Drug Target* **3**, 111–127 (1995).

267. Crowe, J. H. Trehalose as a 'chemical chaperone': fact and fantasy. *Adv. Exp. Med. Biol.* **594**, 143–158 (2007).

268. Du, J., Liang, Y., Xu, F., Sun, B. & Wang, Z. Trehalose rescues Alzheimer's disease phenotypes in APP/PS1 transgenic mice. *J Pharm Pharmacol* **65**, 1753–1756 (2013).

269. Portbury, S. D. *et al.* Trehalose Improves Cognition in the Transgenic Tg2576 Mouse Model of Alzheimer's Disease. *Journal of Alzheimer's Disease* **60**, 549–560 (2017).

270. Khalifeh, M., Barreto, G. E. & Sahebkar, A. Trehalose as a promising therapeutic candidate for the treatment of Parkinson's disease. *British Journal of Pharmacology* **176**, 1173–1189 (2019).

271. Rodríguez-Navarro, J. A. *et al.* Trehalose ameliorates dopaminergic and tau pathology in parkin deleted/tau overexpressing mice through autophagy activation. *Neurobiology of Disease* **39**, 423–438 (2010).

272. Sarkar, S. *et al.* Neuroprotective effect of the chemical chaperone, trehalose in a chronic MPTP-induced Parkinson's disease mouse model. *NeuroToxicology* **44**, 250–262 (2014).

273. Tanaka, M. *et al.* Trehalose alleviates polyglutamine-mediated pathology in a mouse model of Huntington disease. *Nat Med* **10**, 148–154 (2004).

274. Castillo, K. *et al.* Trehalose delays the progression of amyotrophic lateral sclerosis by enhancing autophagy in motoneurons. *Autophagy* **9**, 1308–1320 (2013).

275. Liu, R., Barkhordarian, H., Emadi, S., Park, C. B. & Sierks, M. R. Trehalose differentially inhibits aggregation and neurotoxicity of beta-amyloid 40 and 42. *Neurobiol. Dis.* **20**, 74–81 (2005).

276. Lee, H.-J., Yoon, Y.-S. & Lee, S.-J. Mechanism of neuroprotection by trehalose: controversy surrounding autophagy induction. *Cell Death & Disease* **9**, 1–12 (2018).

277. Agholme, L., Lindström, T., Kågedal, K., Marcusson, J. & Hallbeck, M. An in vitro model for neuroscience: differentiation of SH-SY5Y cells into cells with morphological and biochemical characteristics of mature neurons. *J. Alzheimers Dis.* **20**, 1069–1082 (2010).

278. Raval, N. *et al.* Chapter 10 - Importance of Physicochemical Characterization of Nanoparticles in Pharmaceutical Product Development. in *Basic Fundamentals of Drug Delivery* (ed. Tekade, R. K.) 369–400 (Academic Press, 2019). doi:10.1016/B978-0-12-817909-3.00010-8.

279. Campos, A. M. & Lissi, E. A. Kinetics of the reaction between 2,2'-azinobis (3-ethylbenzothiazoline-6-sulfonic acid (ABTS) derived radical cations and phenols. *International Journal of Chemical Kinetics* **29**, 219–224 (1997).

280. Henriquez, C., Aliaga, C. & Lissi, E. Kinetics profiles in the reaction of ABTS derived radicals with simple phenols and polyphenols. *Journal of the Chilean Chemical Society* **49**, 65–67 (2004).

281. Sekher Pannala, A., Chan, T. S., O'Brien, P. J. & Rice-Evans, C. A. Flavonoid B-ring chemistry and antioxidant activity: fast reaction kinetics. *Biochem. Biophys. Res. Commun.* **282**, 1161–1168 (2001).

282. Katano, H., Tanaka, R., Maruyama, C. & Hamano, Y. Assay of enzymes forming AMP+PPi by the pyrophosphate determination based on the formation of 18-molybdopyrophosphate. *Anal. Biochem.* **421**, 308–312 (2012).

283. Santoro, A. M. *et al.* Pyrazolones Activate the Proteasome by Gating Mechanisms and Protect Neuronal Cells from β-Amyloid Toxicity. *ChemMedChem* **15**, 302–316 (2020).

284. Borissenko, L. & Groll, M. 20S Proteasome and Its Inhibitors: Crystallographic Knowledge for Drug Development. *Chem. Rev.* **107**, 687–717 (2007).

285. Giżyńska, M. *et al.* Proline- and Arginine-Rich Peptides as Flexible Allosteric Modulators of Human Proteasome Activity. *J. Med. Chem.* **62**, 359–370 (2019).

286. Jankowska, E. *et al.* Potential allosteric modulators of the proteasome activity. *Biopolymers* **93**, 481–495 (2010).

287. Dato, A. D. *et al.* Electrostatic Map Of Proteasome α-Rings Encodes The Design of Allosteric Porphyrin-Based Inhibitors Able To Affect 20S Conformation By Cooperative Binding. *Scientific Reports* **7**, 17098 (2017).

288. Hosogi, N., Nishioka, H. & Nakakoshi, M. Evaluation of lanthanide salts as alternative stains to uranyl acetate. *Microscopy (Oxf)* **64**, 429–435 (2015).

289. Greenfield, N. J. Using circular dichroism spectra to estimate protein secondary structure. *Nature protocols* **1**, 2876 (2006).

290. Lanza, V. *et al.* Ubiquitin Associates with the N-Terminal Domain of Nerve Growth Factor: The Role of Copper(II) Ions. *Chemistry – A European Journal* **22**, 17767–17775 (2016).

291. Adzhubei, A. A., Sternberg, M. J. E. & Makarov, A. A. Polyproline-II Helix in Proteins: Structure and Function. *Journal of Molecular Biology* **425**, 2100–2132 (2013).

292. Rustenbeck, I., Matthies, A. & Lenzen, S. Lipid composition of glucose-stimulated pancreatic islets and insulin-secreting tumor cells. *Lipids* **29**, 685–692 (1994).

293. Khemtémourian, L. *et al.* The role of the disulfide bond in the interaction of islet amyloid polypeptide with membranes. *Eur Biophys J* **39**, 1359–1364 (2010).

294. Chen, J. & Kriwacki, R. W. Intrinsically Disordered Proteins: Structure, Function and Therapeutics. *J. Mol. Biol.* **430**, 2275–2277 (2018).

295. Goldflam, M., Tarragó, T., Gairí, M. & Giralt, E. NMR studies of protein-ligand interactions. *Methods in molecular biology* **831**, 233–259 (2012).

296. Ahmed, R. *et al.* Atomic resolution map of the soluble amyloid beta assembly toxic surfaces. *Chem Sci* **10**, 6072–6082 (2019).

297. Blochliger, N., Vitalis, A. & Caflisch, A. High-resolution visualisation of the states and pathways sampled in molecular dynamics simulations. *Sci Rep* **4**, 6264 (2014).

298. Shoval, H., Lichtenberg, D. & Gazit, E. The molecular mechanisms of the anti-amyloid effects of phenols. *Amyloid* **14**, 73–87 (2007).

299. Gargari, S. A., Barzegar, A. & Tarinejad, A. The role of phenolic OH groups of flavonoid compounds with H-bond formation ability to suppress amyloid mature fibrils by destabilizing β-sheet conformation of monomeric Aβ17-42. *PLOS ONE* **13**, e0199541 (2018).

300. A, P. *et al.* Anti-amyloidogenic properties of some phenolic compounds. *Biomolecules* **5**, 505–527 (2015).

301. Romanucci, V. *et al.* Silibinin phosphodiester glyco-conjugates: Synthesis, redox behaviour and biological investigations. *Bioorganic Chemistry* **77**, 349–359 (2018).

302. Di Fabio, G., Romanucci, V., Di Marino, C., De Napoli, L. & Zarrelli, A. A rapid and simple chromatographic separation of diastereomers of silibinin and their oxidation to produce 2,3-dehydrosilybin enantiomers in an optically pure form. *Planta Med* **79**, 1077–1080 (2013).

303. Szurmai, Z., Kerékgyártó, J., Harangi, J. & Lipták, A. Glycosylated trehalose. Synthesis of the oligosaccharides of the glycolipid-type antigens from Mycobacterium smegmatis. *Carbohydrate Research* **164**, 313–325 (1987).

304. Giuffrida, M. L. *et al.* Beta-amyloid monomers are neuroprotective. *J. Neurosci.* **29**, 10582–10587 (2009).

305. Dantuma, N. P., Lindsten, K., Glas, R., Jellne, M. & Masucci, M. G. Short-lived green fluorescent proteins for quantifying ubiquitin/proteasome-dependent proteolysis in living cells. *Nature Biotechnology* **18**, 538–543 (2000).

306. Stewart, J. C. M. Colorimetric determination of phospholipids with ammonium ferrothiocyanate. *Analytical Biochemistry* **104**, 10–14 (1980).

307. Fletcher, R. *Unconstrained optimization. In Practical Methods of Optimization*. vol. 1 (John Wiley & Sons Ltd., 1980).

308. Ewig, C. S. *et al.* Derivation of class II force fields. VIII. Derivation of a general quantum mechanical force field for organic compounds. *J Comput Chem* **22**, 1782–1800 (2001).

309. Davis, I. W. *et al.* MolProbity: all-atom contacts and structure validation for proteins and nucleic acids. *Nucleic Acids Res.* **35**, W375-383 (2007).

310. Senderowitz, H., Guarnieri, F. & Still, W. C. A Smart Monte Carlo Technique for Free Energy Simulations of Multiconformational Molecules. Direct Calculations of the Conformational Populations of Organic Molecules. *J. Am. Chem. Soc.* **117**, 8211–8219 (1995).

311. Ding, H., Karasawa, N. & Goddard, W. A. Atomic level simulations on a million particles: The cell multipole method for Coulomb and London nonbond interactions. *J. Chem. Phys.* **97**, 4309–4315 (1992).

312. Steinbach, P. J. & Brooks, B. R. New spherical-cutoff methods for long-range forces in macromolecular simulation. *Journal of Computational Chemistry* **15**, 667–683 (1994).

313. Huang, J. *et al.* CHARMM36m: an improved force field for folded and intrinsically disordered proteins. *Nature Methods* **14**, 71–73 (2017).

Supplementary material

20S proteasome preliminary assay

A preliminary experiment was done to optimize the experimental conditions of the assay. Silybins were added and pre-mixed to the reaction buffer and incubated during different times before the addition of the proteasome sample. Then, a standard incubation time (for 30 min) proceeded, and the enzymatic reaction started following the addition of the substrate. Supplementary figure S1 evidence that both silybins activate y20S proteasome when the proteasome was added immediately after the silybins (time zero). On the contrary, their stimulating ability decreased when the "pre-mixed" time increased and, after 30 minutes, we observed a total loss of its activity, detecting values similar to control. This result confirms the tendency of silybins to form self-aggregates; extending the incubation time in water solution, the concentration of active monomeric form is reduced, causing a reduced effect on the proteasome.

Therefore, the experiments described in this thesis were performed by adding the proteasome and silybins consecutively, limiting the time that silybins are in the buffer solution without the proteasome, to avoid the formation of silybin self-aggregates.

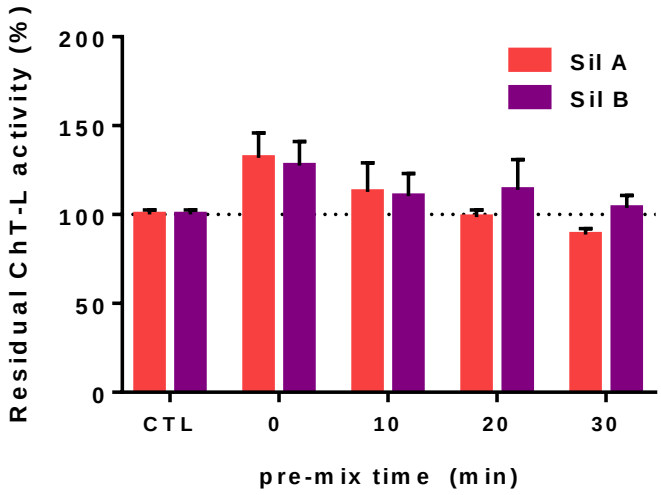

Supplementary figure S1. Normalized values of ChT-L residual activity of y20S measured in presence of 5µM Sil A (red bars) or Sil B (purple bars) at increasing pre-mixing times. Assay buffer: 50 mM Tris buffer (pH 8), 37°C. Results are reported as the normalized percentage of residual activity (± SEM).

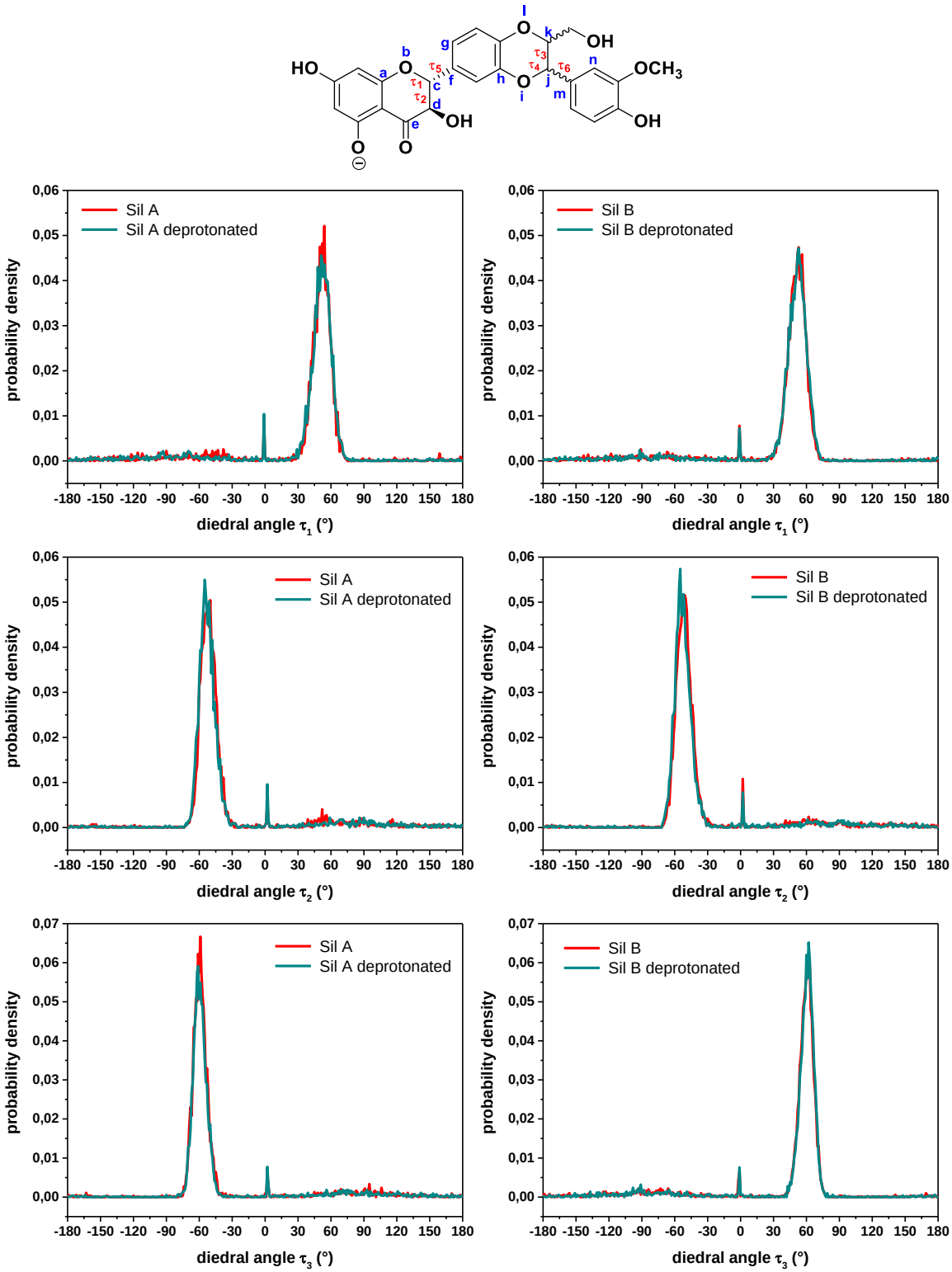

Supplementary figure S2 – Dihedral angles of Sil A and Sil B in their protonated and monodeprotonated (in the hydroxyl group in position 5) states. (a) Torsional angles τ_1, τ_2, τ_3,τ_4, τ_5, and τ_6 defined by the atoms indicated in the figure as abcd, bcde, ijkl, hijk, bcfg, and kjmn, respectively. **(b)** Probability density distribution of the dihedral angle τ_1 of Sil A in both protonated and monodeprotonated states. **(c)** As (b) except for Sil B. **(d)** As (b) except for dihedral angle τ_2. **(e)** As (d) except for Sil B. **(f)** As (b) except for dihedral angle τ_3. **(e)** As (f) except for Sil B.

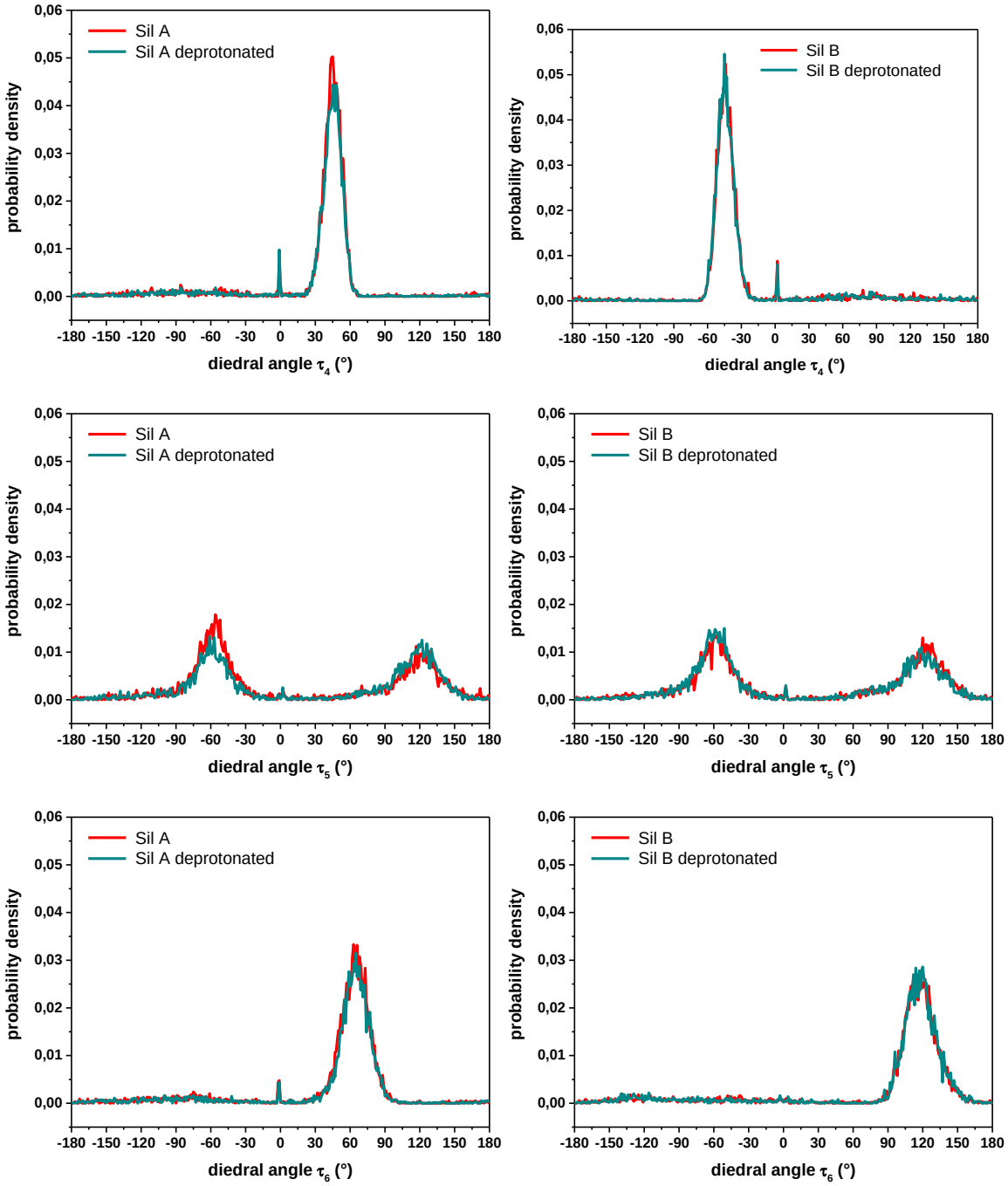

Supplementary figure S3 – Dihedral angles of Sil A and Sil B in their protonated and monodeprotonated (in the hydroxyl group in position 5) states. (a) Probability density distribution of the dihedral angle τ_4 of Sil A in both protonated and monodeprotonated states. **(b)** As (a) except for Sil B. **(c)** As (b) except for dihedral angle τ_5. **(d)** As (c) except for Sil B. **(e)** As (a) except for dihedral angle τ_6. **(f)** As (e) except for Sil B.

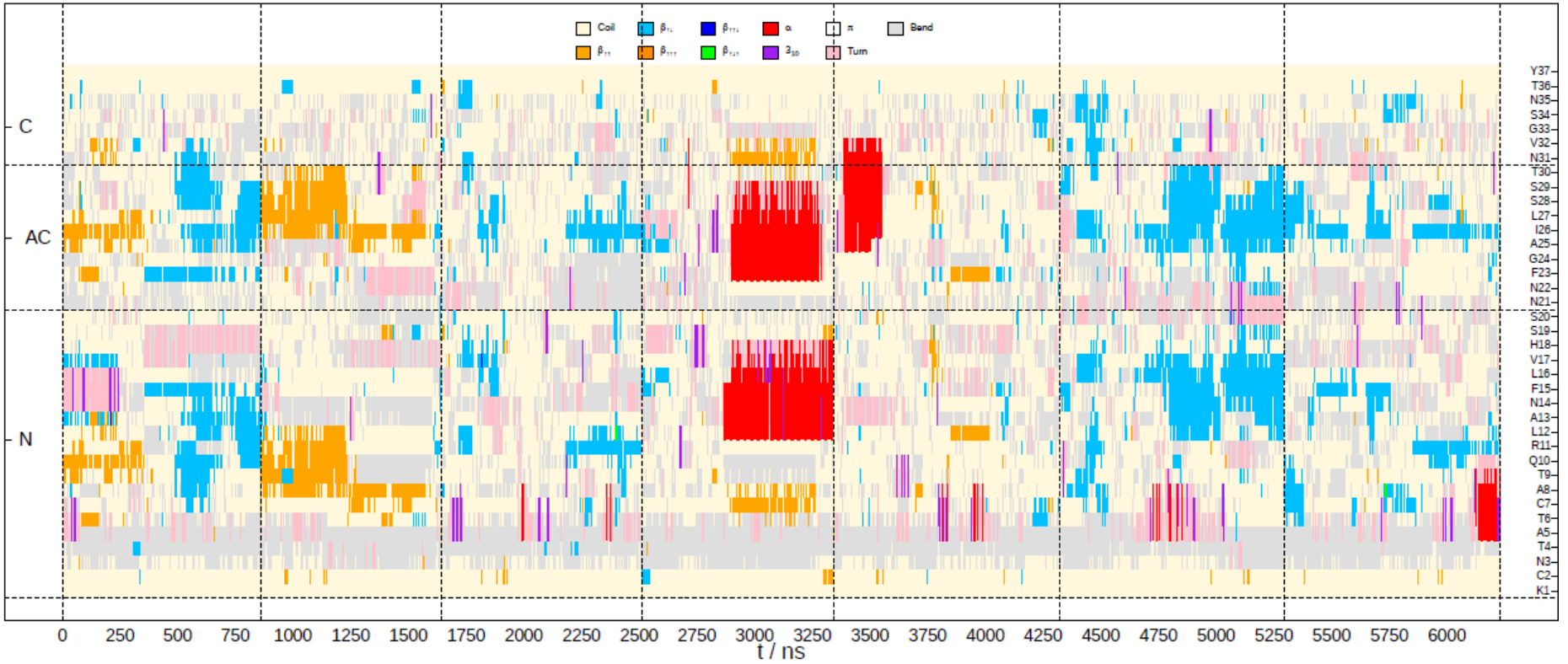

Supplementary Figure S4 – Secondary structure assignment (DSSP). DSSP to the amino acids of hIAPP throughout the concatenated simulations.

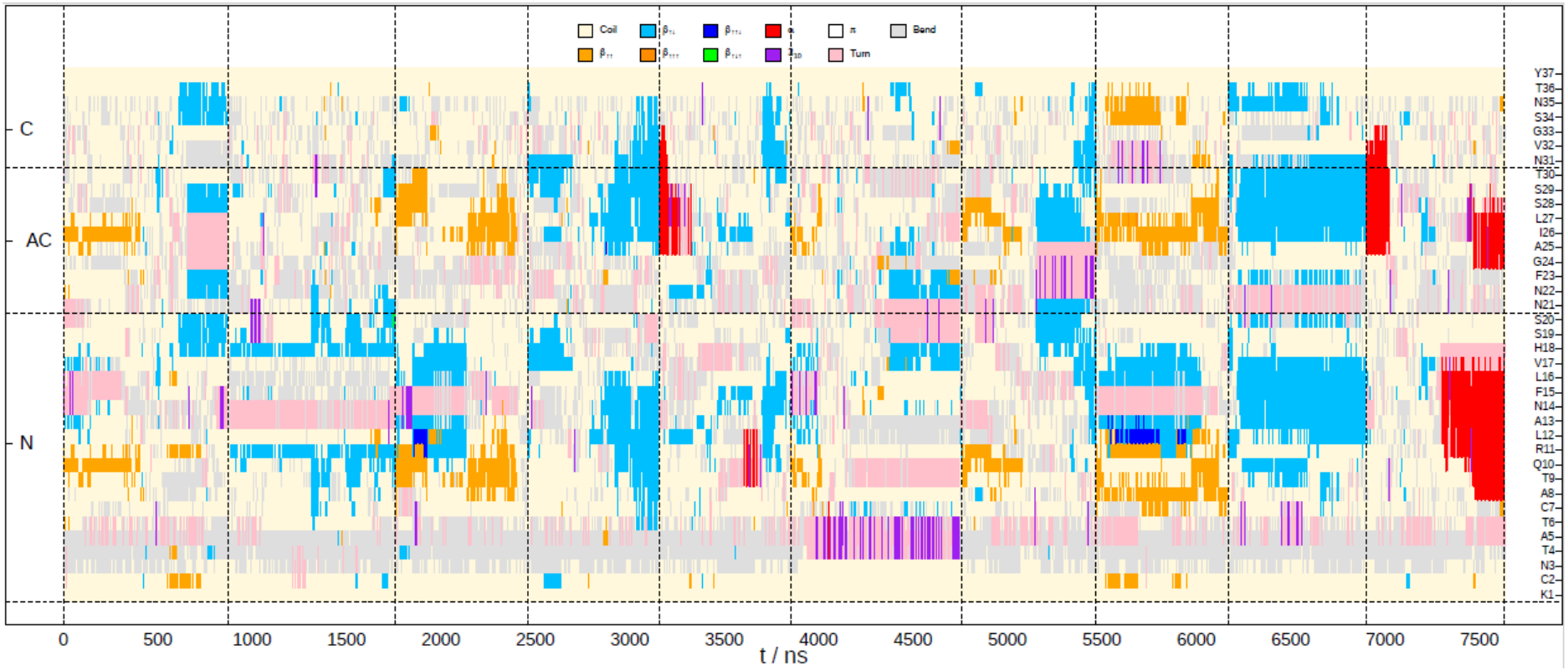

Supplementary Figure S5 – Secondary structure assignment (DSSP). DSSP to the amino acids of hIAPP throughout the concatenated simulations performed in the presence of SilA in a peptide/ligand ratio 1:1)

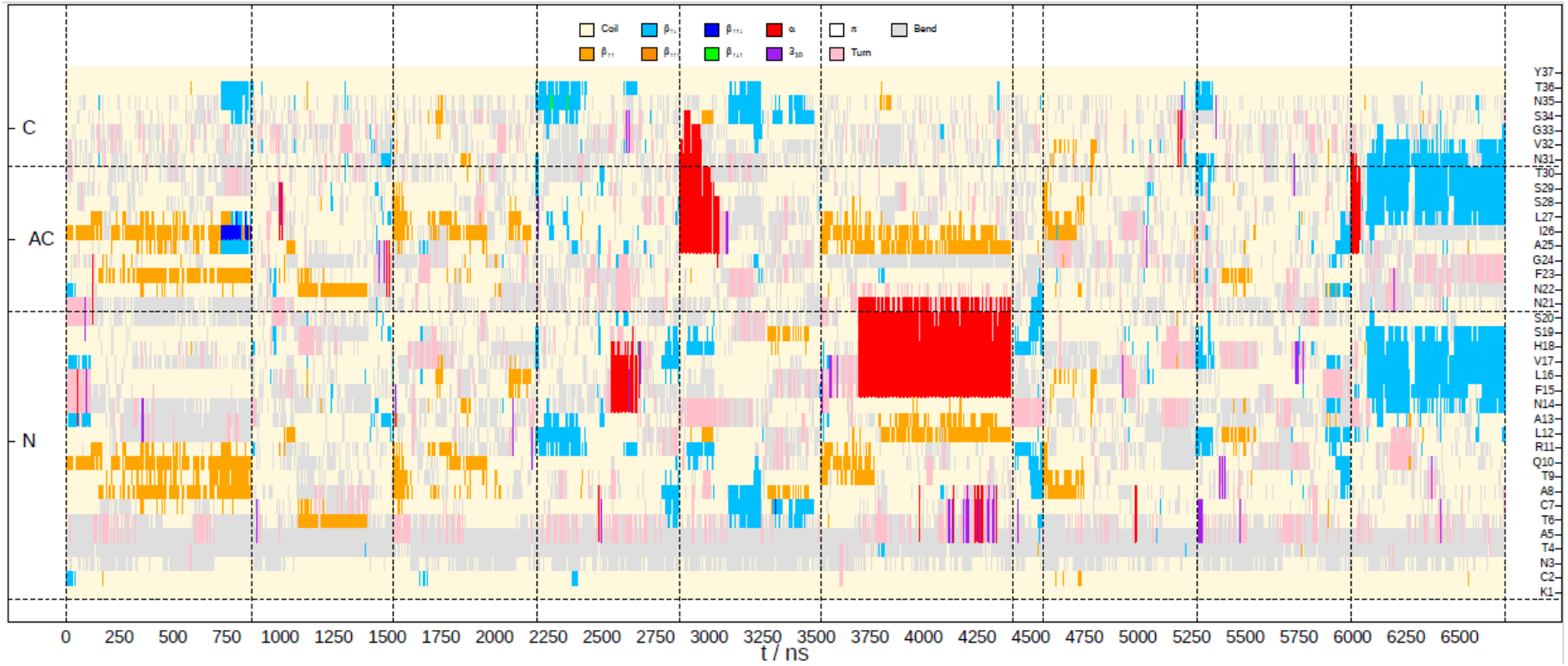

Supplementary Figure S6 – Secondary structure assignment (DSSP). DSSP to the amino acids of hIAPP throughout the concatenated simulations performed in the presence of SilA in a peptide/ligand ratio 1:2).

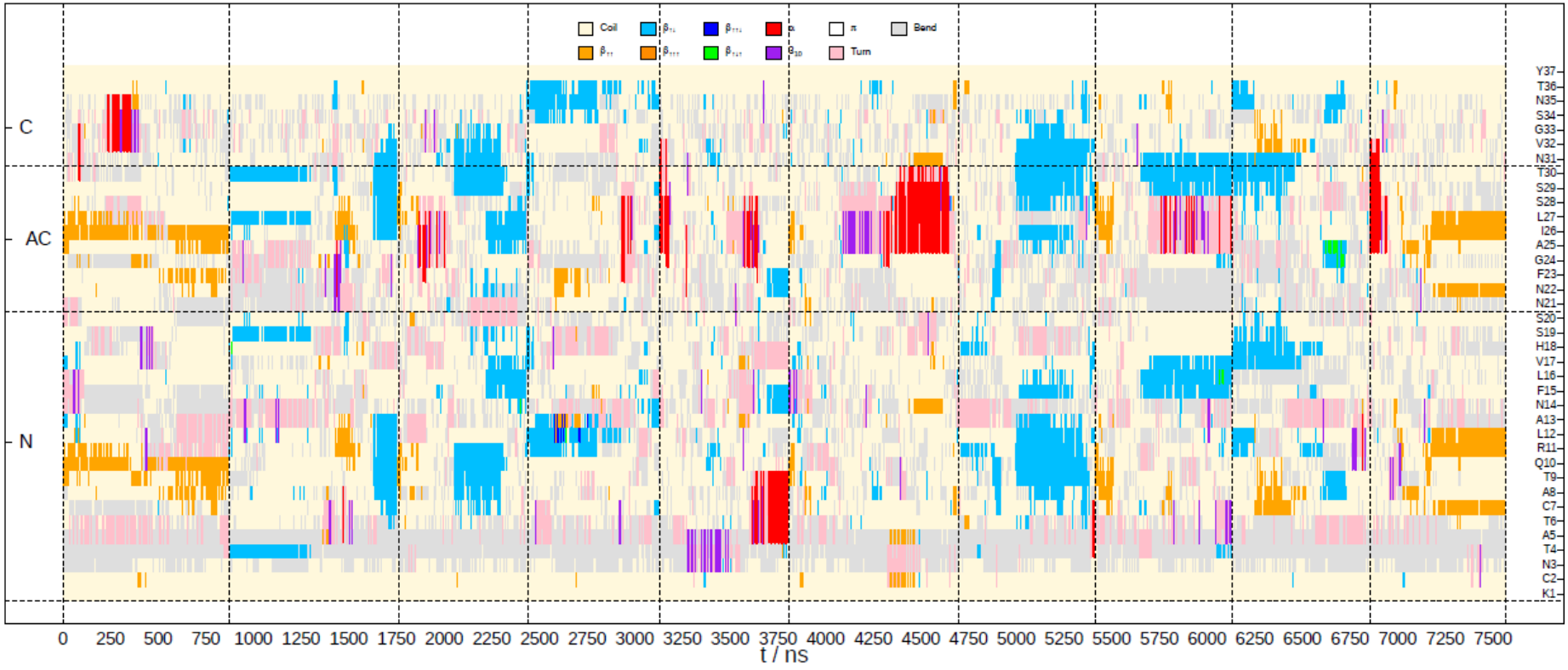

Supplementary Figure S7 – Secondary structure assignment (DSSP). DSSP to the amino acids of hIAPP throughout the concatenated simulations performed in the presence of SilB in a peptide/ligand ratio 1:1)

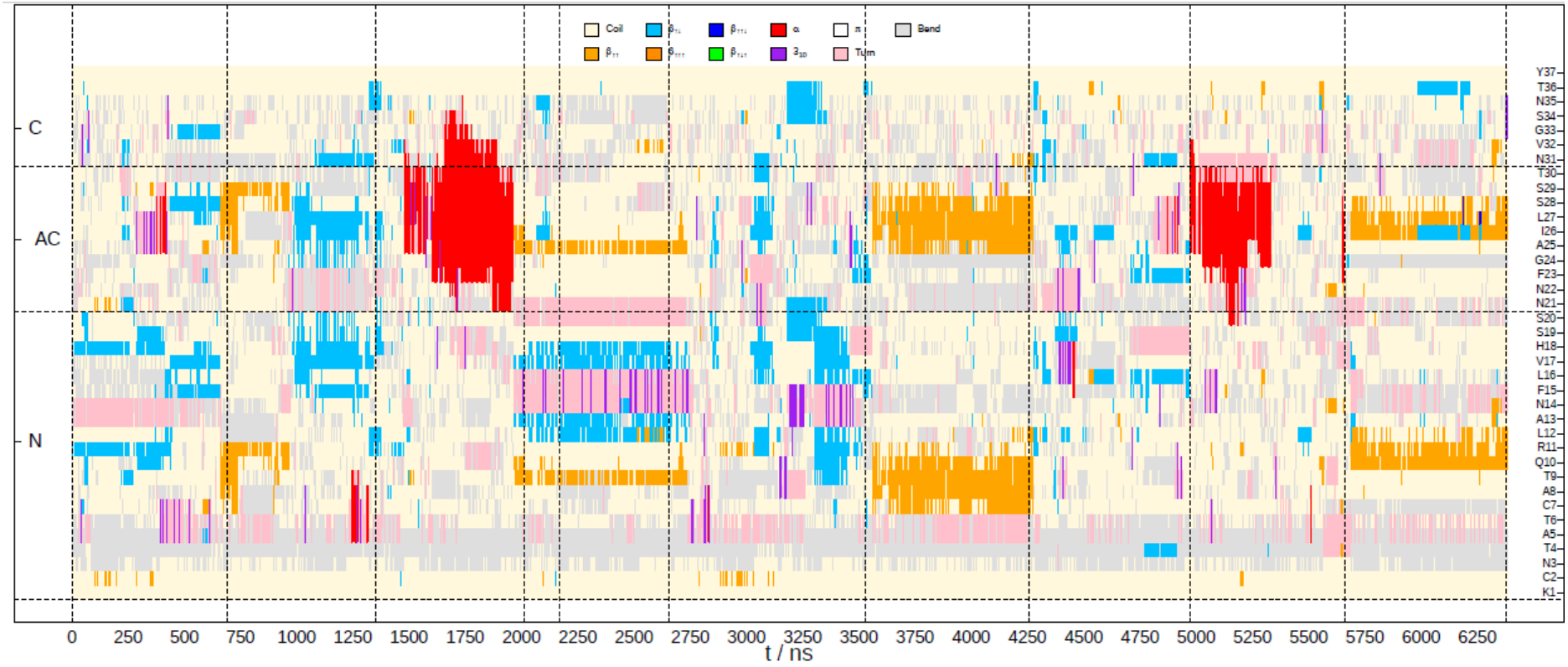

Supplementary Figure S8 – Secondary structure assignment (DSSP). DSSP to the amino acids of hIAPP throughout the concatenated simulations performed in the presence of SilB in a peptide/ligand ratio 1:2).

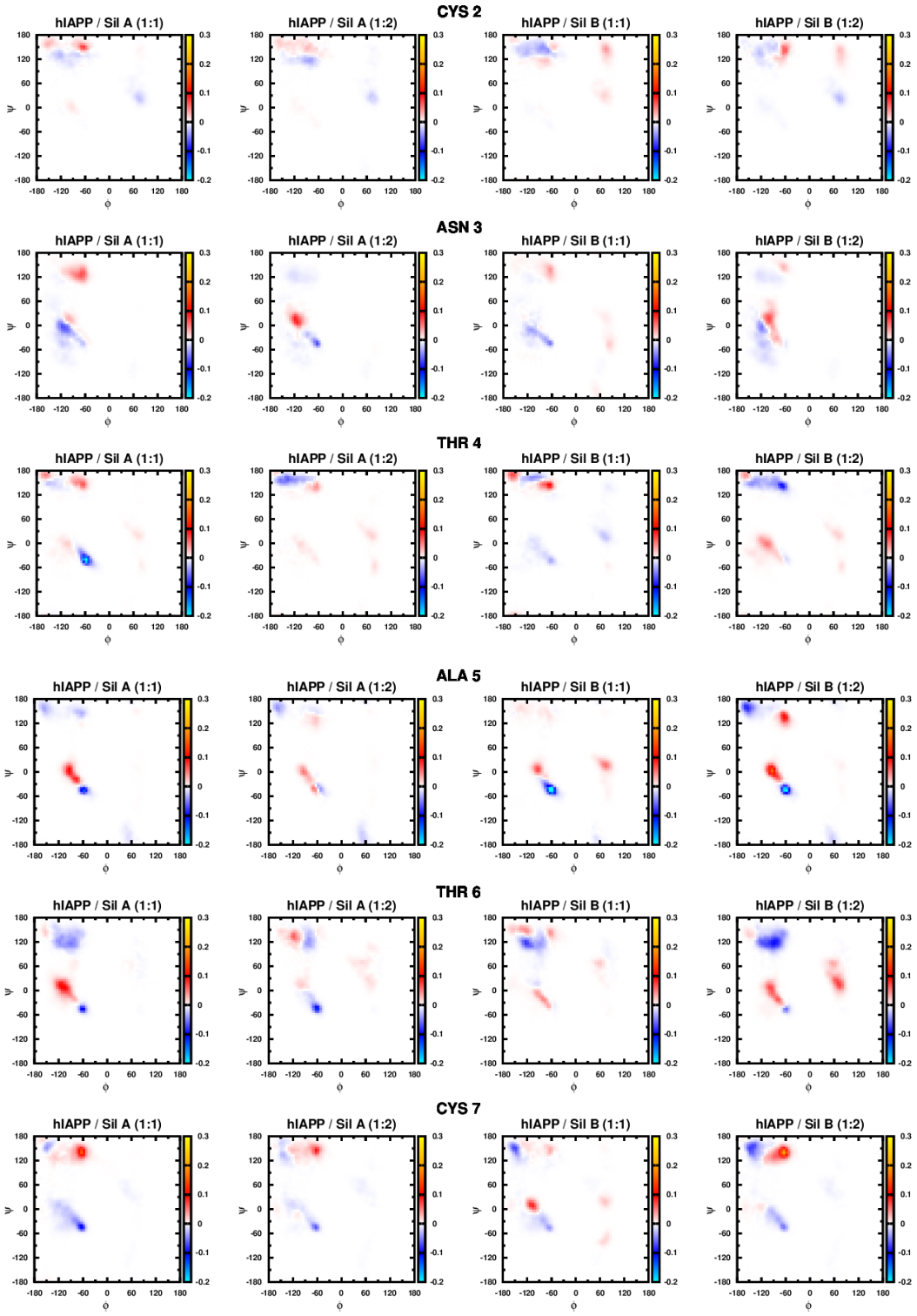

Supplementary Figure S9 – Changes in Ramachandran probability distributions of the residues C2, N3, T4 A5, T6, and C7. Data are represented as the difference between Ramachandran probability distributions of hIAPP in the presence and absence of the ligand. From left to right: hIAPP in presence of Sil A in peptide/ligand ratios 1:1 and 1:2 and hIAPP in presence of Sil B in peptide/ligand ratios 1:1 and 1:2. Positive values (represented in red) indicate an increase in the probability of these dihedral angles and, henceforth, of the corresponding structure, while negative values (represented in blue) indicate a decrease of it.

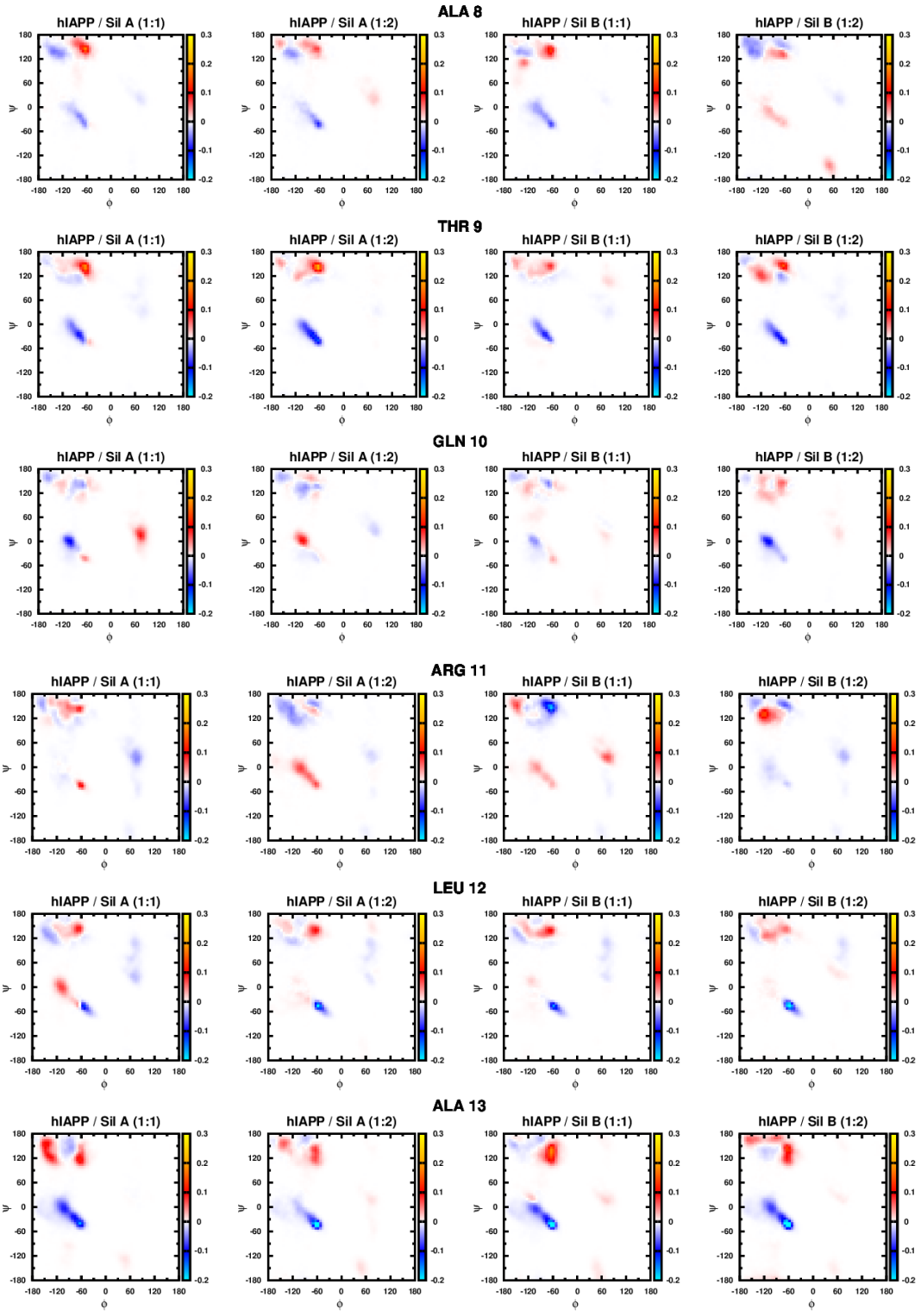

Supplementary Figure S10 – Changes in Ramachandran probability distributions of the residues A8, T9, Q10, R11, L12, and A13. Data are represented as the difference between Ramachandran probability distributions of hIAPP in the presence and absence of the ligand. From left to right: hIAPP in presence of SilA in peptide/ligand ratios 1:1 and 1:2 and hIAPP in presence of Sil B in peptide/ligand ratios 1:1 and 1:2. Positive values (represented in red) indicate an increase in the probability of these dihedral angles and, henceforth, of the corresponding structure, while negative values (represented in blue) indicate a decrease of it.

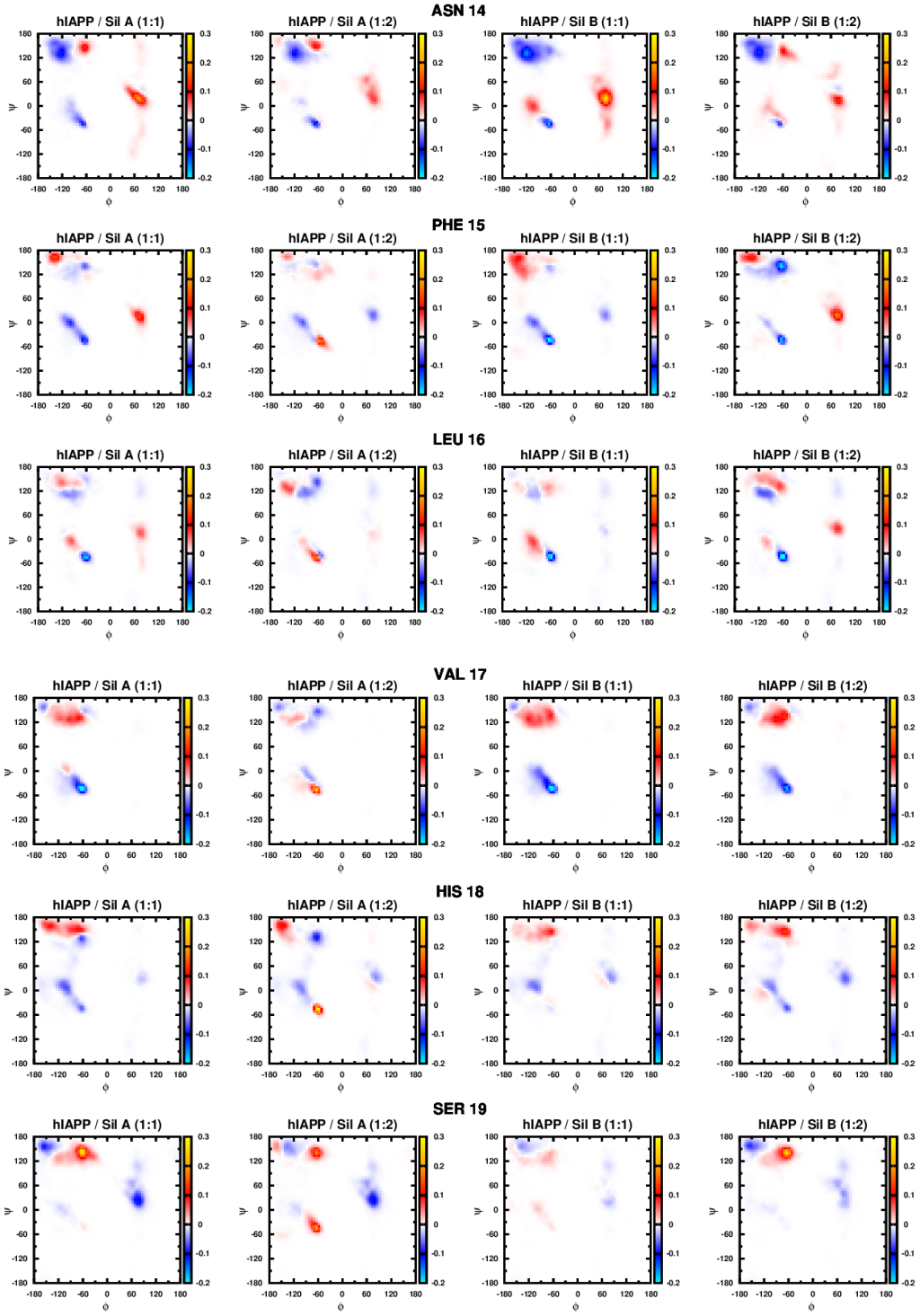

Supplementary Figure S11 – Changes in Ramachandran probability distributions of the residues N14, F15, L16, V17, H18 and S19. Data are represented as the difference between Ramachandran probability distributions of hIAPP in the presence and absence of the ligand. From left to right: hIAPP in presence of SilA in peptide/ligand ratios 1:1 and 1:2 and hIAPP in presence of Sil B in peptide/ligand ratios 1:1 and 1:2. Positive values (represented in red) indicate an increase in the probability of these dihedral angles and, henceforth, of the corresponding structure, while negative values (represented in blue) indicate a decrease of it.

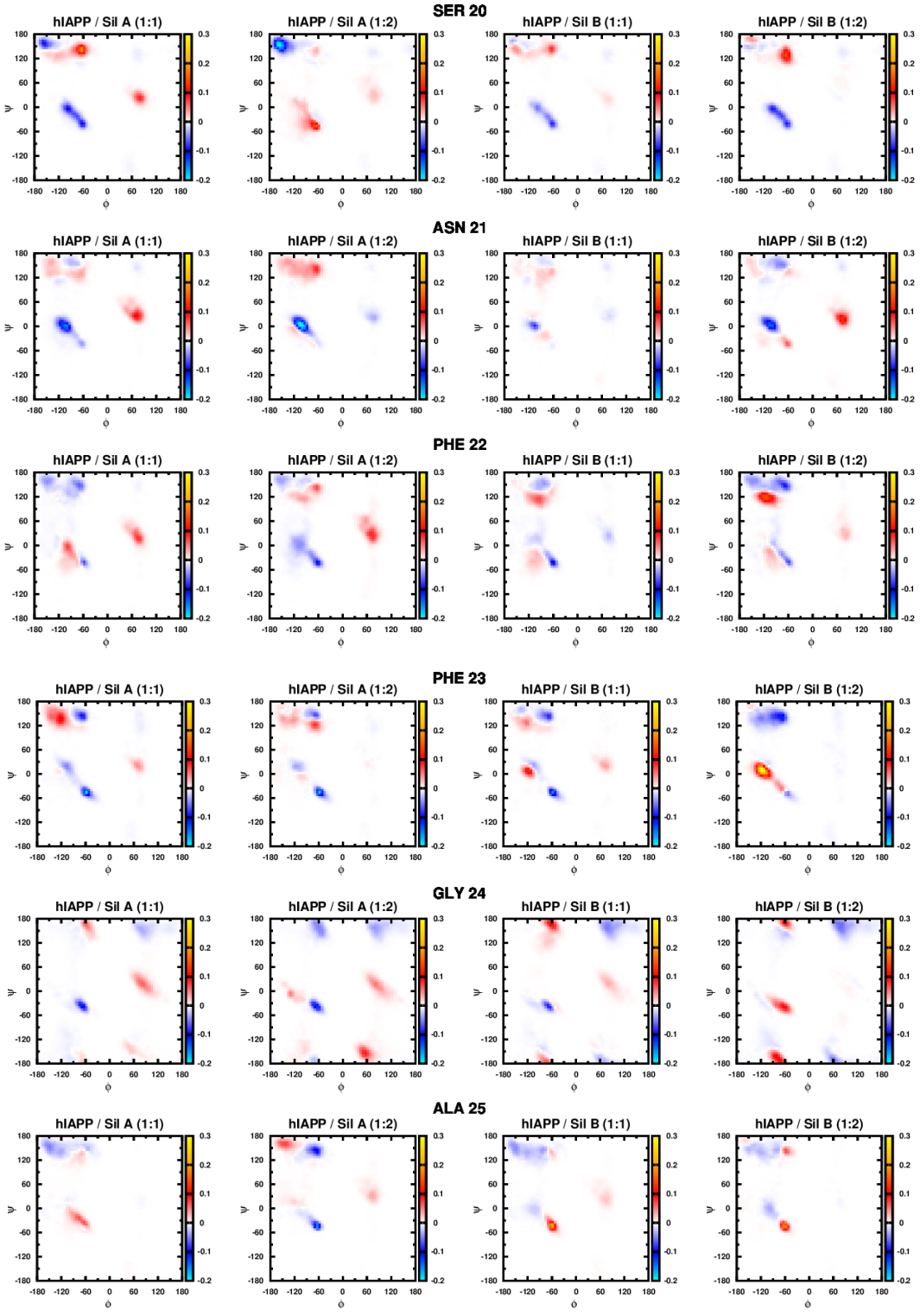

Supplementary Figure S12 – Changes in Ramachandran probability distributions of the residues S20, N21, N22, F23, G24 and A25. Data are represented as the difference between Ramachandran probability distributions of hIAPP in the presence and absence of the ligand. From left to right: hIAPP in presence of SilA in peptide/ligand ratios 1:1 and 1:2 and hIAPP in presence of Sil B in peptide/ligand ratios 1:1 and 1:2. Positive values (represented in red) indicate an increase in the probability of these dihedral angles and, henceforth, of the corresponding structure, while negative values (represented in blue) indicate a decrease of it.

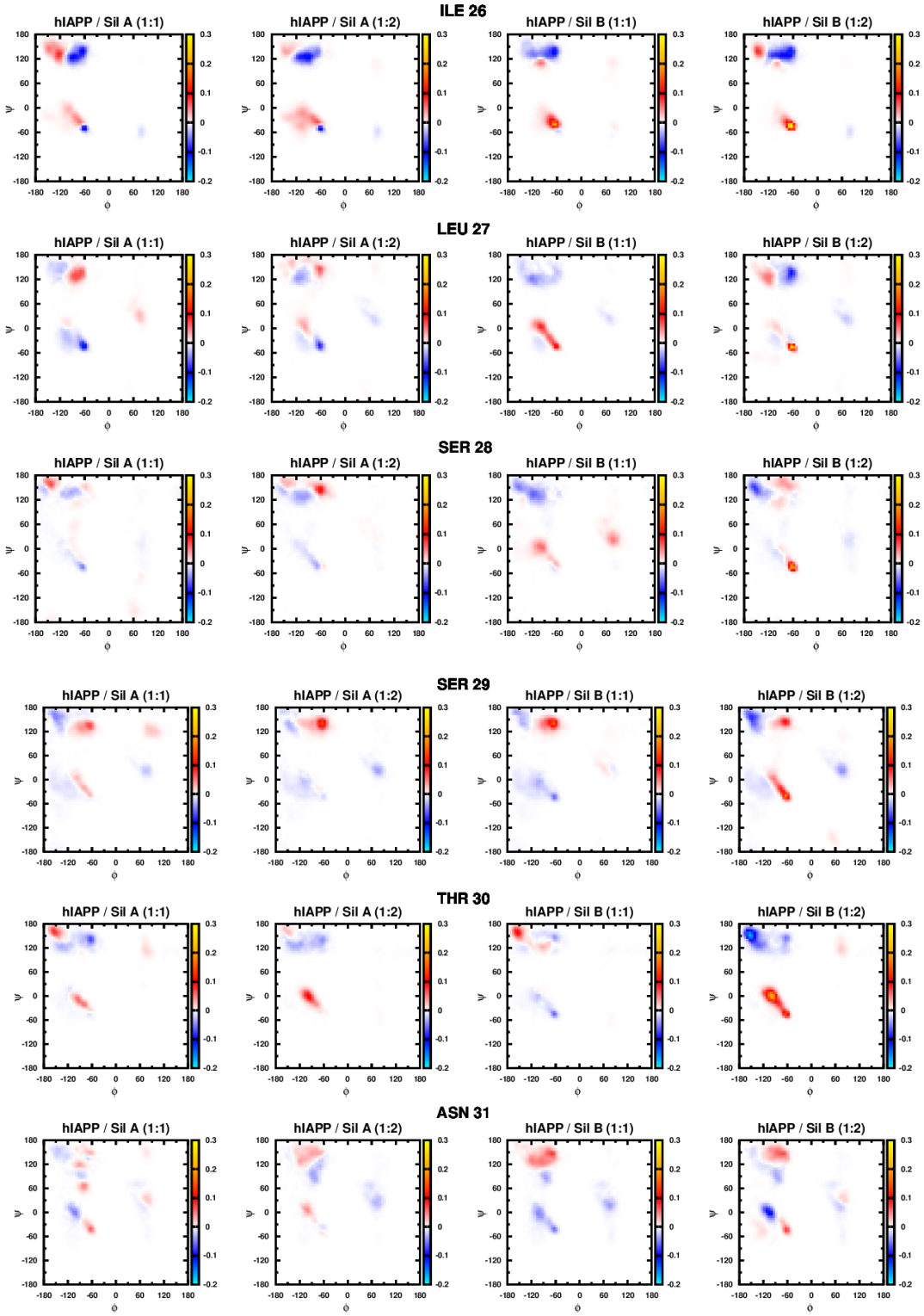

Supplementary Figure S12 – Changes in Ramachandran probability distributions of the residues I26, L27, S28, S29, T30, N31. Data are represented as the difference between Ramachandran probability distributions of hIAPP in the presence and absence of the ligand. From left to right: hIAPP in presence of SilA in peptide/ligand ratios 1:1 and 1:2 and hIAPP in presence of Sil B in peptide/ligand ratios 1:1 and 1:2. Positive values (represented in red) indicate an increase in the probability of these dihedral angles and, henceforth, of the corresponding structure, while negative values (represented in blue) indicate a decrease of it.

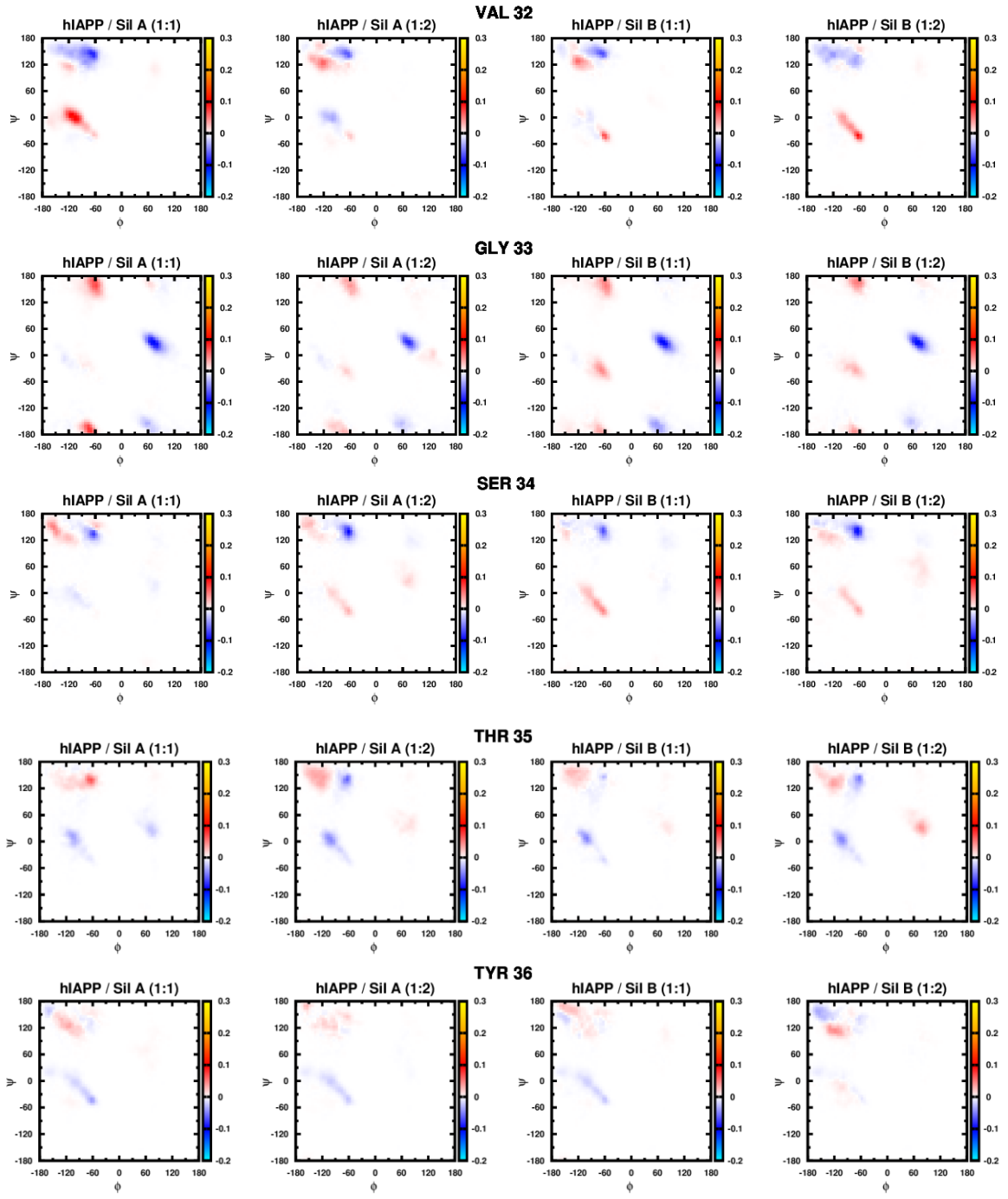

Supplementary Figure S13 – Changes in Ramachandran probability distributions of the residues V32, G33, S34, N35 and T36.Data are represented as the difference between Ramachandran probability distributions of hIAPP in the presence and absence of the ligand. From left to right: hIAPP in presence of SilA in peptide/ligand ratios 1:1 and 1:2 and hIAPP in presence of Sil B in peptide/ligand ratios 1:1 and 1:2. Positive values (represented in red) indicate an increase in the probability of these dihedral angles and, henceforth, of the corresponding structure, while negative values (represented in blue) indicate a decrease of it.